Bio-Micro-Systems for Diagnostic Applications, Disease Prevention and Creating Tools for Biological Research

by

Amrita Ray Chaudhury

A dissertation submitted in partial fulfillment
of the requirements for the degree of
Doctor of Philosophy
(Biomedical Engineering)
in The University of Michigan
2018

Doctoral Committee:

Associate Professor, Nikos Chronis, Chair
Assistant Professor, Timothy M. Bruns
Associate Professor, Catherine Collins
Assistant Research Scientist, Eleni Gourgou
Assistant Professor, Geeta Mehta

Amrita Ray Chaudhury
amritarc@umich.edu
ORCID iD: 0000-0002-1703-1482

DEDICATION

This thesis is dedicated to my family and friends in India and Ann Arbor.

ACKNOWLEDGEMENTS

First and foremost, I would like to express my sincere gratitude to my research advisor Prof. Nikos Chronis for his continuous guidance, mentorship, patience and motivation throughout my graduate school years without which nothing would be possible.

I would also like to thank the members of my committee: Prof. Catherine Collins, Prof. Geeta Mehta, Prof. Tim Bruns and Dr. Eleni Gourgou, for their constant encouragement and insightful feedback that pushed me to improve my research.

My sincere thanks also goes to Shawn O'Grady, Prof. Allen Liu, Prof. Jianping Fu and Prof. John Hoard, who provided access to their laboratory and research facilities. In particular, I would like to thank Prof. Kurabayashi and Prof. Catherine Collins for the encouragement and mentorship that I received from them and their group members.

I thank my exceptionally talented labmates and collaborators Dr. Alexandros Pantazis, Dr. Ryan Insolera, Dr. Ning Gulari, Dr. Maria Dafni Bazopoulou and Dr. Eleni Gourgou for all the stimulating discussions, training, for the hours spent working together before deadlines, and most importantly for all the light-hearted moments that we shared over the last four years.

I would like to extend my deepest gratitude to the Department of Biomedical Engineering for supporting me as a GSI for multiple semesters and for frequently nominating me for scholarships/fellowships/awards. It was an honor and a privilege to have gotten the opportunity to work with Dr. Rachael Schmedlen, Dr. John Gosbee and Prof. Geeta Mehta as their GSI. In particular, I would like to thank Susan Douglas, Maria Steel and Patty Freundl without whom I could not have navigated through the rigors of graduate school.

Last but not the least, I would like to thank my parents, grandmother, cousin, aunt and my friends in Ann Arbor, Mainak, Shiyang and Jau-Ching for their constant emotional and moral support.

PREFACE

Bio-MicroElectroMechanical Systems (BioMEMS) – microfabricated sensors, actuators and microfluidic and lab-on-chip systems- is an emerging field that targets to develop miniaturized devices for the diagnosis, monitoring and treatment of diseases as well as to provide enabling tools to researchers in the life sciences. In the past few years, three dimensional (3D) printing technology has also joined the effort of miniaturization with high resolution 3D printers capable of fabricating micrometer scale objects. Furthermore, the increase in material choice has led to an explosive growth in microfabrication technology based biomedical applications.

This thesis, divided into two parts, describes the development of 5 novel Bio-Micro-System devices (Figure 1). The term Bio-Micro-System has been used here to describe BioMEMS and 3D printed devices, with the dimensions of key device components ranging from micrometers to a millimeter. The first part of the thesis (part A) is focused on 'Medical' Micro-System devices that can potentially solve common medical problems: two intraocular pressure sensors for monitoring glaucoma and a smart skin for combating community acquired infections. The second part of the thesis (part B) is focused on 'Biological' Micro-System devices for facilitating/enabling biological research. Those devices/tools are able to accurately manipulate small model organisms for various in vivo studies.

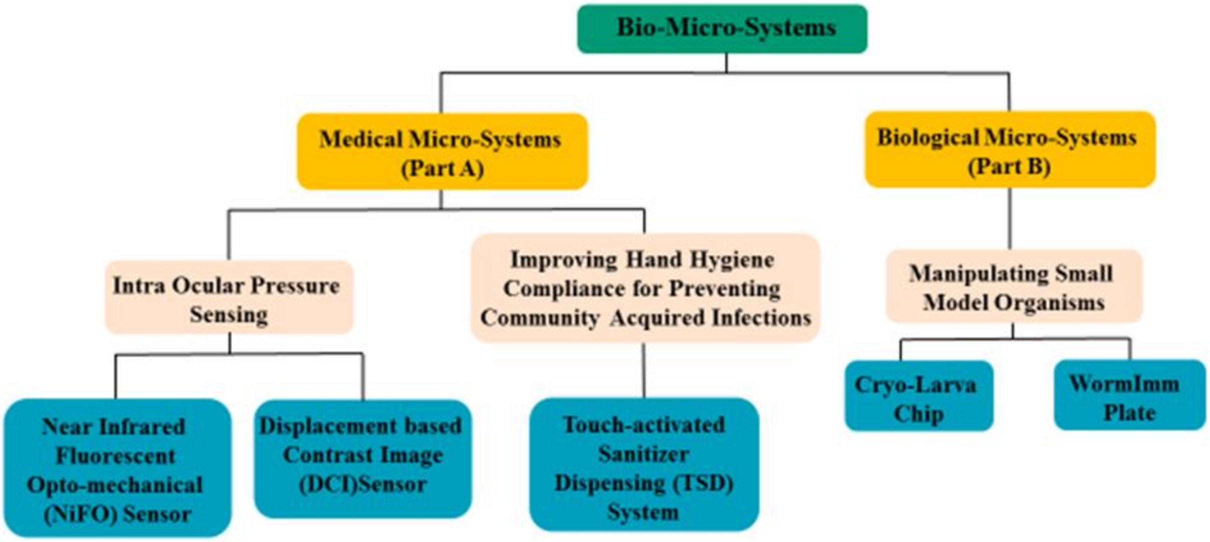

Figure 1: Thesis outline.

PART A- Medical Bio-Micro-Systems

The demand for medical products continues to grow with electronic technologies as their important constituents. Despite being a high-growth sector, electronic components including sensors, power sources, control units, and wireless communication modules increase product complexity, especially for medical implants. The design and manufacturing of those systems is accompanied by several engineering challenges including leak proof integration/packaging, affordable production costs, low energy consumption to avoid frequent battery replacements, MRI compatibility and material biocompatibility. The contribution of this thesis is the development of novel passive, Medical Micro-Systems that have no electronics and therefore they do not require any power to operate. Specifically, Part A describes:

- Implantable, electronics-free, intraocular pressure microsensors. Intra Ocular Pressure (IOP) Monitoring is central to the diagnosis and management of glaucoma and must be frequent and accurate to assess treatment efficacy. The gold standard method, Goldmann Applanation Tonometry (GAT),is bulky, complex and requires clinic visits making frequent IOP monitoring challenging. Motivated by the need for frequent, long-term IOP pressure monitoring, we developed two pressure sensing technologies: 1) ‘Near Infrared Fluorescence-based Optomechanical (NiFO)’ technology and 2) ‘Displacement based Contrast Imaging’ (DCI) technology.

1) NiFO technology: Consists of an implantable, passive, miniaturized pressure sensor that ‘optically encodes’ pressure in the near infrared (NIR) regime. A non-implantable, portable and compact optical head is used to excite the sensor and collect the emitted NIR light. The thesis discusses optimized device architecture and microfabrication approaches for best performance commercialization.

2) DCI technology: We present a proof of concept, fluid pressure sensing scheme that is shown to operate over a pressure range of 0–100 mbar (∼2 mbar resolution between 0–20 mbar,∼10 mbar resolution between 20–100 mbar), with a maximum error of <7% throughout its dynamic range. The thesis introduces the technology and discusses its application as an IOP sensor.

The NiFO technology is expected to not only help manage IOP, but also other elevated pressure conditions such as intracranial, bladder, abdominal, blood and joint pressures. The DCI technology on the other hand, is expected to provide home-based, frequent, life-long IOP self-monitoring for patients with moderate/severe glaucoma.

-A smart-skin for combating community acquired infections. Community Acquired Infections (CAIs) ranging from diarrhea to respiratory diseases are caused by a broad range of vectors which are transmitted through un-sanitized hands. Washing hands with soap and water is the gold standard approach for fighting CAIs, but it requires access to clean water and willingness of the end user to wash their hands. To overcome those issues, a novel device for decontaminating surfaces was developed: the Touch-activated Sanitizer Dispensing (TSD) System.

The TSD can be mounted on any surface that is exposed to high human traffic such as a door handle and consists of an array of passive, human-powered, miniaturized valves that deliver a small amount of an alcohol based disinfectant when touch actuated. The device thereby disinfects the person’s hand that is touching the surface over which the TSD is mounted while being self-sterilized at the same time without requiring any maintenance besides replacing the cartridge that contains the disinfectant. The thesis describes the design and implementation of a proof of concept TSD that can disinfect an area equivalent to the size of a thumb. A significant (~ 10 fold) reduction in microbiological load is demonstrated with a drop in average Colony Forming Units/cm^2 from 1.52 to 0.05 and 0.37 to 0.03 for the fingertip and device surface respectively within the first 24 hours. The size and footprint of the TSD can be scaled up as needed. We believe that its usage in public places will significantly improve hand hygiene compliance and reduce CAIs.

PART B- Biological Bio-Micro-Systems

Small model organisms –such as *Caenorhabditis elegans* and *Drosophila Melanogaster* larvae - are widely used for studying related principles of health and diseases in humans. Being

transparent, they allow direct imaging of biological processes. However, the biggest challenge associated with *in vivo* imaging is ensuring immobilization. Conventional methods (glue or dissection) adversely affect biological processes under investigation. Taking advantage of recent advances in microfabrication and 3D printing, this thesis describes two devices for immobilizing *Drosophila melanogaster* larvae and *Caenorhabditis elegans* respectively. Both devices immobilize the animal on demand and allow *in vivo* imaging while minimizing physiological damage with fast recovery.

- Cryo-Larva Chip: A cryo-anesthesia microfluidic chip for immobilizing Drosophila melanogaster larvae. We developed a microfluidic chip for immobilizing *Drosophila melanogaster* larva by creating a cold micro-environment around the larva. After characterizing on chip temperature distribution and larval body movement, results indicate that the method is appropriate for repetitive and reversible, short-term (several minutes) immobilization. The method offers the added advantage of using the same chip to accommodate and immobilize larvae across all developmental stages (1st instar-late 3rd instar). Besides the demonstrated applications of the chip in high resolution observation of sub cellular events such as mitochondrial trafficking in neurons and neuro-synaptic growth, we envision the use of this method in a wide variety of biological in vivo imaging studies employing the *Drosophila* larval system, including cellular development and other studies.

- The WormImm Plate: A 3D printed millifluidic device for CO_2 immobilization of *Caenorhabditis elegans* populations. We developed a novel 3D printed device for immobilizing populations of *Caenorhabditis elegans* by creating a localized CO_2 environment while the animals are maintained on the surface of agar. The results indicate that the method is easy to implement, is appropriate for short-term (20 minutes) immobilization and allows recovery within a few minutes. We envision its use in a wide variety of biological studies in *Caenorhabditis elegan*, including cellular development and neuronal regeneration studies.

We think that the work demonstrated in this thesis will lead to commercializable devices while also expanding the toolsets available for conducting medical diagnostics and biological research studies.

TABLE OF CONTENTS

PART A - MEDICAL MICRO SYSTEMS

PART B - BIOLOGICAL MICRO SYSTEMS

LIST OF FIGURES

LIST OF APPENDICES

LIST OF TABLES

ABSTRACT

This thesis, divided into two parts, describes the development of 5 novel Bio-Micro-System devices. The term Bio-Micro-System has been used here to describe BioMEMS and 3D printed devices, with the dimensions of key components ranging from micrometers to a millimeter. Part A is focused on 'Medical' Micro-System devices that can potentially solve common medical problems. Part B is focused on 'Biological' Micro-System devices/tools for facilitating/enabling biological research.

Specifically, Part A describes two implantable, electronics-free intraocular pressure (IOP) microsensors for the medical management of glaucoma: 1) Near Infrared Fluorescence-based Optomechanical (NiFO) technology - Consists of an implantable, pressure sensor that 'optically encodes' pressure in the near infrared (NIR) regime. A non-implantable, portable and compact optical head is used to excite the sensor and collect the emitted NIR light. The thesis discusses optimized device architecture and microfabrication approaches for best performance commercialization. 2) Displacement based Contrast Imaging (DCI) technology - A proof of concept, fluid pressure sensing scheme is shown to operate over a pressure range of 0–100 mbar (∼2 mbar resolution between 0–20 mbar,∼10 mbar resolution between 20–100 mbar), with a maximum error of <7% throughout its dynamic range. The thesis introduces the DCI technology and discusses its application as an IOP sensor.

Moreover, Part A also describes a Touch-activated Sanitizer Dispensing (TSD) system for combating community acquired infections. The TSD can be mounted on any surface that is exposed to high human traffic and consists of an array of human-powered, miniaturized valves that deliver a small amount of disinfectant when touch actuated. The device disinfects the person's hand that is touching it while being self-sterilized at the same time. The thesis describes the design and implementation of a proof of concept TSD that can disinfect an area equivalent to the size of a thumb. A significant (~ 10 fold) reduction in microbiological load is demonstrated on the fingertip and device surface within the first 24 hours. The size and footprint of the TSD can be scaled up as needed to improve hand hygiene compliance.

In Part B, we developed a microfluidic chip for immobilizing *Drosophila melanogaster* larva by creating a cold micro-environment around the larva. After characterizing on chip temperature distribution and larval body movement, results indicate that the method is appropriate for repetitive and reversible, short-term (several minutes) immobilization. The method offers the added advantage of using the same chip to accommodate and immobilize larvae across all developmental stages (1st instar-late 3rd instar). Besides the demonstrated applications of the chip in high resolution observation of sub cellular events such as mitochondrial trafficking in neurons and neuro-synaptic growth, we envision the use of this method in a wide variety of biological imaging studies employing the *Drosophila* larval system, including cellular development and other studies.

Finally, Part B also describes a 3D printed millifluidic device for CO_2 immobilization of *Caenorhabditis elegans* populations. We developed a novel 3D printed device for immobilizing populations of *Caenorhabditis elegans* by creating a localized CO_2 environment while the animals are maintained on the surface of agar. The results indicate that the method is easy to implement, is appropriate for short-term (20 minutes) immobilization and allows recovery within a few minutes. We envision its use in a wide variety of biological studies in *Caenorhabditis elegan*, including cellular development and neuronal regeneration studies.

PART A – Medical Micro Systems

CHAPTER 1

INTRODUCTION

1.1 Motivation

Medical electronic devices - A history of 100 years: In the 20th century, biology and medicine have been revolutionized by the development of electronic devices. The first practical electrocardiograph, invented approximately 100 years ago is one of the first electronic devices that helped establish the field of cardiology. Since the 1950s, medical technology, especially the ones involving electronic systems have undergone a significant transformation, leading to the establishment of "bioelectronics", which is a discipline combining biology and electronics [2].

Apart from being critical to the development of radiology (lead to the evolution from single modality X-rays to Magnetic Resonance Imaging (MRI), Computed Tomography (CT), and Positron Emission Tomography (PET)), electronics systems have played a central role in the invention of several e*x vivo* as well as implantable medical devices capable of interfacing with living tissues and organs at milli, micro- and nano-scales.

Advances is electronics technologies has led to a several miniature and wireless devices such as gastric/cardiac pacemakers, cochlear implants, cardiovascular defibrillators, cardiovascular pressure sensors and neuromuscular stimulators being implanted in patients worldwide [2] [3] [4] [5] [6] with Figure 1.1 showing several examples of electronic devices for *in vivo* applications. It is estimated that over 25 million people in the US are heavily reliant on implantable medical devices for critical life-sustaining functions [7] (the number of implantable cardioverter defibrillators being sold alone has increased tenfold between 1990 and 2002 [8]). On the other hand, the field of *ex vivo* medical devices has witnessed a huge growth in the form of electronics devices that are in contact with either skin or mucosa for monitoring critical biomedical parameters as well as for tracking activity (Figure 1.2). These devices generally comprise of sensors (accelerometers for tracking movement, gyroscopes for tracking position, pressure sensors, temperature sensors, humidity sensors, etc), wireless communication systems, user interactive displays and power management units.

Rapid development in semiconductor technology, particularly in the areas of micro-electro-mechanical systems (MEMS) and microfluidic lab-on-chip biomedical systems has enabled the development of these i*n vivo* and ex *vivo* systems for rapid diagnostics and administering complex therapeutics [9] [10] [11] [12] [13] [2].

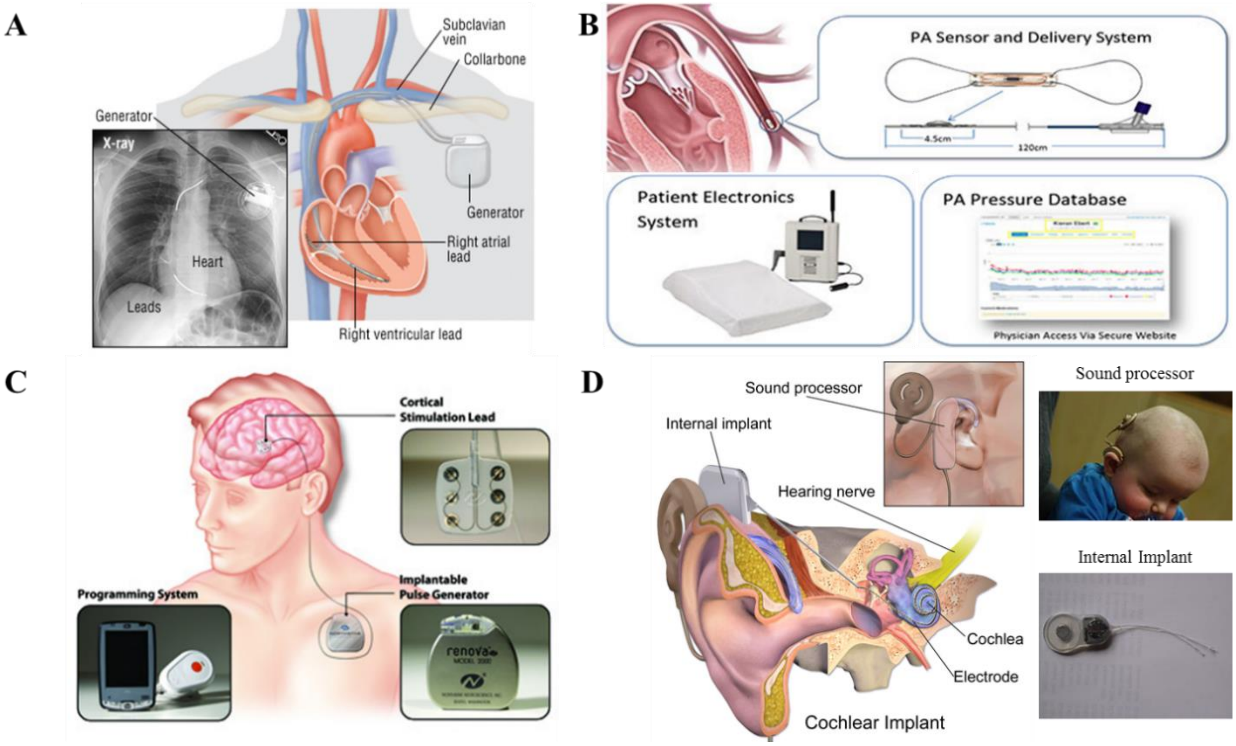

Figure 1.1: *In vivo* medical electronic devices: (A) An implantable cardiovascular defibrillator treats arrhythmias by administering electrical shocks to the heart. It consists of a pulse generator implanted under the skin below the collarbone and analyzes signals form the heart to generate electrical impulses. Electrodes, connected to the pulse generator, travel to the heart to deliver the electric impulses [Figure and caption appears in **[14]**]. (B) The CardioMEMS HF System measures pulmonary artery (PA) pressures using an implantable capacitive telemetric sensor that couples with an external coil unit in patients with heart failure and allows health care professionals to remotely monitor their patients [Figure and caption appears in **[15]**]. (C) The Northstar Stroke Recovery System is an implantable device that enhances neuroplasticity in patients after a stroke. It consists of an implantable pulse generator (IPG) implanted in the pectoral area. A stimulation electrode lead is connected to the IPG and is used to deliver stimulation to the cortex. A programming handheld computer communicates with the IPG to control it. [Figure and caption appears in **[16]**] (D) The Medline Plus Cochlear implant (CI) is an implantable device that provides a sense of sound to a person who is profoundly deaf. It bypasses the normal hearing process with a sound processor that resides on the outside of the skin (worn behind the ear) amd consists of microphones, electronics, battery, and a coil which transmits signals to the implant. The implant has a coil to receive signals, electronics, and an array of electrodes which is placed into the cochlea, which stimulate the cochlear nerve [Figure and caption appears in **[17]**]

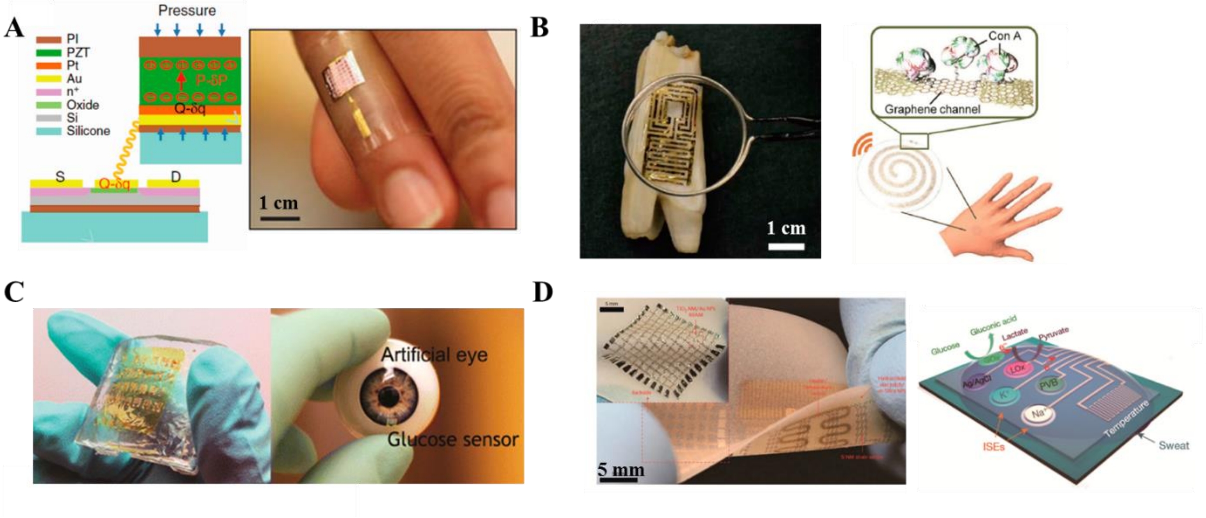

Figure 1.2: *Ex vivo* medical electronic devices: (A) Physical sensing – An ultrathin inorganic piezoelectric pressure sensor patterned on an elastomeric substrate enables the measurement of small changes in arterial pressure after mounting on skin in order to detect early onset of cardiovascular disease [Figure and caption appears in **[18]**]. (B) Wireless sensing – Graphene, a material that is highly sensitive to analyte detection, is printed onto water soluble silk followed by the biotransfer of graphene nanosensors onto tooth enamel to create a fully biointerfaced sensing platform. Using the self-assembly of antimicrobial peptides onto graphene, the sensor is capable of detecting bacteria at the single-cell level. Incorporation of a resonant coil enables wireless data transfer [Figure and caption appears in **[19]**]. (C) Chemical sensing – A thin, sensitive In_2O_3 -based conformal biosensor on ultrathin polyimide films based on field-effect transistors using facile solution-based processing. Immobilized In2O3 field-effect transistors functionalization with glucose oxidase enabled D-glucose detection at physiologically relevant levels [Figure and caption appears in **[20]**]. (D) Multiplexed sensing - A flexible and fully integrated sensor array for performing in situ perspiration analysis. The device simultaneously and selectively measures sweat metabolites (glucose and lactate) and electrolytes (sodium and potassium ions) while also measuring skin temperature. Plastic-based sensors have been merged with silicon integrated circuits on a flexible circuit board for complex signal processing while measuring the detailed sweat profile of human subjects engaged in prolonged indoor and outdoor physical activities to assess in real time the physiological state of the subjects [Figure and caption appears in **[21]**].

1.2 Current challenges

1.2.1 *In vivo* implantable electronics devices

In spite of substantial innovations in the development of biomedical electronic systems, they are still faced with a number of challenges [22] [23] [24] [2].

Size and weight: There is increased focus towards diminishing the size and weight (less than 2% of the patient's body weight [22]) of *in vivo* devices in order to make them compatible with normal human activities, to enable the surgeon to implant them easily and to enhance host comfort. Batteries (single-use or rechargeable) significantly contribute to the device weight and size.

Commonly used single-use, non-rechargeable batteries in particular, such as those found in cardiac pacemakers and deep brain stimulators, have a predetermined lifespan at the end of which they have to be surgically replaced which significantly increases costs [2].

Power management and interference: In the i*n vivo* environment, good device functionality and reliability is critical in order to support real-time stimulation, data collection, data compression and fast wireless data transmission to external components of the electronics system. All these requirements increases the complexity of the signal processing circuitry and adds to the power budget of the device, which should ideally remain very low if the device is to remain operational for extended periods of time. For instance, even though an ultra wide band technology provides high-speed data transfer between the implanted device and the medical practitioner, its power consumption is very high which severely restricts its implementation in an i*n vivo* medical device. Furthermore, wireless devices are susceptible to interference as they operate in an electromagnetically shared environment. For example, external electromagnetic pulses and electric fields as well as those generated from other *in vivo* electrical devices can all generate electromagnetic interference. Additionally, since health practitioners can easily interrogate implanted devices (pacemakers, glucose-monitoring and insulin-delivery systems, neural stimulators and smart prosthetics), they are vulnerable to hacking [25] [26] [2] which means that apart from having access to sensitive patient information, the devices can be reprogrammed, thereby interfering with correct device operation. Therefore, security measures like security check protocols, firewalls, data encryption and restricted network access needs to be included which further adds to device cost as well as complexity [2].

MRI compatibility: The biological effects from the electromagnetic field sources that electronics devices produce have become a serious cause for concern. The magnetic resonance (MR) environment may pose problems to patients with electromagnetic field generating implants like MRI-related heating and the creation of artifacts which are big negatives, given the growing importance of MRI as a diagnostic imaging modality for many disease conditions. Besides tissue heating, there might be athermal effects, like the increased risk of cancer, on the biological environment of the electromagnetic field generating implant.

Durability and biocompatibility: The *in vivo* environment is harsh as the implant is constantly being attacked by conductive and corrosive fluids containing biochemically reactive molecules. Additionally, large mechanical forces and torques could be applied to the device *in vivo*. Therefore, the device has to be both mechanically as well as chemically durable to survive this environment. Efforts towards creating small, light and flexible electronics devices, although highly desirable, may undermine mechanical robustness. Aggressive cleaning procedures, if used prior to implantation, may further contribute to the structural breakdown of the device. Besides being detrimental to the performance of the device, mechanical/chemical degradation could lead to device failure such as electrical shorting thereby requiring subsequent surgical removal. Furthermore, the implanted device along with any debris/by-products from degradation may stimulate activation of a range of immune responses like inflammation and tissue damage with leachant/fragment toxicity hindering recovery of adjacent damaged tissues. Therefore, due to the dynamic and complex nature of the *in vivo* environment as well as the host's immune response to synthetic and organic materials used in electronics device fabrication, achieving biocompatibility is extremely challenging. In applications where *in vivo* sensing or stimulation is required for a short period of time, resorbable implantable electronic devices made up of biodegradable materials can provide a solution that overcomes the challenges of inflammation/infections that are commonly associated with long-term implantation with the degradation products eliciting a minimal toxicity response [27] [2]. However, fabricating complicated high-performance electronic systems from entirely biodegradable materials is a difficult undertaking, particularly at sub-millimeter scales.

Component lifespan: Most electronic components have life cycles that are shorter than the life cycle of the end product itself which is especially true for medical devices. While most consumer electronics have lifecycles of around 18 months, many medical device implants have a product life in excess of a decade. Medical devices are typically not fitted with technology upgrades because of high costs and lengthy development times. Therefore, there are often significant challenges to modify, upgrade, and maintain electronics systems over the entire life of the device. The majority of medical devices are “safety critical", and therefore require time-consuming and costly qualification and certification cycles, even for seemingly minor design changes. As a result, medical device OEMs are more focused on sustaining their products for long periods of time (often 5–10 years or longer) rather than upgrading them. Obsolescence issues occur when the 'slow-to-change' medical device industry relies on a supply chain that was originally and primarily developed to support a rapidly changing consumer electronics industry. The medical device industry typically has less control over their electronic part supply chain because they have relatively low production volumes compared to consumer electronics. To add to the electronic component obsolescence problem, any change to a medical device design requires an evaluation related to product risk and performance. The change of a critical component, especially if it is part of an implant, would require notification and re-certification with the FDA with a revision to the existing 510(k) submission or PMA. Therefore, the need to replace a critical component that goes obsolete can be extremely expensive from a cost, resource and time perspective [2] [28].

In conclusion, application of nano- and micro-scale technologies for design and fabrication of implantable circuitry can lead to remarkable advancement in integration density and dynamic power dissipation [29] [2]. However, current biomedical nano and micro technologies are still faced with several challenges such as low long term reliability, high stand-by power consumption, high thermal dissipation within the implant circuitry and electron leakage due to insufficient insulation [30] [31] [2]. Given the high costs and time associated with surgical device implantation followed by extended patient recovery, long-term reliability of the device is crucial.

1.2.2 *Ex vivo* electronics devices

Several *ex vivo* electronic device systems have been proposed by the scientific community and quite a few of them have even been commercialized for monitoring biomedical parameters. However, there still remain some challenges towards implementing these device technologies as discussed below:

Accuracy: The accuracy of high performance devices, particularly sensors, is highly affected by external noise sources such as human motion. In order to perform noise cancellation, additional signal processing circuitry must be incorporated along with the involvement of advanced packaging and manufacturing methods, all of which increase system complexity, size and cost [32] [33].

Risk of injury: Even mild electric shocks maybe a hazard for devices that come into contact with skin. Additionally, since these is a tendency for the internal temperatures of electronic components to rise over time, there is a risk of burning the skin. Depending on the situation or the environment in which batteries are used, there is a possibility of ignition/explosion due to a sudden increase in temperature. The presence of metal in electronic devices could cause skin allergies due to prolonged contact. Exposure to continuous electromagnetic field energy could cause an increase in the core body temperature and high frequency burns [32] [33].

Comfort: Devices that make prolonged contact with skin must be easy to wear, easy to carry and above all, they must be comfortable. Existing devices are made up of bulky components that must be miniaturized to ensure patient/user comfort [32] [33].

Durability: Electronic devices are generally not robust to extreme temperature and humidity conditions with waterproofing being challenging in particularly wet conditions [32] [33].

1.3 Need for innovation: Electronic-free devices

Given these problems, passive electronics-free devices are becoming increasingly desirable for medical applications. Unlike active devices, they do not require on-board batteries and the problem of replacing the power supply does not exist. They are significantly less complicated, smaller, cheaper and require no maintenance resulting in a virtually unlimited lifespan. This thesis introduces a new generation of medical devices and demonstrates the design and implementation of three novel, powerless, electronics-free, wireless, MRI-safe transducer systems. In these devices, the transduction is achieved directly by the human body. They can be used as standalone devices or in conjunction with each other for biomedical sensing, diagnosis and disease prevention applications (Figure 1.3).

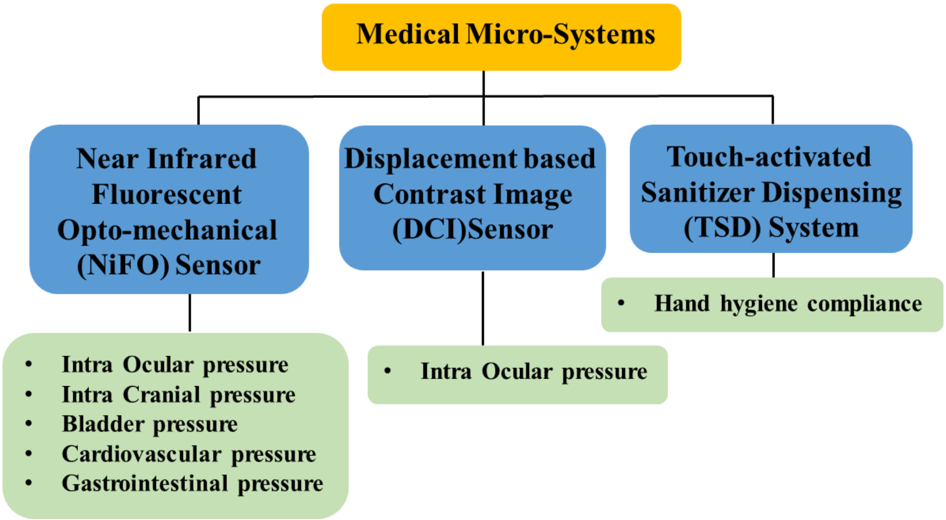

Figure 1.3: Overview of the medical devices presented in the thesis showing biomedical applications of these device technologies.

In this thesis, 3 novel (2 *in vivo* and 1 *ex vivo*), electronics free, medical micro device will be described:

1) <u>Near Infrared Fluorescence-based Optomechanical (NiFO) Sensor:</u> Pressure sensor for frequent and continuous intraocular pressure monitoring for the medical management of glaucoma. This is a platform technology that may also be used for other biomedical pressure monitoring applications like intracranial, arterial blood, bladder and gastrointestinal pressure.
2) <u>Displacement based Contrast Imaging (DCI) Sensor:</u> Pressure sensor for use in the diagnosis, medical management and treatment of intraocular hypertension related diseases like glaucoma.
3) <u>Touch-activated Sanitizer Dispensing System (TDS):</u> Device for use in improving hand hygiene compliance for preventing hospital and community acquired infections.

1.4 Biomedical pressure monitoring

Pressure in various organs of the body is highly regulated and its value can provide an indication of patient health and/or disease progression [34]. In diseases where this ability to regulate pressure is lost, impairment of organ function or even death may result. Monitoring the variation of internal pressures allows diagnosis of the disease condition as well as tracking the progress of any medical intervention [34].

In current medical practice, it is common to obtain a single pressure data point in the clinic for a patient. However, this information captures just limited snapshots of the organ's dynamic pressure profile. It does not capture peak/trough values or profile changes that can provide important clues to plan appropriate intervention strategies. Also, the measurements may be perturbed by the stress experienced by some patients when visiting clinical settings [34]. Therefore, advances in sensing technology to enable convenient, accurate, and continuous pressure monitoring that can extend to settings outside the clinic may enable more effective disease management.

Taking advantage from recent developments in the MEMS field, we propose and develop two electronics free medical pressure sensing technologies that overcome the limitations that have been discussed up until now, the 'Near Infrared Fluorescence-based Optomechanical (NiFO)' technology and the 'Displacement based Contrast Imaging (DCI)' technology. The thesis focuses on monitoring Intra-Ocular Pressure (IOP) for the medical management of glaucoma as the end application for both sensing technologies. While the DCI technology has the potential to efficiently manage and treat ocular hypertension diseases like glaucoma, the NiFO technology, besides monitoring IOP, can be used in a variety of biomedical applications including, intracranial, cardiovascular and gastrointestinal pressure monitoring as well.

1.4.1 Clinical need for monitoring IOP

Primary Open-Angle Glaucoma (POAG or simply known as ‘glaucoma’) is a chronic eye disease that results in the insidious, gradual visual field loss and finally total blindness due to the progressive damage of the optical nerve [35]. POAG accounts for 90% of the total glaucoma cases, it is responsible for more than 120,000 blind people in the US and it is the foremost cause of preventable blindness [36]. According to the The Eye Diseases Prevalence Research Group at the National Institute of Health, the prevalence of glaucoma is 2% between the ages of 60 and 69, spiking to 8% in the age category 80 and over [37]. This corresponded to a prevalent U.S. population of 2.2 million in 2000, growing at a compound annual growth rate of 1-1.5% to 3.36 million by 2020 over [37]. Estimates put the total number of POAG patients at 44.7 million worldwide [38], with 58.6 million cases projected worldwide by 2020 [39].

In a healthy eye, a clear fluid (called aqueous humor) circulates inside the anterior portion. To maintain a constant and normal IOP, the eye continually produces a small amount of aqueous humor while an equal amount of the fluid is drained out through the trabecular meshwork. POAG occurs when this drainage system becomes inefficient over time, causing fluid pressure inside the eye to rise. This build up of fluid pressure in the eye over time may cause damage to the optic nerve. Therefore, a major risk factor for POAG is considered to be the elevation of IOP [40], a condition also known as ocular hypertension (when IOP > 21 mmHg). IOP management is based on IOP monitoring and the daily use of eye drops (or eye surgery in severe cases) that lowers the IOP. These treatments can decelerate the progress of the disease but they cannot regain vision [41].

Currently, IOP is measured during the patient’s visit in a hospital or in an ophthalmological clinic by a trained nurse. Such a ‘sporadic’ IOP monitoring practice has two significant drawbacks:

- It might give a ‘false’ IOP value at the time of the examination as studies have shown that IOP fluctuates as high as 6-8 mmHg during a 24-hour period period [42]. These studies also revealed that peak 24-hour IOP values were higher than peak IOP values measured during office hours in 60-70% of the cases, resulting in an immediate treatment change in the majority of the cases.

• It is not practical to closely monitor short-term IOP variations (e.g. in severe glaucoma cases) as that would require weekly or bi-weekly visits. That becomes problematic especially with older people (where POAG is prevalent) who might need assistance to reach the hospital.

It is therefore necessary to continuously monitor IOP for life in POAG patients to: (i) capture the daily IOP fluctuations and therefore establish maximum IOP values, (ii) assess the short-term and long-term progression of the disease, and (iii) evaluate the efficacy of medical or therapies in optimizing IOP control.

1.4.2 Current practices for monitoring IOP

Goldmann Applanation Tonometry (GAT) is the gold standard for measuring IOP in a clinical setting [43]. It employs a force transducer (or an air puff [44]) that flattens part of the outer surface of the eye (Figure 1.4). The IOP is obtained by measuring the force and the deflected area (area of applanation). Despite the fact that tonometry is a non-invasive and simple to execute technique, it has several disadvantages:

- it is an indirect technique and therefore subject to errors. The measured IOP value depends on the corneal thickness and biomechanical properties of the applanation area, the exact position of the measurement on the cornea, the body habitus, and finally the skills of the ophthalmic technician or physician taking the measurement. Studies have estimated that tonometric IOP measurements are not precise enough to measure the true IOP within an error of few mmHg [45].
- it requires a visit to the hospital or to a clinic as the measurement is performed by a trained personnel (e.g. a nurse). Therefore, tonometry is not a practical solution for closely monitoring IOP in PAOG patients.

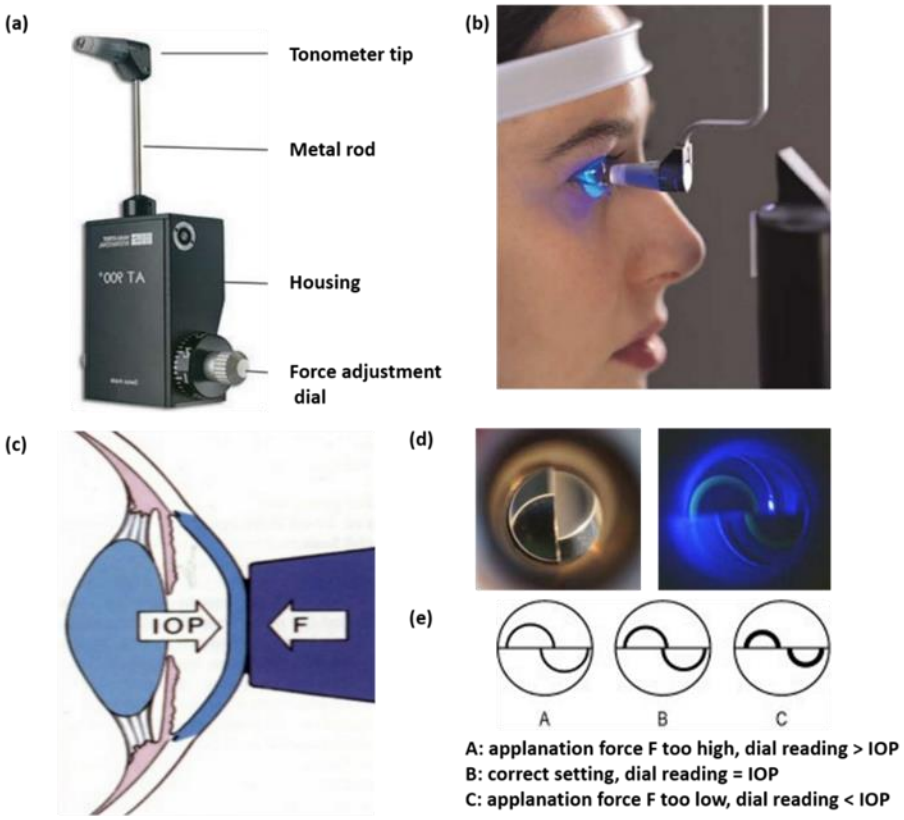

Figure 1.4: (a) Image showing parts of the Goldmann applanation tomoneter. (b) Image showing the tonometer being used to measure IOP of a patient. (c) Schematic showing principle of operation of the instrument. (d) Bright field as well as fluorescent image showing the tip. (e) Schematic showing observed positions of the tip and what they represent. [Figures and captions appear in are taken from **[46]**]

Two alternative schemes have been proposed and are on the path to commercialization so far for point-of-care, continuous IOP monitoring: (a) contact lens-based IOP monitoring [47], and (b) direct IOP monitoring using implantable sensors [48] [49]. The former technology is a non-invasive, indirect approach that integrates a MEMS (Micro-ElectroMechanical Systems) pressure sensor into a contact lens (currently commercialized by *Sensimed AG*, Figure 1.5). It suffers from inaccuracy (inherent to all indirect techniques) and high levels of 'IOP noise' due to the non-rigid adherence of the contact lens into the eye. In the latter approach, a MEMS pressure sensor is inserted along with an Intra Ocular Lens (IOL) inside the lens capsule (currently under clinical trial by *Eyemate*, Figure 1.6) or it is permanently attached to the iris. It is a direct technique and therefore more accurate than tonometry. As it requires a surgery, it is targeted to severe POAG cases or POAG patients undergoing cataract surgery.

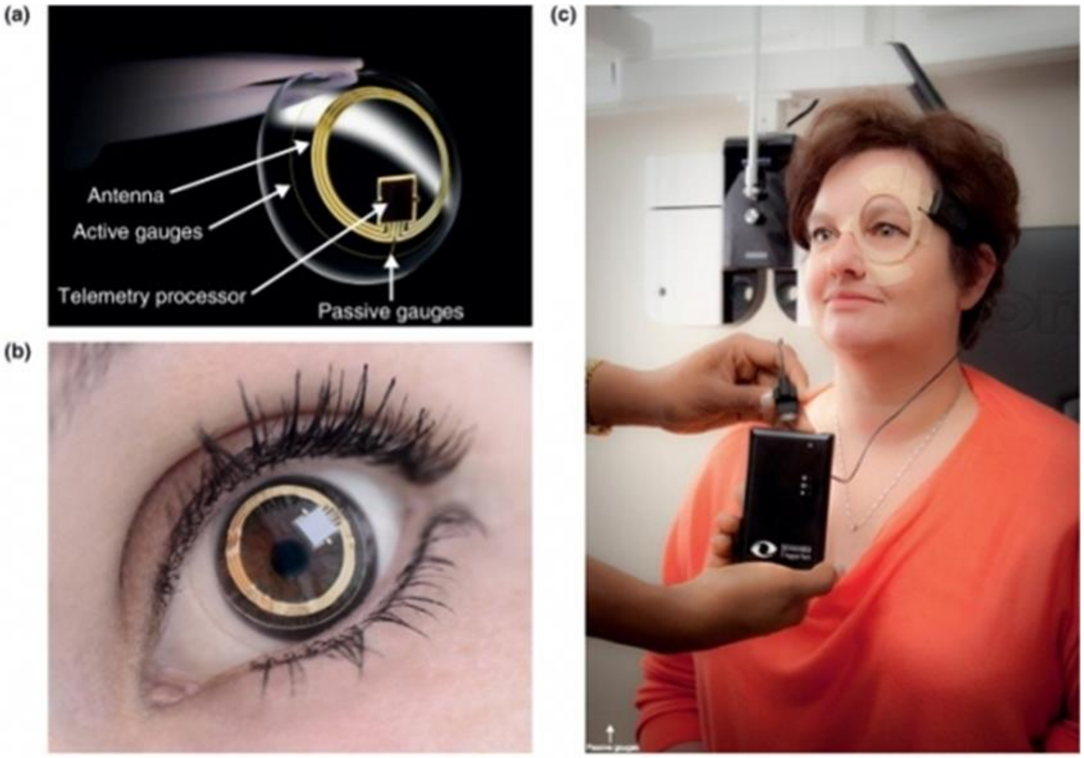

Figure 1.5: (a) A soft contact lens developed by Sensimed Triggerfish for long-term (up to 24 hours) active measurement of intra-ocular pressure, a key indicator of glaucoma. Within the lens are small gauges and a transmitter. (b) The device placed on the surface of the cornea. (c) The transmitter sends an output signal to a larger antenna affixed to a bandage worn around the eye. This antenna is then cable-connected to a recorder. From the recorder, the data is downloaded to the practitioner's computer via Bluetooth. [Figures and captions appear in and are taken from **[50]**]

Figure 1.6: (a) The EYEMATE® IOP pressure measurement system consists of an implantable micro sensor, responsible for pressure sensing which is surgically inserted into the eye behind the iris. The system also consists of an external hand held device which transfers energy to the micro sensor telemetrically and is responsible for data read out and storage. (b) Measurement data is transferred to an internet-based database which allows the physician to remotely access information about the disease status of the patient. [Figures and captions appear in and taken from **[51]**]

The major disadvantage of both these methods is the need for a wireless transmission unit that is built into the pressure sensor. The entire transducer that integrates low-power electronics, telemetric elements (e.g. antennas) and/or batteries is bulky (of a typical size of ~2 mm x 2 mm x 0.5 mm, not including the battery) resulting in partial blocking of the visual field. An optical, electronic-free approach is therefore needed that will reduce the device size while matching or even improving upon performance.

1.5 Preventing hospital and community acquired infections

Infectious diseases, dating back to the beginning of mankind, present an important public health concern as they cause both increased morbidity as well as mortality. Infections maybe broadly categorized as either community-acquired or hospital-acquired.

Hospital Acquired Infections (HAIs) are infections affecting patients and healthcare personnel in hospitals and other health-care facilities that are not present at the time of admission. The prevalence of HAIs is extraordinary: of every 100 hospitalized patients, 7 in developed and 10 in developing countries will contract at least one health care-associated infection [52]. In the US, HAIs infections are responsible for over 100,000 deaths every year [53]. According to the European Centre for Disease Prevention and Control more than 4 million episodes of HAIs are reported every year in Europe [54], accounting for ~40,000 deaths. Apart from morbidity and mortality, HAIs cause prolonged medical stays, and a remarkable increase in the annual cost for medical treatment. Annual financial losses due to HAIs are estimated to be $6.5 billion in the US. HAIs are caused by bacteria and microorganisms that are transferred from a contaminated surface in a health-care unit (e.g. a door handle, a medical tool, etc.) to a patient. These pathogens are able to survive for prolonged period of time on surfaces and even transiently colonize the hands of health care workers [55].

The term "Community Acquired Infections (CAIs)" includes many infections we may encounter in practice and continues to evolve based on the ongoing diversification and aging of the population, climate change and travel. From the reemergence of vaccine-preventable diseases to sporadic outbreaks of plague, community-acquired infections have drawn more attention in the healthcare community, particularly those that are transmitted between people due to poor hygiene. Among the several sources of community acquired infections, feces is the most common source of pathogens like *Salmonella*, *E. coli* O157, and norovirus. Feces can also spread some respiratory infections like adenovirus and hand-foot-mouth disease. Pathogens can get onto hands after people use the toilet or change a diaper, but also in less obvious ways, like after handling raw meats. Germs can also get onto hands by touching objects that have germs on them either because someone coughed or sneezed on the surfaces or the surfaces were touched by some other contaminated object. When hand washing is practiced, germs can be passed from person to person thereby spreading community acquired infections.

Therefore, most places, especially the ones seeing high human traffic, are filled with contaminated surfaces that are transmitted to humans by touch and lead to HAIs and CAIs.

1.5.1 Clinical need for improving hand hygiene

Hands are primary agents for the transmission of pathogens [56] [57] [58] [59] as they become easily contaminated when they touch dirty surfaces, then carry the pathogens and eventually transmit them to other environmental surfaces and/or people. Hand hygiene is the most important factor for minimizing if not preventing both HAIs well as CAIs. Increasing hand hygiene compliance (HHC) has been shown to decrease rates of nosocomial disease and is an important step in the fight to break the chain of pathogen transmission through contact [60] [61] [62].

1.5.2 Current practices for improving hand hygiene

Minimizing HAIs and CAIs is a challenging task. Current practices have been focused on improving hygienic protocols, more importantly ensuring appropriate hand hygiene with handwashing being the single most important measure for preventing infection. Washing with soap and water has been and continues to be the gold standard for enforcing hand hygiene [63]. Water and soap infused with antiseptic agents rapidly eliminates most types of skin flora by using a combination of both a mechanical detergent like scrubbing effect as well as sustained chemical antimicrobial activity on remaining flora. Effective handwashing with soap requires reliable access to clean water supplies but more than three billion people worldwide do not have access to piped water [64]. Even in countries that are not plagued with water scarcity, there are a lot of instances where people might not have immediate access to soap, water, sinks and towels like for instance, while traveling by public transport.

Alcohol-based antimicrobial disinfectant formulations (liquids/gels/foams) have excellent activity against a wide spectrum of Microorganisms (bacteria, viruses and fungi), act rapidly (~ 15 seconds) and hand rubbing with alcohol involves lesser steps than washing hands with soap and water [65]. Most importantly, using alcohol based hand rub formulations does not require the use of water making them the preferred agents for enforcing hand hygiene and are they thus termed "waterless hand disinfection" agents. Additionally, due the their low surface tension, alcohol based hand sanitizers have good spreading quality and dry quickly due to evaporation making them very convenient for the routine, day-to-day decontamination of hands. However, even with the adoption of waterless alcohol based hand sanitizers, enforcing and improving HCC, especially in public places, has been an ongoing battle. Attempts have been made to implement several strategies to improve compliance including - 1: increasing awareness of the significance of hand hygiene through signs and education [66], 2: enabling real-time monitoring/reminders through technologies that provide visual (or other) cues to direct attention to hand hygiene during routine work [67] and 3: making it easier to clean hands by installing facilities like sanitizer dispensers in convenient locations, of which this last method has proven to be the most effective [68]. However, factors such as forgetfulness, high workload, ergonomics of resource placement [69], proximity, cost, staff acceptance [70], device durability and maintenance [71] have significantly affected ease of access to sanitizer dispensers. Therefore, HCC continues to be unacceptably low, particularly in public settings. Moreover, besides disinfecting skin on hands, keeping surfaces that come into contact with skin very frequently, clean and microbe free is another significant challenge. Microorganisms are transferred from contaminated surfaces (e.g. a door handle, a medical tool, toilet seat etc.) to people, especially in high traffic areas like hospitals, restrooms, schools and while using public transport. These pathogens are able to survive for prolonged periods of time on surfaces and eventually, transiently colonize the skin on hands [72]. As already discussed, traditional chemical cleaning methods - such as hand washing and frequent cleaning of surfaces- are the gold standard. However, most pathogens can persist for a long period of time on inanimate surfaces – from a few days up to few months – and it becomes impractical for maintenance personnel to perform constant cleaning in order to keep the surfaces decontaminated. Thus, according to investigations in multiple health care and community based facilities, more than a half of the surfaces with high human traffic were found to be inadequately clean [73]. Therefore, the need for developing advanced, easy to access and easy to use disinfecting technologies that do not depend on end user willingness emerges inevitably.

1.6 Research goal and objectives

Part A of this thesis aims to utilize state of the art microfabrication and 3D printing technologies to develop passive, electronics free clinical tools for biomedical sensing, diagnosis and disease prevention applications. We have three goals:

1. To develop an implantable, near infrared fluorescent optomechanical (NiFO) MEMS biomedical fluid pressure sensing platform that is amenable to commercialization.

We designed and fabricated the NiFO sensor that “optically encodes” pressure changes by converting it to light intensity changes in the near infrared (NIR) regime. NIR device operation minimizes light absorption while maximizing device output and eliminates any tissue damage. The architecture of the sensor consists of a microlens that focuses NI light into a two-wavelength quantum dot (QD) micropillar that sits on top a fluid-exposed flexible membrane. A change in fluid pressure results in a change in the fluorescence intensity ratio emitted by the QD bilayer as the membrane moves with respect to the focal plane of the microlens. A non-implantable, portable and compact optical head is used to excite the QDs and collect the emitted NIR light.

The first prototype of the NiFO technology was developed in 2012 to monitor Intra Cranial Pressure (ICP) [74]. A smaller sized NiFO senor was developed shortly after to monitor IOP after incorporation into a Boston Keratoprosthesis (KPro) Type I implant [75]. In this thesis, we develop and present the next generation of potentially commercializable, biocompatible, more optimized NiFO IOP sensor that maybe incorporated with both the Boston KPro Type I corneal implant as well as an IOL implant.

2. To develop a passive, miniaturized displacement based contrast imaging (DCI) fluid pressure sensor.

We designed and fabricated the DCI sensor that integrates a thin, flexible membrane that is exposed to fluid pressure and a non deformable surface. The membrane and the rigid surface form an air tight cylindrical micro chamber. The inner faces of the membrane as well as the rigid surface are patterned in order to enhance the optical contrast between the membrane material and the air in the micro chamber. The DCI sensor essentially senses displacement: fluid pressure deflects the thin membrane and the distance between the 2 inner surfaces is measured using a precision, a compact off the shelf z-scanning module that auto-focuses at the 2 patterned surfaces and finds the distance between them.

In this thesis, we introduce the DCI pressure sensing technology, demonstrate proof of concept and discuss how the DCI sensor maybe used as a standalone device as well as integrated with an IOL to continuously monitor IOP.

3. To develop a touch activated 3D printed disinfectant dispensing device that minimizes infections caused by direct contact of human skin with contaminated surfaces and improves hand hygiene.

We designed and fabricated a proof of concept device that disinfects the person’s hand that is touching it’s surface while being self-sterilizing at the same time. The device consists of an array of passive, human-powered, milli-valves that deliver a fluid disinfectant from a refillable reservoir when the hand comes in contact with the surface of the array. The milli-valves are closed when no human touch/force is present. When a person touches the surface of the device, the milli-valves are slightly pushed in and the disinfectant flows out through them under the influence of hydrostatic pressure, onto the person’s hand as well as its own surface, thereby sanitizing both target regions by reducing the microbiological load.

In this thesis, we present a device which has a simple architecture, is biocompatible and may be easily incorporated with/mounted upon/form part of a door handle which maybe considered to be a high risk surface for causing hand contamination. The implementation of this technology is cheap and is expected to greatly improve hand hygiene compliance.

1.7 Thesis organization

The work presented in this thesis is organized as follows :

Chapter 2 – Literature Review

This chapter reviews the recent development of implantable devices for monitoring of intraocular pressure as well as disinfecting devices for improving hand hygiene.

Chapter 3 - Opto-Mechanical Intra Ocular Pressure Sensing

This chapter presents two different technologies: NiFO and DCI, for continuously monitoring intra ocular pressure. Both technologies employ implantable sensors that were fabricated using standard, state of the art, surface and bulk micromachining methods. We present their architectures, demonstrate their applicability for measuring fluid pressure and discuss methods that make their fabrication commercializable.

Chapter 4 - A 3D Printed Touch-Activated Sanitizer Dispensing System for Improving Hand Hygiene

This chapter presents a ‘proof of concept’ 3D printed disinfectant dispensing device that may be incorporated onto contaminated surfaces in high human traffic areas. We present the device architecture and demonstrate its applicability for disinfecting human skin to improve hand hygiene compliance while being self-sterilizing at the same time.

Chapter 5 – Conclusions and Future Directions

This chapter summarizes the work presented in Part A of the thesis and discusses future directions for the medical micro-systems that have been developed.

CHAPTER 2

LITERATURE REVIEW

2.1 Introduction

This chapter presents biomedical devices that have been designed and developed for i) continuous monitoring of intra ocular pressure and ii) minimizing the spread of infections by disinfecting contaminated surfaces in public places.

2.2 Intra ocular pressure sensors

This section reviews prominent intraocular pressure sensing technologies and discusses their principle of operation, advantages as well as their drawbacks. Research groups have developed several technologies that are meant to continuously monitor IOP and they may be broadly classified as shown in Figure 2.1.

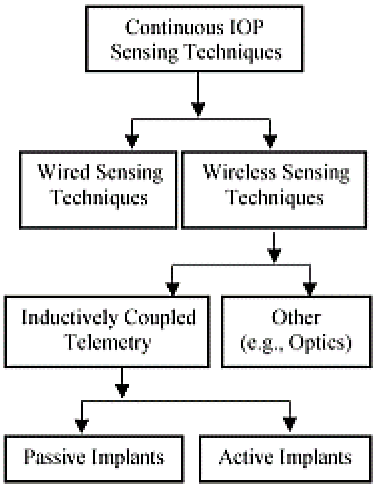

Figure 2.1: IOP sensing technologies [Figure and caption appears in **[49]**]

Wired sensing techniques: Gillman and Greene [76] developed an external, noninvasive pressure sensor consisting of a contact lens that is embedded with a strain gauge. The sensor is placed over the meridional angle on the corneal surface at the corneoscleral junction. A variation in IOP causes a change in the meridional angle at the corneoscleral junction which is measured by the strain gauge. However, to detect this angular change, the contact lens has to be custom molded to exactly conform to the patient's eye which is a big limitation of this method. Walter *et al.* [77] developed a piezoresistive strain gauge and mounted it in a curved holder that maybe positioned on the surface of the eyeball. It is held in place by the lower eyelid and suction created by the sensor holder. The deformation of the strain gauge due to its contact with the eyeball gives an indication of IOP. Wire leads from the sensor pass through the holder, over the lower eyelid and finally connect to external monitoring circuitry. However, a significant drawback of this technique is that pressure measurements are heavily influenced by scleral rigidity. Moreover, even though it maybe worn for 24 hours, it is neither comfortable nor convenient for the patient. Similar to the device developed by Gillmann and Greene, Leonardi *et al.* [78], [79]developed a soft contact lens embedded with a Wheatstone bridge strain gauge (Figure 2.2). The device measures change in IOP by detecting the associated change in the central corneal radius of curvature [80] [81].

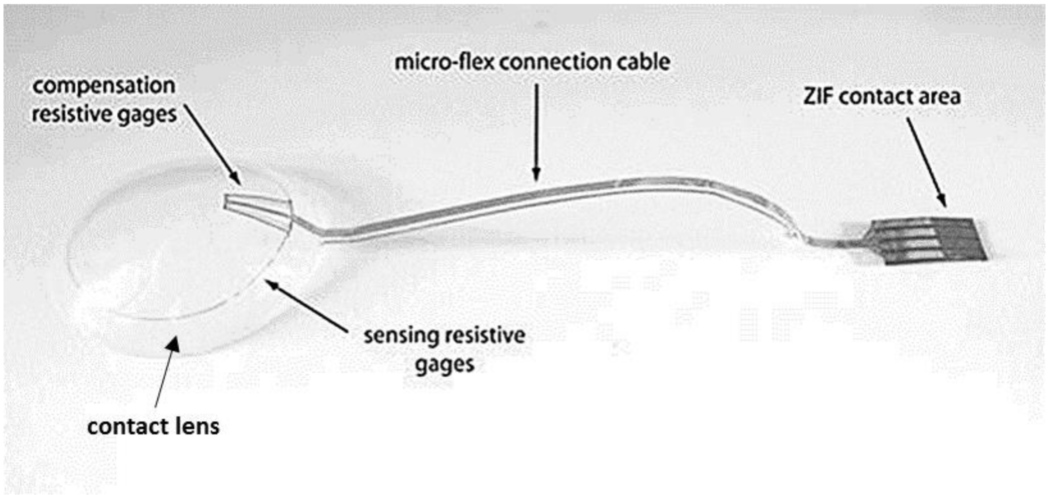

Figure 2.2: The pressure sensing contact lens showing the location of the active gauges, which are placed circumferentially for sensing changes in the corneal curvature due to IOP. The passive gauges are for thermal compensation and are placed radially, where no strain should be measured. The gauges are made of thin metallic film patterned by surface micromachining on a polyimide microflex substrate, which is then embedded into the silicone soft contact lens. [Figure and caption appear in and are taken from **[78]**]

Even though these methods are noninvasive, sensor accuracy is severely affected by the mechanical properties of tissue such as thickness and rigidity. Furthermore, the size of the eye as well as eye movement and lid pressure also influence measurement accuracy. Additionally, given that strain gauges are sensitive to temperature, a mechanism for thermal compensation is required to correct for sensor drift which increases device size and design complexity [49].

Inductively coupled telemetry: Inductively coupled telemetric systems, either active or passive, use capacitive pressure sensing. The advantages of capacitive transduction include low power consumption, low noise, high sensitivity, low temperature drift and long term stability [49]. Additionally, the advances made in microfabrication has enabled further miniaturization of device footprints.

Passive Devices: One of the first passive devices for monitoring IOP was developed by Collins [82]. The transducer consists of a gas bubble inside a cylinder with one of the surfaces made up of a flexible polyester membrane. The inner surface of the membrane is attached to coaxial spirals that are connected to form a single winding. When pressure is applied on the outer surface of the membrane, polyester stretches to push the two coils together which increases their mutual inductance, thereby changing the resonant frequency of the transducer. The frequency sweep is performed of an external inductively coupled oscillator to monitor the resonant frequency. Even though the principle of operation is relatively simple, the device is 1-2 mm thick and 6 mm in diameter which is too large to be implanted into the eye [49] or form part of an existing commercial ocular implant.

The device developed by Collins *et al.* was improved by Bucklund *et al.* [83] who incorporated a capacitive pressure sensor made using fusion bonding of silicon. Similar to Collins's technique, a passive frequency sweep is used for pressure sensing and the resonance frequency is detected using a grid dip configuration [49]. The size of the device is reported to be 5 mm in diameter and 2 mm in thickness and was tested in a cannulated rabbit eye.

Schuylenbergh and Puers [84] further improved this technique by fabricating flat coil electrodes to form LC tank circuits. The resonance frequency of the tank circuits maybe obtained by inductive excitation. The two coils are connected with the spirals acting cooperatively as a single coil. As the capacitive coupling between the coils is changed by pressure, the gap between the coils changes which causes a change in the resonant frequency of the device. Eventually, Puers *et al.* [85] fabricated the inductive element by depositing copper on a chip with a pressure sensitive diaphragm. In this design, one half of the inductor is placed on the flexible diaphragm and the other half is fixed on the substrate. A diode connected in parallel to the chip overcomes any weak inductive coupling between the detector coil and implant as well as results in the generation of higher harmonics with maximum magnitude at resonance. The sensor implant size was reported as 4 x 4 x 1 mm [49].

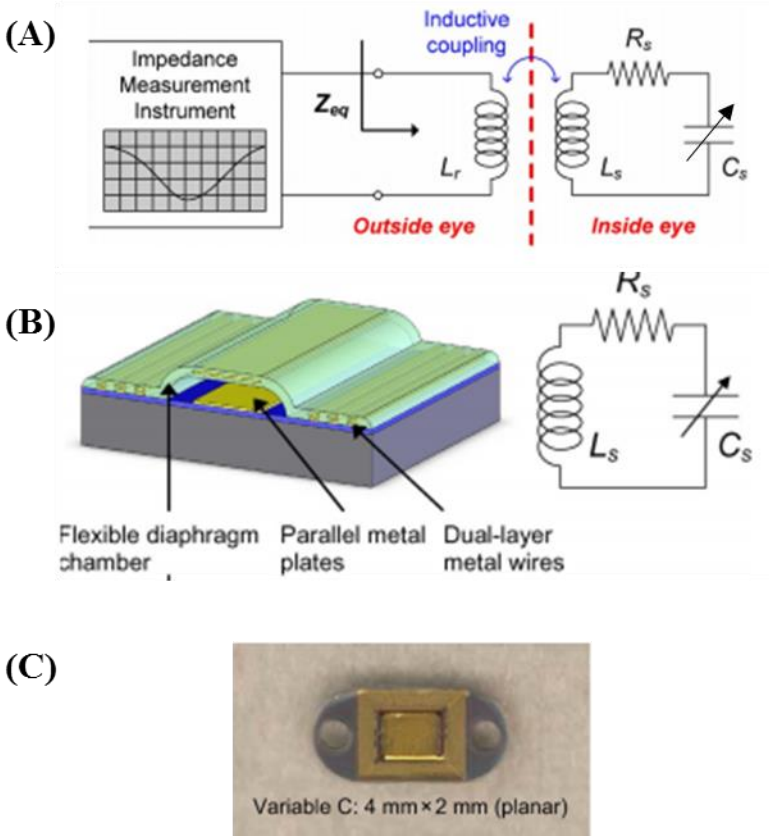

Figure 2.3: (A) Passive wireless LC tank circuit based IOP sensing concept. The implanted sensor can faithfully register pressure variations using corresponding capacitance changes, which are measured using an external reader through wireless inductive coupling. (B) Cross sectional view of sensor design (not to scale) showing variable capacitor. The deformable diaphragm with respect to changing applied pressure realizes pressure-sensitive electrical characteristics of the sensors. (C) Image of microfabricated device. [Figures and captions appear in and are taken from **[86]**]

Similarly, Akar *et al.* [87] developed an absolute capacitive pressure sensor using LC resonance technique. The fabrication of the inductor inside the sealed cavity of the capacitor inside the chip lead to an implant size of 2.6 x 2.6 x 1.6 mm. Due to the low Q factor of the sensor coil, the coil separation distance is however only 2 mm [49].

Several other passive sensors have been reported [88] [89] [86], however, the implant size needs to be further miniaturized to be viable for surgical placement in the eye. Additionally, since the size of the coil inside the implant is limited, these devices require high coupling between the external antenna and implant for reliable pressure measurements. If the coupling is weak, even small changes in the relative positions of the implant and the external device affects pressure measurement accuracy. Therefore, the sensor and detector circuits need to be very close to, and aligned with each other with the distance being strictly controlled which makes the implementation of this type of technology tedious and error prone [49].

Active Devices: Compared to passive devices, active devices have the ability to transmit data over larger distances, have higher signal to noise ratios and the capability to store calibration data on chip. Therefore, they maybe considered to be more robust than passive devices for miniaturized IOP sensing implants [49].

Schuylenbergh *et al.* [90] [91], developed a sensor that was implanted in an IOL (size 3.5 mm ID x 8 mm OD x 0.5 mm thickness) and operated with a power of 100 µW, delivered by a tuned coil system. Using a switch capacitor circuit, a differential pressure measurement between the reference capacitor and the pressure sensor was performed [49]. McLaren *et al.* [92] implanted a commercially available telemetric pressure transducer under the skin on the neck of rabbits. IOP was then measured by inserting the tip of a catheter in the anterior eye chamber that conducted pressure to the commercial pressure transducer. Given that this is an invasive technique, the drawbacks include eye irritation and corneal scarring [49].

Schnakenberg *et al.* [93] [94], developed a telemetric pressure sensor that is integrated into the haptic portion of an IOL and transmits data digitally to an external reader unit that is placed on a pair of spectacles worn by the user. The size of the sensor is reported to be 15 mm in diameter and 4.5 mm in thickness. Performance was evaluated in rabbit eyes which showed promising results. Stangel *et al.* further improved the design of the system by incorporating a temperature sensor and additional reduction of parasitic capacitances [48] [95] [96]. The modified device is reported to be 10.5 mm in diameter and was implanted in rabbit eyes for six months [49].

Even though active devices are superior to passive devices in terms of having better performance, their design is much more complex. Additionally, there is no robust batch manufacturing process that enables the incorporation of the antenna into the implantable chip. Moreover, the size of the implants need to be further miniaturized in order to be comfortably placed surgically and accommodated inside the eye [49].

Other techniques: Fink *et al.* [97] developed an optically powered wireless IOP sensor, consisting of an IR photodiode, capacitor, resistor, pressure actuated switches and a solar cell power source. The pressure actuated switch consists of two electrodes that are part of a compressible gas filled chamber. When IOP increases above a certain threshold, the switch is collapsed thereby discharging the capacitor which in turn is detected by an external read out unit. The main drawback of this technique is that it does not provide a continuous measurement for IOP. Additionally, as there is no data, it is not evident if the device has been put into practice [49].

Bae *et al.* [98] [99], developed a piezoresistive pressure sensor with an electromagnetically actuated membrane valve for fluid flow control. The piezoresistive element is incorporated onto the surface of the valve membrane and a Wheatstone bridge circuit is used to detect the change in resistance in response to applied pressure on the membrane. Tests were conducted to evaluate sensor performance and noise was identified as a limiting factor for piezoresistive sensors. Given that the device is made up of materials like PDMS that is not suitable for long term implantation, the biocompatibility of the device is questionable. Additionally, the final size of the entire device (9 mm x 9 mm x 2 mm) is quite large to be implanted in the anterior chamber of the eye [49].

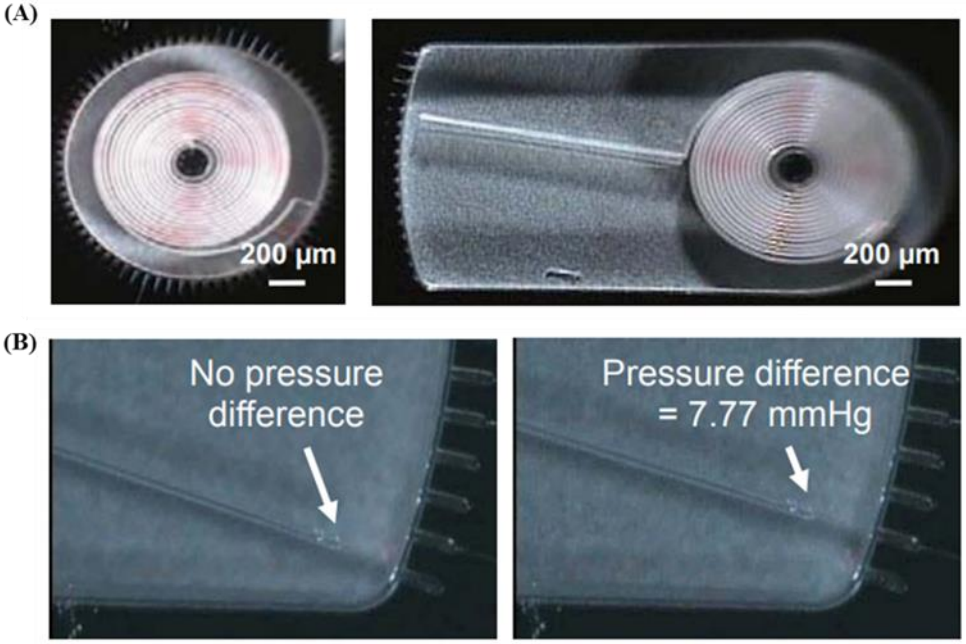

Figure 2.4: (A) Microfabricated highly sensitive parylene IOP sensor with 1.1 mm diameter spirals. (B) Pressure response of the sensor with a lateral sensing trajectory and pressure difference being applied between interior and exterior of the parylene tube. [Figures and captions appear in and are taken from **[100]**]

Chen *et al.* [101] [102] [100]developed a purely mechanical passive pressure transducer comprising of a bourdon tube fabricated in the form of a spiral (Figure 2.4A). The device is pre-pressured to 1 atm and then sealed. When fluid pressure is applied, the tube gets elongated circumferentially which is optically tracked to estimate pressure (Figure 2.4B). Results show a linear dependence between pressure and tube elongation. Although simple, the device has not been demonstrated to be able to detect diurnal variations in IOP. Furthermore, the location of the external read out unit in relation to the implant needs to be very precise in order to minimize measurement error [49]. Given that the pressure sensor is designed to be implanted in the iris in order to allow for optical access, a separate surgery is required solely for implanting the sensor at an increased cost to the patient.

2.3 Devices for disinfecting contaminated surfaces in public places

Eliminating HAIs and CAIs has been a challenging task. Even though current practices have mostly been focused on improving hygienic protocols, there have been several research efforts to develop and implement novel disinfection technologies [103].

UV disinfection: Ultraviolet (UV) light has been proposed for disinfecting contaminated surfaces [104]. UV light has been proven to contribute to a radical reduction of the survival of microorganisms and bacteria. This technology requires the use of strong UV lamps that need to be installed in public spaces (Figure 2.5). A major drawback of UV light is its reduced effectiveness in decontaminating shadowed surfaces, which has led to the limited practical use of this technology [105]. In addition, UV light exposure cannot be used in high-traffic areas, e.g. corridors and waiting rooms, as people cannot be exposed to UV light. An improved variation of the above technology is to use UV light activated surface coatings [106]. Those coatings produce cytotoxic species after irradiation causing a remarkable reduction in the survival of microbial colonies. However, those coatings do not affect adequately all different types of pathogens and it is difficult to implement them in a public environment as they require a constant source of photoactivation.

Figure 2.5: A portable UV robotic system that precisely measures reflected UV light and automatically determines the optimal dose required for disinfecting health care environments. [Figure and caption appear in and are taken from **[107]**]

Metal coatings: Coatings impregnated with metals, such as silver or copper have also been studied as self-sterilized surfaces and they have been proven to be effective up to several hours [108]. However, those metal surfaces need to be coated with corrosive inhibitors that lower the effectiveness of their antimicrobial action. A similar approach based on coatings containing quaternary ammonium silyl oxide and titanyl oxide moieties was shown to efficiently reduce the number of colony-formed units for weeks [109]. This claim remains highly questionable as the validation procedure was combined with normal cleaning procedures and even within the second week of use, some of those coatings were found not to meet the critical limit of less than 5 CFU/cm^2.

Micropatterned surfaces: More recently, micropatterned surfaces were proposed as a potential solution for preventing microorganisms from adhering to a surface. Several geometries comprising of micropilars or microchannels have been developed [110] and they are currently in the commercialization phase by Sharklet Technologies Inc (Figure 2.6). Although this technology seems promising, rigorous clinical validation of this technology has not yet been performed. More importantly, it remains questionable if it can compete against the chemical treatment methods that are able to kill all present pathogens and viruses.

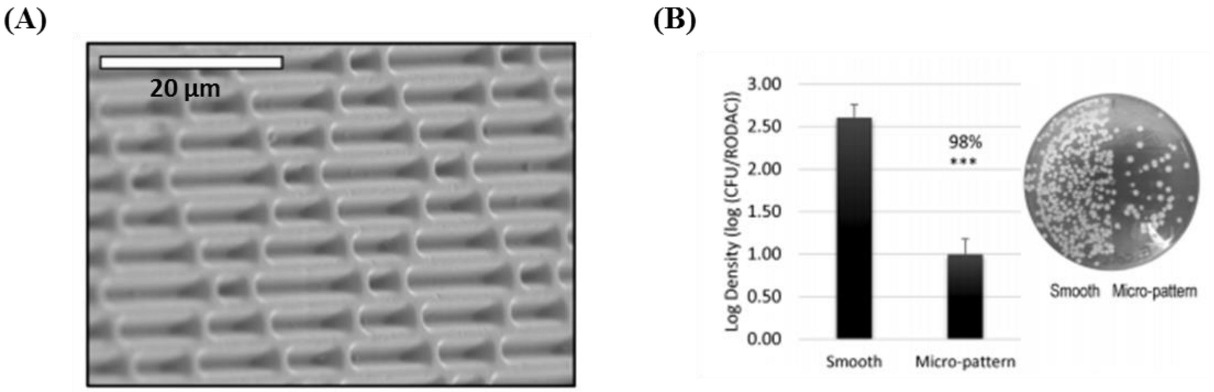

Figure 2.6: (A) Scanning electron micrograph of Sharklet micro-patterned acrylic surface. (B) Microbial persistence of Sharklet surface. Smooth and micro-patterned acrylic films were coated with a sprayed inoculum and dried for 30 minutes. Log densities of bacteria present on the surfaces of the Sharklet layer compared to smooth controls are plotted with the associated standard error of mean. A representative image of an agar contact plate after inoculum sampling, the Sharklet surface (right) has fewer bacteria compared to the smooth surface (left). $p < 0.005$ (***) $n = 3$. [Figures and captions appear in and are taken from **[110]**]

PullClean door handle: Only a few from the aforementioned technologies have reached commercialization and the most successful story seems to be the 'PullClean' door handle (Altitude Medical Incorporated). This is a low-tech handle that simply integrates a hand sanitizer –contained in a disposable cartridge- on a door handle (Figure 2.7). The main drawback of this product is that it relies on the willingness of the person entering the door to employ it, making its effectiveness difficult to predict. In addition, it is hard to envision, how such a handle can be integrated in every surface in an area that sees a lot of human traffic.

Figure 2.7: The PullClean device designed as a door handle with a built-in hand sanitizer dispenser that requires the user to willingly actuate it. [Figure and caption appear in and are taken from **[111]**]

2.4 Conclusions

2.4.1 Intraocular pressure sensing

In this chapter, a comprehensive review of the state-of-the-art in IOP sensing technologies has been presented. Among them, wired non-telemetry based techniques are not suitable for continuous IOP measurement as they cause patient discomfort. Given that they provide an indirect measurement due to their non-invasiveness, these techniques are sensitive to either corneal or scleral rigidity [49].

Passive telemetry sensors provide a direct measurement of pressure and driven by the advances that have been made in monolithic ultra miniaturization technologies, they have small footprints and simple on-chip circuitry. However, a smaller footprint entails a smaller coil which reduces inductive coupling efficiencies. The resulting low Q-factor requires the sensing coil to be precisely aligned and placed very close to the sensor coil thereby making the acquisition of measurements challenging, particularly if communication over larger distances is required. Even if RF signals are used, they will quickly dissipate while passing through soft tissue [34].

Active sensors are popular due to their superior data processing and transfer capabilities. However, long term monitoring with active devices would require long lasting battery units/power supply and implantable power sources are large in size. The presence of signal processing and power management circuitry further increases design complexity and device footprint [34].

The majority of the current IOP implant devices have been designed without taking into consideration the spatial constraints inside the eye, the surgical complexity involved and the reliability of the device, thereby making them impractical [49].

First and foremost, the surgical procedure to insert the implant must be as minimally intrusive as possible requiring just a small incision (< 2.8 mm) in the tissue that can heal by itself without any stitches. Therefore, it is important that the mechanism that deploys the sensor is flexible enough to be easily insertable through the incision. Additionally, the sensor must fit inside the anterior chamber, a region that has not been used efficiently by current sensor designs as well as the devices presented in this chapter. The anterior chamber is the most viable location for sensor placement inside the eye since it causes the least damage and post-surgical complications like infection, retinal detachment and fibrosis. Given that the cornea is 0.5 mm along the optical axis and 1 mm at the ends, the lens diameter is 16 mm and a cylindrical region along the optical axis is not usable (to allow for unimpeded vision), a hollow cylinder with an ID of 7 mm, an OD of 8 mm and height of 0.5 mm is available for sensor placement [49]. Additionally, the implant should not be near the irido-corneal angle in order to not hinder the flow of aqueous humor as well as to not adhere to the iris and cornea. Also, the ability to easily incorporate the sensor with a commercial implant that is already associated in some form with patients who are at risk of developing glaucoma will be a huge benefit in terms of minimizing cost and recovery time since an additional surgery dedicated for just inserting the sensor would no longer be required [34].

The design of telemetric electronics components for implantation into the eye requires optimization of power consumption, coil size and even communication frequencies. Implanting electronics components requires careful consideration of the characteristics of the electromagnetic radiation used for device communication to ensure minimization of tissue heating and radiation specific absorption in the environment. Any potential dielectric heating during an MRI examination must be evaluated as well as interactions with X-rays in order to determine microcontroller damage [34].

Finally, in order to be viable as a long term implant, it is critical to consider materials and packaging methods that will survive the *In vivo* environment without causing any toxicity. The device must integrate with the neighboring tissue, bio-fouling must be minimal, must be hermetically sealed so that sensor performance does not get compromised, must be sterilizable, must not have sharp corners, must have long term mechanical and chemical stability. Especially for electronic sensors, proper sealing and material choice is critical for there to be no electrolyte intrusion, corrosion, failure or sensor drift [34].

In conclusion, there is a need to develop a miniaturized, implantable sensor for direct IOP measurement that is 1: free of any electronics components, 2: wireless, 3: biocompatible, 4: can be manufactured using a batch fabrication process, 5: maybe incorporated into an existing commercial ocular implant, 6: must be compatible with the spatial limitations of the eye's anatomy and 7: must be easy to insert surgically.

2.4.1 Technologies for infection control

The review of technologies for infection control that have been discussed in this chapter show that eliminating HAIs and CAIs still remains a great challenge due to technical limitations of existing disinfectant methods, their inconvenience for large scale use in public spaces, as well as low end user compliance. Therefore, a novel, cost-effective solution for decontaminating any given surface that will not interfere with current cleaning practices and workflow, that will work reliably at all times and will not be subjected to the end-user willingness, needs to be developed.

CHAPTER 3

OPTO-MECHANICAL PRESSURE MICROSENSORS FOR MONITORING INTRAOCUALR PRESSURE

3.1 Introduction

Intraocular pressure monitoring is an invaluable tool for the diagnosis and management of glaucoma, a medical condition involving severe optic nerve damage due to elevated IOP. It is clinically desired to monitor these fluctuations as frequently as possible in order to assess the efficacy of treatments and disease progression [112]. IOP monitoring systems, since their introduction in the 60’s, have undergone very few design changes with the gold standard for IOP measurement being the Goldmann applanation tonometer. One of the major drawbacks of the tonometer is that, due to its complexity, only trained personnel can operate the equipment which means that the patient needs to visit the clinic every time an IOP measurement needs to be taken [113]. The tonometer cannot continuously monitor IOP variations over time because it is designed for single pressure measurement snapshots [75] in the clinic. Frequent and life-long IOP monitoring is therefore expensive, inconvenient and taxing for both patients and their family members who transport and accompany them. Besides the need to acquire frequent IOP measurements, the measurement accuracy is equally crucial in the screening, diagnosis, and management of glaucoma. Given that the GAT is not directly exposed to fluid inside the eye, this method assesses IOP indirectly based on force required to flatten the corneal surface by a certain amount. GAT accuracy is therefore heavily influenced by corneal thickness, curvature, rigidity, viscosity, elasticity and hydration [114]. These biomechanical properties show large variability between individuals which increases GAT measurement error. Additionally, biomechanical properties are significantly affected by surgery such as keratoplasty (a corneal transplant procedure which is a potential precursor to the development of glaucoma due to surgical complications), making GAT an unsuitable method for reliably monitoring IOP in these patients [115]. Furthermore, since GAT involves a physical probe that touches the surface of the eye, the method introduces the risk of infections if the probe is not disinfected adequately between patient use and can potentially cause corneal abrasions during the IOP measurement process [116].

Motivated by the need for frequent, long-term, direct pressure monitoring, the lack of commercially available fully implantable IOP microsensors, and taking advantage of recent developments in the MEMS field, this thesis chapter presents two opto-mechanical, passive IOP sensing technologies that overcome the limitations mentioned above.

Both technologies can potentially provide home-based, frequent and life-long IOP self-monitoring for patients with POAG, the most common type of glaucoma.

3.2 Filling the gap: NiFO and DCI technologies

As discussed in Chapter 2, there is no commercially available IOP monitoring technology that: (i) directly monitors IOP (ii) is portable and therefore point-of-care, (iii) is easy-to-use and does not require trained personnel to operate, (iv) is affordable, (v) allows continuous recordings to be made during the day, (vi) its accuracy is comparable to that of GAT. Here, two novel types of IOP monitoring technologies are developed, termed '***Near Infrared Fluorescence-based Optomechanical (NiFO***)' sensing technology and the '***Displacement based Contrast Imaging (DCI)'*** technology.

Both the NiFO and DCI technologies are designed to have the following characteristics:

- Frequent IOP monitoring
- Allow the patient to perform IOP measurements at home
- Require no sensor maintenance (e.g. battery replacement)
- Increased accuracy as IOP is measured directly
- Very small footprint (~1.5 mm^2)
- Magnetic resonance imaging (MRI) compatible

Table 3.1: Summary of and comparison between the properties of GAT, NiFO and DCI IOP monitoring technologies.

	GAT (Tonometry)	**NiFO/DCI Technologies**
Method of IOP assessment.	Indirect	Direct
Influence of biomechanics of corneal surface on IOP measurements.	Dependent	Independent
Portability	No	Yes
Frequency of IOP	Sporadic	Frequent
Point of care	No	Yes
Application of topical anesthesia.	Yes	No
Invasiveness	Non invasive	Invasive

3.3 Impact

We expect that both the NiFO and DCI technologies will be primarily used by: (1) patients with diagnosed moderate (IOP > 25 mmHg) or severe (IOP > 31 mmHg) POAG, (2) POAG suspects (IOP > 21mmHg) that undergo cataract surgery, (3) patients for whom prior anterior segment surgery precludes the need for monitoring IOP (e.g. eyes with KPro implants), and in (4) patients with severe ocular hypertension (traumatic hyphema, orbital edema, etc). In categories 1, 3, and 4, the NiFO sensor maybe implanted in the iris after fitting with a KPro device while the DCI sensor maybe implanted as a standalone device in the anterior chamber. In case 2, the DCI sensor may be an integral part of an IOL. Additionally, for case 2, the NiFO sensor can be introduced into the IOL by creating a pouch like/recess structure on the IOL. Monitoring IOP using a portable readout unit with the NiFO sensor and/or a smart phone with the DCI sensor will not only enable easy readout by patients or their families, but also assist in data collection, analysis and improving communication with the clinician to facilitate better outpatient monitoring and management.

We estimated that a total of 2-3 million people will benefit from the proposed NiFO and DCI technologies [112]. Additionally, these sensors will significantly reduce the medical management costs of glaucoma which is currently estimated at $2.6 billion per year

[117].

3.4 NiFO Technology

The NiFO technology was initially described by Ghannad Rezaie *et al.* [74] [118] for monitoring intracranial and intraocular pressures. The key element of the NiFO technology is the use of two layers of Near Infra-Red (NIR) Quantum Dots (QDs) (absorbing light at 785 nm and emitting light at 840 nm and 940 nm) that are separated by an optical spacer (SU-8 layer). This forms a ‘two color’ QD micropillar that sits on top of a flexible membrane that is exposed to fluid pressure. A microlens is used to focus incoming NIR light onto the pillar and to collect the emitted light from the QD micropillar. The intensity of the emitted light is a function of the microlens-QD pillar distance that depends on the applied pressure.

The first generation of the NiFO microsensor (Figure 3.1) was fabricated using low stress silicon nitride as the membrane material and 850 nm and 940 nm lead (Pb) based QDs. The emitted fluorescent intensity at the two wavelengths was measured as a function of the applied pressure in order to calculate the intensity ratio. The obtained intensity ratio was shown to have a linear correlation to the applied pressure in the clinically relevant applied pressure range of 10-45 mm Hg. Additionally, the NiFO microsensor demonstrated an accuracy better than 2 mm Hg in the entire 0-45 mm Hg range with less than 1 mm Hg zero drift over a 14 day period in studies [118]. However, in these prototype devices, each individual microlens has to be manually incorporated into the sensor which makes the fabrication process very labor intensive. Additionally, Poly-Di-Methyl-Siloxane (PDMS) is used to hold the microlens in place in the sensor. Given that PDMS absorbs fluids and swells, it cannot be used for long term implantation in the environment. Furthermore, the QDs are directly exposed to the biological environment which means that heavy metal ions can leach out into surrounding tissue that could lead to cytotoxic effects [119].

The work presented in this chapter is an improvement over the first generation NiFO senor prototype in the following ways: (i) Two distinct device architectures are presented: one for incorporation with Type 1 Keratoprosthesis (KPro) implant devices and the other for incorporation with intra ocular lenses. (ii) The material of the pressure sensing membrane is changed from silicon nitride to polysilicon in order to get higher deflection and therefore improve sensitivity over the initial prototype. Additionally, the membrane has a thinner geometry and lower pre-stress that further improves deflection response to pressure.

(iii) Unlike the first generation device, the QD micropillar sitting on top of the membrane is enclosed in a glass microchamber around the membrane. This is intended to prevent any direct exposure of heavy metal based QDs to the biological environment as they are known to have cytotoxic effects . Additionally, the concentration of QDs has been increased five times with a 20% increment in quantum yield and improved fluorescence stability. (iv) A fabrication process is developed that is meant to produce a high yield of devices without requiring manual placement of individual microlenses into the sensor. The sensors are produced in the form of an array of 20 devices each, where a 4” wafer can accommodate 9 such arrays. Each fabricated batch will therefore yield 180 devices. v) The use of polymers such as PDMS has been eliminated to improve long term biocompatibility. vi) The entire fabrication process is setup to be amenable to being outsourced to contract manufacturers for future commercialization of the technology.

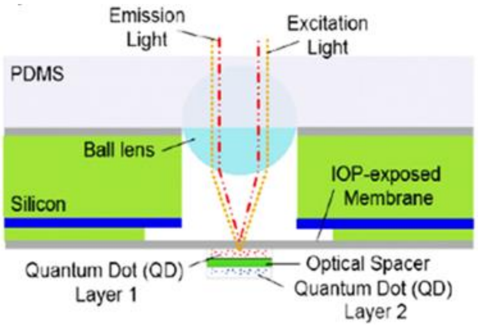

Figure 3.1: The architecture of the first generation NiFO microsensor prototype developed by Ghannad-Rezaie *et al.* [Figure appears in and is taken from **[118]**].

3.4.1 Device architecture and system overview

The NiFO IOP monitoring technology consists of the implantable NiFO sensor and an external (non-implantable), portable optical readout system (Figure 3.2). That readout system integrates an optical head consisting of an NIR laser source, optical filters and photodetectors along with a data acquisition and display unit that is used to excite, collect and analyze the emitted fluorescent light from the NiFO sensor. Operating the NiFO sensor in the NIR regime is critical for minimizing light absorption by the skin and the eye tissue [120].

The implantable NiFO sensor consists of: (i) a flexible low stress (< 5 MPa) polysilicon membrane (600 µm diameter, 200 nm thickness) with a 2-layer QD (CdSeTe/ZnS with TOPO, HDA) structure (the ‘QD micropillar’) that emits a two-color (840 nm and 940 nm) NIR fluorescent light and (ii) a plano-convex (500 µm diameter, 147 um thickness) lens (we use the term ‘microlens’).

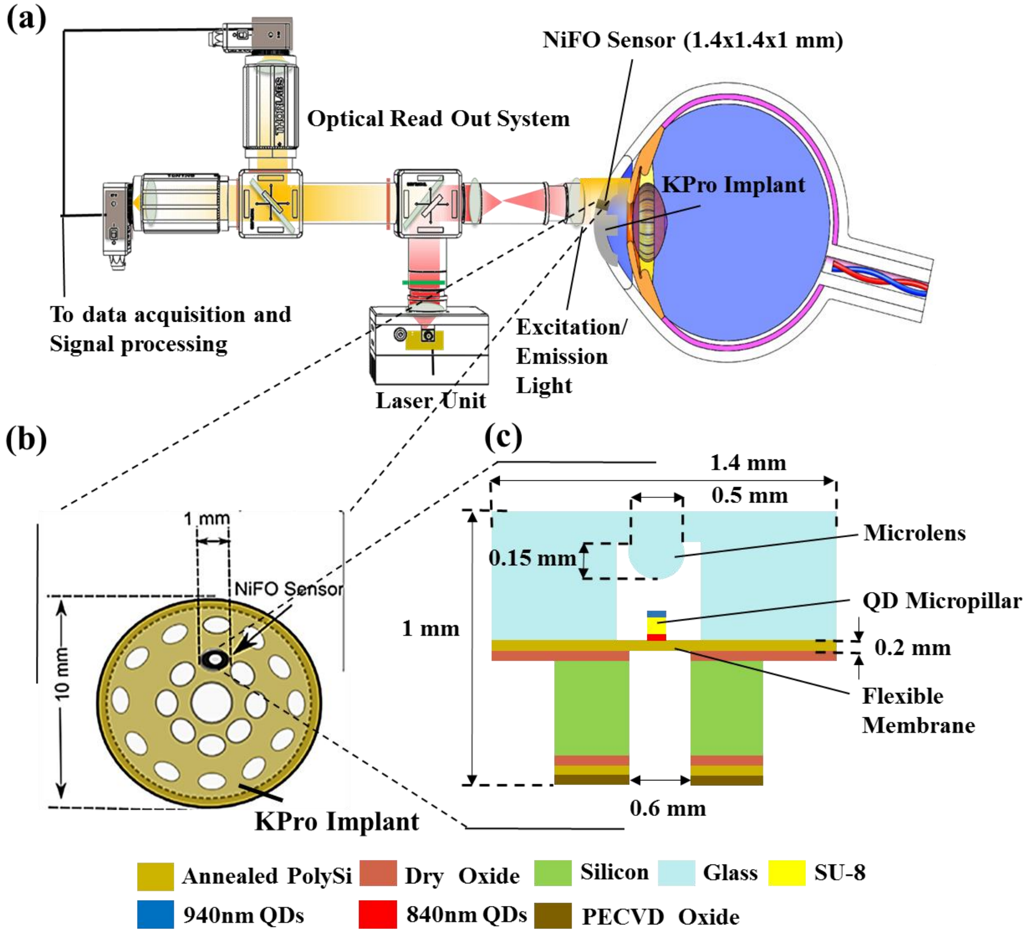

Figure 3.2: (a) Overview of the NiFO IOP pressure monitoring system. The NiFO sensor can be integrated into a KPro implant which is surgically placed in the eye. A portable optical readout system maybe used in order to both excite the sensor as well as to collect the emission from it.(b) Schematic showing placement of the sensor in the KPro implant. (c) Cross–sectional schematic of the NiFO pressure sensor showing critical device dimensions.

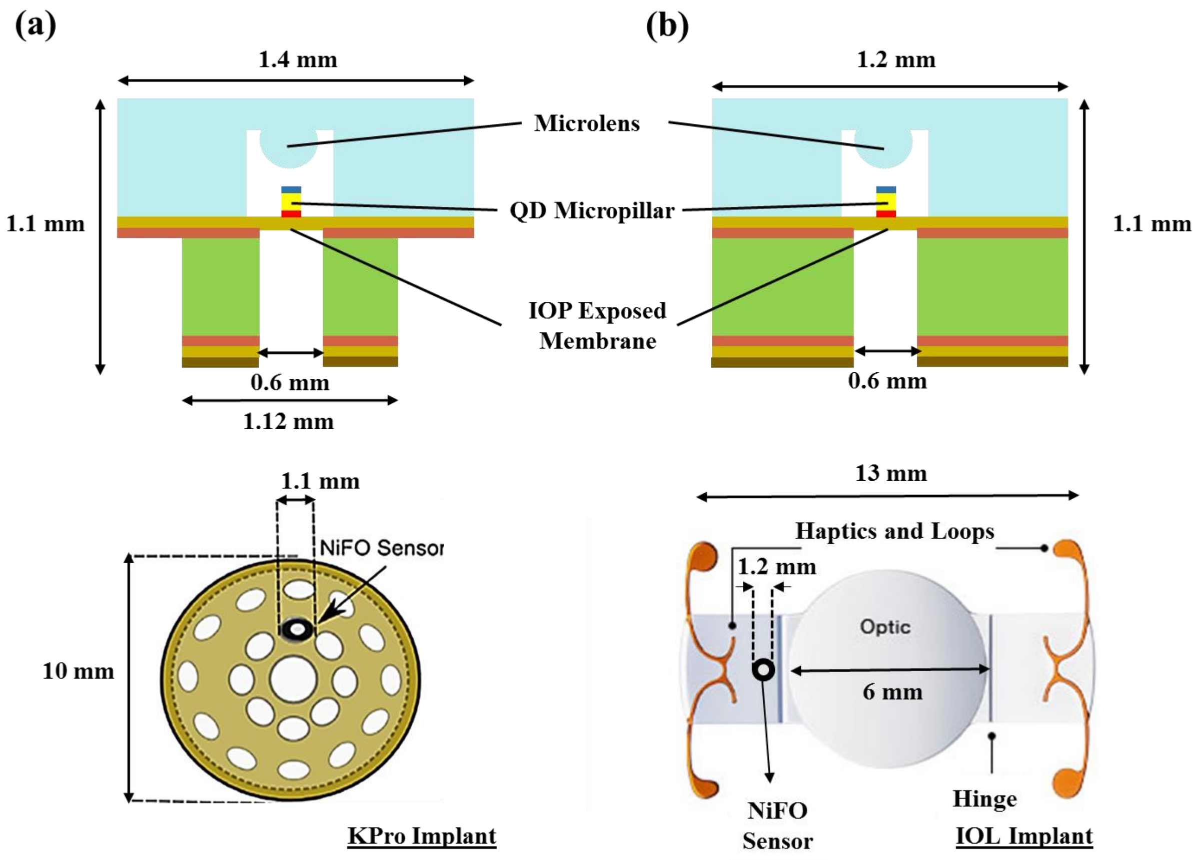

Figure 3.3: The NiFO sensor has two distinct architectures that can be integrated into (a) a suturing hole located in the back plate of a KPro implant or (b) in a recess created in the haptic region of an IOL implant. Both the KPro and IOL implants are surgically placed in the eye.

There are two distinct device architectures (Figure 3.3), one for incorporation with a Boston KPro Type I implant (for glaucoma or at risk of developing glaucoma patients with severe corneal disease that has lead to compromised vision) and the other for incorporation with an intra ocular lens (for glaucoma or at risk of developing glaucoma patients undergoing cataract surgery).

NiFO architecture for incorporation into KPro implant: When the cornea becomes severely diseased and vision is heavily compromised due to tissue opacity, corneal transplantation from human donors becomes necessary. However, in a lot of cases, the procedure fails as the graft is either rejected or the patient shows poor prognosis that prevents future grafting. For such cases, the only alternative is in the form of an artificial cornea that is popularly referred to as the Boston KPro implant. The KPro implant is surgically inserted using a procedure known as keratoplasty but even after surgery, nearly 64% of patients develop glaucoma during postoperative recovery [121] [122] [123]. Therefore, it is critical that IOP be monitored frequently to detect the onset of and to check the progression of postoperative glaucoma to ensure normal recovery.

The KPro implant (available in Types I and II) is essentially an artificial cornea consisting of an optic portion for vision, a front plate that accommodates the optics, a back plate and a locking mechanism (in the form of a C ring) which when assembled, resembles a collar button that positions and holds the device in place. The implant is made up of clear plastic polymethylmethacrylate (PMMA) and the C-ring is made up of titanium. Given that the implant is mostly made up of infelxible plastic, using GAT to monitor IOP would result in inaccurate pressure measurements due to the artificially enhanced corneal surface rigidity caused by the presence of the implant. On the other hand, the NiFO technology, being a direct method to measure IOP, is independent of the mechanical stiffness of the cornea. Therefore, the incorporation of the NiFO sensor into the KPro implant would lead to reliable long term IOP monitoring to perform risk management for glaucoma in these patients.

The type I device, which is the most frequently used configuration, is then sutured into the patient's cloudy cornea in a surgical procedure similar to a standard transplant. The holes in the back plate allow the surgeon to pass suturing thread through them while letting the aqueous humour provide nutrients to expedite recovery as the patient's own tissue grows into the holes to anchor the device at the surgical site. The titanium locking ring prevents the unscrewing of the front plate and holds the assembly in place. The type I device has a smaller footprint and does not protrude through the eyelid. Therefore, it is usually recommended for patients with good eyelid anatomy and ability to blink without problems [124]. The type II version is very similar in design to the type I style except for the fact that it has an additional 2 mm in length anterior cylinder that protrudes through the eyelids (Figure 3.4). Unlike type I, type II is mainly used for disease conditions involving poor tear function [124]. Several modifications in device design have improved success rates with the latest FDA approved design having 8 holes (1.1 mm diameter) in the back plate for both types I and II. The base of the NiFO sensor (Figure 3.3(a)) has a diameter of 1.12 mm that is only slightly larger than the diameter of the circular fluidic/suture holes in the KPro backplate. When heated to 90^0C, the KPro device gently expands and the holes in the backplate also get larger. This allows the insertion of the NiFO sensor base into one of the fluidic/suture holes. After insertion, the integrated unit is cooled down to room temperature to obtain a tight fit between the sensor and the KPro implant, thereby seamlessly integrating the two devices without interfering with the locking mechanism that connects the front and back plates.

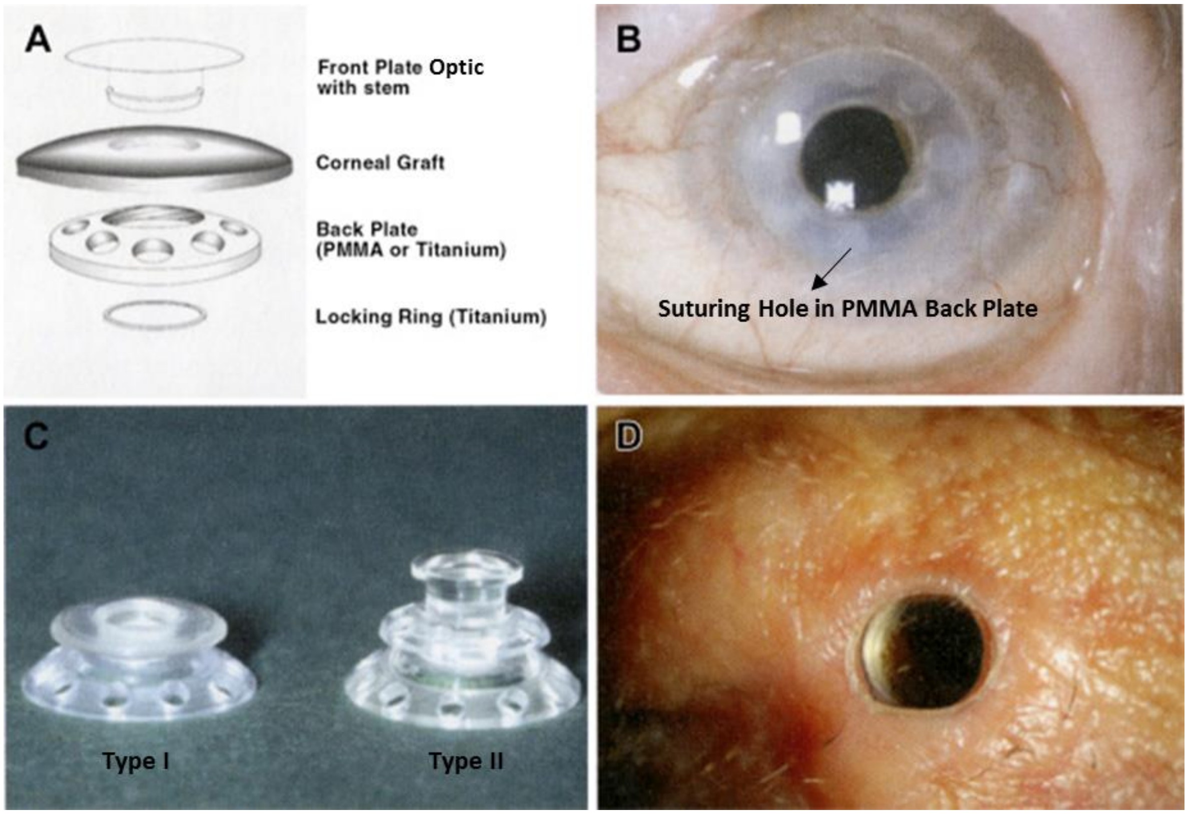

Figure 3.4: (A) Assembly showing components of a Boston keratoprosthesis type I implant. (B) Slit-lamp photograph of a Boston keratoprosthesis type I implant with a polymethyl methacrylate (PMMA) back plate with suturing holes. (C) Boston keratoprosthesis type I and II devices with PMMA back plates. (D) Slit-lamp photograph of a Boston keratoprosthesis type II implant with the optic extending through an eyelid that is surgically shut [Figures and captions appear in and are taken from **[125]**].

<u>NiFO Architecture for incorporation into IOL Implant:</u> The natural crystalline transparent lens that is located in the capsular bag and suspended by a circular ligament complex, is bi-convex and along with the transparent cornea, forms the ocular diopter that allows vision. During an extremely prevalent condition called cataract, the lens becomes opaque. The light entering the eye is therefore diffracted and scattered. Visual acuity is therefore gradually lost along with an altered perception of color/hue and the emergence of refractive defects/glare [126]. Given that there is no treatment to stop this opacity from developing, surgically removing the diseased lens and replacing it with an artificial IOL is the only available medical intervention. Besides restoring vision, the IOL can also correct any other pre-existing defects like myopia, hyperopia, astigmatism and presbyopia. Although there is no direct association between cataract and glaucoma, both conditions are common with age with more and more people developing both after the age of 60 [127]. Given that cataract surgeries are now commonplace, the IOL can be an excellent vehicle to accommodate probes inside the eye and it is therefore logical to incorporate a pressure sensor like the NiFO sensor to monitor IOP [128].

Cataract surgery uses minimally-invasive lasers that break up natural lens material without damaging tissue around it. By creating a small incision, (~ 2.2 mm) the surgeon inserts an ultrasound emitting tube to suction out the broken up lens debris in a process called ultrasonic phacoemulsification [126]. A flexible artificial IOL is then folded and inserted through the same incision. Once positioned inside, the folded IOL springs into place within the lens capsule. In most cases, the 2.2 mm incision is self-healing and therefore does not require suturing thereby minimizing any inconvenience to the patient. IOLs have an optics portion that focuses light as well as a haptics portion that holds it in place inside the lens capsule. The diameter of the optic portion ranges between 5.5 to 7.0 mm and overall length varies between 12 to 13 mm. While preserving the same membrane size, QD micropillar and microlens geometries as the KPro architecture, the NiFO sensor footprint is reduced to ~ 1.2 mm^3 in order to incorporate it into either the edge of the optic or at the base of the haptic (Figure 3.3(b)). A 1.15 mm in diameter and 0.3-0.5 mm in depth recess maybe created in the IOL (edge or haptic) followed by the manual placement of the NiFO sensor inside it. Given the dimensions of the NiFO sensor, which is much smaller than the lens, placing the sensor at the edge of the optics is not expected to cause any optical aberrations or any other negative effects on image quality. This is supported by clinical findings where small irregularities or scratches sustained on an IOL during the insertion process which were comparable to the size of the recess/ NiFO sensor assembly did not cause significant optical aberrations or patient complaints [129]. Alternatively, placing the NiFO sensor in the haptic would further eliminate any chances of producing optical effects such as glare. Furthermore, the size of the recess-NiFO sensor unit is small enough to likely not interfere with the ability of the surgeon to manipulate the IOL during insertion. Moreover, the recess maybe easily created by employing a process such as femto second laser machining which is a technology that is already widely used in ophthalmology for manufacturing IOLs and in clinical procedures (creating corneal incisions, capsulotomy, and lens fragmentation) [126].

External optical read out unit: The ORS has (Figure 3.5) an optical head and a data acquisition and display unit that consists of an excitation laser, two photodiodes, a data acquisition board and an interactive display unit. A key aspect of the optical design is the fact that the IOP measurements are independent of the distance between the optical head and the NiFO sensor as light enters/exits the sensor collimated.

The optical head unit consists of metal housing components containing a beam expander (AC080-016-B, LB1471-B, Thorlabs Inc.), a dichroic mirror (T810lpxr, Chroma Technology Corp.) which separates the NIR excitation from the emitted fluorescent light, a filter to block any ambient light (800AGLP, Omega Optical Inc.), another dichroic mirror (NC424630-880dcrx, Chroma Technology Corp.) that separates the two QD wavelengths, two corresponding emission filters (ET845/55m, Chroma Technology Corp., 950DF70, Omega Optical) and two collecting lenses (ACL2520-B, Thorlabs Inc.) that ultimately focus the collected light onto two ultrasensitive photo detectors (PDF10A, Thorlabs Inc.), each one monitoring the intensity at 840 nm and 940 nm respectively.

The photo detectors produce a voltage output each that are fed into two channels of a data acquisition board (Arduino Mega 2560) to read, analyze the signals and display measured IOP on a LCD touchscreen module (MEGA2560 5" LCD Extend TFT Shield for Arduino, 5" 5 inch TFT LCD 480X800 Arduino DUE MEGA2560 R3 Raspberry Pi, SainSmart Inc.).

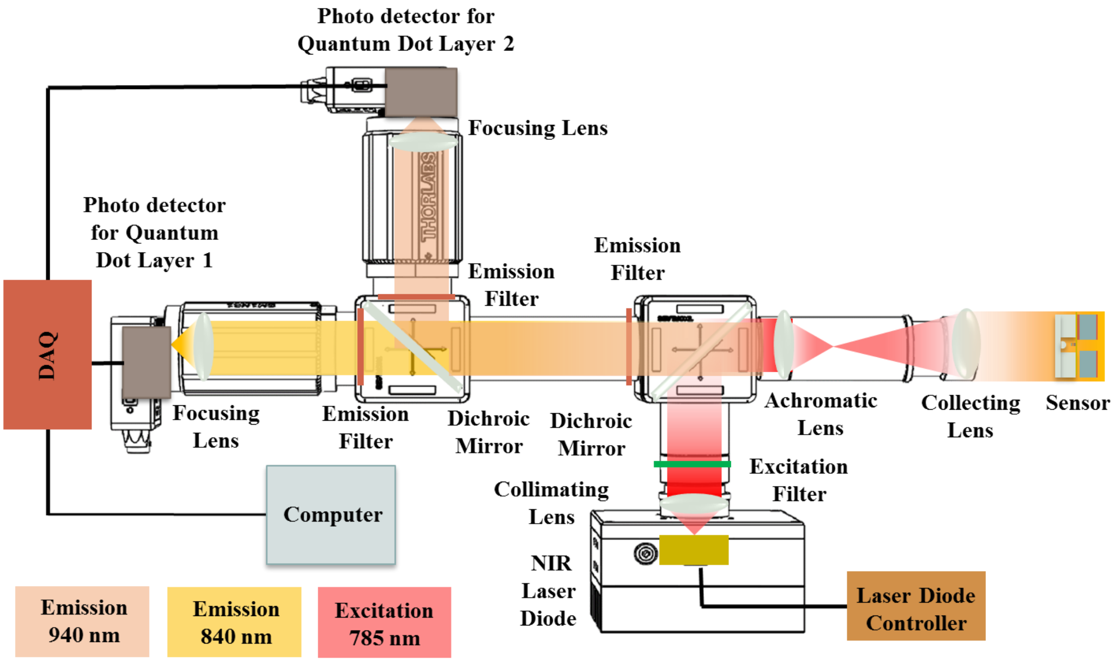

Figure 3.5: Schematic showing the ORS that has two units (i) an optical head and (ii) a data acquisition and display unit that consists of an excitation laser, two photodiodes, an electronic amplifier, a data acquisition board and an interactive display unit.

The QDs are excited using a 785 nm, variable power laser diode (LD785-SH300, Thorlabs Inc.) whose light goes through a collimating lens (A280TM-B, Thorlabs Inc.) and excitation filter (FL780-10, Thorlabs Inc.) before reaching the first dichroic mirror (T810lpxr, Chroma Technology Corp.). The 785 nm wavelength is ideal for penetrating eye tissue as it is not visible, therefore more comfortable for the patient and it does not cause any tissue damage [130]. The presence of the laser collimator makes sure that light enters/exits the housing cube collimated. The beam expander is designed to produce a laser beam diameter of ~19 mm in order to ensure that the beam reaches the NiFO sensor even if misalignment is present. The user can turn the laser on or off and control its power through the touch screen interface.

The laser diode is attached to a heat sink mount (TCLDM9, Thorlabs Inc.) to dissipate heat and prevent laser damage. The laser current, and therefore optical power is regulated by a laser controller (LDC205C, Thorlabs Inc.).

The ORS housing has been manufactured using precise CNC machining to maintain focal distances and optical alignment.

3.4.2 Principle of operation

NiFO technology consists of an implantable MEMS sensor (the ‘NiFO’ sensor) and a portable, optical readout system.

As seen in Figure 3.6, the NiFO sensor functions as an ‘analog optical encoder’ when excited by a near infrared (~785nm) laser. Changes in IOP are converted into intensity-based ratiometric changes of a two-wavelength fluorescent light in the NIR regime (840 nm – 950 nm). The fluorescent light emitted by the sensor passes through the outer surface of the eye and is collected by an optical head. Operating the device in the NIR regime is crucial for effectively transmitting the NIR light through the eye (the absorption coefficient of the eye tissue (cornea, retina, etc) in the 700-950 nm window is extremely low [130] and for minimizing retinal damage.

Key design element of the NiFO sensor is the vertical integration of a microlens with a two-layer (two- color/wavelength) quantum dot (QD) pillar, termed the ‘QD micropillar’. Each of the two QD layers contains QDs that emit fluorescent light at a specific NIR wavelength (at 840 nm and 940 nm respectively). A third ‘blank’ layer separates the two QD layers and functions as an optical spacer. The QD micropillar sits on top of a flexible membrane that is exposed to IOP (Figure 3.6). At zero-IOP, collimated light passing through the microlens is focused at the top surface of the QD micropillar, resulting in the excitation of the first QD layer. Due to the finite focal volume of the focused excitation light, the second QD layer is also excited but with lower intensity. An increase in IOP causes deflection of the membrane resulting in the first QD layer to exit and the second QD layer to enter the focal volume respectively. The IOP is thus ‘fluorescently encoded’ as the IOP changes are converted into changes in the fluorescent ratio intensity between the two QD wavelengths. Finally, the emitted light is collected by the microlens and exits the NiFO sensor collimated.

As previously discussed, the NiFO sensor can be either integrated into an IOL, or it is surgically mounted after fitting it into a KPro implant (Figure 3.3). In both cases, the NiFO sensor is exposed directly to the IOP of the aqueous humor.

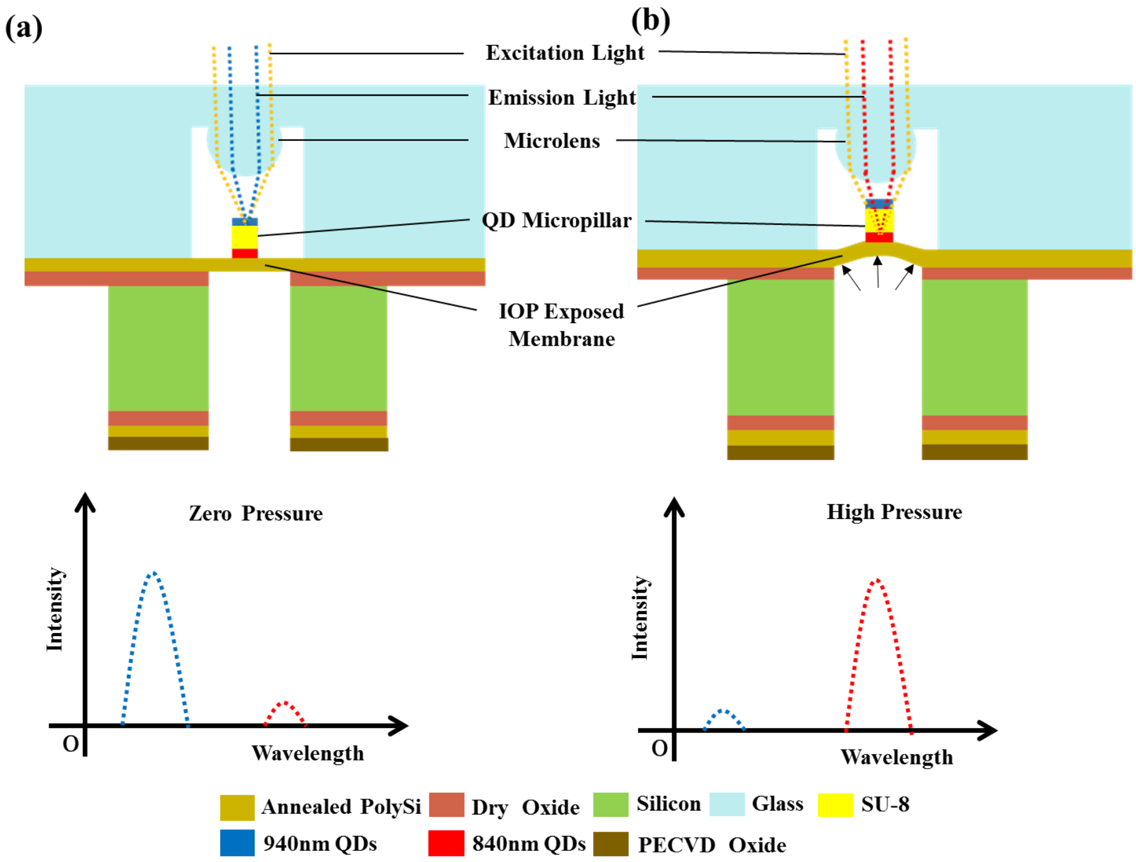

Figure 3.6: The sensor has a micro lens that is vertically integrated with micro pillar on top of a flexible membrane containing two layers of quantum dots that are separated by an optical spacer. When excited by a NIR laser: (a) at zero-IOP, collimated light passing through the microlens is focused at the top surface of the QD micropillar, resulting in the excitation of the first QD layer. (b) An increase in IOP causes deflection of the membrane resulting in the first QD layer to exit and the second QD layer to enter the focal volume respectively. Therefore, changes in IOP are converted into intensity based ratiometric changes of a two wavelength fluorescent light in the NIR regime.

3.4.3 Micro-fabrication

A combination of bulk and surface micromachining processes have been used to microfabricate the integrated NiFO sensor as shown in Figure 3.7. 1: A 0.2 µm thick layer of dry oxide was created by the thermal oxidation of a standard 4” silicon wafer followed by 2: the deposition of 0.2 µm of polysilicon using Low Pressure Chemical Vapor Deposition (LPCVD). The polysilicon layer was then annealed to result in a tensile film stress of ~ 5MPa. 3: A 2 µm layer of oxide was then deposited on one side of the wafer using Plasma Enhanced Chemical Vapor Deposition (PECVD). The side containing the PECVD oxide was patterned using a 7 μm thick layer of photoresist (SPR 220). 4 & 5: The opposite side of the wafer was then patterned using QDs in PMMA and SU-8 to obtain 9 arrays of QD micropillars with each array yielding 20 devices (Figure 3.7). To boost the fluorescent signal, the QD micropillar is made out of extremely concentrated CdSeTe/ZnS QDs (5mg/ml) embedded in PMMA polymer. To microfabricate the QD micropillar, 840 nm QD solution was mixed into pre-polymerized PMMA photoresist and then spun cast and cured (Appendix A, Sections A1, A2). SU-8 (2010) photoresist was then spun and patterned on top of the first QD/PMMA layer to form the 8 μm thick optical spacer. The second 940 nm QD/PMMA layer was then spun cast and cured using an identical process followed by spin casting and curing a 1 μm layer of SU-8 (2002) on top of the cured 940 nm QD layer. Finally, Reactive Ion Etching (RIE) was used to remove the PMMA layers deposited on polysilicon around the patterned QD micropillars. A microlens array, containing 20 half ball lenses and with spacing conforming with the micropillar arrangement was custom made using a glass molding process. A glass piece with through holes was manufactured using ultrasonic machining to act as a spacer between the polysilicon membrane and the microlens array. The thickness of this glass spacer was calculated to accommodate the thickness of the microlens as well as its effective focal length to ensure that the incoming laser beam will be focused on the QD micropillar by the microlens. The wafer was then diced to yield 9 arrays consisting of 20 QD micropillars each. 6: A Deep Reactive Ion Etch (DRIE) was performed on the side containing PECVD oxide up until a depth of ~ 350 μm into bulk silicon. 7: Subsequently, each microlens array, spacer and polysilicon chip with QD micropillars were meant to be laser bonded to form a glass microchamber around the membranes that encloses each QD micropillar. However, as laser bonding could not be performed (Section 3.4.4.7), UV curable glue (NOA 60, Norland Optical Adhesives) was used to bond the microles array, spacer and the polysilicon surface with the patterned QD micropillars at which point the individual devices were diced from the array. 8: This was followed by an isotropic xenon difluoride (XeF_2) etching step to remove silicon. Finally, reactive ion etching was performed to remove the dry oxide layer and create the IOP-exposed polysilicon membrane.

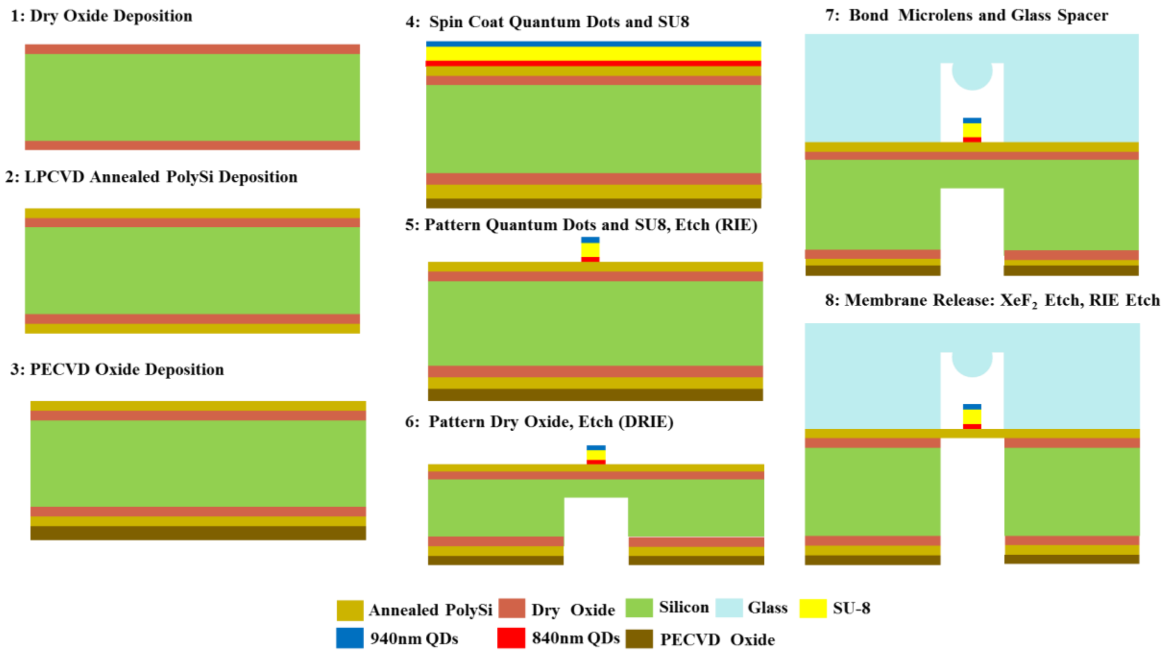

Figure 3.7: The NiFO sensor consists of a silicon chip, a glass spacer and a micro-lens layer assembled on top of each other. The key element of the design, the QD micropillar, consists of two QD layers separated by SU-8 layers that are photolithographically patterned on top of the IOP-exposed membrane of the silicon chip.

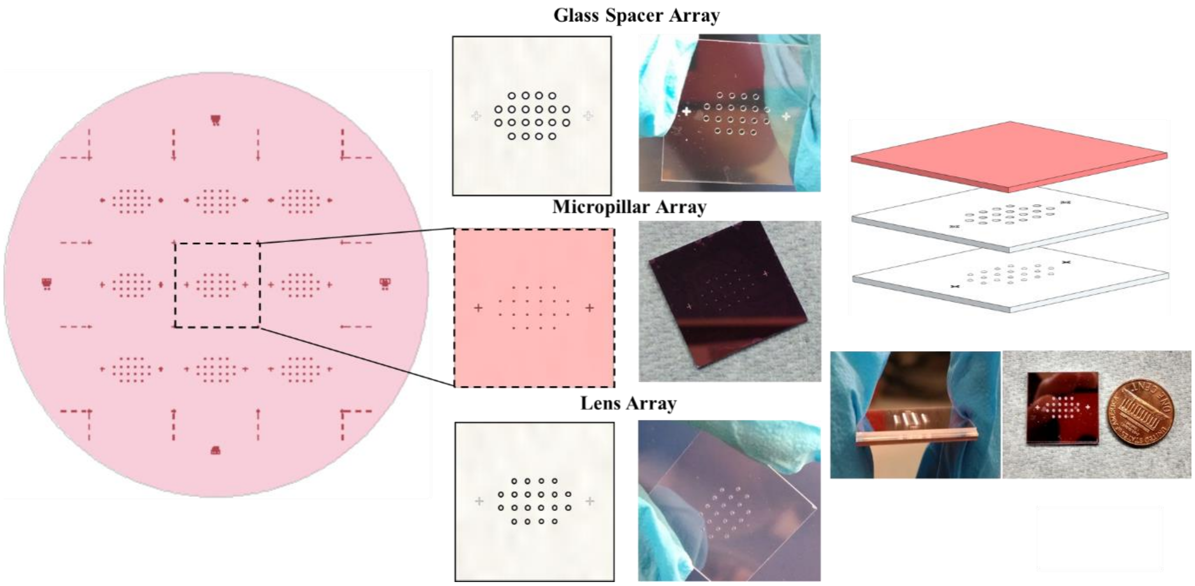

Figure 3.8: A 4” wafer yields 180 devices with each array comprising of 20 devices. The micropillar array, the glass chip with through holes and the microlens array are aligned and bonded together to yield 20 NiFO devices per array.

3.4.4 Results and discussion

3.4.4.1 Material selection

As tissue scatters and absorbs more light at shorter wavelengths, NIR light can (600 – 1000 nm) penetrate biological tissue the most efficiently [130]. However, from Figure 3.9 it can be seen that at wavelengths < 750 nm, significant absorption takes place by hemoglobin (HHb) in blood. Additionally, at wavelengths longer than 950 nm, there is a sharp increase in absorption by water and lipids. Therefore, a clear window exists at wavelengths between 750 nm and 950 nm for optical imaging of live tissue. Taking advantage of this window, the NiFO technology uses a laser that has a wavelength of 785 nm to excite the QDs. The QDs in turn have been chosen to absorb light at 785 nm and emit at peak wavelengths of 840 nm and 940 nm respectively. Since all these wavelengths lie within the NIR window, the amount of laser light reaching the NiFO sensor is maximized which in turn maximizes the amount of light emitted by the QDs and collected by the photodetectors in the external optical readout unit, thereby maximizing the signal to noise ratio.

The QDs used previously by Ghannad-Rezaie *et al.* [118], consisting of just a lead sulfide (PbS) core dissolved in toluene, had a quantum yield of ~ 15%. By using cadmium selenium tellurium (CdSeTe) QDs with a zinc sulfide (ZnS) shell, the photoluminescence quantum yield is improved to 35-40%. Additionally, the presence of surfactants like trioctylphosphine oxide (TOPO) and hexadecylamine (HDA) provides greater tolerance to processing conditions necessary for incorporation of QDs into the NiFO sensor by reducing QD aggregation.

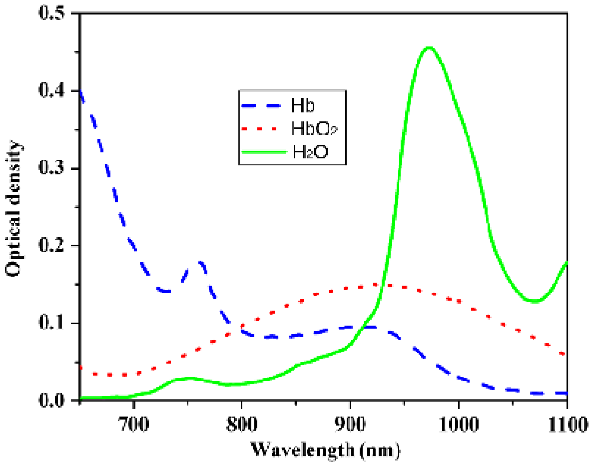

Figure 3.9: Absorption spectra of deoxyhemoglobin (Hb), oxyhemoglobin (HbO_2), and water (H_2O) in the visible and NIR regions. [Figure and caption appear in and are taken from **[131]**].

All the materials used in the NiFO sensor (silicon, polysilicon, silicon dioxide, SU-8, PMMA, L-LAM 72 glass) maybe considered to be biocompatible except for the QDs.

With the advent of biomedical MEMS devices, several research groups have implanted silicon/polysilicon-based devices to study their biologic response. When silicon electrodes where implanted in the peripheral taste nerve fibers in rats for 91–118 days, normal nerve regeneration was observed [132] [133] with minimal tissue response. Additionally, when the thin film samples of LPCVD polysilicon developed by Kotzara *et al.* [133] were subjected to physiochemical, cytotoxic and histopathology tests after implantation in rabbits, the amount of residue that was formed was found to be well below detectable levels. Additionally, there was negligible change in pH which indicates good biocompatibility potential of polysilicon as an implant material.

Silicon dioxide (SiO_2) has also been tested by transecting a peripheral nerve electrode coated with silicon dioxide onto a nerve in a rabbit. The conduction properties of the implant was confirmed and it was also observed that the EMG of the affected muscles had recovered 32 days post surgery. Furthermore, the affected muscles were indistinguishable from the contralateral control muscles after 150 days [134] which demonstrates the biocompatibility of SiO_2.

SU-8, commonly used to fabricate high aspect ratio MEMS structures, was used as an insulating agent on neural electrodes as well as in cell cultures performed by researchers at the Ecole Polytechnique Federale de Lausanne. As the cultures were performed over a span of more than 3 months which represents a chronic application, the researchers concluded that SU-8 could be considered to be biocompatible [133].

PMMA is known to have a good degree of compatibility with human tissue and is used in several biomedical implants such as bone cement while performing joint replacements, in dentures, in cosmetic surgeries where is injected under the skin to reduce wrinkles/scars, in body building to create artificial muscle and even in the treatment of tuberculosis where the pleural space is filled with PMMA balls to compress and collapse the infected portions of the lungs [135]. Specifically, due to its excellent anti-inflammatory properties [136], the most widespread use of PMMA has been to use it to manufacture intraocular lenses.

It must be noted that with reference to the NiFO sensor, the structures made up of SU-8 and PMMA being fully enclosed inside the device, are not exposed to the environment which makes the biocompatibility of SU-8 and PMMA non critical.

Ceramics span a wide range of inorganic materials, including glasses that are thermally and chemically resistant. In terms of medical applications, they have been used in dental and orthopedic implants due to their robust and biocompatible properties. Glass in particular, is a very popular choice for the encapsulation of electronics components in medical MEMS implants for long term applications [137]. Besides having the properties of ceramics such as biocompatibility and excellent resistance to biological fluids, L-LAM 72, being lead free, eliminates the possibility of heavy metal leaching into surrounding tissues thereby minimizing chances of cytotoxicity.

Since the NiFO sensor uses heavy metal based QDs, discussing the potential for any systematic cytotoxicity of QDs is of critical importance. To date, a large amount of studies on cytotoxicity of QDs for their practical biological and biomedical applications have been carried out [138] [139] [140] [141]. Bhatia *et al.* showed that there is a correlation between the release of free cadmium ions from Cd based organometallic QDs and cell death [142] [143]. Yamamoto *et al.* found that apart from the nanoparticles themselves, the cytotoxicity of QDs could also be the result of the molecules covering the surface of QDs [143]. Park *et al.* further demonstrated that, in addition to the release of cadmium ions, precipitation of QDs on the cell surface impairs cell viability [141] [143]. Even though these studies prove cytotoxicity of QDs and some of the underlying mechanisms, the QD micropillar in the NiFO sensor is fully encapsulated by the polysilicon membrane on one side and glass on the other, thereby having no direct contact with biological tissue. Additionally, the QDs are trapped inside a PMMA matrix that further hinders its ability to leach outside the micropillar. Even though the chances of the QDs inside the NiFO sensor coming into contact with tissue is remote, it might be worthwhile to explore the possibility of using non heavy metal based NIR QDs such as silver chalconide QDs in the future.

Finally, due to the complex nature of the meaning of the term “biocompatibility”, one cannot automatically conclude that all these materials will pass the full battery of ISO 10993 testing. Even though preliminary results from tests published in literature form a good reference point for choosing these materials by showing that silicon, polysilicon, silicon dioxide, SU-8 epoxy photoresist, PMMA and glass with their respective MEMS processing methods are suitable for implantable medical devices, any changes introduced by processing methods used while fabricating the NiFO sensor might potentially affect material biocompatibility. Therefore, it should be noted that additional testing will be required to meet the ISO 10993 requirements for the NiFO implants.

3.4.4.2 Characterization of membrane deflection

The membrane deflection-pressure dependence is an important aspect of the sensor design as it specifies sensor dynamic range and sensitivity. The greater the membrane deflection, the greater the sensitivity as well as the range over which pressure can be measured.

The shape of pressure sensor membranes can be square, rectangular or circular. To maximize area efficiency (active area/dice area) and simplify fabrication processes such as dicing, square and rectangular membranes are commonly used. However, for the same active area used, a circular diaphragm gives the largest sensitivity and the rectangular diaphragm gives the smallest sensitivity [144]. Furthermore, since there is no sharp corner on the circular diaphragm, the maximum stress on the edges is reduced compared to the other two shapes. This causes the center deflection and in turn sensitivity, to be the largest in circular membranes [145]. Therefore, for applications in which maximum deflection plays an important role such as in the NiFO sensor, the circular shape is preferred and has been used.

The deflection-pressure behavior of the thin circular membrane maybe analytically modeled by the following equation [145]:

$$P = \frac{Eh^4}{a^4}\left[\frac{16y}{3(1-v^2)h} + \frac{(7-v)y^3}{3(1-v^2)h^3} + \frac{4a^2\sigma y}{(1-v)Eh^3}\right] \text{------------- (1)}$$

Where y, h and a are the maximum deflection (deflection at the center of the membrane), thickness and radius of the membrane, P is the applied pressure, σ, E are the residual stress and Young’s modulus (169 GPa) of the polysilicon film and v (0.22) is the Poisson’s ratio. From the analytical equation, it can be seen that maximum membrane deflection is directly proportional to diameter and inversely proportional to thickness, residual stress and Young’s modulus.

Analytical deflection-pressure characterization curves for circular membranes of diameter 600 µm, thickness 200 nm, residual stress of 5 MPa and different materials (silicon nitride and polysilicon) were obtained (Figure 3.10). Since polysilicon has a lower modulus of elasticity (E) compared to silicon nitride (E = 290 GPa, the material used in the device developed by Ghannad Rezaie *et al.* [118]), the maximum deflection for the same amount of applied pressure is larger for polysilicon membranes. Therefore, by simply switching the material to polysilicon, the maximum deflection is improved by ~ 1 µm in the physiological pressure range (0-20 mmHg) and ~ 2 µm in elevated IOP cases (20-45 mmHg) compared to the results obtained from a silicon nitride membrane.

The deflection-pressure characterization results in Figure 3.11 show that for circular membranes, the larger the membrane diameter, the greater the maximum deflection obtained. Given that the device footprint is limited and after taking into account, the minimum area required to bond the glass spacer to polysilicon (see Section 3.4.4.7), the maximum size of the membrane can be 1 mm (in diameter). However, making the membrane 1 mm in diameter would result in a very fragile base that would not be able to fit into the KPro without breaking. Having a membrane of diameter 400 µm would result in a much stronger base but the maximum membrane deflection (under 5 µm at 40 mm Hg) would be very low. Therefore, to maximize membrane deflection while also maximizing the amount of material to strengthen the base to be able to withstand insertion into the KPro device, a membrane of diameter 600 µm was chosen for the NiFO sensor.

During the process of thin film deposition used to fabricate the membrane, the thermal expansion coefficient mismatch between different materials causes the buildup of residual stress in the membrane. A compressive residual stress results in higher deflection sensitivity but the membrane has the risk of buckling under compression. A very tensile membrane, though stable against buckling, has reduced membrane deflection (as shown in Figure 3.12) and can break in the presence of excess pressure or high temperature gradients. The residual stress of the polysilicon membrane was therefore controlled to be slightly tensile at 5 MPa to eliminate the risk of buckling without significantly compromising the ability of the membrane to deflect.

Membrane thickness typically seen in MEMS devices range from 0.15–1000 µm. From Figure 3.13, it maybe seen that the thinner the membrane, the greater the membrane deflection. Given that polysilicon membranes which are thinner than 0.15 mm are very hard to manufacture without holes and are generally not strong enough to withstand pressure loads [145], a membrane thickness of 0.2 µm was used to fabricate the NiFO sensor.

The results shown in Figures 3.10, 3.11, 3.12 and 3.13 depict a nonlinear regime at the physiological pressure range (0–20 mmHg) and a linear regime at higher pressures (20–45 mmHg).

The membrane deflection-pressure dependence characteristics can be affected by the weight of the QD micropillar resting on the membrane. To study this loading effect of the QD micropillar, the membrane along with the QD micropillar was simulated using Finite Element Analysis (FEA) in ANSYS to evaluate maximum membrane deflection with varying pressure. From the results of the simulation depicted in Figure 3.14, it may be seen that within the clinically relevant pressure range of 0-45 mm Hg, there is a maximum difference in membrane deflection of ~ 1.2 µm at 45 mm Hg with and without the QD micropillar . In contrast, there is a maximum difference in membrane deflection of ~ 3 µm and ~ 4.7 µm for membrane diameters of 800 µm and 1000 µm respectively, which demonstrates a greater QD micropillar loading effect with increasing membrane size. Furthermore, the membrane deflection-pressure dependence FEA results (without QD micropillar) match closely with the analytical results (as seen in Figure 3.16) thereby validating the simulated model of the membrane.

A mechanical failure, besides rendering the NiFO sensor useless, poses a risk to the patient. As the membrane is the most fragile element of the sensor, the possibility of failure was evaluated with an FEA. The stress distribution across the membrane while subjecting it to a pressure load was evaluated. It is critical that the maximum stress of the membrane, the von Mises stress, has to be smaller than the (tensile) yield strength of polysilicon (~2.5 GPa [146]) as increased stress can lead to plastic deformation and/ or microcracks. In the FEA simulations, pressure was varied between 0 and 100 mmHg for a 600 µm diameter, 200 nm thickness membrane with 5 MPa residual stress. The results shown in Figure 3.15 suggest that even at extreme IOP values (e.g. 100 mmHg), the maximum von Mises stress is one order of magnitude lower than polysilicon's yield strength. As expected, the maximum stress always appears at the edges which are anchored.

To experimentally estimate deflection-pressure dependence, the backside of the polysilicon membrane was exposed to a pressure range representing physiological (0-20 mmHg) and elevated IOP cases (20-45 mmHg). With the top side of the membrane maintained at atmospheric pressure, the bottom side of the membrane was exposed to fluid pressure. After housing the sensor in a custom holder that fits into a pressure chamber, air inside the sealed pressure chamber was used to apply the desired fluid pressure while membrane deflection was measured using white light interferometry, as described in Section 3.4.5.1. Deflection-pressure characterization curves for a 600 µm diameter, 200 nm thickness circular membrane with a residual stress of 5 MPa were obtained (Figure 3.17). The pressure was regulated from 0 mmHg to 45 mmHg by manually adjusting the dial of a pressure regulator and the corresponding membrane deflection was measured for every 5 mmHg. The results depict a non-linear regime at the physiological range (0-20 mmHg) and a linear regime at higher pressures (20-45 mmHg). No plastic deformation was observed and none of the membranes failed despite repetitive loading at 45 mm Hg (maximum applied pressure) which indicates robust operation with the experimental results matching closely with the analytical solution (Figure 3.17).

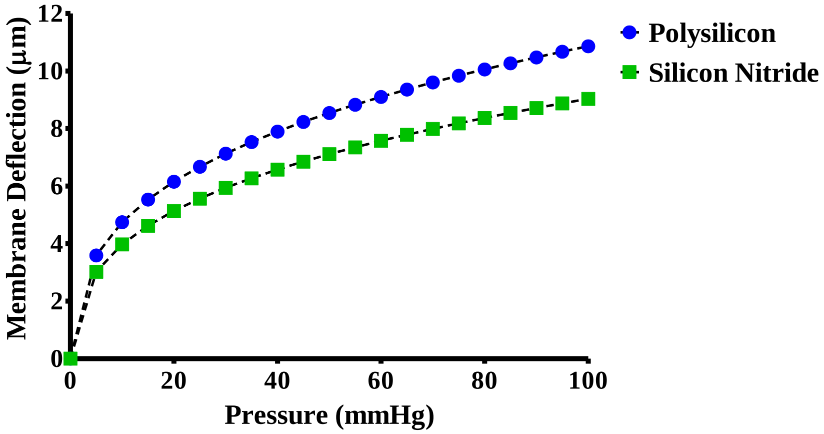

Figure 3.10: Maximum membrane deflection versus applied pressure for circular membranes of diameter 600 µm, thickness 200 nm, residual stress of 5 MPa and different materials (silicon nitride and polysilicon).

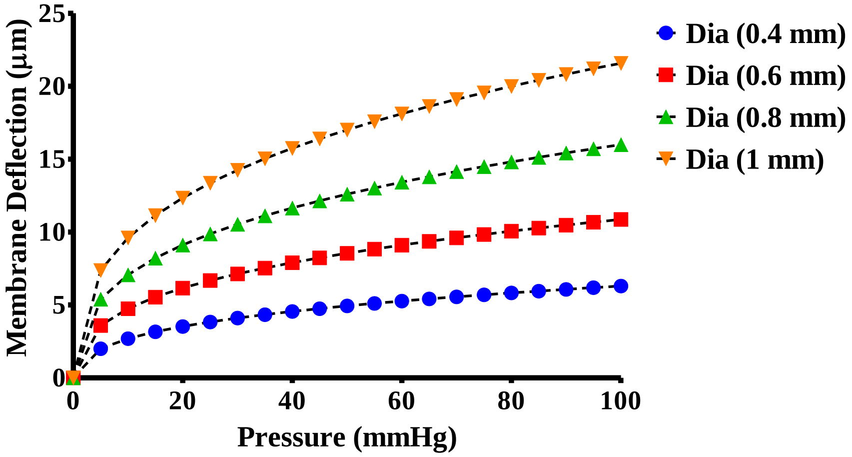

Figure 3.11: Maximum membrane deflection versus applied pressure for circular polysilicon membranes of 4 different diameters (0. 4 mm, 0.6 mm, 0.8 mm, 1.0 mm), thickness 200 nm and residual stress of 5 MPa.

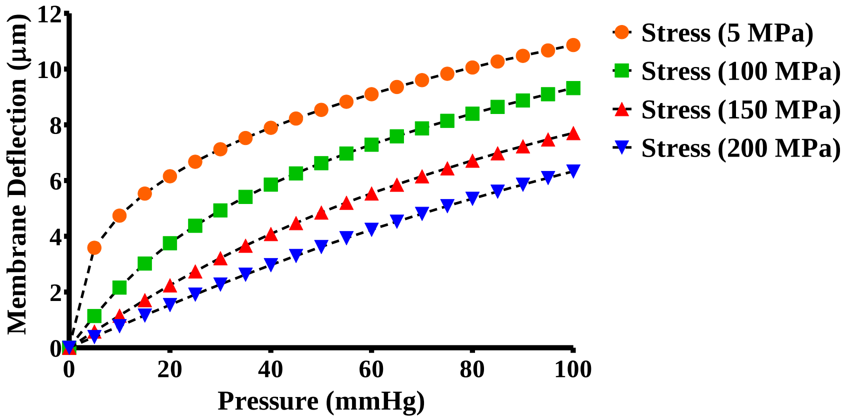

Figure 3.12: Maximum membrane deflection versus applied pressure for circular polysilicon membranes with 4 different residual stresses (5 MPa, 50 MPa, 100 MPa, 150 MPa), diameter of 600 µm and thickness of 200 nm.

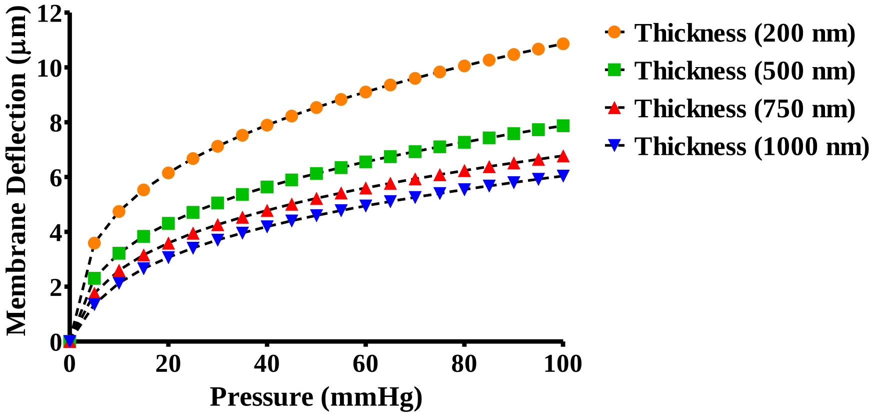

Figure 3.13: Maximum membrane deflection versus applied pressure for circular polysilicon membranes with 4 different thicknesses (200 nm, 500 nm, 750 nm, 1000 nm), diameter of 600 µm and residual stress of 5 MPa.

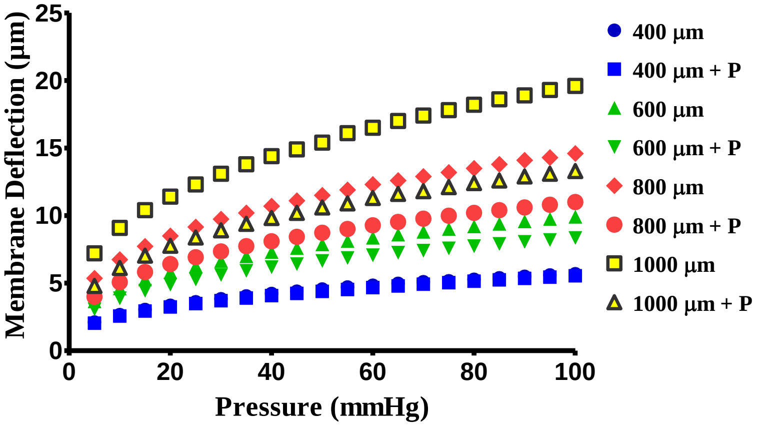

Figure 3.14: Maximum membrane deflection versus applied pressure for circular polysilicon membranes of 4 different diameters (0. 4 mm, 0.6 mm, 0.8 mm, 1.0 mm), thickness 200 nm and residual stress of 5 MPa with and without QD micropillar loading.

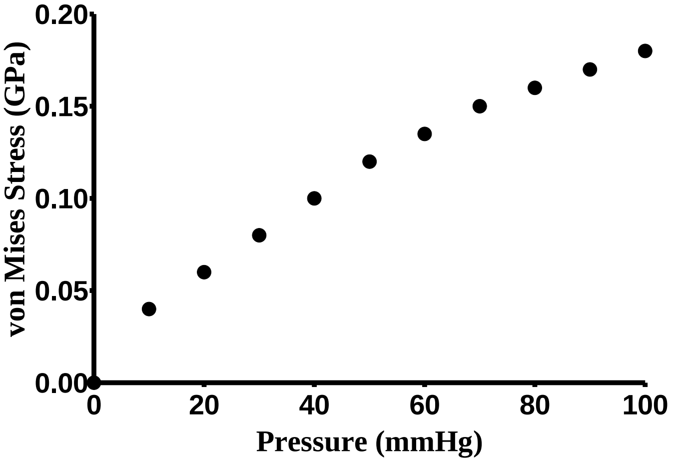

Figure 3.15: The maximum von Mises stress at different applied pressure in a 600 µm diameter, 200 nm thickness membrane with a residual stress of 5 MPa.

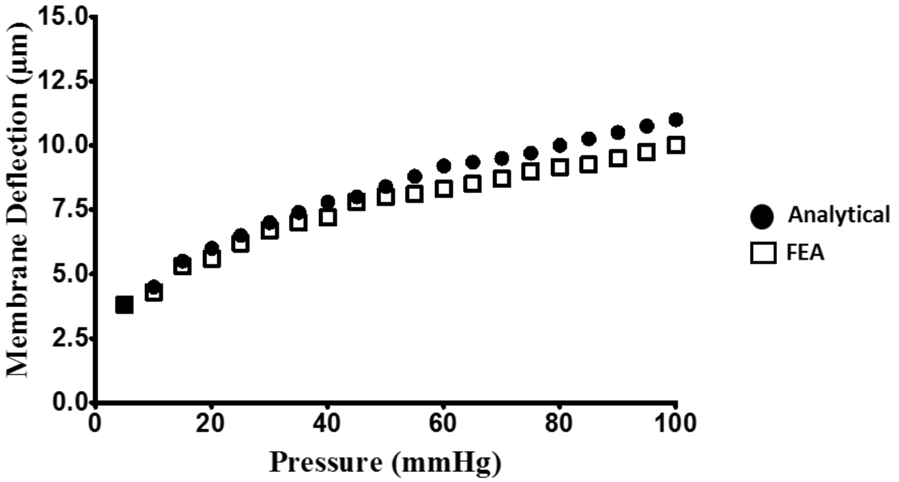

Figure 3.16: Maximum membrane deflection versus applied pressure for circular polysilicon membranes of diameter 600 µm, thickness 200 nm and residual stress of 5 MPa determined analytically and from FEA simulations.

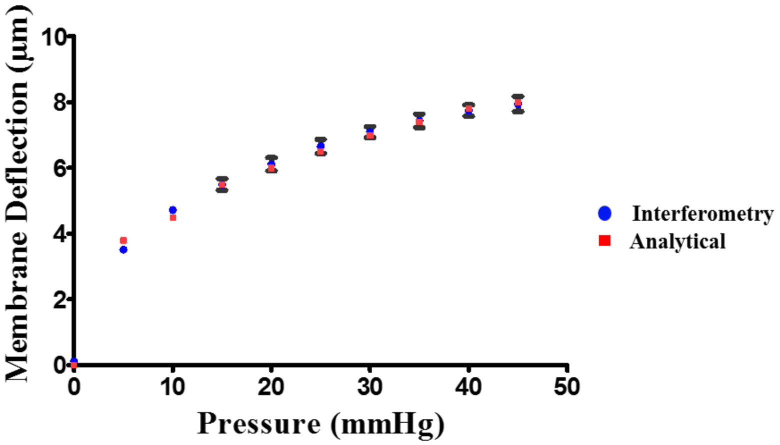

Figure 3.17: Maximum membrane deflection versus applied pressure determined experimentally and analytically for circular membrane of diameter 600 µm, thickness 200 nm and a residual stress of 5 MPa. Error bars represent standard error of the mean (SEM) from 3 measurements (taken from one device).

3.4.4.3 Fluorescence from QD micro-pillar

A readout platform was built to characterize the opto-mechanical performance of the NiFO sensor (see Section 3.4.5.2.) using which, the emitted fluorescent intensity was measured at 940 nm and 840 nm as a function of the applied pressure. The emission intensity for each QD layer was quantified by measuring the average intensity in the 815 nm - 855 nm and 915 nm – 975 nm spectral windows respectively. Subsequently, the normalized 940 nm / 840 nm intensity ratio was calculated (Figure 3.18). For the 600 µm diameter membrane, it maybe concluded that the dependence of pressure to the intensity ratio and to membrane deflection is identical in the clinically relevant pressure range of 0-45 mmHg.

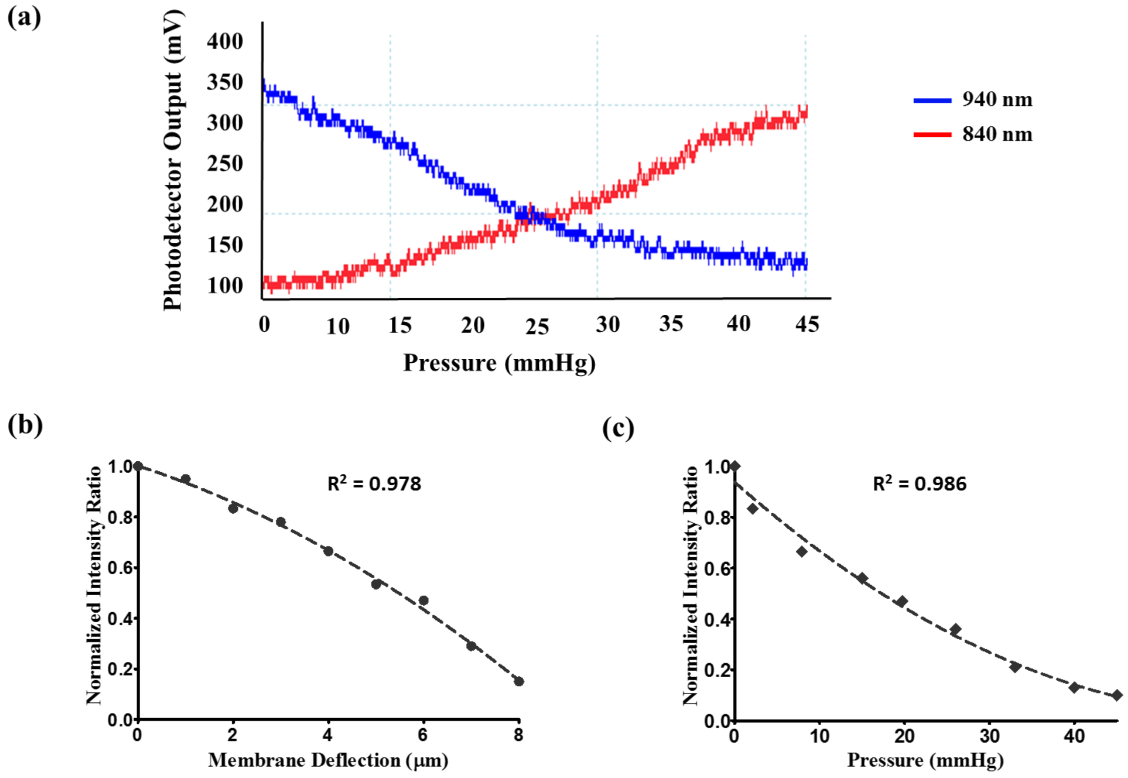

Figure 3.18: (a) The fluorescent intensity obtained from each QD layer (taken from one device). Normlaized intensity ratio versus (b) membrane deflection and (c) applied pressure for a NiFO sensor consisting of a 600 µm diameter, 200 nm thickness, 5 MPa residual stress circular membrane. The dashed lines represent a fit by a third-order polynomial.

3.4.4.4 Characterization of micro-lens array

The magnitude of the fluorescent signal collected from the QD micropillar depends upon the design of the microlens. The characteristics of the microlens that influence its fluorescent light gathering capacity include its Numerical Aperture (NA) and the Depth of Field (DOF). Furthermore, the variation of these and related parameters such as lens diameters and focal lengths between microlenses in each array directly determines production yield and is therefore equally important.

The microlens arrays were custom made by Isuzu Glass Inc. using high temperature compression molding of L-LAM 72, a high refractive index glass material that is used to make optics. The lenses have optical quality surface finish (Scratch & Dig - Surface 1 : 160-50; Surface 2 : 80-50), tight dimensional tolerances (2.5 µm) and excellent broadband transmission (> 99% between 480-1800 nm).

The amount of light collected by the microlens maybe quantified by its numerical aperture that is given by: NA = $n_M \cdot \sin\theta$, where n_M is the refractive index of the medium that the lens is placed in and θ is the half angle of the cone of rays collected by the lens. The maximum half angle θ and therefore the maximum NA can be obtained when the sample, in this case the QD micropillar, is located at the focal length of the lens. In order to increase the NA, one can increase the refractive index of the medium and/or increase the angle θ. Since the lens is sealed onto the NiFO sensor to create an air cavity around the micropillar, n_M is given by the refractive index of air which is 1. The angle θ can be increased by choosing a high refractive index lens material since the higher the refractive index of the lens, the shorter the focal length and therefore, the wider the optical cone which translates to a larger θ. L-LAM 72, a popular industrial glass material, was chosen due to its high refractive index (1.72) for NIR wavelengths, superior NIR spectral transmission (> 99%) and amenability to be compression molded at high temperatures with good surface finish.

Given the dimensions of the polysilicon membrane (0.6 mm in diameter), the diameter of each microlens was chosen to be 0.5 mm to allow for a clearance of 0.1 mm to perform alignment while assembling the sensor. The focal length of each microlens in the array was experimentally determined using the method described in Section 3.4.5.3. From the results shown in Figure 3.19(a), it can be seen that the maximum variation in focal length between microlenses in an array is ~ 55 µm while the variation in average focal lengths in between arrays is under 10 µm.

Based on the experimentally determined focal lengths and a lens diameter of 0.53 mm, the NA is subsequently calculated from Equation 3 and was found to be ~ 0.5. Figure 3.19(b) shows the NA for each microlens in 5 separate lens arrays.

Apart from the NA, the excitation focal volume is also determined by the DOF of the microlens. Based on the NA and for a wavelength (λ) of 785 nm, Figure 3.19 (c) shows the DOF of individual microlenses in 5 separate lens arrays estimated from Equation 4 is ~ 3 µm. Being greater than the thickness of each quantum dot layer in the micropillar, this DOF makes the focal volume large enough to capture all the fluorescent flux from one layer without overlapping with the other layer.

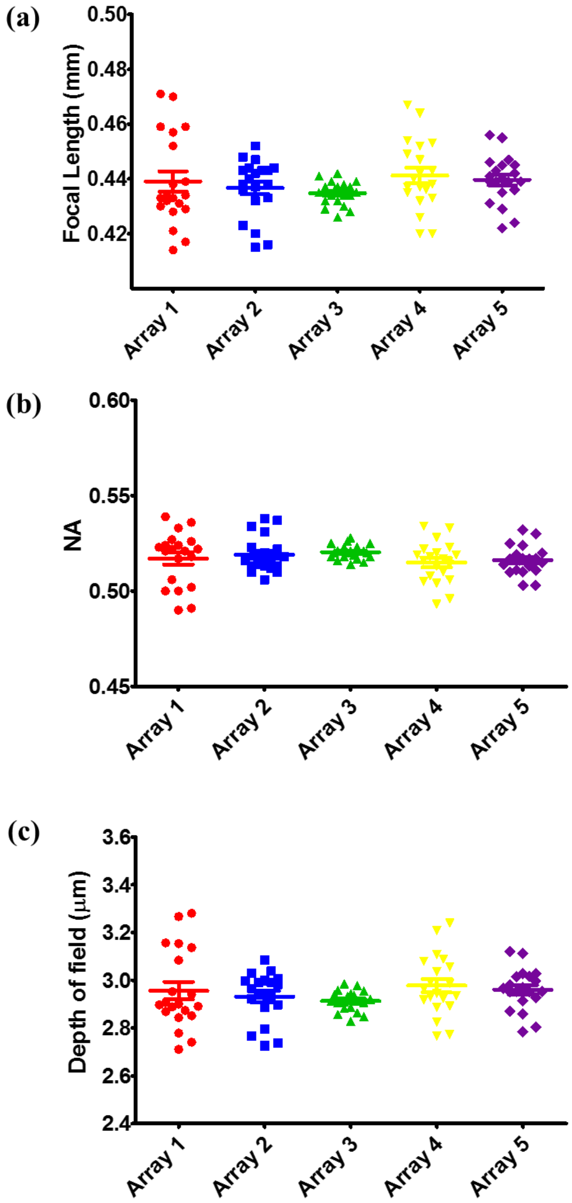

Figure 3.19: Scatter plots showing variations in (a) EFL, (b) NA and (c) DOF of 20 microlenses in each lens array.

3.4.4.5 Patterning quantum dot micro-pillars

In recent years, the nanoscale quantum confinement shown by semiconductor QDs have attracted a lot of attention for various photonic and optoelectronics applications including communications, [147] displays, [148] and biology [149]. While there are many methods for synthesizing them, semiconductor QDs formed in colloidal solutions via chemical synthesis has been the most popular method [150]. In colloidal solutions, however, QDs are suspended in a solvent, making them less practical for microfabrication and integration of photonic and optoelectronic devices. The introduction of such QDs into a solid-state matrix, therefore, is of great interest. One approach incorporates the QDs into polymer thin films and has shown great promise [151] [152]. The incorporation of QDs into a thick, bulk polymer matrix has also been investigated by using many complicated synthesis techniques to prevent aggregation of QDs [153]. In order to realize the NiFO sensor, CdSeTe/ZnS quantum dots of wavelength, 840 nm and 940 nm (purchased from Nano Optical Materials, Inc) dispersed as a colloidal suspension in toluene were used. Cd based core/shell QDs provide narrower band fluorescent emission and provide higher levels of photoluminescence and stability when compared to core only complexes. The QDs are surface coated with organic surfactants that make them lipophilic and soluble in organic solvents such as toluene, chloroform, and hexane.   We implemented a simple method to embed these QDs in PMMA using the pre-polymerization of PMMA monomers to obtain a uniform distribution of QDs and to prevent them from separating from the polymer matrix [154]. Furthermore, the incorporation of QDs in other polymers that are routinely used in MEMS based microfabrication processes such as SU8 and PDMS were also explored.

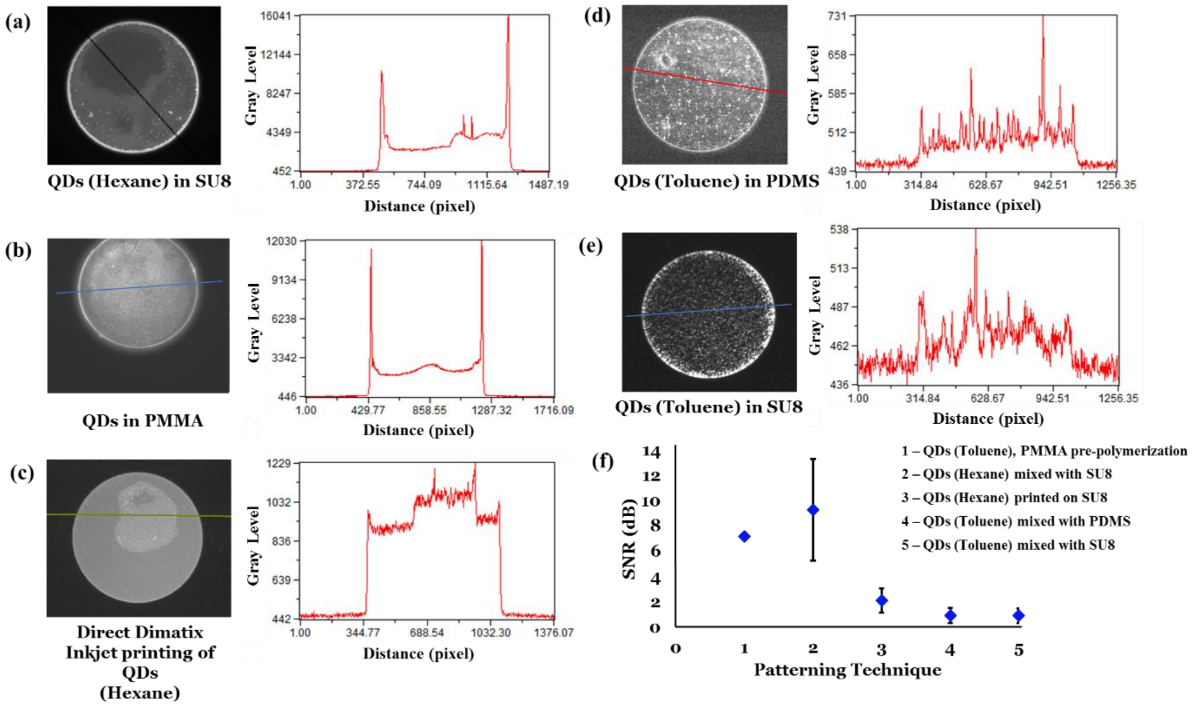

Figure 3.20: Grayscale micrographs showing fluorescence from QD micropillars fabricated with (a) QDs in hexane, photo-lithographically patterned after mixing with SU-8, (b) QDs in toluene, pre-polymerized in PMMA, spin cast and cured on SU-8, (c) QDs in hexane printed on cured SU-8, (d) QDs in toluene, mixed with PDMS, spin cast and cured on SU-8, (e) QDs in toluene, photo-lithographically patterned after mixing with SU-8 with corresponding line scans data. (f) Plot showing fluorescence signal to noise ratios obtained from each patterning technique. Error bars indicate standard deviation of measurements performed on five different micropillars on the same wafer and belonging to the same array.

QD-PMMA composite: The synthesis of the QD-PMMA composite is based on the radical polymerization of MMA (methyl methacrylate). Under vigorous stirring, a quantity (Appendix A, Section A1) of nanoparticle colloidal solution of QDs in toluene was slowly added into distilled MMA with a concentration of radical initiator benzoyl peroxide. It is commonly known that the uniform dispersion of nanoparticles in the polymer–QD composites is hampered by cluster aggregation which separates the QDs from the polymer matrix. Direct polymerization of QDs, in which the QD-MMA solutions was placed in a thermostatic water bath at 60 ^{0}C for 1 hour exhibited serious non-uniformity and clustering of the QDs. When the QD-MMA solution was, however, first placed into a thermostatic water bath at 90 °C for about 5 min for a short and quick pre-polymerization, and then was transferred into a thermostatic bath at 60 °C to completely polymerize for 20 min, before proceeding to spin cast and cure for 10 minutes at 110 ^{0}C, a uniform distribution of QDs in PMMA (layer thickness of ~ 100 nm) was observed without any aggregation (Figure 3.20(b)). The rapid polymerization of MMA monomers form oligomers, which envelope the QDs and prevent them from aggregating during the following post-polymerization process.

Additionally, it was observed that when the temperature for curing PMMA was increased from 110 ^{0}C to 150 ^{0}C, the QDs displayed a quenching effect with more than a 2 fold reduction in photoluminescence as shown in Figure 3.21(a). Furthermore, the amount of PMMA-QD deposited during the spin casting process was higher at the center of the wafer compared to the edges by about ~ 0.3 µm, as demonstrated by an increase in photoluminescence from the micropillars patterned at the center of the wafer compared to those at the edges (Figure 3.21(b)). The lack of any statistically significant variation in photoluminescence sampled from comparable locations across two wafers show that the patterning process is repeatable (Figure 3.21(b)).

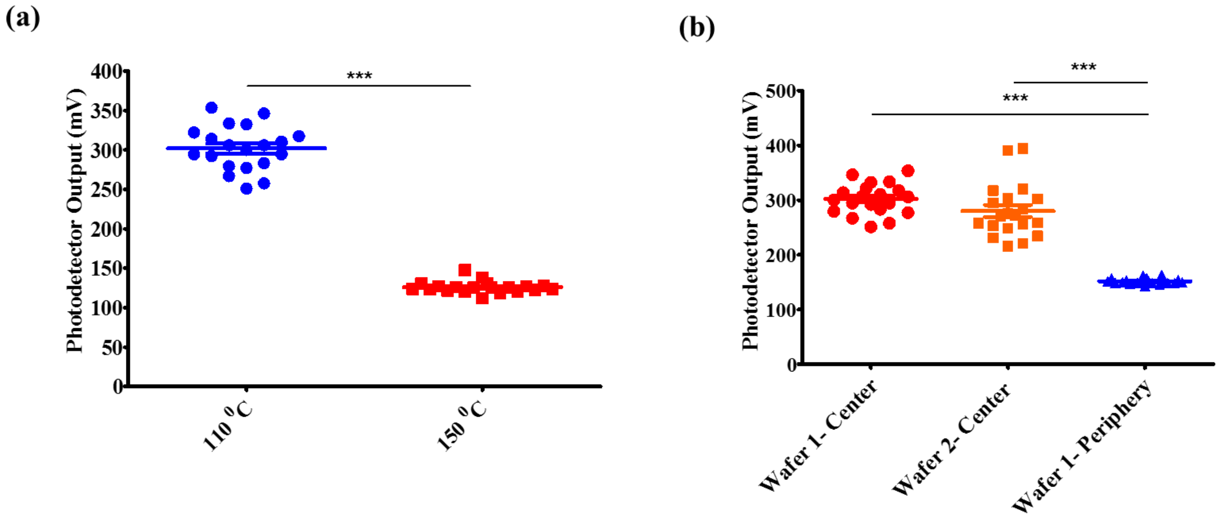

Figure 3.21: (a) Scatter plots showing variations in fluorescence from micropillars (840 nm QD layer) patterned at the center of the 4” wafer (middle array of 20 micropillars) with the PMMA-QD matrix cured at 110 ^{0}C and 150 ^{0}C respectively. (b) Scatter plots showing variations in fluorescence from micropillars (840 nm QD layer) patterned at the center of a 4” wafer 1 (middle array of 20 micropillars), from micropillars patterned at the center of another 4” wafer 2 (middle array of 20 micropillars) and from micropillars patterned at the periphery of the 4” wafer 1. [$p < 0.1$; * $p < 0.05$; ** $p < 0.01$; *** $p < 0.001$;]

<u>QD-SU8 Composite:</u> SU8 has been used as an UV sensitive material in microelectromechanical systems [155], and in holographic lithography [156]. Given that the spacer between the QD layers in the NiFO sensor is made up of SU8 and due to the superior adhesion between consecutive SU8 layers, we attempted to create SU8–QD composites to form the QD bilayer structure.

Because of the incompatibility of SU8 with toluene, which is the solvent of the QD colloid, the QDs were first transferred into hexane which is a SU8 compatible solvent. A volume of the QD solution in toluene was mixed with an excess of methanol (10 times the volume of QD solution in toluene). The mixture was then centrifuged to precipitate the QDs, the clear supernatant was discarded and the precipitated QDs were then mixed with hexane to achieve the desired concentration (5 mg/mL). Given that methanol can wash the surfactants from the surfaces of the QDs, several rounds of precipitations lead to the QDs losing their brightness and aggregation to occur. However, one cycle of methanol washing and precipitation had negligible effects on aggregation levels and QD brightness. The QDs in hexane solution was then added into the SU8 (2002) solution very slowly with strong stirring to prevent clustering of QDs in SU8. Compared with the aforementioned PMMA–QD composite, the QD concentration in the SU8–QD composite cannot be increased arbitrarily high due to the low dispersibility of QDs in the viscous SU8–polymer solution.

A SU8–QD composite layer was prepared by spin coating the solution onto a substrate followed by a soft bake at 65 °C for 5 min. The PL in the SU8–QD composites was measured as shown in Figure 3.20(a). It was observed that despite solvent compatibility between hexane and cyclopentanone (the solvent found in SU-8) and vigorous mixing, the QDs continued to aggregate, leading to the formation of a highly non-uniform distribution of QDs in cured SU8. Additionally, the variation in the thickness of the SU-8-QD composite layer was also very large (~ 4 um).

QD-PDMS composite: PDMS (Polydimethylsiloxane), commonly used in soft lithography, is a polymeric organosilicon [157] with a band gap of ~4.77 eV and is transparent to light with wavelengths longer than 260 nm [158]. Being chemically inert and weather resistant, its applications include its use in contact lenses, medical devices and as an elastomer. Additionally, it is viscoelastic so given a long flow time, or high temperature it will mold to the imperfections of a surface. This mechanical property allows PDMS to be easily applied to many surfaces as a protective layer or as a carrier of certain substances. Given that it is one of the most commonly used materials for regulating flow in microfluidic chips, PDMS is regularly used in soft lithography [159]. Due to these properties of PDMS, its availability and low cost, we explored the possibility of using it as a carrier for the QDs to fabricate the NiFO sensor. 0.5 mL of the 5mg/mL QDs was added to 3 mL of a 10:1 (ratio of elastomer to curing agent) mixture of PDMS and thoroughly mixed with the help of a mechanical stirrer. However, despite having a visually uniform post mixing appearance, the combination when spin cast on a wafer and cured, lead to the formation of QD aggregates, as shown in Figure 3.20(d).

Printing QDs directly onto the micropillars: An attempt was also made to deposit QDs directly on patterned SU8 to explore the possibility of increasing fluorescence by achieving a higher concentration of QDs while creating more uniform layers. To implement this approach, the Dimatix inkjet printer (DMP-2831) was used with the QDs suspended in a mixture of hexane and liquid SU8 (2000.5) as the ink. The printer allows the deposition of fluids directly onto the substrate by utilizing a disposable piezo inkjet cartridge. QDs in hexane was mixed with liquid SU8 to reduce evaporation and encourage spreading of the ink on the patterned and cured SU8 spacer substrate. As seen from Figure 3.22, the ink did not spread uniformly on the substrate before the solvent evaporated, despite efforts to promote spreading by subjecting the substrate to oxygen plasma treatment. Furthermore, the evaporation of the solvent lead to the aggregation of the QDs in SU-8 leading to a quenching of fluorescence. Additionally, besides requiring multiple passes (> 40) to cover a circular area of diameter 150 µm with ink, the printing nozzles on the cartridge had to be moved sequentially from one patterned feature to the next which made this approach very time intensive and low throughput.

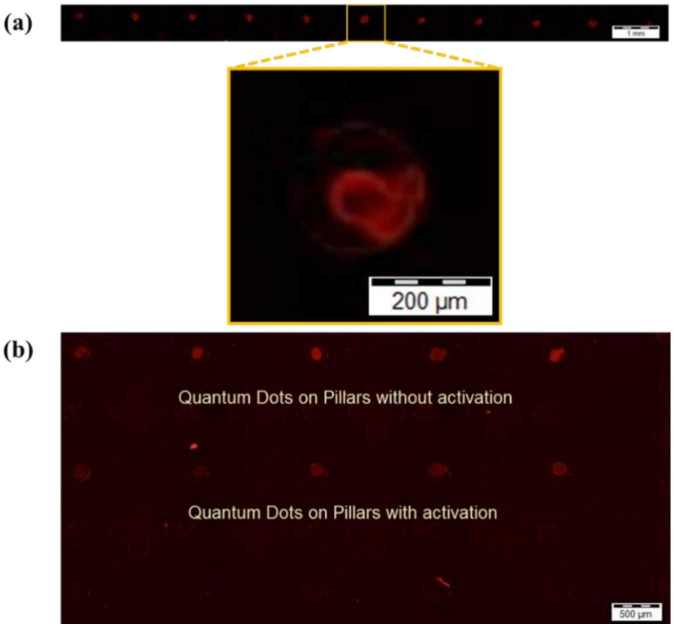

Figure 3.22: (a) Pseudo-color micrographs showing fluorescence from a row of QD micropillars fabricated with QDs in hexane printed directly onto cured SU-8. The inset is a single micropillar demonstrating QD distribution on the surface of the micropillar after solvent evaporation. (b) Pseudo-color micrographs showing fluorescence from two rows (without and with surface plasma activation) of QD micropillars fabricated with QDs in hexane printed directly onto cured SU-8.

3.4.4.6 Glass micro-machining

The microlens array is incorporated above the QD micropillar array and into the device via a glass spacer consisting of through holes as shown in Figure 3.8.

Since glass is difficult to be machined precisely at a micro scale, several methods to create the through holes were considered. Sandblasting, which is a technique in which a high velocity jet of abrasive particles is directed towards the sample for material removal by mechanical erosion, could not be used due to the formation of V shaped, tapered etch profiles that are produced with this method. Given the fixed distance requirement that needs to be maintained between consecutive through holes in accordance with microlens placement and hole depth, there is not enough room to accommodate V shaped etch profiles. Wet etching of glass has been investigated by many researchers [160] [161] with the advantages of this method being its simplicity, high etching rate, high mask selectivity and low surface roughness. However, due to its isotropic etching behavior, the aspect ratio that is achievable with this method is limited and the etch profile is U shaped with huge undercuts making it unsuitable for creating the through holes in the glass spacer. Additionally, metal masks (Cr-Au) are required in this method making it costly. Coming to RIE, even though this method has been used extensively to create high aspect ratio structures with vertical walls in silicon, there is very little literature that mentions deep glass etching with smooth surface, vertical etch profiles and high aspect ratio structures. The aspect ratio that can be created in glass is limited due to low selectivity between glass and mask material. While attempting to create the through holes with this method using the SPTS APS Dielectric Etch tool and with KMPR photoresist as the masking layer, the etch depth was limited to about 50 µm. Beyond this etch depth, the sample developed cracks that might have originated from stresses created in the material by the conditions inside the etching chamber. Mechanical drilling with a silicon carbide drill bit was also employed to fabricate the through holes after mounting the sample on a carrier (for mechanical shock absorption during the drilling process) with UV curable glue. However, despite the stabilizing support provided by the carrier, the mechanical vibrations created by the drill bit caused sample cracking. Additionally, the holes produced had significant blow out around the sides/edges that prevented any possibility of achieving good bonding between the spacer and the microlens array. Finally, ultrasonic drilling (Bullen Ultrasonics Inc.) was used to create the through holes in the glass spacer. Ultrasonic machining has a low material removal rate and is a loose abrasive machining process in which the mirror image of a shaped tool can be created in hard, brittle materials such as glass. Material removal is achieved by the direct and indirect hammering of abrasive particles against a work piece by means of an ultrasonically vibrating tool. Even though the process is physical, it induces minimal stresses in the work piece. Being non-thermal, non-chemical, and non-electrical, the chemical and physical properties of the work piece are left unchanged. Ultrasonic machined features can have high aspect ratios with vertical side walls, enabling us to preserve valuable space in between the through holes. Like wet etching and RIE, multiple features can be machined at the wafer or substrate level simultaneously, making the process scalable and low cost.

3.4.4.7 Laser bonding microlens array

Bonding glass to glass substrates and other combinations typically requires heating of the substrates to obtain bonding diffusion of the materials across the substrate boundaries unless adhesives are employed. Various examples of current bonding practices are fusion bonding, anodic bonding of sodium rich glass to silicon and adhesive bonding.

Fusion bonding glass to glass involves placing the two glass substrates in contact with each other and then applying pressure and heat. The glass is brought up to at least its first transition temperature to soften it thereby melting the two surfaces together to create one bonded piece. Besides requiring both surfaces to have matched TCEs (Thermal Co-efficients of Expansion), the method is highly susceptible to the formation of air bubbles due to sensitivity to impurities that compromises bonding. Additionally, the surface of the glass becomes distorted. Even though it is possible to use this method to bond the microlens array to the glass spacer consisting of the through holes, any distortion of the lens array will drastically affect the optical path which would significantly reduce device yield.

Anodic boding, which is commonly used to bond glass with silicon, cannot be used to perform glass to glass bonding. Glass containing sodium is essential for bonding which takes place at very high temperatures of around 400 ^{0}C and over a period of several hours. A potential difference is then applied to drive the sodium atoms across the glass-silicon boundary that creates a sodium-oxide bond at the interface. However, this method cannot be applied to fabricate the NiFO sensors as both SU-8 as well as the QDs would not be able to survive such high temperatures.

There are adhesives specifically designed to bond glass to glass and glass to silicon. While they are easy to apply, it is usually very difficult to make a bubble free joint. It would be very challenging to pattern the adhesive on polysilicon around the patterned QD micropillars to perform glass to polysilicon bonding. Alternatively, the adhesive could be applied to the lower surface of the glass spacer but there would still be a large possibility for the glue to squeeze out from between the surfaces after they are joined and cover the membrane thereby affecting its deflection properties. Additionally, most adhesives absorb fluids and swell over time, leading to leaks at the joints. This especially makes the method unsuitable for sealing implantable devices.

Therefore, due to the limitations of the above mentioned conventional bonding methods, we attempted to bond the microlens array, the glass spacer with the through holes and the polysilicon layer with patterned QD micropillars using a low (room temperature) laser bonding technique developed and patented by Invenios Inc. (US 20130112650 A1).

The process for room temperature bonding involves two substrates, with one of them being transparent to laser of a certain wavelength (usually glass). The interface created by the two substrates is therefore characterized by a transmissivity change. A change in transmissivity maybe accomplished by depositing a heat absorbing coating like a metal, semiconductor or ceramic which maybe as thin as 10 Å on either one of the substrates. When laser light is irradiated through the transparent substrate and focused onto the heat absorbing layer at the interface, a localized high temperature region is created from the energy being supplied by the laser. As more and more energy is absorbed, the glass around softens, a plasma is created and the temperature rises to enable diffusion to take place. At some point, the heat absorption layer diffused into glass and therefore becomes transparent to the laser. Once the heat absorption layer becomes transparent, the plasma collapses and the two substrates fuse to form a permanent bond.

Given that the heat absorption layer diffuses at a temperature that is higher than the first transition temperature of glass, the glass becomes soft and bonds to the neighboring material. The method is therefore fairly robust as it is not sensitive to the presence of particles. Additionally, the bulk of both substrates remain at room temperature during the bonding process. Only the heat absorption layer and the material immediately adjacent to the bond-line are elevated to the diffusion temperature. The width of a single bond-line can vary from approximately 0.001 µm to 100 µm. The depth is usually 500 nm but can be as deep as upto several micro-meters. Finally, the heat affected zone is approximately 1 µm. The spacing in between consecutive NiFO devices is such that there is a 200 µm space around the membrane in each device for bonding polysilicon to glass, thereby satisfying this requirement. Moreover, there is ample space around the through holes to allow laser bonding the glass spacer to the glass microlens array.

When bonding one substrate to another, a surface flatness of under 50 nm is needed to achieve acceptable bond quality. From Figure 3.24, it maybe seen that for the glass spacer, the shape of the sample resembles a “potato chip” with the surface flatness being ~1.5 µm for both sides. For the sample consisting of the patterned micropillars on polysilicon (Figure 3.25), the surface flatness is 0.79 µm on the side of the QD micropillars and 0.63 µm on the opposite side. Even though these values are well above 50 nm, it is possible to achieve this target as they can be forced flat with pressure and laser bonded. However, for the microlens array (Figure 3.23), the surface flatness for both top (side with the lenses) as well as bottom surfaces (plain side) is ~ 2 µm. For these samples however, force flattening would not be possible as that would damage the lenses. Therefore, in order to proceed with room temperature laser bonding, the molding process that is used to manufacture the microlens arrays must be improved to achieve a surface flatness of 50 nm that shall be employed in a future iteration. Additionally, since this process does not require bonding to take place over the entire surface of the glass, but rather the samples can be seam sealed, the target flatness of 50 nm maybe achieved with minimal modifications to the molding process.

Therefore, room temperature laser bonding is still a viable method that can be employed to assemble the NiFO sensors while ensuring maximum production yield.

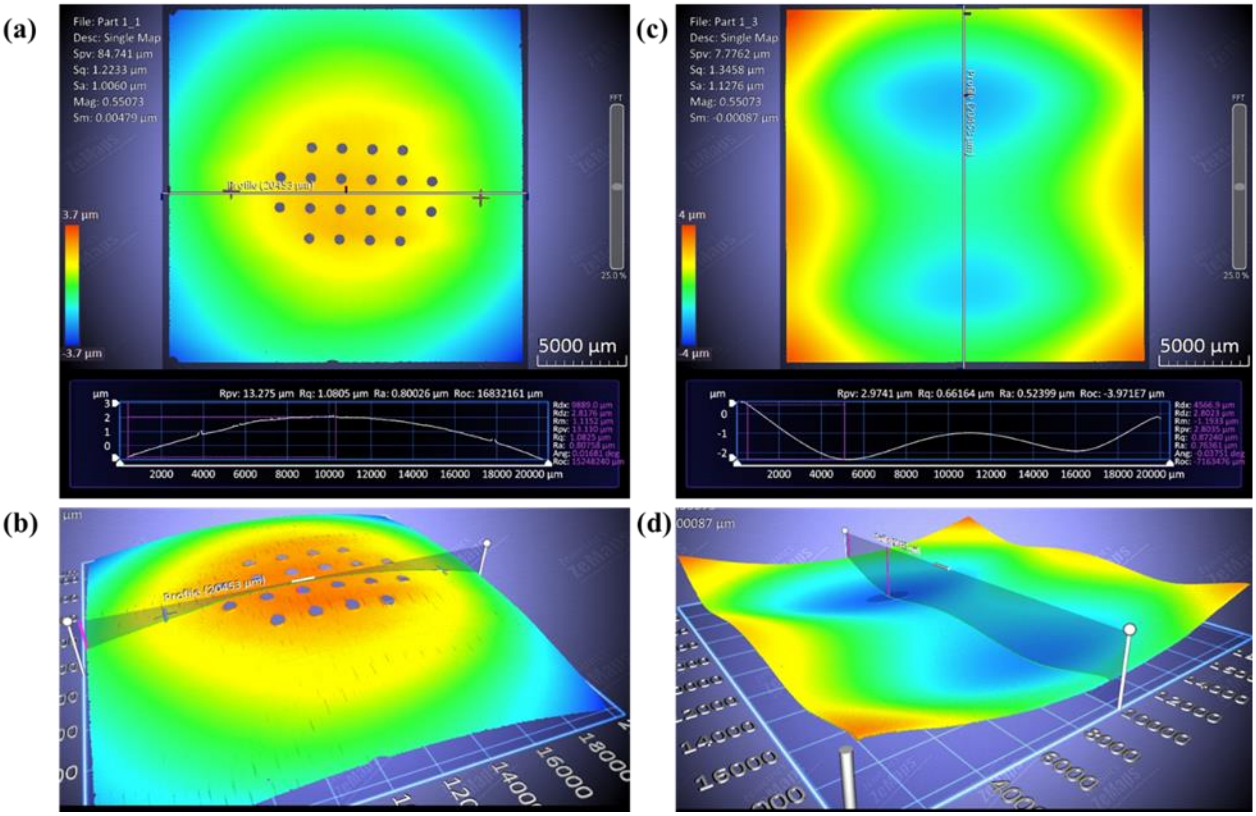
File: Part 1_1
Desc: Single Map
Spv: 84.741 µm
Sq: 1.2233 µm
Sa: 1.0060 µm
Mag: 0.55073
Sm: 0.00479 µm

Rpv: 13.275 µm Rq: 1.0805 µm Ra: 0.80026 µm Roc: 16832161 µm

File: Part 1_3
Desc: Single Map
Spv: 7.7762 µm
Sq: 1.3458 µm
Sa: 1.1276 µm
Mag: 0.55073
Sm: -0.00087 µm

Rpv: 2.9741 µm Rq: 0.66164 µm Ra: 0.52399 µm Roc: -3.971E7 µm

Figure 3.23: Microlens array (a) bottom surface (lens side) showing a maximum flatness non uniformity of 2 µm and a (b) buckled, bowl shaped profile. Microlens array (c) top surface (flat side) showing a maximum flatness non uniformity of 2 µm and a (d) warped profile with two valleys.

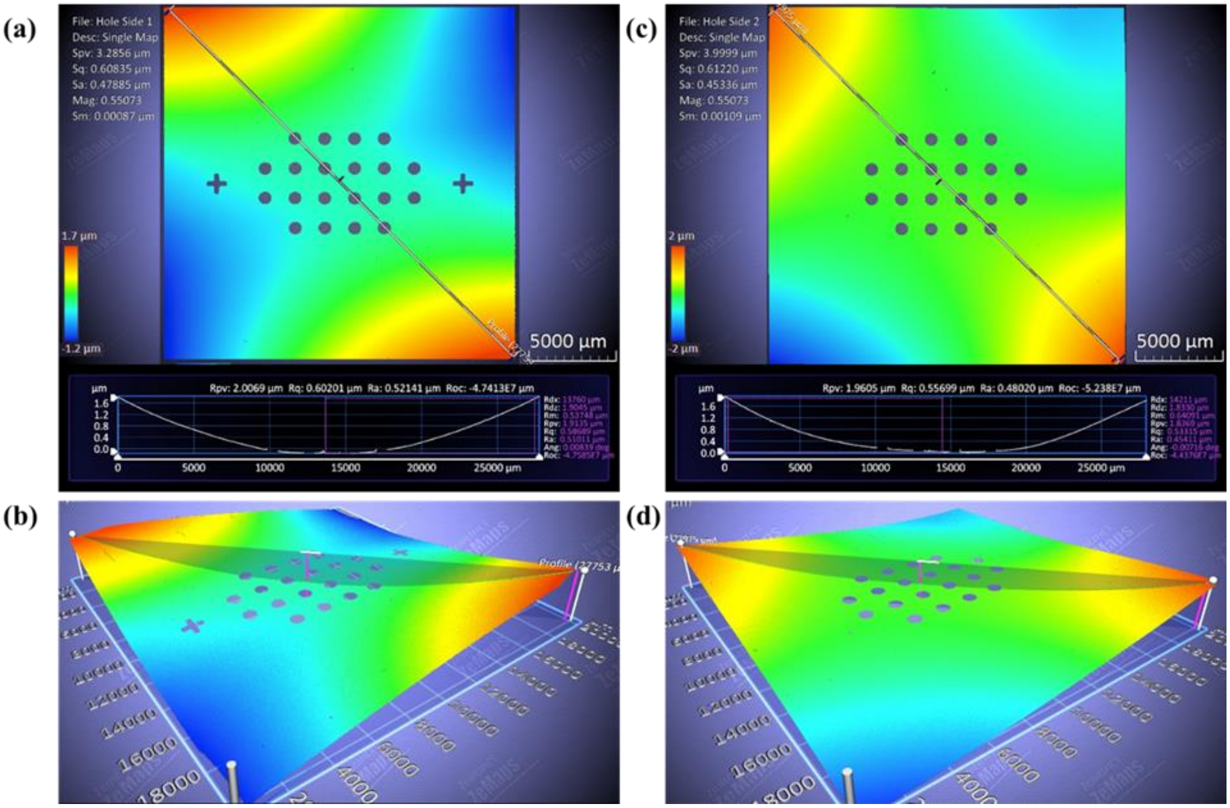

Figure 3.24: Glass spacer (a) bottom surface (with alignment cross marks) showing a maximum flatness non uniformity of 1.5 µm and a (b) twisted bowl shaped profile. Glass spacer (c) top surface (without alignment cross marks) showing a maximum flatness non uniformity of 1.5 µm and a (d) twisted bowl shaped profile.

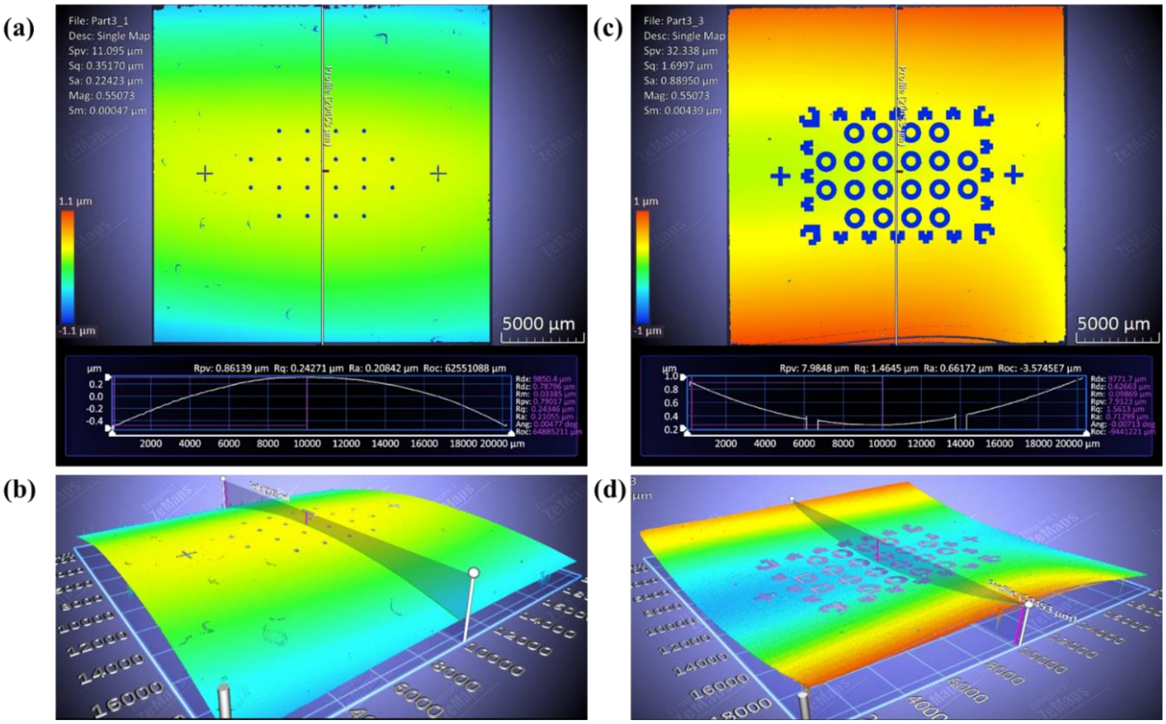

Figure 3.25: Silicon piece with array of patterned QD micropillars (a) top surface (with QD micropillars) showing a maximum flatness non uniformity of 0.6 µm and a (b) buckled, bowl shaped profile. Silicon piece with array of patterned QD micropillars (c) bottom surface (membrane side) showing a maximum flatness non uniformity of 0.7 µm and a (d) buckled, bowl shaped profile.

3.4.5 Experimental methods

3.4.5.1 Characterization of membrane deflection

The experimental setup for characterizing the NiFO sensor membrane deflection consists of a custom made pressure chamber, an external fluid reservoir, an air pressure regulator (Elveflow microfluidic AF1 pressure pump), an external fluid pressure sensor (MMG005USBHT6ME0T9A10, USB pressure transducer, Omega Engineering), an external temperature sensor (KHSS-14G-RSC-2, USB K Type thermocouple, Omega Engineering), a 3D printed holder and the NiFO sensor's readout unit (Figure 3.26).

The NiFO sensor (without its microlens) was placed in a 3D printed holder that fits into the lid of a pressure chamber. The pressure chamber, consisting of a base and a lid, is machined out of brass. The lid consists of three threaded openings, one for accommodating the 3D printed NiFO sensor holder, one for accommodating a brass compression fitting (BRLK-14-14, Omega Engineering) through which the temperature probe maybe passed and one for accommodating the threaded end of the external fluid pressure sensor. The edges of the lid have multiple (eight) threaded holes to accommodate screws that fix the lid to the base. The base has a recess in its top surface that houses an o-ring and eight threaded holes. The screws (standard M6 threading) when inserted through the lid, passes through into the base and hold the lid in place while the o-ring creates a leak proof seal in between the two parts. The base has an opening at the bottom that is connected to a ferrule through which tubing (dimensions) is inserted. The tubing connects the base to an external fluid reservoir which is in turn connected to an air pressure regulator. Fluid (can be air or distilled water) pressure inside the pressure chamber was maintained by using the air pressure regulator. The pressure chamber was placed on a hot plate at 37^0C to maintain fluid at physiological temperatures.

The setup was then placed on the stage of a non-contact optical 3D profiler (Zygo NewView 5000). Using high resolution scanning white light interferometry, the membrane inside the NiFO sensor was imaged. By mapping the microstructure and topography of membrane surface, the deflection was measured by regulating the fluid pressure inside the chamber at physiological temperatures.

3.4.5.2 Characterizing fluorescence from quantum dot micro-pillar:

A 20x, 0.75 NA objective lens (UPLANSAPO, Olympus), was fixed in front of the optical read out unit with the photodetectors attached to a two channel oscilloscope (PicoScope 3425, Pico Technology). The 785 nm laser was operated in continuous mode with a driving current of 150 mA, which corresponds to a laser power of 60mW. Using a camera (Hamamatsu Digital Camera, C11440-22C, Orca Flash 4.0), the lens was initially focused on the top QD (940 nm) layer. While regulating the fluid pressure inside the chamber as described in Section 3.4.5.1, the fluorescence from the QD layers was collected by the two photo-detectors and recorded using a two channel oscilloscope (Pico Technology, picoscope 5000 series).

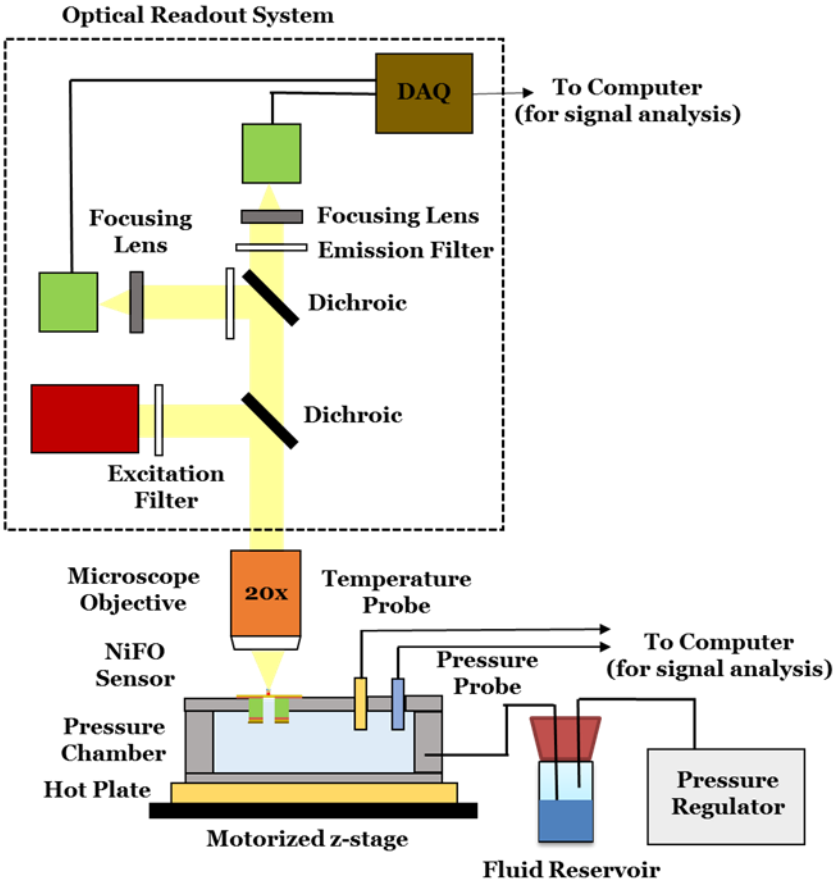

Figure 3.26: Schematic of the device characterization and testing platform. Chamber pressure may be varied to simulate IOP fluctuations in the eye along with temperature regulation.

3.4.5.3 Characterizing micro-lens array:

To obtain the optical properties of the microlenses, 5 arrays consisting of 20 lenses each were characterized. The focal length of individual microlenses was measured using a custom-made optical setup (Figure 3.27) and a 2- step sequence was followed: i) the top surface of a microlens was visually identified and set as the reference plane (plane I), and ii) the plane containing the image of the focused laser beam was brought into the imaging plane of the microscope objective (plane II) by vertically moving the microlens. The distance between these two planes (I and II) may be used to estimate the focal length of the microlens. Plane II was identified as the plane of maximum light intensity through the image analysis software (Metamorph®).

The NA of the microlenses (for use in air) was estimated from the following equation where a and F represent the microlens radius and effective focal length respectively.

$$NA = \sin\left[\tan^{-1}\left(\frac{a}{F}\right)\right] \text{-----------(3)}$$

The DOF was estimated theoretically from the NA and wavelength (λ=785 nm) using the following equation [162].

$$DOF = \frac{\lambda}{NA^2} \text{-------------}(4)$$

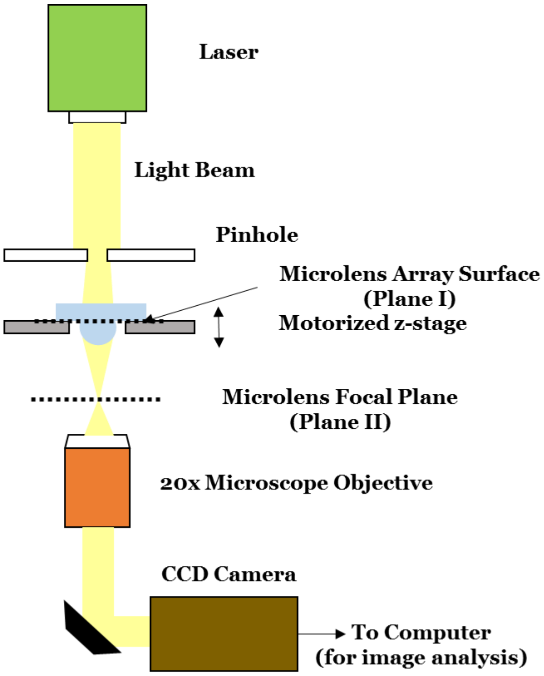

Figure 3.27: Schematic of the experimental setup for characterizing individual focal lengths of microlenses in a lens array.

3.4.6 Conclusions

A novel NIR, optomechanical, electronic-free and powerless implantable pressure sensor that can potentially monitor intraoccular pressure was developed. The sensor can monitor pressure within the clinically desired IOP range (0-45 mmHg) seen in patients suffering from POAG. The sensor does not suffer from photobleaching and has a maximum error of under 15%. The experimental results indicate that the sensor can accurately as well as repeatedly respond to fluid pressure changes in the range (0-45 mmHg) without breaking, as predicted by analytical and FEA models. Upon evaluation of the possibility for mechanical device failure, the maximum von Mises stress at 100 mmHg fluid pressure was found to be one order of magnitude lower than the polysilicon yield strength (2.5GPa).

The NiFO IOP sensing system presented in this thesis is a significant improvement over the first generation proof of concept device developed by Ghannad-Rezaie *et al.* Although the device developed by Ghannad Rezaie *et al.* does meet the clinical requirements for IOP monitoring, the choice of materials are not suitable for long term use in the *in vivo* environment.

Additionally, as per the design of the first generation prototype, the QD micropillar is directly exposed to the fluid inside the anterior chamber of the eye that raises questions about the cytotoxic effects of heavy metal based QDs on surrounding tissue. Also, the fabrication process does not provide good device yield as the microlenses have to be individually arranged and aligned manually on each device which is very laborious. Furthermore, the fabrication process cannot be outsourced easily to external contract manufacturers for commercialization. The sensor design/microfabrication approach presented here addresses these issues by 1) reducing the device footprint to ~ 1.4 mm x 1.4 mm x 1 mm and ~ 1 mm x 1 mm x 1 mm for incorporation with KPro and IOL implants respectively, 2) preventing direct exposure of cytotoxic QDs to biological tissue and 3) describing a batch fabrication process that is amenable for future commercialization of the NiFO technology.

We envision that the proposed NiFO sensing technology can be extended to other biomedical applications where pressure monitoring is required such as arterial, intracranial and gastrointestinal pressure monitoring.

3.5 DCI Technology

3.5.1 Device design

The DCI sensor [163] is an electronic-free, image contrast based sensor which can measure fluid pressure (Figure 3.29). The pressure value can be extracted by imaging the sensor using an objective lens, a Charge Coupled Device (CCD) camera and z-scanning module. Key design element of the sensor is the incorporation of a deformable, 10 µm thick, semi-transparent PDMS membrane (indicated as ‘s-PDMS’ in Figure 3.29) that is exposed to pressure. The membrane is attached to a thick PDMS slab that contains a circular microchamber, a microfluidic channel and one inlet that is used to pressurize the membrane. A rigid thick glass substrate seals the entire sensor.

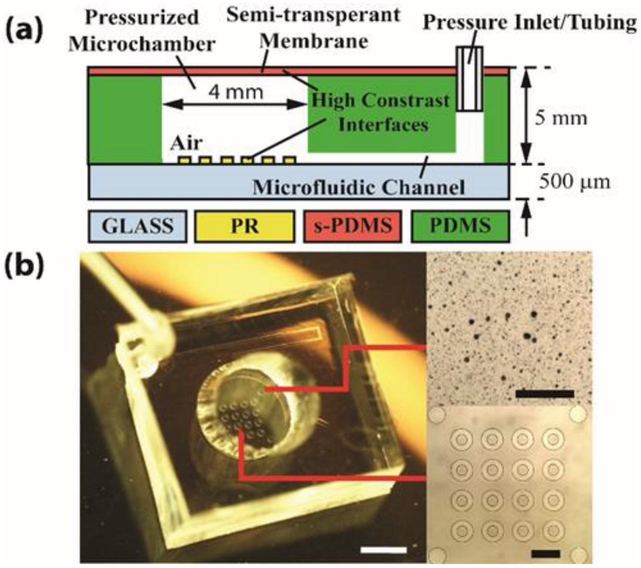

Figure 3.28: (a) Cross–sectional schematic of the PDMS pressure sensor. ‘PR’ and ‘s-PDMS’ stand for ‘PhotoResist’ and ‘Semi-transparent PDMS’ respectively.(b)Stereoscopic image of the fabricated sensor (scale bar, 2 mm) along with bright field micrographs of the PDMS membrane with food color aggregates (top right) as well as the photoresist patterns on the glass substrate (bottom right) (scale bars, 400 µm).

3.5.2 Principle of operation

The pressure sensor functions as a ‘displacement sensor’ (Figure 3.30): pressure deflects the thin, PDMS membrane and the distance between the membrane and the top surface of the glass substrate is measured using a precision, z-scanning module. This module consists of a microscope lens (5x) and a computer controlled, high speed (10 ms /step) piezoelectric stage (Figure 3.30). The z-scanning module focuses first at the inner (bottom) surface of the semi-transparent, membrane and then at the inner (top) glass surface of the microchamber using a custom-made image contrast analysis algorithm. The z-scanning module is able to focus on those two surfaces because the refractive index changes significantly from PDMS to air and from air to glass and therefore those interfaces (PDMS/air and glass/air interfaces) have high image contrast.

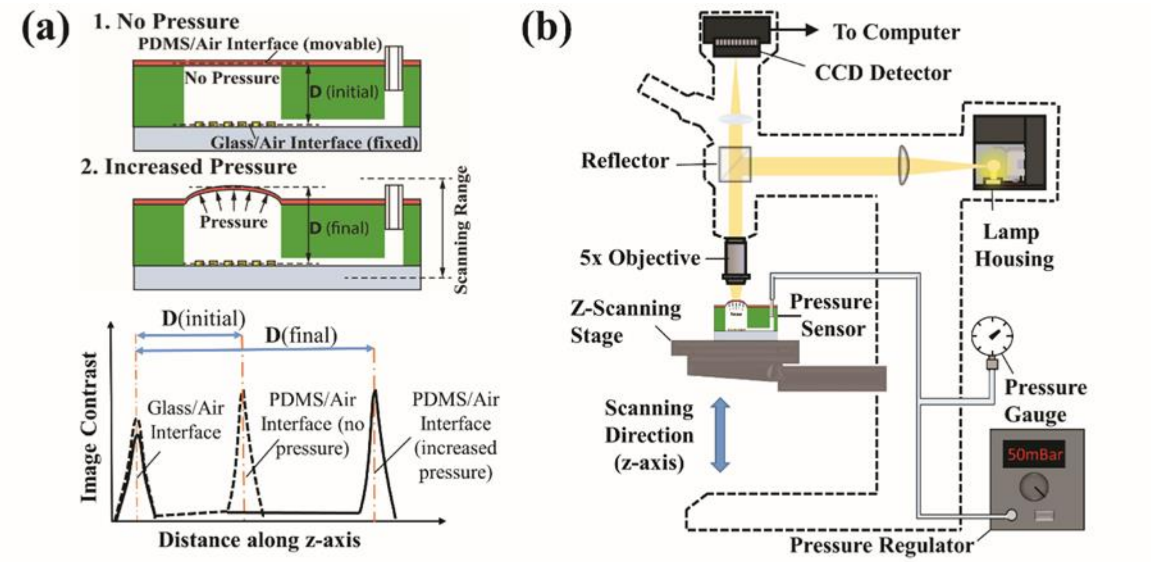

Figure 3.29: (a) Principle of operation of the contrast image based pressure sensor. The plot depicts the changes in the image contrast as the sensor is being scanned in the z-direction for the ‘no pressure’ (dashed line) and ‘increased pressure’ (solid line) cases. (b) The z-scanning setup for measuring the distance between the 2 interfaces. The same setup was used to characterize the sensor.

3.5.3 Micro-fabrication

An inexpensive fabrication process was employed using a combination of low cost materials and standard soft lithography techniques to manufacture the sensor which consists of 3 layers: (a) a 5 mm thick, PDMS slab. The slab was replicated from an SU-8 mold and contains the microfluidic channel which is 10 mm long, 200 µm wide and 100 µm thick. After the slab was peeled off from the SU-8 mold, two through holes - corresponding to the microchamber and pressure inlet- were made using a hole puncher, (b) a 10 µm thick, semi-transparent PDMS layer. This layer contains the pressurized membrane and was fabricated by spin casting and curing on a bare silicon wafer a mixture of 30% by weight of food color (Nourriture Coloration, FD&C Red #3, 0.5% in Aqueous Solution) and PDMS elastomer (10:1 weight ratio), and (c) a 500 um thick borosilicate glass substrate that mechanically supports and seals the sensor. A 20 µm thick photoresist film (*KMPR*® 1000, MicroChem) was photolithographically patterned on the top surface of the glass substrate. The photoresist patterns were used to increase image contrast (Figure 3.29). The glass substrate was then aligned and irreversibly bonded to the bottom surface of the slab after treating the surfaces with air plasma (700 mTorr chamber pressure, 50 W, 60 s exposure time) [164]. The slab was finally bonded to the 10 µm thick, semi-transparent layer. The portion of the membrane covering the pressure inlet hole was pierced to create the inlet and to allow the insertion of a metallic needle in order to pressurize the microchamber.

Food color was added while fabricating the 10 µm thick membrane to make it semi-transparent and, thereby, to increase its optical contrast. Even though the food color aggregation improves contrast (top right micrograph in Figure 3.29), the membrane is still relatively clear, allowing to visualize the patterned glass substrate.

3.5.4 Results and discussion

The normalized image contrast along the z axis of the sensor for various values of applied pressure is shown in Figure 3.31. Changes in image contrast depend on changes in the refractive index along the z-axis, e.g. at focal planes that coincide with the glass/air and PDMS/air interfaces. As a result, the image contrast has two peak values: the first peak corresponds to the patterned glass/air interface while the second peak corresponds to the semi-transparent membrane (PDMS/air interface). Because the membrane is thinner than the scanning step (20 µm), only one peak is observed when scanning along the membrane. Since the glass surface is rigid, the position of the first peak -corresponding to this fixed surface does not change with applied pressure. The second peak moves as the membrane deflects under pressure. The increased distance between the two peaks is therefore an indication of the membrane being deflected. A decrease in the normalized image contrast of the first peak with increased pressure was also observed. This can be attributed to the reduced illumination/reflection light that reaches/reflects from the glass substrate when the membrane is deflected and therefore curved.

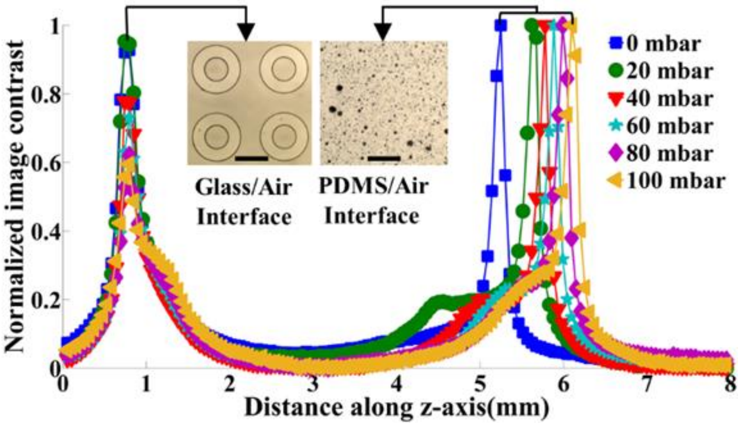

Figure 3.30: Normalized image contrast versus z scan position for six different values of applied pressure.as extracted from the image processing algorithm. The two micrographs depict the 2 interfaces that the maximum contrast is observed (scale bars, 200 µm).

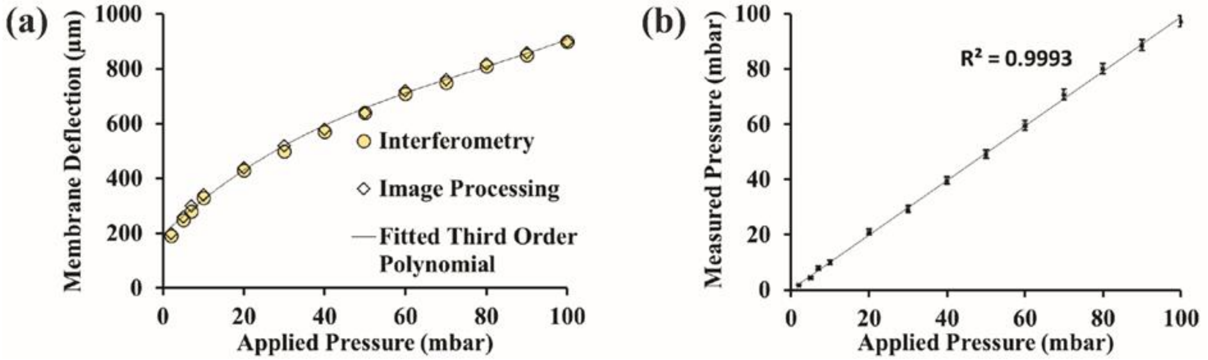

Figure 3.31: (a) Membrane deflection of PDMS sensor versus applied pressure estimated from our image processing algorithm and measured experimentally using interferometry. The solid line represents a fit by a third-order polynomial. (b) Pressure values obtained from the PDMS sensor versus known (accurately-controlled) applied pressure. Error bars indicate standard deviation of three measurements performed on the same device. The solid line represents best fit by linear regression and the square of the correlation coefficient R demonstrates a very good agreement between applied and measured pressures.

Experiments were performed over the 0-100 mbar pressure range for a 10 µm thick, 4 mm diameter membrane in order to validate the image processing algorithm and to obtain the calibration curve of the sensor (Figure 3.32(a)). For a given pressure (measured with an external pressure gauge), the membrane deflection was measured using a scanning white light interferometer (Zygo NewView 5000) as well as using our scanning module and image processing algorithm. The image processing algorithm estimates membrane deflection with a maximum mean absolute percentage error of 9.5% when compared to interferometric data. Below 20 mbar, membrane deflection is non-linear and increases rapidly with applied pressure. Above 20 mbar, the increase in membrane deflection with applied pressure is linear and pressure sensitivity decreases to ~6 µm/mbar. Taking into account the fact that depth of focus of the objective lens (~59 µm) is the limiting factor for measuring membrane deflection with accuracy, we estimated that the resolution of our setup (PDMS sensor and scanning module) is ~2 mbar in the 0-20 mbar pressure range and ~10 mbar in the 20-100 mbar pressure range.

By fitting the data obtained from our image processing algorithm to a least squares 3rd order polynomial function (solid line in Figure 3.32), the calibration curve of the sensor (having a 4 mm diameter, 10 µm thick PDMS membrane) can be obtained:

$$P = -2.450\times10^{-8}D^{3} + 1.709\times10^{-4}D^{2} - 0.024D - 0.055 \quad \text{--------(5)}$$

Where P (mbar) is applied pressure and D (µm), the deflection of the membrane from its undeflected position. Using this equation, an unknown applied pressure value can be obtained by measuring D using the z-scanning module and the image processing algorithm.

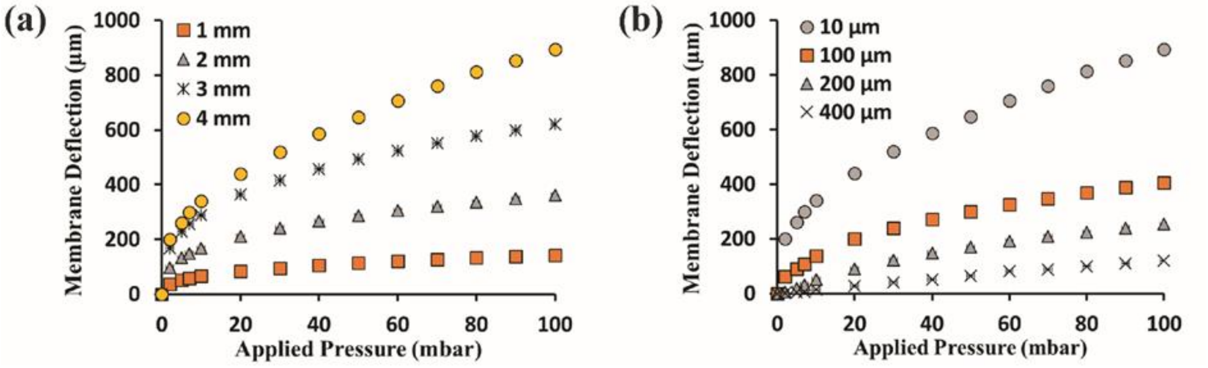

Figure 3.32: Membrane deflection versus applied pressure for PDMS sensors of: (a) 4 different diameters (1, 2, 3 and 4 mm). All sensors had a 10 µm thick PDMS membrane and, (b) 4 different thicknesses (10, 100, 200 and 400 µm) having 4 mm in diameter PDMS membranes.

Furthermore, sensors were fabricated with membranes of various diameters and thicknesses and measured their performance using our image processing algorithm and scanning module (Figure 3.33). As membrane thickness is increased and diameter decreased, membrane deflection and sensitivity for a given pressure decreases, while the regime of linear response extends to lower pressures. Therefore, both dynamic range as well as sensitivity can be tuned by simply changing the diameter and/or thickness of the membrane. Additionally, the resolution of pressure measurement can be increased by selecting an objective lens with a smaller depth of focus (higher NA) and a sensor with reduced thickness (such that the membrane deflects more). The use, for example, of a 10x objective lens which has a typical depth of focus of 15 µm, will result a resolution of ~0.5 mbar and ~2.5 mbar in the 0-20 mbar and 20-100 mbar pressure ranges respectively.

Finally, the proposed technology was validated by comparing pressure measurements obtained from the DCI pressure sensor (using the calibration equation (1)) to readings obtained from an external pressure gauge (2174 Ashcroft Digital Pressure Gauge) (Figure 3.32(b)). The sensor operates with a maximum mean absolute error of 0.94 mbar in the 0-20 mbar pressure range and maximum mean absolute error of 2.64 mbar in the 20-100 mbar pressure range. The maximum relative standard error is therefore ~7% throughout its dynamic range.

3.5.5 Experimental methods

To characterize pressure sensor performance, a bright-field microscope (Olympus BX-51**)** in reflection mode equipped with a high speed z-scanning stage, colored CCD camera (Olympus DP72 Microscope Digital Camera) and a pressure pump with a built-in pressure regulator (Elveflow microfluidic AF1 pressure pump) (Figure 3.30(b)) was used. The pump, which is connected to the sensor inlet using a metallic needle, was used to pressurize the microchamber with air and deflect the membrane to the desired pressure value. The PDMS sensor was mounted on the z-scanning stage and imaged through a 5x microscope objective (MPLFLN5x, Olympus). At a given pressure, the CCD camera acquired a stack of bright field images while scanning the entire thickness of the sensor along its z axis with a step of 20 µm. A MATLAB image analysis algorithm was developed to calculate image contrast for every focal plane at the end of each scan.

In order to calculate the image contrast, a 2D matrix containing intensity values for each pixel in the region of interest (ROI) – which is typically 800 µm x 800 µm, is formed. The ROI in every image is at the center of the PDMS membrane where the deflection has the maximum value. The microfabricated patterns on the glass surface are used to accurately locate the center of the PDMS membrane and therefore the ROI. Additionally, processing over the ROI instead of the entire image results in faster computation time. The total computation time for processing a stack of 400 images which covers the entire depth of the sensor is ~11 seconds. A contrast function is implemented which first calculates the intensity gradient by computing the change in intensity along both x and y directions of the 2D matrix. The directional gradients are used in order to evaluate the magnitude of the intensity gradient. The contrast over the ROI is then equal to the average value of the magnitude of the intensity gradient [165]. Contrast is further normalized to yield an image quality ranging between 0 and 1, with 0 being no contrast (uniform gradient over

ROI) and 1 being maximum contrast (maximum gradient change over ROI). The flowchart of algorithm, is shown in Figure 3.34.

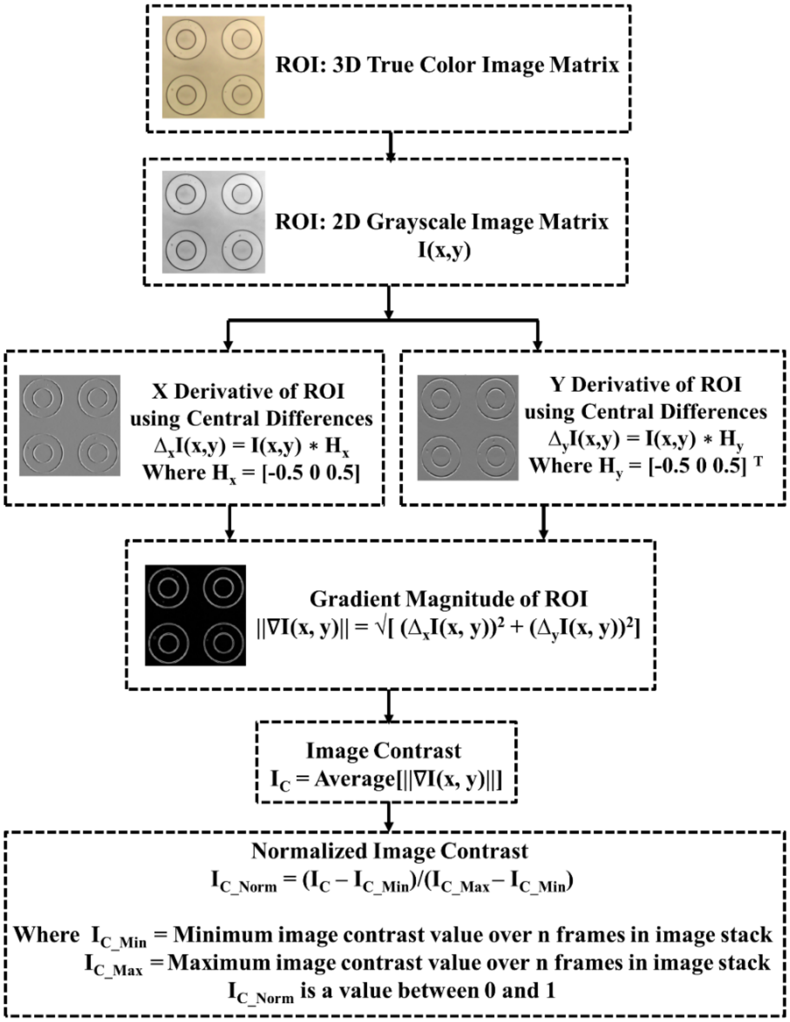

Figure 3.33: Flowchart of image process algorithm employed in the DCI technology.

3.5.6 Conclusions

In this chapter, we have described a novel image contrast based fluid pressure sensor that is low-cost while being easy to fabricate. The sensor architecture is distinct compared to traditional MEMS pressure sensors as it does not require the use of any on chip electronic elements which means that there is no need for powering the sensor. There is also the possibility to build a more compact readout unit consisting of cheaper components obtained from the consumer electronics industry such as autofocus mechanisms, lenses used in cameras and CCDs used in smartphones.

A disadvantage of the current version of the DCI sensor prototype is low measurement speed. This is mainly due to the relatively large high resolution image acquisition and computer storing time (~3 minutes to acquire and store 400 images), which can be significantly reduced by: (i) reducing the sensor thickness in order to collect fewer images, and (ii) by performing high-resolution z-axis scanning only near the glass/air and PDMS/air interfaces which are critical for accurately measuring the distance between them.

Additionally, membrane deflection might vary slightly from one device to another due to inherent non uniformities in repeatability of the fabrication process such as variations in the thickness of the membrane, elastomer-curing agent mixing ratios, Young’s modulus of PDMS and the amount of food color aggregates formed. To circumvent the effects of this non uniformity, each device will have its own calibration curve to maintain accuracy and device performance.

We anticipate that this novel pressure monitoring concept can be used in various biomedical applications such as monitoring IOP for the medical management of glaucoma as well as in the consumer electronics industry.

CHAPTER 4

A 3D PRINTED TOUCH-ACTIVATED SANITIZER DISPENSING SYSTEM FOR IMPROVING HAND HYGIENE

4.1 Introduction

Poor hand hygiene plays an important role in the transmission of pathogens [60] [166] [167] [63]. Hands become easily contaminated when they touch dirty surfaces, carrying the pathogens and eventually transmitting them to other commonly touched surfaces (e.g. door handles/knobs, credit cards) and to people (e.g. shaking hands). Hand hygiene is the most important prevention strategy for reducing Healthcare Acquired Infections (HAIs) as well as Community Acquired Infections (CAIs). Increasing Hand Hygiene Compliance (HHC) has been shown to decrease pathogen transmission through contact, resulting in reduced rates of nosocomial diseases [168] [169] [58] [59].

Washing with soap and water is the gold standard for enforcing hand hygiene [170]. Soap infused with antiseptic agents rapidly removes and/or kills most types of microorganisms present on the skin. Effective handwashing with soap requires access to clean water which might not be accessible at all times (e.g. in resource-limited settings).

Alchohol-based formulations of soaps are a great alternative that eliminating the need for water. Those formulations, termed ‘hand sanitizers’, have excellent killing activity against a wide spectrum of microorganisms (bacteria, viruses and fungi) and they act rapidly (~ 15 seconds). Additionally, due the their low surface tension, hand sanitizers spread easily and dry quickly due to the evaporation of alcohol. The optimum concentration of alcohol varies between 60%–90% by volume [171] [172] with the most commonly used formulation being 70% ethanol (v/v). In fact, if a consumer does not have access to soap and water, the U.S. Centers for Disease Control and Prevention (CDC) recommends the use of an alcohol-based hand sanitizer that contains at least 60% (v/v) alcohol [173].

However, even with the adoption of waterless alcohol based hand sanitizers, enforcing and improving HCC, especially in public places, has been an ongoing battle. Attempts have been made to implement several strategies to improve compliance including - 1: increasing awareness of the significance of hand hygiene through signs and education [67], 2: enabling real-time monitoring/reminders through technologies that provide visual (or other) cues to direct attention to hand hygiene during routine work [68] and 3: making it easier to clean hands by installing facilities like sanitizer dispensers in convenient locations, of which this last method has proven to be the most effective [174]. For instance, a multicenter study by Bischoff *et al.* [175] assessing HHC among health care workers, found that an education/feedback system coupled with sink and soap handwashing failed to improve HHC but HHC increased significantly (23%-48%) following the simple introduction of easily accessible alcohol-based waterless sanitizer dispensers at sites where they are needed. The authors therefore concluded that higher HHC was driven by a mere improvement in access to and the ease of use achieved with the dispenser. Moreover, keeping surfaces that come into contact with skin, clean and microbe-free is another significant challenge. Microorganisms are transferred from contaminated surfaces (e.g. a door handle, a medical tool, toilet seat etc.) to people, especially in high traffic areas like hospitals, restrooms, schools and while using public transport. These pathogens are able to survive for prolonged periods of time on surfaces and eventually, transiently colonize the skin on hands. Efforts for assessing the microbiological status of surfaces, especially in hospitals, has resulted in two major criteria for cleanliness [176]: (i) the presence of a specific indicator pathogen, and (ii) the total colony number in colony-forming units (CFU)/cm^2. Scientific data indicate that the CFU number should be less than 5 CFU/cm^2 in order to minimize pathological infections. However, most pathogens can persist for a long periods of time on inanimate surfaces – from a few days up to few months – and it becomes impractical for maintenance personnel to perform constant cleaning in order to keep the surfaces decontaminated. Thus, according to investigations in multiple health care and community based facilities, more than a half of the surfaces with high human traffic were found to be inadequately clean [177]. Therefore, the need for developing easy to access and easy to use disinfecting technologies emerges inevitably.

Research efforts to develop and implement novel disinfection technologies [103] like ultraviolet (UV) light has been proposed for disinfecting contaminated surfaces [104]. UV light has been proven to contribute to a radical reduction of the survival of microorganisms and bacteria. This technology requires the use of strong UV lamps that need to be installed in public spaces. A major drawback of UV light is its reduced effectiveness in decontaminating shadowed surfaces, which has led to the limited practical use of this technology [105]. In addition, UV light exposure cannot be used in high-traffic areas, e.g. corridors and waiting rooms, as people cannot be exposed to UV light. An improved variation of the above technology is to use UV light activated surface coatings. [106]. Those coatings produce cytotoxic species after irradiation causing a remarkable reduction in the survival of microbial colonies. However, those coatings do not affect adequately all different types of pathogens and it is difficult to implement them in a public environment as they require a constant source of photoactivation. Coatings impregnated with metals, such as silver or copper have also been studied as self-sterilized surfaces and they have been proven to be effective up to several hours [178]. However, those metal surfaces need to be coated with corrosive inhibitors that lower the effectiveness of their antimicrobial action. More recently, micro-patterned surfaces were proposed as a potential solution for preventing microorganisms to adhere to a surface. Several geometries comprising of micro-pillars or micro-channels have been developed [179] and they are currently in the commercialization phase by Sharklet Technologies Inc. Although this technology seems promising, rigorous clinical validation of this technology has not yet been performed. Only a few from the aforementioned technologies have reached commercialization, the most successful story seems to be the ‘PullClean’ door handle (Altitude Medical Incorporated). This is a low-tech handle that simply integrates a hand sanitizer –contained in a disposable cartridge- on a door handle. The main drawback of this product is that it relies on the willingness of the person entering the door, making its effectiveness difficult to predict. In addition, it is hard to envision, how such a handle can be integrated in every surface in a public setting. Therefore, a novel, cost-effective solution for decontaminating surfaces that will not interfere with routine workflow, that will work reliably at all times, will not be subjected to the end-user willingness and which uses an alcohol based sanitizer formulation as the decontaminating agent needs to be developed.

In this work, we present the development of a passive, 3D printed, dispensing device that can be mounted on any flat surface such as the surface of a door handle or of a medical equipment. The device disinfects the person’s hand that is touching the surface over which it is mounted while it is being self-sterilized at the same time. It consists of an array of passive, touch-powered, miniaturized valves that deliver a small amount of a disinfectant to the hand when the hand comes in contact with the surface of the array. The miniaturized-valves are normally closed - when no human touch/force is present. When a person touches the surface of the device, the miniaturized-valves open and the disinfectant flows through them onto the person’s hand as well as its own surface, thereby decontaminating both target regions. The device, we use the term ‘Touch-activated, Sanitizer Dispensing (TSD) system’, requires no maintenance besides replacing the cartridge that contains the disinfectant. In the following sections, we describe the design and characterization of a small-size TSD that can disinfect an area equivalent to the size of a thumb. Apparently, the size and footprint of the TSD can be scaled up as needed. We believe that the usage of TSD in public places will significantly improve hand hygiene and reduce HAIs and CAIs.

4.2 Device design

We designed and fabricated a prototype of the TSD system using 3D printing technology (Figure 4.1). The TSD system consists of a 4x4 Dispensing miniaturized Valve Array (DVA) that is connected to a sanitizer-filled cartridge through plastic tubing (Figure 4.1). Each milli-valve in the DVA consists of a pin-type piston, a piston chamber and an off-the-shelve, compression spring. An orifice is formed between the piston and the piston chamber. The piston and the orifice have a diameter of 1 mm and 1.2 mm respectively. The piston protrudes 1 mm over the orifice, as it is being pushed against the recess of the orifice under the action of the spring. In this position, the valve is closed and the sanitizer does not flow through the orifice. Each piston chamber has an opening at its bottom that facilitates the assembly of the piston and the spring. This opening is sealed with a base plug after the assembly is completed. All the milli-valves are connected through a network of fluidic channels to an internal reservoir at the bottom of the DVA. The inlet of the internal reservoir is formed into a hose barb and it is connected to the external reservoir/cartridge (we used a syringe as a cartridge) through a 3/8” internal diameter (I.D.) tubing.

The DVA has 3 important dimensions (Figure 4.1C): (i) the active area of the DVA that comes into contact with human skin when touched (active touch region). For demonstration purposes, the size of that area (11.5 mm x 11.5 mm) was chosen to match the surface of a human thumb (~ 100 mm^2), (ii) the distance between two valves (edge-to-edge valve spacing). This distance has been set to 1.8 mm in order to minimize the dead area between the valves that might not get disinfected properly. Smaller distances, although they are desirable, would compromise the mechanical integrity of the DVA, (iii) the protrusion length and the diameter of the piston. The protrusion length affects the maximum force that is required to fully open each valve as well as user comfort. The protrusion length has been set to 1 mm in order to be minimally noticeable to human touch and also to enable the finger to fully open the valves in a short period of time (under 2 seconds) with a minimum force (~ 0.54 N is required to fully open each valve). The diameter of each piston was set to 1 mm, as this value allowed the placement of the maximum number of valves within the active area without compromising the mechanical stability of the DVA.

A helical compression spring was chosen to actuate each piston milli-valve with a stiffness of 3.1 lbf./inch. Each spring is pre compressed by 1.35 mm, inside the piston chamber upon insertion of the base plug to create a leak proof seal in between the piston base and the piston holder. The springs are made up of music wire steel (Material ASTM No. A228) which is a type of steel known for its high tensile strength, high elastic limit, ability to withstand high stresses under repeated loadings and continuous performance under many normal cyclic applications. It is not as corrosion resistant as stainless steel but plating can easily be performed with tin or zinc to improve anti corrosiveness properties for longer life.

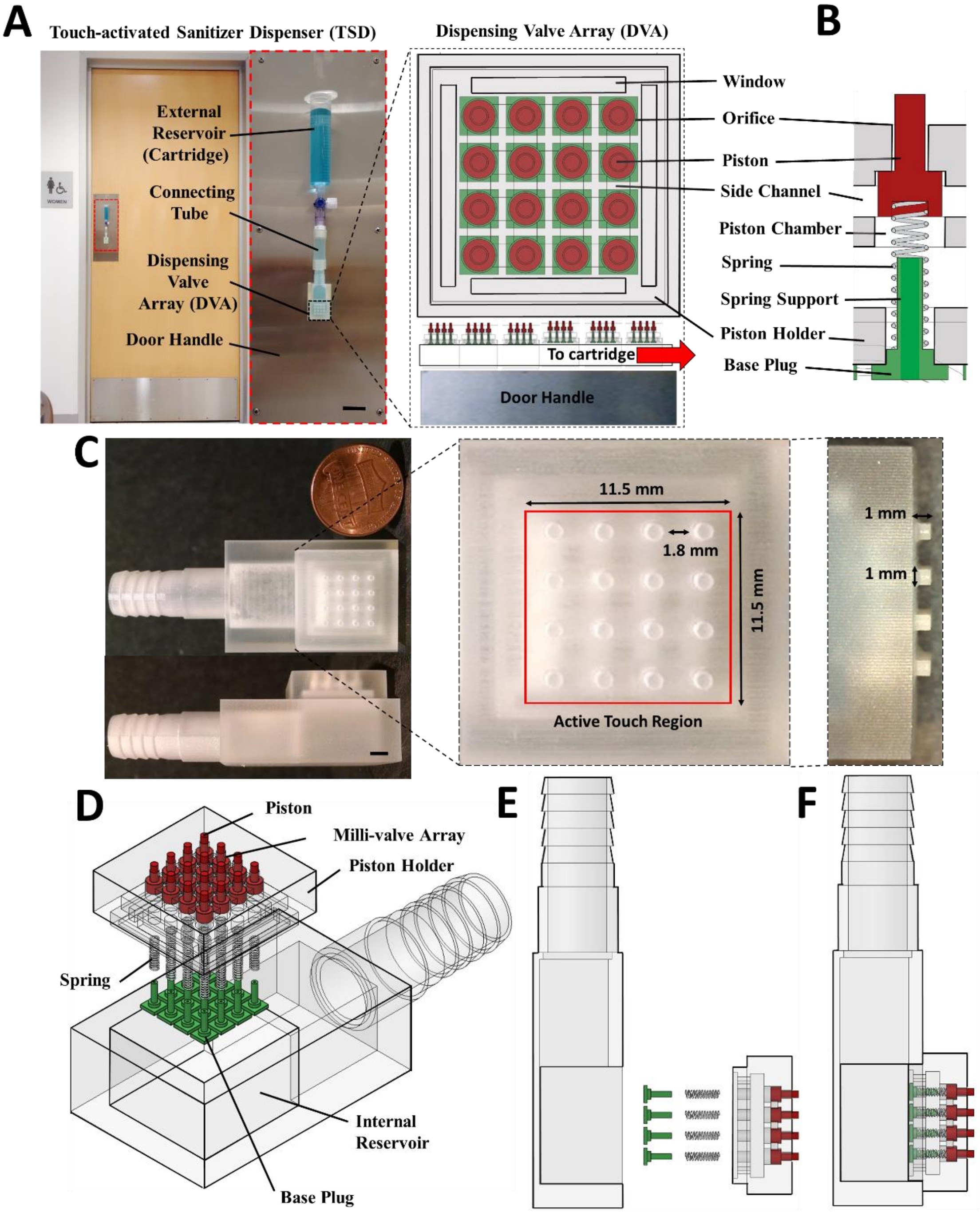

Figure 4.1: (A) Schematic of the TSD along with external fluid reservoir (cartridge) mounted onto a door handle (scale bar, 20mm). (B) Schematics of a single piston milli-valve inside the piston holder showing device architecture and assembled sub-components (C) Bright field images of front and side views of the 3D printed device (scale bars, 4mm) showing active touch region (given by the 11.5 mm x 11.5 mm region bounded by the red box) and other critical device dimensions. Schematics showing exploded (D) isometric and (E) side views of TSD demonstrating order of assembly of device sub-components. (F) Schematic showing assembled TSD.

4.3 Principle of operation

The valves are normally closed when no external force is applied (Figure 4.2(I)). Disinfecting fluid is filled into the internal reservoir. If more fluid needs to be added, tubing maybe be attached to the barb fitting on the device with the other end plugged into an external fluid reservoir/cartridge as shown in Figure 4.1. As more fluid is added, the higher the height of the liquid column in the reservoirs (both internal and external) above the milli-valves and the greater the hydrostatic pressure exerted by the fluid at the milli-valves. Under the influence of this pressure, the fluid flows from the reservoir and enters the piston chambers as well as the fluidic channels connecting the chambers inside the piston holder (Figure 4.2(I), (IA), (IB), (IC)). However, as the milli-valves are closed, the fluid is prevented from flowing out. Given that the height of each piston chamber is less than the length of each compression spring, the springs are pre-loaded and therefore create a tight seal in between the pistons and piston holder. This ensures that there is no fluid leakage from the orifices when the milli-valves are closed. When the piston milli-valves are pushed in/actuated with a finger, they are opened and the disinfectant flows through the annular orifices around the piston handles under the influence of hydrostatic pressure, exits the milli-valve array and is deposited on the finger (Figure 4.2(II), (IIA), (IIB), (IIC), (IID)). When the actuating force is removed, the compression springs snap back to close the milli-valves and in that process, the pistons lift the fluid above that has been accumulated in the piston chambers during milli-valve actuation. This lifting mechanism expels the fluid through the orifices and deposits it onto the surface of the device around the piston handles. The deposited fluid then spreads and the device thereby self sanitizes itself (Figure 4.2(III), (IIIA), (IIIB), (IIIC)).

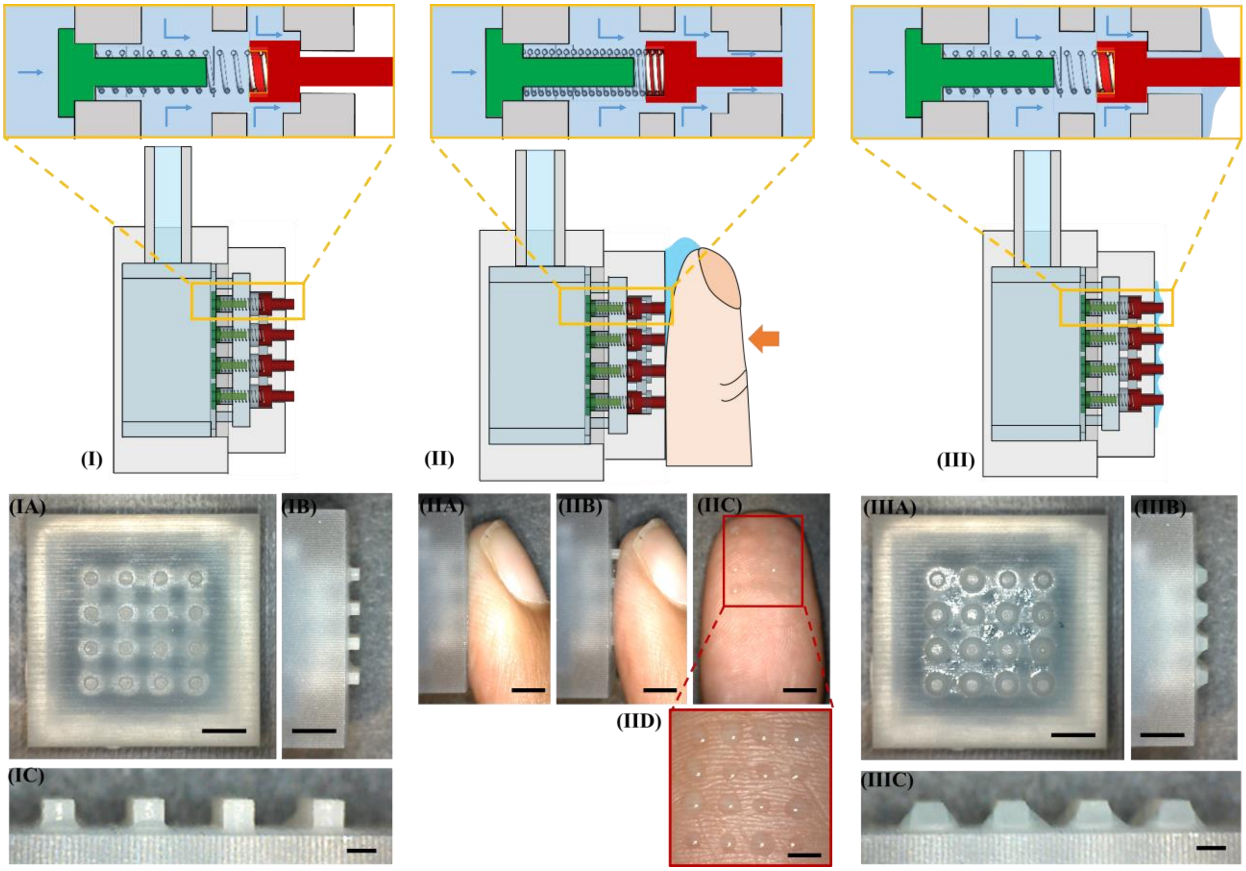

Figure 4.2: (I) Schematic showing piston milli-valves in the closed state before actuation with the pre-loaded springs pushing each piston base (shown in red) against the piston holder (shown in grey). The disinfectant (shown in blue) is contained inside the piston chamber. (IA) Image showing front view of the active touch area (scale bar, 4mm). (IB) (scale bar, 4mm) & (IC) (scale bar, 1 mm) Side view images of the active touch area in which the piston handles are shown to be protruding above the surface of the piston holder. (II) Schematic showing piston milli-valves in the open state upon actuation by finger. The disinfectant (shown in blue) flows out from the internal reservoir, piston chamber and the side channels through the orifice around the piston handle onto the finger. (IIA), (IIB) & (IIC) Images showing piston milli-valves being actuated by the finger (thumb), (scale bars, 4mm). (IID) Image showing 16 drops of liquid disinfectant (1 drop per piston milli-valve) dispensed onto surface of thumb after device actuation (scale bar, 2 mm). (III) Schematic showing piston milli-valves in closed state after actuation. The disinfectant (shown in blue) above the piston base is lifted up by the piston upon finger release and this displaced fluid flows out of the orifice and onto the surface of the active touch area (on and around the piston handles). (IIIA) Image showing top view of active touch area with disinfectant on device surface (scale bar, 4mm). (IIIB) (scale bar, 4mm) & (IIIC) (scale bar, 1 mm) Side view images of the active touch area showing disinfectant on device surface. Blue arrows represent hydrostatic pressure and direction of fluid flow.

4.4 Fabrication

The piston holder, pistons, base plugs and internal reservoir were 3D printed in M3 crystal resin using the Fused Deposition Modeling (FDM) [180] method on the ProJet 3500 HD Max printer. During the printing process, polymer materials were heated and ejected from the nozzles of the inkjet printer onto an aluminum build plate. The print was performed vertically upwards with a layer resolution of 16 µm in the axial direction and 32 µm in the lateral resolution. Building (VisiJet EX 200, 3D Systems Inc., Rock Hill, SC, USA also known as M3 Crystal) [181] and sacrificial materials (VisiJet S100, 3D Systems Inc., Rock Hill, SC, USA) [182] were deposited alternatively from dual nozzles to form the printed parts, in which the building material defines the solid structures in the device, while the sacrificial material occupies the hollow channels/cavities. Upon completion of the printing process, the 3D structures and the aluminum plate were placed in a refrigerator at 4°C for 20 minutes to easily remove the structure from the plate. The structures were then subjected to a post-printing procedure to remove the sacrificial material. First, the entire 3D-printed sample was immersed in a mineral oil (Bayes® high performance food-grade mineral oil) bath at 60 °C while sonicating at ~ 45 kHz for 2 hours to dissolve the sacrificial material. Second, the residual mineral oil was removed by thoroughly washing the parts in detergent soap and water (both at 60 ^{0}C, sonicated at ~45 kHz) baths in sequence. The structures, being delicate, were then air-dried for 24 hours to remove any water remaining inside the channels/cavities.

Off the shelf springs (PC007-057-11.000-MW-0.250-C-N-IN, Access Spring Co.) were purchased and inserted manually into each piston chamber inside the piston holder. The 3D printed base plugs were treated with a primer (#770, Loctite Bonding Primer) followed by the application of a waterproof adhesive (#4014, Lactate® High-Purity Instant-Bonding Adhesive) on top of the dried primer layer after 1 hour. The primer improves plastic-to-plastic bonding. The plugs were then glued to the base plate in order to permanently secure the springs inside the device with the adhesive reaching full bond strength after 24 hours. The piston holder with the fully assembled milli-valve array was then inserted and glued to the internal reservoir using the same primer and adhesive combination.

4.5. Results and discussion

4.5.1 Force needed to operate the valves

The activation force required to open the valves in the DVA was calculated using Hooke' law and measured experimentally. This force is equal to the force required to compress the helical spring by 1 mm (1 mm is the protruding length of the piston) and was calculated to be 0.54 N per valve (for a spring constant k = 3.1 lbs/in, provided by the manufacturer). The force to actuate the

DVA comprising of 16 milli-valves is therefore 8.6 N (0.54 N x 16 = 8.6 N). A piezoresistive force sensor (Section 4.6.1) was used to experimentally obtain the actuation force. The sensor was calibrated prior to the experiment using standard gram weights. The DVA was pressed against the surface of the sensor until all the valves were fully open and the voltage across the sensor was measured using a digital voltmeter. From the calibration curve (Appendix B, Figure B2), the force required to actuate the DVA was estimated to be 7.90 ± 0.7 N, which is in close agreement with the theoretical value. We used the theoretical valve of 8.6 N in our finite element analysis as this represents the worst case scenario.

4.5.2 Finite Element Analysis (FEA) of the base plate under normal loading

When the pistons in the DVA are being pushed in under the action of a normal (vertical) force, then the base plate is being deformed. This loading scenario, which can result in failure (plastic deformation or breakage) of the supporting beams of the base plate, was modelled using FEA analysis (Section 4.6.2). In our FEA (Solid Works Simulation Package) model, we anchored the edges of the base plate (shown in green with orange arrows, Figure 4.3B) to prevent movement in the x,y and z directions. 16 normal forces with a magnitude of 0.54 N were applied to the areas of the base plate that are in contact with the plugs (shown in red with purple arrows in Figure 4.3B, the normal force is transferred through the springs and the plugs to those areas). The simulation results indicate that the maximum von Mises stresses are being developed at the supporting beams, while the maximum displacement appears at the center region of the base plate (Figure 4.3D). The maximum von Mises stresses are ~20% of the yield strength of the M3 crystal resin. The material properties for M3 Crystal used in the simulations were obtained from the manufacturer and have been provided as part of Appendix B, Table 1. The maximum deflection of the base is ~ 73 µm (Figure 4.3C). The FEA analysis demonstrates that there is no risk of failure for the base plate. Based on the value of the maximum, von Mises stress, we anticipate that the base plate can withstand more than several million cycles of loading before failing (we assume that the M3 crystal resin has a similar fatigue performance to the ABS plastic material as there aren’t any fatigue data available for the M3 crystal resin) [183]. The maximum von Mises stresses could further be reduced by increasing the thickness of the supporting beams and/or by rounding their sharp corners.

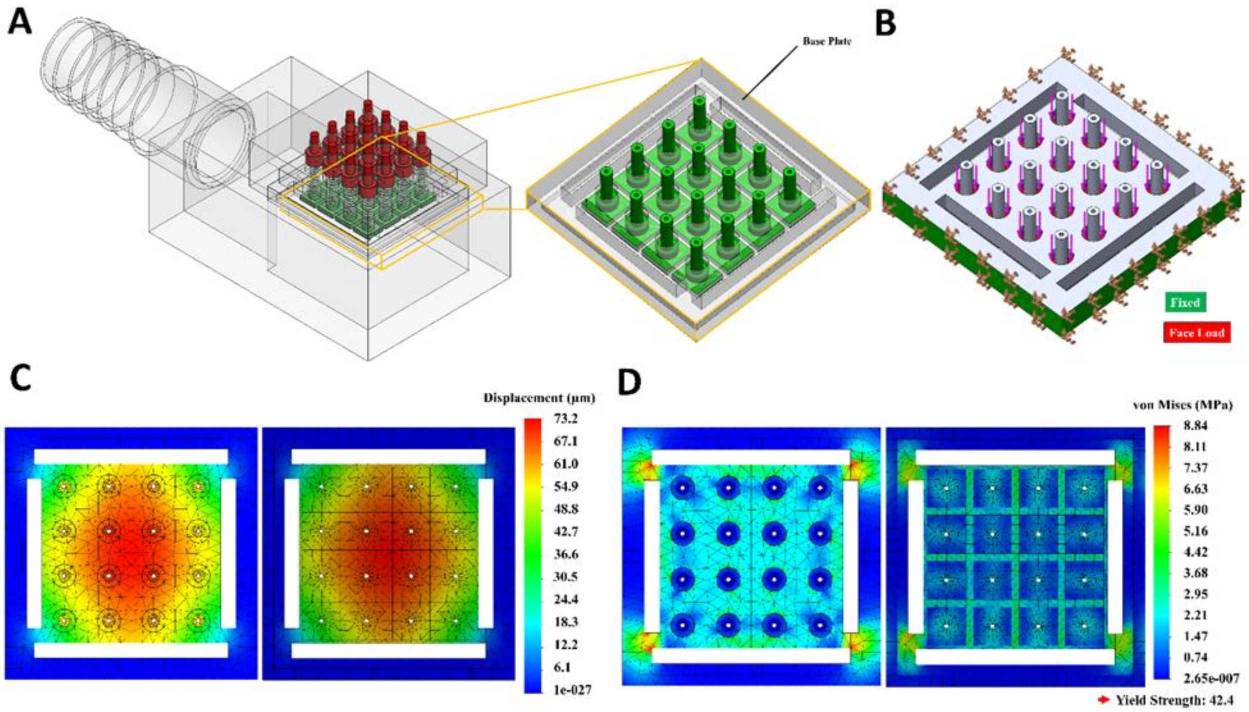

Figure 4.3: (A) 3D schematic of TSD and the base plate consisting of 16 base plugs (in green) attached to the base of the piston holder (in grey) on which FEA has been performed. (B) Schematic of base plate showing faces subjected to force loading (in red, force direction shown by purple arrows) and fixed constraints (in green, directional constraints shown by orange arrows). Color maps for base plate top and bottom surfaces showing distribution of (C) displacement and (D) von Mises stress when a normal force is applied on surfaces where the springs compress against during device operation.

4.5.3 Finite Element Analysis (FEA) of the piston under shear loading

The human hand, when touches and activates the DVA, can possibly slide against the DVA. In this case, a shear force will be applied to the top surface of the pistons, the pistons will tilt, hit the orifice and possibly break. We modeled this loading scenario (Section 4.6.2) by assuming that the generated shear force is proportional to the normal force that is required to open the valves (0.54 N per valve) times the human skin-plastic coefficient of friction. Given that the coefficient of static friction between human skin and plastic is around 0.46 [184], we estimated that a shear force of 0.25 N (0.54 N x 0.46 = 0.25 N) will be applied to the top surface of each piston (shown in red with purple arrows in Figure 4.4B). A fixed constraint was applied to the piston base and support (piston holder) (shown in green with orange arrows in Figure 4.4B) to prevent displacement in x,y and z directions.

The FEA results indicate that the piston handle as well as the piston holder support are subjected to a maximum stresses at the point where they collide with each other under the influence of the applied shear force (Figure 4.4D). At this location, the maximum von Mises stress is ~1/5 of the yield strength of the M3 crystal (Figure 4.4D) and therefore the risk of failure (e.g. by having plastic deformation of the material) is minimum. By introducing a bevel around the orifice, the von Mises stress concentration at this point maybe further reduced to ~ 0.13 times the yield strength (Figure 4.4E). Apart from reducing localized stress concentration, the bevel will potentially help with distributing the disinfectant fluid more uniformly over the device surface once dispensed after device actuation.

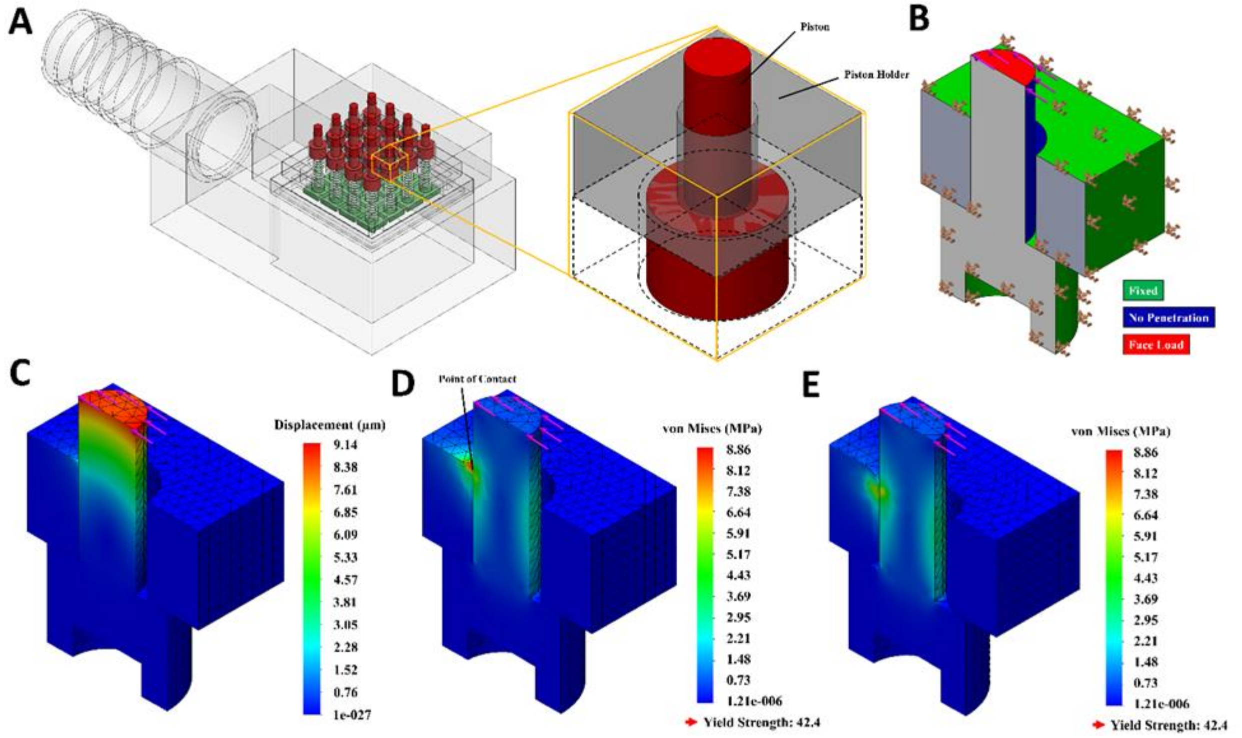

Figure 4.4: (A) 3D schematic of TSD and a single unit consisting of a piston (in red) and surrounding piston holder structure (in grey) on which FEA has been performed (B) Schematic of piston with surrounding piston holder support structure showing faces subjected to force loading (in red, force direction shown by purple arrows), fixed constraints (in green, directional constraints shown by orange arrows) and no penetration contacts (in blue). Color maps showing distribution of (C) displacement,(D) Von Misses stress without and (E) with the circular edge filleted, when a force that is tangential to the top surface of the piston handle is applied.

4.5.4 Theoretical analysis of helical compression spring performance

A helical compression spring was chosen to actuate each piston milli-valve with a stiffness of 3.1 lbf./inch. Each spring is pre compressed by 1.35 mm, inside the piston chamber upon insertion of the base plug to create a leak proof seal in between the piston base and the piston holder. Given the dimensions of the piston and piston chamber as well as the amount of pre-compression applied while securing it inside the device, the maximum allowed deflection of the spring is 2.35 mm which is well above its minimum working length (1 mm) that is required to maintain linear behavior without any mechanical failure. It is known that if the deflection of a compression spring is too large for a given free length, the spring may buckle. Alternatively, if the spring's free length is too long in comparison to its mean diameter, the spring is likely to buckle. After performing a stability analysis (Appendix B, Section B3), the factor of safety against buckling was found to be 1.02 and the spring slenderness ratio was found to be 5. Since the factor of safety is barely above 1 and the slenderness ration slightly greater than 4, the spring might buckle inside the piston chamber. To limit any buckling to be < 100 µm during normal device operation, a spring support in the form of a rod guide/shaft (height 3 mm, diameter 0.9 mm) is incorporated as part of each base plug around which the spring is inserted (Figure 4.1B).

An analysis was performed to inspect the stresses in the compression spring while applying a cyclic load (Appendix B, Section B1) that uses Zimmerli’s data [185] to calculate endurance limit based on Gerber, Sines and Goodman fatigue failure theories [186]. The material properties for music wire steel was obtained from Nisbett.K. et.al. [187]. The factors of safety against fatigue for each of the three fatigue failure theories was found to be 1.6, 2.1 and 1.4 meaning that the expected stresses are below the endurance limits for all three criteria. Since the endurance limit indicates infinite life for a material, these factors of safety show that theoretically, the spring has an infinite life under given loading conditions.

When a spring is going to be used in an environment where there is repetitive loading, the loading frequency should be much lower than (at least 20 times lower) the spring's natural frequency [188]. Resonance will amplify damaging stresses in the spring, since the internal damping of spring materials is quite low. An analysis was performed to calculate the natural frequency of the helical compression spring whose one end is fixed and the other end is loaded by applying a cyclic force (Appendix B, Section B2). The natural frequency was found to be 3970 Hz meaning that the maximum allowed loading frequency should be ~ 200 Hz. It is expected that the maximum loading frequency is going to be ~ 1-2 Hz which is well below this limit.

4.5.5 Amount of the sanitizer dispensed by the TSD system

As per the standards set by the American Society for Testing and Materials (ASTM E 1174-94), it is recommended that 1.5-2 mL of commercial alcohol based hand sanitizers is sufficient to ensure adequate coverage of both hands [189]. Given that the average surface area of male hands is 448 cm^2 [190], the volume of sanitizer needed to cover the surface area of a fingertip is ~ 5 μ L.

In order to ensure that the DVA dispenses enough volume of fluid for covering a fingertip, we measured the dispensed fluid volume under different experimental conditions. Specifically, we filled the TSD system -for practical purposes, we used a syringe as a cartridge- with a solution of 70% ethanol in water (v/v). We adjusted the height of the hydrostatic fluid column inside the syringe to achieve different value of the dispensing pressure. The valves were then activated by manually pressing the pistons with a finger for ~2 seconds which is the time required to fully open the valves (Figure 4.5B). The volume of the sanitizer dispensed on the fingertip as well as on the surface of the DVA was aspirated from those 2 surfaces using a 0.01 mL graduated syringe (Perfektum tuberculin, 1 mL capacity syringe, Sigma Aldrich) and measured by visually inspecting the syringe. Measurements of the total dispensed volume of the sanitizer were also performed by varying the actuation time (Figure 4.5B). As expected, the higher the hydrostatic pressure, the higher the velocity of fluid exiting the orifices and therefore, the higher the volume of sanitizer dispensed by the TSD system (Figure 4.5A). At the same time, for a given height of the liquid column, the longer the valves are actuated, the greater the volume of the dispensed sanitizer is (Figure 4.5B). Figure 4.5 also indicates that this target of 5 μ L is achieved even while using the device with the lowest height of fluid level in the reservoir.

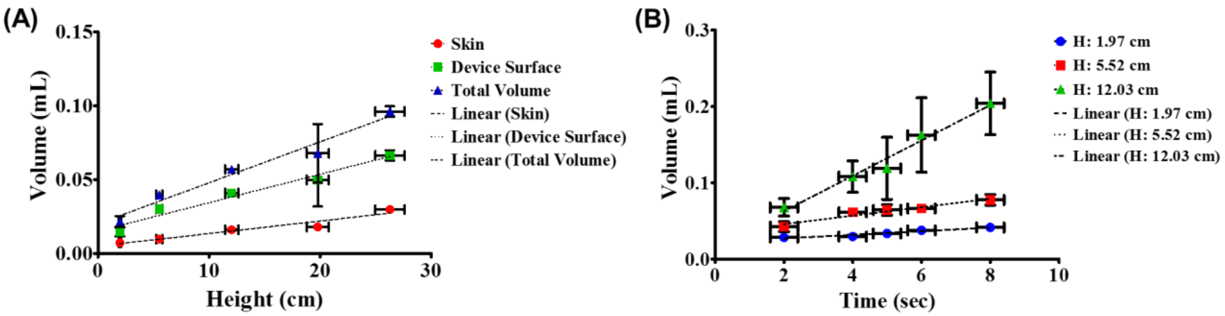

Figure 4.5: (A) Plot showing volume of liquid disinfectant dispensed by the device when actuated for ~ 2 seconds on the finger as well as on the surface of the device (active touch region) for varying heights of fluid levels in the reservoir. (b) Plot showing total volume of liquid disinfectant dispensed by the device (on finger as well as the device surface) for varying time durations of device actuation for three different heights of fluid levels in the reservoir. The dashed lines represent best fit by linear regression and the square of the correlation coefficient R demonstrates a good linear relationship between: (a) height of fluid in reservoir and measured volume of fluid dispensed and (b) time duration of actuation and measured volume of fluid dispensed. Error bars indicate the standards error of mean (SEM) of three measurements performed with the same device.

Any excess fluid that is dispensed will evaporate in a few minutes, which is sufficient to disinfect the entire DVA.

4.5.6 *Ex vivo* validation on human skin

The device demonstrates a significant (~ 10 fold) reduction in microbiological load of the contaminated surfaces with a drop in average CFU/cm^2 from 1.52 to 0.05 and 0.37 to 0.03 for the finger and device surface respectively within the first 24 hours. Figure 4.6(AIII), (BIII) shows CFU/cm^2 covering the plate after 36 hours as well as after 72 hours.

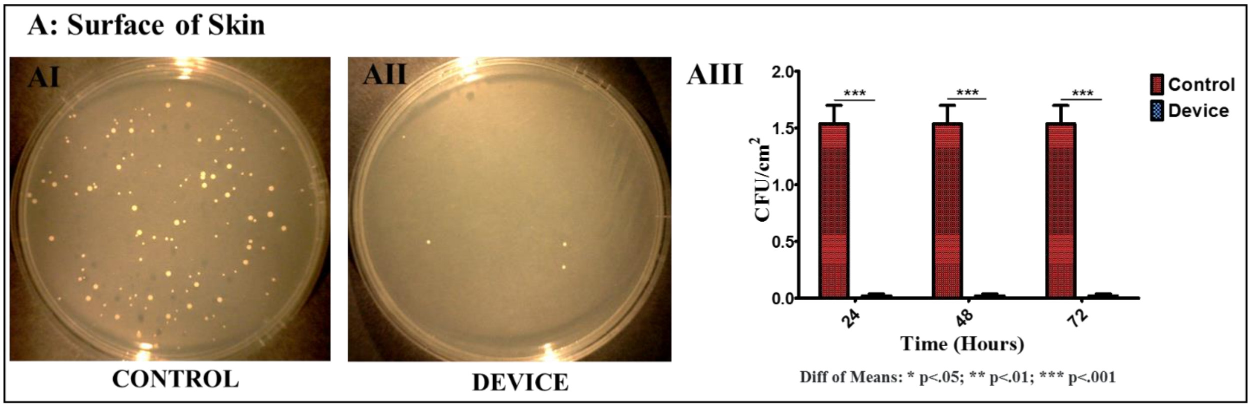

A: Surface of Skin

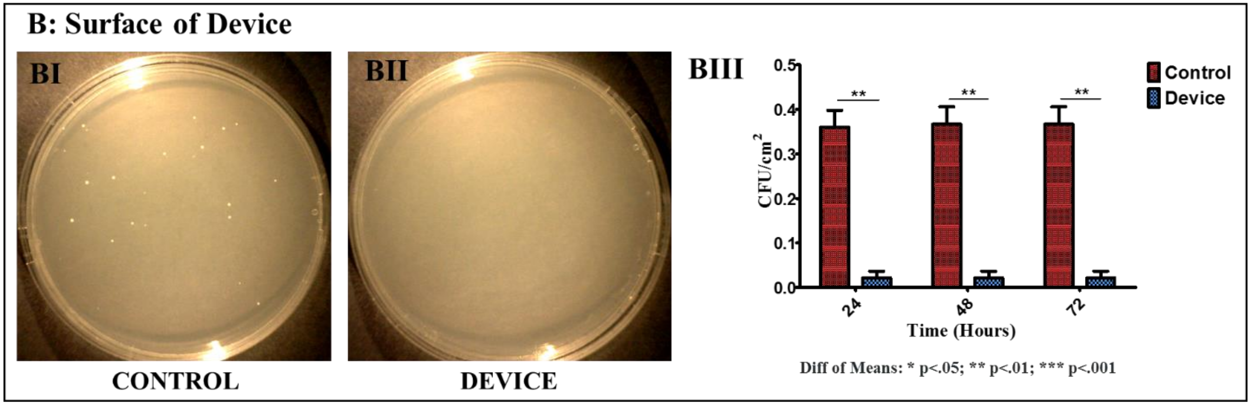

B: Surface of Device

Figure 4.6: (AI) Image showing surface of agar plate containing bacterial colonies cultured (after 24 hours) from finger surface (right thumb) without using the device (control). (AII) Image showing surface of agar plate containing bacterial colonies cultured (over 24 hours) from finger surface (right thumb) after using the device. (AIII) Plot showing CFUs/cm^2 measured by counting the number of colonies formed by culturing samples from skin before and after device actuation over 24, 48 and 72 hours. (BI) Image showing surface of agar plate containing bacterial colonies cultured (after 24 hours) from the active surface of the device before actuation (control). (BII) Image showing surface of agar plate containing bacterial colonies cultured (over 24 hours) from the active surface of the device after actuation. (BIII) Plot showing CFUs/cm^2 measured by counting the number of colonies formed by culturing samples from the active surface of the device before (control) and after actuation over 24, 48 and 72 hours. Error bars indicate standard error of mean (SEM) of three measurements performed with the same device.

Furthermore, the average bacterial load on the thumb after washing hands with the commercially available PURELL® Advanced Instant Hand Sanitizer (70% ethanol (v/v)) formulation was found to be 0.03 CFU/cm^2. This is comparable to the average bacterial load (0.05 CFU/cm^2) on finger after using the device.

4.5.7 Evaporation of the sanitizing fluid through the device

Due to surface roughness of 3D printed parts (~ 30 µm), the contact surfaces that form the milli-valves do not form a perfect seal thereby allowing the disinfectant to evaporate through the gaps. Additionally, some evaporation can take place through the material due to the porosity of the plastic. The volume of disinfectant fluid evaporated after a week was found to be ~ 25% of the starting volume (Appendix B, Figure B1). The rate of evaporation of the disinfectant through the 3D printed material can be reduced by coating the device with a low gas permeability material like parylene c to minimize material porosity at the device surfaces. Additionally, the rate of evaporation through the 100 µm gaps around the piston handles can be minimized by incorporating miniature o-rings in each piston chamber to create a perfect seal in between the piston and the piston holder.

4.6 Methods

4.6.1 Force needed to operate the valves

The force required to fully actuate the milli-valves was estimated both analytically using Hooke's law, the technical specifications of the helical compression spring (Appendix B, Table 1) as well as experimentally.

To estimate the actuation force experimentally, a piezoresistive force sensor was used (Square Force-Sensitive Resistor (FSR) 406, Interlink Electronics). The sensor was connected as part of a voltage divider circuit formed by itself along with a 10k Ohm fixed resistor. The voltage across the FSR was measured with a digital voltmeter and calibrated using standard gram weights. The area of the sensor over which the weights were applied is comparable to the area of the fingertip (~ 100 mm^2). Upon completion of the calibration process, the device was pressed against the surface of the sensor until all the milli-valves were fully open and the voltage across the sensor measured. From the calibration curve (Appendix B, Figure B2), the actuation force was estimated.

4.6.2 Finite Element Analysis (FEA) of TSD

Finite element structural analysis using the Solid Works Simulation package was performed on the 3D printed components that are acting as load bearing structures in the TSD to assess mechanical failure. A static non-linear study was performed on the piston handle as well as on the base plate, the two main load bearing structures in the device, in order to test for permanent deformation under various conditions encountered during device operation.

A tangential force of 0.25 N (shown as purple arrows, Figure 4.4B) was applied to the top surface of each piston handle (shown in red, Figure 4.4B). A fixed constraint was applied to the piston base and support (piston holder) (shown in green with orange arrows, Figure 4.5A) to prevent displacement in x,y and z directions. A no penetration contact pair was specified between the cylindrical touching surfaces (shown in blue, Figure 4.5B): surface of the piston handle and surface of the orifice inside through which the piston handle passes.

A face load of 0.54 N (8.64 N distributed over 16 piston base plug surfaces) was applied to those areas (shown in red, Figure 4.6B) on the base plug where each spring pushes against it while being compressed during normal device operation. A fixed constraint was applied to the edges of the base plate (shown in green with orange arrows, Figure 4.6B) to prevent displacement in x,y and z directions.

The material properties for M3 Crystal used in the simulations were obtained from the manufacturer and have been provided in Appendix B, Table B1. The results of the static analysis was used to determine structural deformation under applied load, distribution of Von Misses stress as well as to estimate load factor of safety against permanent deformation at each location.

4.6.3 Theoretical analysis of helical compression spring performance

A theoretical analysis was performed on the helical compression spring to assess failure under both single and cyclic static loading events. The parameters influencing spring design as well the governing equations used in the analysis have been provided in Appendix B, Sections B1, B2 and B3.

4.6.4 Amount of the sanitizer dispensed by the TSD system

The device was filled with varying quantities of 70% ethanol in water (v/v) to achieve different heights of the liquid disinfectant fluid column in the reservoir behind the DVA. For volumes larger than 6.5 mL (volume capacity of the internal fluid reservoir), an external fluid reservoir (15 mL syringe) was interfaced to the device through Luer attachments and tubing (3/8” hose barb size, Masterflex C-Flex ULTRA tubing) connected to the barb fitting on the internal fluid reservoir.

While vertically orienting the device and for a given height (H) of the liquid column above the milli-valves, the milli-valves were fully actuated by manually pressing the piston handles for varying periods of time. The volume of fluid dispensed by the device on skin as well as on the surface of the device itself was measured by aspirating the fluid using a 1 mL capacity, 0.01 mL graduated syringe (Perfektum tuberculin syringe, Sigma Aldrich). Measurements were also acquired using the same procedure by actuating the milli-valve for 2 seconds (measured with a stop watch) while varying the height of the liquid column H.

4.4.5 *Ex vivo* validation on human skin

The internal fluid reservoir of the device was filled with 6.5 mL of 70% ethanol in water (v/v) and the open end closed after inserting a low gas permeability tubing (3/8” hose barb size, Masterflex C-Flex ULTRA tubing) on the barb fitting. The other end of the tubing was sealed by inserting interlocking Luer connectors with Teflon tape linings.

As part of the control experiment, a sterile swab dipped in sterile DI water was rolled over the right half the fingertip of the right thumb (dominant hand). The swab tip was then dipped in 300 µL of sterile Luria Broth (LB) and manually stirred for 5 minutes to transfer the bacteria from the swab tip to the LB medium. The LB medium was then mixed using a shaker (40 rpm, Labline 3527 Orbital Incubator Shaker) at 37 ^{0}C for 1 hour. To culture the bacteria, the LB medium was then transferred to a 10 cm diameter LB Agarose plate and distributed uniformly using the spread plate method: the bacterial suspension was spread over an agar plate using a flame sterile metal rod that evenly distributed the bacterial suspension. The bacteria was then incubated for 1-3 days at 37 ^{0}C under aerobic conditions, with colonies starting to form after 24 hours. The device was then actuated by the right thumb for ~2 seconds, which is the time that it takes to fully depress the piston handles. A sterile cotton swab dipped in sterile DI water was used to uniformly spread the dispensed alcohol solution to cover the surface of the finger (~100 mm^2 area). After waiting for 1 min to ensure that all the alcohol has evaporated and the finger is completely dry, a sterile swab dipped in sterile DI water was rolled over the left half of the fingertip of the right thumb and subjected to the same procedure as that of the control experiment. The experiment was repeated two more times on two consecutive days.

The above procedure was repeated for evaluating the self-disinfecting performance of the device by collecting a swab from the surface of the device (both from the tops of the 16 piston handles and the gaps in between the handles) after actuating the device containing 70% ethanol (v/v) for ~ 2 secs. The sampling area on the device was comparable to the area of the fingertip. As part of the control experiment, swabs were collected from the surface before actuating the device.

The experimental procedure was also repeated where swabs were collected from fingers before and after washing hands with the commercially available PURELL® Advanced Instant Hand Sanitizer (70% ethanol (v/v)) formulation to compare with and assess efficacy of the 3D printed TSD.

Each culture plate was then inspected under a stereo microscope and the number of colony-forming-units (CFU)/cm^2 was quantified by manually counting the colonies formed on each agar plate.

The two tailed unpaired t test along with Welch's correction was done to test the significance of the difference in mean of CFU/cm^2 between experimental and control cases.

4.6.6 Evaporation of the sanitizing fluid through the device

The internal fluid reservoir of the device was filled with 6.5 mL (starting volume) of 70% ethanol in water (v/v) and the open end closed after inserting a translucent, 5 cm long, low gas permeability tubing (3/8” hose barb size, Masterflex C-Flex ULTRA tubing) on the barb fitting. The other end of the tubing was sealed by inserting interlocking Luer connectors with Teflon tape lining. Two drops of food color (Nourriture Coloration, FD&C Blue #3, 0.5% in Aqueous Solution) was added to the ethanol solution for better visualization of the liquid level in the tube. The change in height of the liquid level in the tube was monitored every 24 hours using a pair of calipers. Given the measured drop in fluid level as well as known device and tubing dimensions, the volume of liquid lost due to evaporation was estimated.

Evaporation was allowed to take place through the 100 µm annular gaps around the milli-valves as well as through the 3D printed material itself, both of which are possible during normal device operation. A translucent low gas permeability tubing was chosen to easily visualize the fluid level while minimizing evaporation of fluid through the walls of the tubing. Furthermore, while not taking any measurements, a piece of parafilm was wrapped around the Luer connectors, tubing and barb fitting portion of the device to further minimize any chances of evaporation from gaps in those areas.

4.7 Conclusions

In conclusion, we have demonstrated a 'proof of concept', smart 3D printed TSD prototype device using a low-cost, easy to fabricate technology. Its unique features include: (1) zero power requirements as it consists of a passive hand-powered milli-valve array, (2) the use of liquid antimicrobial disinfectants which is currently the best known disinfection approach, (3) device dimensions can be scaled up or down providing versatility on what type of disinfectants can be used (liquid/gel/foam), (4) maximum prevention as the device disinfects both the surface on which it is applied (e.g. the door handle) as well as the human skin, (5) minimum fluid consumption as disinfection is localized at the contact areas (all milli-valves operate independently - no touch/no activation), (6) biocompatibility of the material that is coming in contact with skin (USP Class VI certified) and (7) mechanical durability over an extended period of operation. Even though 3D printing has been employed to fabricate the proof of concept prototype device, we should emphasize that microfabrication technology can be easily employed to develop a ‘MEMS skin’ version of the device for low-cost, mass production in the future and its fast adoption by hospitals and other community facilities (Section 4.8).

A disadvantage of the current version of our device is its large actuation force (~ 9 N) compared to the force required to open a door (under 5N). This is mainly due to the relatively large individual stiffness (k = 3.1 lbs/in) of the springs that have been employed to prevent any leakage from the milli-valves. This limitation can be easily overcome by reducing the stiffness of the springs while preventing valvular leakage by incorporating miniature o-rings into the design to create a good seal between the pistons and the piston holder. Reducing spring stiffness and incorporating o-rings will further optimize the volume of fluid dispensed and minimize any wastage in the form of excess fluid. There is a chance that the 100 µm gaps could get clogged if the device is placed in an extremely dusty environment with prolonged periods of disuse. However, since the device is meant to be placed in high human traffic areas indoor, it is expected to be in almost continuous use and therefore, clogging due to accumulation of dust is not likely to occur. Additionally, since the long term chemical resistance and warping reaction to polar solvents of M3 Crystal is not well known, a material like Alloy 910 maybe used instead to enhance chemical resistance. Furthermore, other biocompatible materials like Bendlay, thermoplastic elastomers (TPE), Polyethylene Terephthalate(PET) and Polyamide (Nylon) may be used for 3D printing more flexible versions of the device to make it more ‘skin’ like and conformal to surfaces of varying shapes. These plastics may also be used to 3D print the springs thereby enabling easier device assembly.

We anticipate that the proposed platform technology, implemented in community based facilities of any kind, promises to provide a radical reduction of infections while greatly increasing HHC, and therefore reduce mortality rates and the associated healthcare cost. The technology could easily be scaled up and implemented in high traffic public places such as hospitals, schools, toilets, stadiums and buses. The results could be remarkable as the hygiene conditions of an entire population will improve and the transmission of parasites and bacteria will be prevented. Even though the device in its current form is targeted towards disinfecting hands which is one of the most common ways that infection is transmitted, the device can be employed for disinfecting any other type of surface by a simple change in geometry which is easily accomplished due to advances in 3D printing technology. Finally, the low fabrication, operational and maintenance cost of the device renders it ideal for implementation in the developing world and other resource-poor settings.

CHAPTER 5

CONCLUSIONS AND FUTURE DIRECTIONS

5.1 Conclusions

The important contributions of Part A in this thesis include:

5.1.1 NiFO sensing technology

We developed a novel near infrared, optomechanical, electronic-free and powerless implantable pressure sensor that can potentially monitor intraoccular pressure. The sensor, consisting of a mini-lens, a two-wavelength QD micropillar and a polysilicon membrane, converts pressure changes into fluorescent intensity ratio changes when illuminated with a laser. As tissue is transparent to NI light, operating the sensor in the NI regime is critical for obtaining a high signal to noise optical signal. The sensor can monitor pressure within the clinically desired IOP range (0-45 mmHg), it has a maximum error of less than 15% and it does not suffer from photobleaching and drift. The experimental results indicate that the sensor can accurately respond to IOP changes in the clinically relevant pressure range (0-45 mmHg), as predicted by analytical and FEA models. Upon evaluation of the possibility for device failure, the maximum von Mises stress at 100mmHg was found to be one order of magnitude lower than the polysilicon yield strength (2.5GPa).

The NiFO IOP sensing system is a significant improvement over the first generation proof of concept device developed by Ghannad-Rezaie *et al.* Although the device developed by Ghannad Rezaie *et al.* does meet the clinical requirements for IOP monitoring, the choice of materials are not suitable for long term use. Additionally, the QD micropillar is exposed to IOP that raises questions about the cytotoxic effects of heavy metal based QDs on surrounding tissue. Also, the fabrication process, besides being very laborious as the microlenses have to be individually arranged and aligned manually on each device, does not provide good yield and cannot be outsourced easily to external contract manufacturers for commercialization. The sensor design/microfabrication approach presented here addresses these issues by reducing the device footprint to ~ 1.4 mm x 1.4 mm x 1 mm and ~ 1 mm x 1 mm x 1 mm for incorporation with KPro and IOL implants respectively, preventing direct exposure of cytotoxic QDs to biological tissue and describing a batch fabrication process that is amenable for future commercialization of the NiFO technology.

We envision that the proposed NiFO sensing technology can be extended to other biomedical applications where pressure monitoring is required such as arterial, intracranial and gastrointestinal pressure monitoring.

5.1.2 DCI sensing technology

We have developed a novel image contrast based pressure sensing scheme using a low-cost, easy to fabricate sensor. Its architecture is distinct compared to traditional (e.g. capacitive, piezoresistive) micromachined pressure sensors as it does not require the use of any on chip electronic elements (CMOS circuitry, inductors, batteries, etc). The need for powering the sensor is therefore eliminated. There is also the potential to build a more compact readout unit consisting of cheaper components obtained from the consumer electronics industry (e.g. autofocus mechanisms and lenses used in cameras, CCDs used in smartphones).

A disadvantage of the current version of our sensor is low measurement speed. This is mainly due to the relatively large high resolution image acquisition and computer storing time (~3 minutes to acquire and store 400 images), which can be significantly reduced by: (i) reducing the sensor thickness in order to collect fewer images, and (ii) by performing high-resolution z-axis scanning only near the glass/air and PDMS/air interfaces which are critical for accurately measuring the distance between them.

Additionally, membrane deflection might vary slightly from one device to another due to inherent non uniformities in repeatability of the fabrication process (e.g. variations in the thickness of the membrane, elastomer-curing agent mixing ratios, Young’s modulus of PDMS and the amount of food color aggregates formed). To circumvent the effects of this non uniformity, each device will have its own calibration curve to maintain accuracy and device performance.

We anticipate that this novel pressure monitoring concept can be used in various biomedical applications such as monitoring IOP for the medical management of glaucoma as well as in the consumer electronics industry.

5.1.3 TSD System

In this thesis, we have demonstrated a 'proof of concept', 3D printed TSD prototype device using a low-cost, easy to fabricate technology. It has zero power requirements as it consists of a passive hand-powered milli-valve array. It uses liquid antimicrobial disinfectants which is currently the best known disinfection approach and device dimensions can be scaled up or down providing versatility on what type of disinfectants can be used (liquid/gel/foam). It enables maximum prevention as the device disinfects both the surface on which it is applied (e.g. the door handle) as well as the human skin with minimum fluid consumption as disinfection is localized at the contact areas (all milli-valves operate independently - no touch/no activation). The material that comes in contact with skin is biocompatibility (USP Class VI certified) and provides mechanical durability over an extended period of operation. Even though 3D printing has been employed to fabricate the proof of concept prototype device, we should emphasize that microfabrication technology can be easily employed to develop a ‘MEMS skin’ version of the device for low-cost, mass production in the future and its fast adoption by hospitals and other community facilities (Section 5.2.4).

A disadvantage of the prototype device is its large actuation force (~ 9 N) compared to the force required to open a door (under 5N). This is mainly due to the relatively large individual stiffness of the compression springs but this limitation can be easily overcome by reducing the spring stiffness while preventing valvular leakage by incorporating miniature o-rings to create a good seal between the pistons and the piston holder. Reducing spring stiffness and incorporating o-rings will further optimize the volume of fluid dispensed and minimize any wastage in the form of excess fluid. Since the device is meant to be placed in high human traffic areas indoor, it is expected to be in almost continuous use and therefore, clogging of the milli-valves due to accumulation of dust is not likely to occur. Additionally, since the long term chemical resistance and warping reaction to polar solvents of M3 Crystal is not well known, alternative materials like Alloy 910 maybe used instead to enhance chemical resistance.

Due to the fact that it can be easily scaled up, we anticipate that the TSD system, implemented in community based facilities of any kind, promises to provide a radical reduction of infections while greatly increasing HHC, and therefore reduce mortality rates and the associated healthcare cost. Even though the device in its current form is targeted towards disinfecting hands, the device can disinfect any other type of surface by a simple change in geometry.

5.2 Future directions

We envision that the work presented in Part A of this thesis chapter can be extended in the following research directions:

5.2.1 NiFO sensing technology

The microlens array needs to be integrated into the NiFO sensor by i) increasing surface flatness (< 50 nm) for performing laser bonding and ii) by reducing microlens sags to minimize variations in focal lengths (< 3 µm), both of which can be achieved with better annealing control during the glass molding process. Additionally, by using a higher refractive index material and by increasing the diameter of each microlens to 800 µm, the NA as well as the f number will increase, thereby increasing its light gathering capacity from the QD micropillar. Moreover, using a higher concentration of QDs (25 mg/mL) to pattern the micropillar would further increase fluorescence output.

Micro-lens Array: Improving surface flatness and increasing NA: As the microlens array is fabricated using a glass molding technique in a heat press, the glass shrinks after the molding process is complete which leads to variations in the surface profile as seen in Figures 3.24, 3.25 and 3.26. However, with annealing, the flatness can be significantly improved to achieve the required specification of 50 nm to allow laser bonding to take place. Additionally, this improvement in flatness will also lower microlens sag and therefore, the variations in focal lengths will also be much lower (< 3 µm). The refractive index of L-LAM 72 is ~1.7 for NIR light which corresponds to a NA of ~0.5. If a higher refractive index material like S-LAH79 is used, which has a refractive index of 2.003 for NIR light, the NA would increase to ~0.62 indicating an improved light gathering capacity.

The microlenses may also be fabricated insides recesses to create a one piece array that can be directly bonded to polysilicon instead of creating the spacer with through holes as a separate piece, thereby further streamlining the manufacturing process.

Increasing fluorescence from quantum dot micro-pillars: Fluorescence from the QD micropillar maybe increased by incorporating a higher concentration of QDs in PMMA. However, the higher the concentration of QDs in solution (on the order of 10-25 mg/mL), the higher the chances of aggregation. To minimize aggregation, higher concentrations maybe achieved by increasing the amount of surfactants being used to make the QDs in solution more stable. Additionally, the thickness of the QD-PMMA layers maybe increased to increase the amount of QDs in the micropillar. However, if the layers are made too thick (> 1 µm), the deflection sensitivity of the membrane will reduce due to the loading effect introduced by the increased weight of the pillar.

NiFO Temperature Sensor: There are two existing theories, mechanical and vascular, that help explain the causes that are responsible for the development of glaucoma. The mechanical theory is the most popular one which claims that elevated IOP causes the laminar beams to stretch inside the eye, damages the retinal ganglia and thereby causes vision loss. On the other hand, the vascular theory claims that an insufficient supply of blood either due to elevated IOP or some other risk factor leads to glaucoma.

In conditions like congenital glaucoma, angle-closure glaucoma, or secondary glaucomas, it has been clearly demonstrated that increased IOP leads to glaucoma. However, in conditions such as normal-tension glaucoma, optic nerve damage and visual field loss progress despite seemingly normal IOP which seems to partially support the vascular theory. The majority of studies about Ocular Blood Flow (OBF) report reduced ocular perfusion in glaucoma patients compared with normal subjects. Furthermore, the reduction of OBF often precedes nerve damage associated with glaucoma [191]. Blood flow in glaucoma patients can also be reduced in other body parts such as the extremities. Temperature has been a popular but indirect method for assessing organ blood flow. It is well known that limbs get colder if their blood flow is decreased and the same phenomenon also holds true for the eye. Corneal temperature correlates significantly with blood flow in the ophthalmic artery, suggesting that OBF indeed influences corneal temperature. Reports indicate that the eyes of patients with glaucoma are cooler than those of patients without glaucoma by almost 0.5 ^{0}C. Furthermore, reports also show that an increase in OBF induced by medication that reduces IOP, increases corneal temperature [192].

Given that QD photoluminescence is sensitive to temperature, the NiFO sensor maybe used as a temperature sensor as well (Figure 5.1). The device architecture is the same, except for the fact that the polysilicon membrane is absent and the QD micropillar is directly patterned on a silicon wafer substrate. With a 20x objective lens having a NA of 0.75, a temperature measurement sensitivity of ~ 2.5 ^{0}C was obtained. By choosing a higher NA lens to collect more light, by increasing the amount of the QDs in the device (increasing the thickness of the QD layer or the concentration of QDs) or by measuring the shift in emission wavelength with temperature [193], a higher detection sensitivity might be achieved to potentially allow for an alternative medical management method for certain forms of glaucoma.

Other potential applications of the NiFO sensor include detecting cardiovascular plaques [194] as well as monitoring temperatures in therapeutic/interventional procedures such as laser ablation surgeries [195].

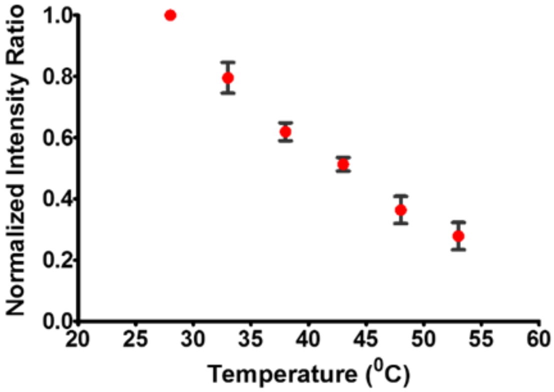

Figure 5.1: Normalized intensity ratio curve for a NiFO sensor (membrane not released) versus temperature. Error bars represent SEM from 5 measurements from the same device.

5.2.2 DCI sensing technology

The DCI pressure sensor prototype is not appropriate for implantation in the eye: it has a very large size (membrane size is 4 mm) and low resolution (1.5-7.5 mmHg) as the image contrast between the PDMS and air within the microchamber is low. In addition, the PDMS microchamber is not sealed air-tight (PDMS is air/liquid permeable) and its long term mechanical stability is questionable. Here, a new design/manufacturing methodology is described that may be implemented in the future to address these issues.

The DCI operating principle maybe materialized in 2 different directions by manufacturing (1) A high-resolution, stand-alone DCI sensor that can be potentially inserted over the iris (or integrated into an IOL), (Figure 5.2A) and (2), modify the design of a commercial IOL, such that the IOL itself becomes the DCI sensor (no separate integration is required)(Figure 5.2B). In the latter case, the IOL lens has the IOP sensor embedded into it. As a result, the overall geometry and the dimensions of the IOL do not have to be significantly modified, which is critical for the potential adoption of the proposed technology by IOL manufacturers.

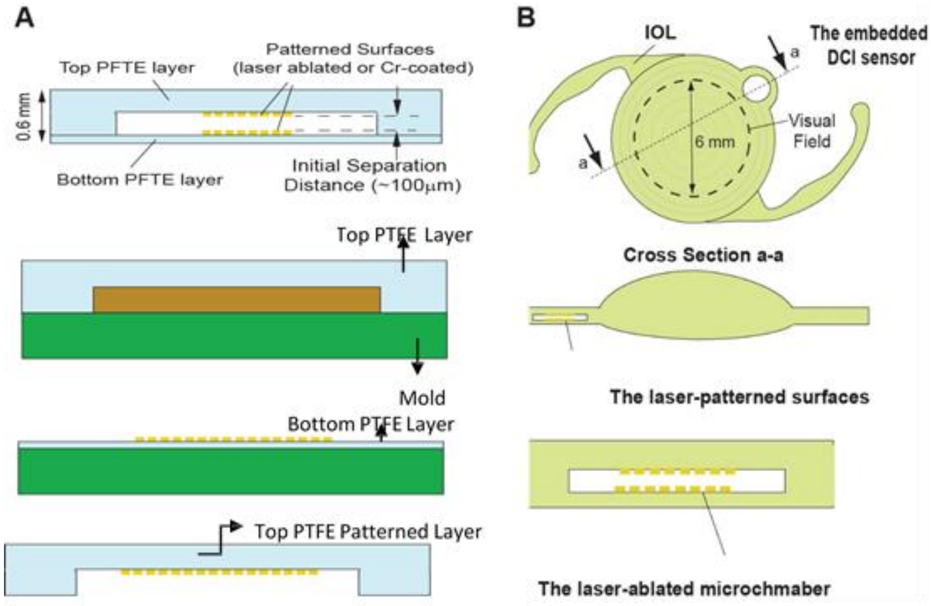

Figure 5.2: (A) Fabrication of the stand alone DCI sensor, (B) the embedded DCI sensor into an IOL.

Optimization of sensor for incorporation into iris implant: For the first version of the sensor (Type 1), a microfabrication approach can be used to create a compact, high-resolution DCI sensor (Figure 5.2A). The sensor can be made out of Polytetrafluoroethylene (PTFE – also known as 'Teflon'). PTFE has exceptional resistance to chemical stability, excellent performance in thermal and mechanical strength, it is biocompatible and gas impermeable. It is worth mentioning that the fist FDA-approved implantable MEMS pressure sensor (the CardioMEMS sensor) is made out of PTFE [196]. The DCI sensor will consist of two PTFE layers bonded together. The top, thicker, PTFE layer can be molded on a silicon mold that maybe microfabricated using DRIE. The bottom layer maybe spin casted to the desired thickness on top of a supporting substrate. To increase the image contrast of the two layers, laser ablation maybe used to create ridged patterns (eg. concentric circles) on the inner PTFE surfaces of the microchamber or by patterning chrome/gold using the lift-off process (dry film photoresist deposition might be necessary to uniformly cover the top PTFE layer). After patterning, the 2 PTFE layers maybe thermally, irreversibly bonded.

Similar to the NiFO sensor, the overall device footprint should not exceed 2 mm x 1.5 mm in order to fit through a 2 mm corneal incision (typical of suture-less cataract surgeries) and to not damage the corneal endothelia cells. Given that the device is going to be located on the surface of the iris instead of being part of the KPro implant, its thickness must be limited to under 0.6 mm as per anatomical constraints inside the anterior chamber. In order to secure the device, a haptic maybe incorporated into the device similar to the design developed by Haque *et al.* [197]. The iris, being mostly made up of muscle, is very flexible and is expected to stretch out and hold the device in place once inserted by the surgeon thereby allowing for a simple suture free procedure that seamlessly integrates with the workflow involved in performing a cataract surgery.

Optimization of sensor for incorporation into IOL implant: For the second version of the of the DCI sensor (Type 2), femto second laser micromachining [198] maybe used to ablate material from a commercial IOL lens in order to create the microchamber and the thin membrane. Since commercial IOLs are made up of different materials (PMMA, silicone, hydrophobic/hydrophilic acrylic), lasing energy, pulse repetition rate and other relevant parameters must be optimized for each case. A FEA based simulation software like COMSOL maybe used to model and optimally design a pressure sensitive membrane by determining size and thickness while trying to minimize device footprint for each type of IOL material. This needs to be followed by experimentation with different dimensions of the patterned concentric circles, e.g. the spacing, width and thickness (50 nm-1 µm thick) of the chrome– coated or laser ablated patterns of circular lines.

External optical read out unit: To be able to extract data from the DCI sensor from home, a compact, portable, light weight and easy to use Optical Readout System (ORS) must be engineered. The ORS will acquire bright field images of the two surfaces forming the DCI sensor by scanning the entire thickness of the sensor. It will then estimate image contrast for every focal plane from which the distance between the two surfaces will be calculated. This distance is related to the amount by which the IOP exposed membrane deflects. Based on the amount of deflection, the ORS will display measured pressure from the calibration data for each DCI sensor.

The ORS (Figure 5.3) will consist of two parts: (i) an optical head and (ii) a data acquisition, processing and display unit. The optical head will be made up of a precision, high resolution, motorized z scanning module which houses an objective lens and an eyepiece (optical adaptor). The z scanning module enables images to be captured at different focal planes along the thickness of the DCI sensor which includes images of the two surfaces. This module is connected to a high resolution monochromatic digital board camera sensor with its own objective lens. The board camera in turn is attached to a motorized x,y mini stage. The x-y mini stage is used to find the position of the DCI sensor and center it with respect to the position of the sensor on the board camera. The images acquired by the sensor is transmitted via USB to a low cost, credit-card sized computer (Raspberry Pi) that plugs into a display shield, both of which form the data acquisition, processing and display unit of the ORS. The mini computer is programmed to run a gradient calculation based image processing algorithm, similar to the one used to characterize the prototype DCI sensor, using a computer software like Open CV.

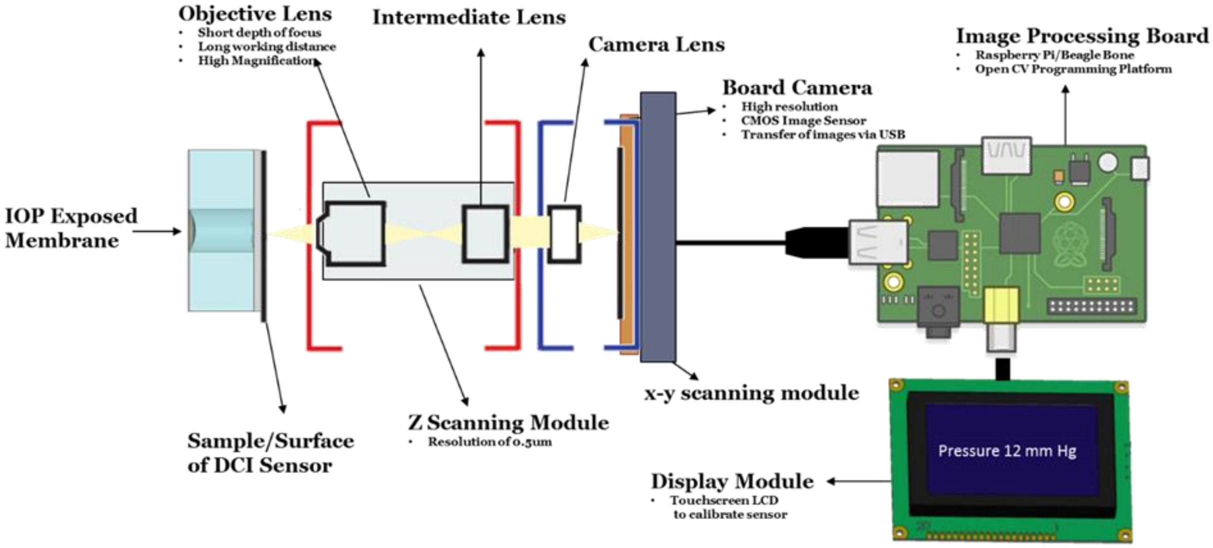

Figure 5.3: Schematic of optical read out unit for DCI sensor.

Alternatively, the optical adaptor, z scanning module and mini x-y stage can be attached in front of a smart phone camera that uses an app to perform gradient based image processing, followed by estimating and displaying measured pressure. The sizes of the optical head (3 cm x 3 cm x 3 cm) and processing/display unit (8.5 cm x 6 cm x 4 cm) are compact to ensure portability.

5.2.3 *Ex vivo* and *in vivo* validation of NiFO and DCI sensing technologies

The NiFO and DCI sensor's specifications will need to be established (dynamic range, precision error, etc.) by immersing the sensors into a bath containing aqueous humor (i*n vitro* testing) followed by testing in human cadaver eye globes (*ex vivo*). Testing should be performed according to the standards recommended by the Association for the Advancement of Medical Instrumentation (AAMI). The test protocol would involve immersing the IOP sensors in a bath containing aqueous humor. The bath will be tightly sealed, its temperature will be maintained at 36.5-37^{0}C to mimic physiological temperature and its pressure (that represents IOP) will be precisely regulated. By monitoring the 940 nm / 840 nm intensity ratio, the dynamic range and precision error post microlens incorporation must be determined for the NiFO sensor. The sensor must be subjected to static (for upto 4 weeks with pressure monitored every 8 hours) and dynamic pressure loading (to simulate IOP fluctuations) conditions to determine any zero drift that might be caused due to changes in the material properties of the IOP exposed membrane as well as long term stability. Additionally, by varying pressure as step inputs, the times response of the sensor needs to be determined by estimating the time that is required for the intensity ratio to reach equilibrium.

Similarly the dynamic range, precision error, zero drift, long term stability and response time for the various design variations of the DCI sensor need to be determine. Additionally, the optimal image contrast of the laser ablated/chrome plated surfaces must be evaluated for maximum deflection measurement sensitivity.

Ex vivo experiments should be conducted to evaluate the performance of the NiFO and DCI microsensors over a 14 day period. Standard surgical procedure can be used to integrate each microsensor assembly into a human cadaver eye globe. The IOP can be increased up to 45 mm Hg by manually injecting saline into the eyeball using a syringe and then measurements can be taken periodically while the IOP is decreased. The pressure readings from the microsensor can be compared to the readings from a digital manometer that is directly connected to the ocular anterior chamber. The experiment should then be repeated 14 days after implantation. The experiments cannot last more than 14 days due to tissue degradation.

In vivo testing of the NiFOand DCI sensors (both Types 1 and 2) should be performed in the rabbit model in order to determine long term device performance (especially sensor drift) and biocompatibility (absence of localized irritation and toxicity). Signs of material change like fatigue, erosion, creep, etc may be observed as these will invariably impact the device performance. The operation procedure is simple and approximates that used clinically in humans and the post operative appearance of the graft is similar to that seen in humans. One eye of each animal should be operated while the non operated eye should be used as a control for IOP assessment. Animals can be examined with a hand held slit lamp and submitted to IOP measurements, for one week prior to surgery, to train them for evaluation after surgery and to establish IOP baseline for each eye. After surgery, prednisolone acetate 1% can be used as an anti-inflammatory drug as well as to induce intraocular hypertension. If further elevation of IOP is required, cannulation of the eye under general and topical anesthesia should be performed. IOP measurements should be made at different pressure points and should be monitored intermittently for the duration of the experiment of thirty (30) days (at 1 day, at 1 week, and at 1 month time points), via digital manometry, pneumotonometer, tonopen, and Icare tonometer to be compared with the wireless IOP monitor, possibly requiring no anesthesia or restraining device. In case of failure of measurement, the animal should be sedated, to minimize erratic IOP readings as a result of forceful squeezing of eyes by the frightened animal. This will also avoid sympathetic responses affecting the IOP, reported with animal restraining and with contact tonometry. Rabbits should be euthanized if they are not standing, alert, and eating for a 24 hour period. Otherwise, they should be euthanized at the end of the experimental procedure at 1 month after which the eye should be removed, exposed to a fixative agent and examined for gross pathological evidence of inflammatory response, tissue damage and protein aggregation. A similar procedure can be adopted for testing the DCI sensors after incorporation with IOLs and onto the iris.

5.2.4 TSD system

The DVA of the proof-of-concept prototype has a footprint of ~ 11.5 mm x 11.5 mm, a limited spatial resolution (~ 1 mm) and they cannot be miniaturized any further due to the limitations of the 3D printing technology. This is a critical requirement in order to ensure that the device thoroughly covers the soft and deformable shape of the human hand, and therefore the sanitizer is dispensed fast and uniformly to the entire contact surface. In addition, the 3D printed valves are very stiff in the vertical direction (due to the presence of the spring) but at the same time they cannot support tangential forces (shear stress). Moreover, 3D printing, being a rapid prototyping method, is not presently a technology that is amenable for mass production. Therefore, implementing the concept as a MEMS device by microfabricating an array of silicon-based microvalves and optimizing their mechanical design is a better alternative that would address the issues with 3D printing as well as ensure proper and robust operation.

Similar to the 3D printed prototype, the operating principle of the MEMS-based, smart ‘skin’ is based on the idea of an array of passive, human-powered, microvalves that deliver a liquid sanitizer when the human hand comes in contact with the surface of the array (Figure 5.4). The microvalves are closed when no human touch/force is present. When a person touches the surface of the MEMS skin, the microvalves are slightly pushed in and the disinfectant flows through them (Figure 5.4B). Each microvalve contains: (i) a movable piston, (ii) a set of 2 or 4 cantilever beams that support the piston and that act as a mechanical spring, (iii) a circular disk that has tens of microholes (~80-100 µm in diameter) and, (iv) a fluidic microchamber. The microchambers could be connected through a glass microfluidic network to a disposable cartridge that contains the disinfectant. All those elements maybe easily microfabricated (with high precision) in a wafer-level process.

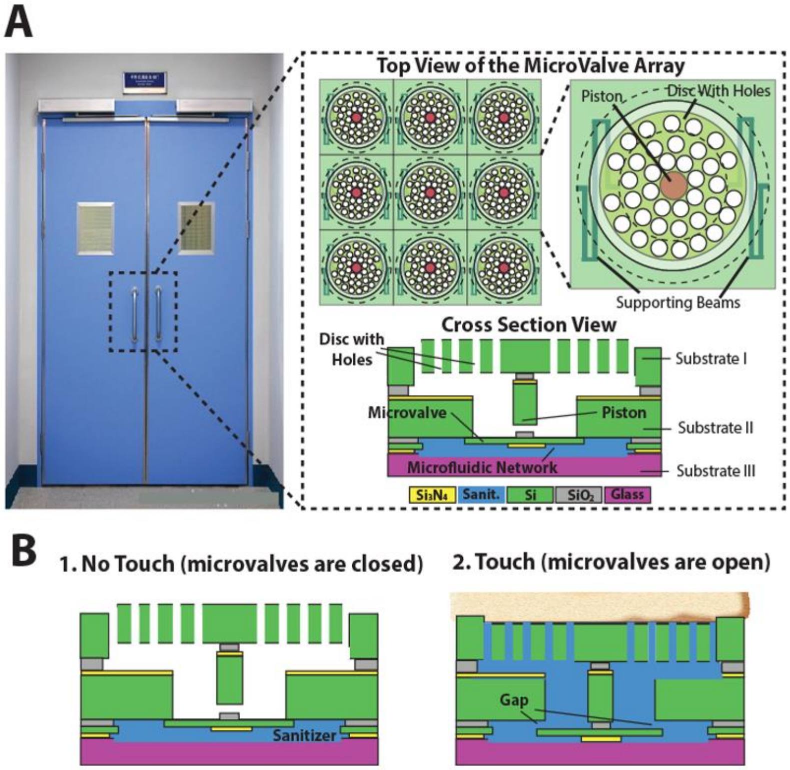

Figure 5.4: (A) The architecture of the MEMS smart, skin consisting of thousands of passive microvalves. (B) The operation principle of a single microvalve. The sanitizer fills the microvalve when the disc of the array is touched.

The MEMS valve microarray could consists of 3 bonded wafers. As seen in Figure 5.5, the middle wafer is an SOI (Silicon-On-Insulator) wafer: it has a thick single crystal silicon layer (~500 µm thick), a buried thin layer of silicon dioxide (2 µm thickness) and a second thin silicon layer (~5 µm thick). The process starts with the LPCVD deposition of a 0.5 µm thick silicon nitride film (Si_3N_4) on the SOI wafer. The Si_3N_4 film –that is patterned in both sides of the SOI wafer- has a dual role: (i) it is used as a hard masking layer for patterning the front side of the wafer (step 4 in Figure 5.5) and (ii) it bends –after release- the suspended Si beams upward so the microvalve is always closed. The bending of the Si_3N_4/Si beams is due to the tensile stress of the Si_3N_4 film. The patterned SOI is then anodically bonded to a DRIE-etched silicon wafer that contains the disc with the holes and to a glass wafer that contains the microfluidic network. Finally, the 3-stack is time-etched released in HF (the SiO_2 is partially etched). After release, a thick oxide layer of SiO_2 is deposited to make the array hydrophilic and therefore facilitate the flow of the sanitizer through each microvalve. Finally, the microfluidic network is connected to the sanitizer reservoir and is allowed to fill the array.

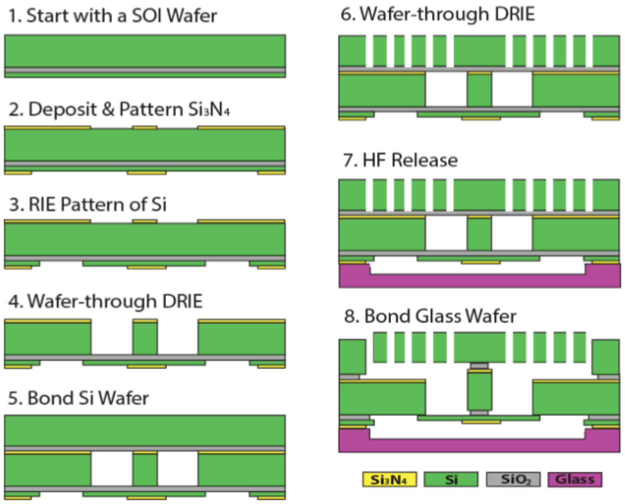

Figure 5.5: The microfabrication process of the MEMS smart skin. The MEMS skin consists of 2 silicon wafers and 1 glass wafer that are bonded together.

From Figure 5.6, it can be seen that the area of the disc that comes in contact with the human hand needs to be optimized to ensure rapid and uniform distribution of the sanitizer. The microvalve-to-microvalve spacing needs to be minimized as dead areas between the microvalves might not get disinfected properly. Additionally, the thickness and length of the suspended beams need to be optimized as these dimensions would affect the force that is required to open each microvalve.

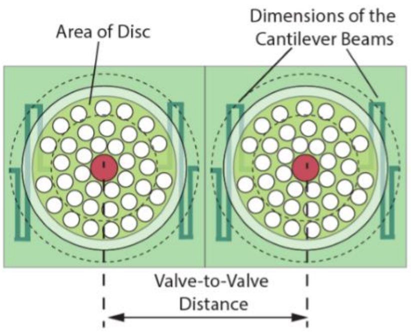

Figure 5.6: The critical dimensions of the microvalve array that must be optimized.

The processes used for fabricating the microvalve array (e.g. DRIE, anodic bonding) are well-established which means that there should not be any difficulties. A minor concern –which seems unlikely- is leakage from the microvalves. If leakage is present, a thin film of parylene maybe selectively deposited at the bottom surface of the piston. Parylene is slightly hydrophobic, can be deposited uniformly and it is therefore expected to provide excellent sealing. Finally, it is possible that after long term tem, the holes in the disc will filled up with dust particles. In this case, the diameter of the holes can be increased, such that the increased flow rate of the sanitizer through the holes will remove any deposited particles.

The design of MEMS valves is distinct from the 3D printed valves: (1) the small size of the valves allows uniform and rapid distribution of the sanitizer, (2) the piston of the valve is suspended through a set of cantilever beams. That ensures that the piston will move in the vertical direction under a light touch and it will not tilt/rotate when a tangential force is applied to (in the 3D printed valves, the piston is free-floating and it could get easily misplaced) and (3) all of the components of the MEMS valves are batch-microfabricated so there is no need for manual assembly.

Due to the small distances travelled by the piston (few microns) and the small mass of the microvalves, the time for the disinfectant to reach the top surface of the array is expected to be in the millisecond (ms) range. That short operation time is more than enough, as the time required opening a door or moving a cart is at least few seconds. The unique features of the MEMS skin include: (1) zero power requirements as it consists of a passive hand-powered microvalve array, (2) the use of liquid antimicrobial disinfectants which is the best known disinfection approach, (3) versatility on what type of disinfectants can be used, (4) maximum prevention as the MEMS skin does disinfect both the surface on which it is applied (e.g. the door handle) as well as the human skin, (5) minimum sanitizer consumption as disinfection is localized at the contact areas (all microvalves operate independently - no touch/no activation) Finally, it should be emphasize that the use of MEMS technology is critical for the low-cost, mass production of the MEMS skin in the future and its fast adoption.

PART B – Biological Micro Systems

CHAPTER 6

INTRODUCTION

6.1 Motivation

Key goals in the fields of neuro and developmental biology are to understand how living systems operate macroscopically through morphogenesis and behavior and how this operation is governed by microscopic activities such as gene expression and cell signaling. To address these questions, the most common method is to directly observe biological processes in living organisms followed by the extraction of meaningful information from the observations. This process of imaging generally uses fluorescence microscopy and over the past several years, enormous advances in optical techniques have made possible the ability to perform high content imaging with excellent spatiotemporal resolution to observe structures that are located deep within intact tissue. On the other hand and in parallel, engineers have made advances, especially in the field of microfluidics, to enable high throughput observations that supplements high content, high resolution imaging to produce vast amounts of biological data.

Caenorhabditis elegans (nematodes) and *Drosophila melanogaster* (fruit flies) are two of the most widely-used invertebrate model organisms that are used by biologists to study human diseases [199] [200]. The ability to manipulate these small-scale organisms that includes their delivery, orientation, and immobilization plays a critical role in the success of biological imaging to answer fundamental questions about causes, pathways and treatments for human diseases. Besides imaging, other examples of applications where manipulation is highly demanded are in cell ablation [201], microinjection [202] and dissection [203] of these organisms.

Conventional manual methods [204] and recent microfluidic techniques [205] [206] [207] used to manipulate model organisms are typically non-reversible and time-consuming at a single animal level. In conventional manual methods, animals are oriented with picks or tweezers, then glued or trapped for imaging [208]. These procedures require high levels of expertise while being non-reversible and time-consuming. Recent microfluidic-based methods have demonstrated manipulation of nematode and fruit fly larvae with acceptable efficiencies, but only yielding limited orientation directions (i.e., lateral or dorsal) [209] and poor levels of animal immobilization. Therefore, there is a need for developing tools that produce a reversible effect, are easy to implement, whose implementation is not labor intensive and that have the potential to enable high speed, high throughput imaging on intact *C. elegans* and *Drosophila melanogaster* across multiple developmental stages.

In this thesis, 2 separate, novel approaches for immobilizing and imaging *Drosophila melanogaster* larvae and *C. elegans* nematodes are described and discussed. Both methods are simple to implement, the operator does not need to have any specialized skills to implement them, allow reversible immobilization to perform imaging in whole organisms and enable precise manipulation of the animals. Furthermore, both methods are amenable to computer automation.

1. Cryo-Larva Chip: Microfluidic chip for cryo-aneasthesia of *Drosophila* larvae for high resolution imaging applications: The thesis describes a microfluidic method for short term, repetitive immobilization of *Drosophila melanogaster* larvae to perform high resolution imaging on intact animals for neurobiological studies. The method is easy to implement, allows complete larval recovery and can be used to immobilize larvae of different developmental stages. It can be subjected to multiple uses while making the larval loading process extremely quick and easy. The microfluidic device is also equipped with feeding ports to enable food supply to the larva and avoid starvation in order to maintain the animal on chip for long term time lapse imaging experiments.

2. The WormImm Plate: A 3D Printed Millifluidic Tool for CO_2 Immobilization of *C. elegans* on Agar for Population Studies and *In vivo* Imaging Applications: The thesis describes an easy to use, 3D printed milli-fluidic tool for immobilizing on demand, entire populations of *C. elegans* as they are grown and maintained on an agar surface. The method is appropriate for short-term (20-30 minutes) worm immobilization which is sufficient for performing several experiments on worm populations like scoring lifespan assays and performing fluorescence imaging under a stereoscope. Besides allowing quick recovery, the method offers the additional advantage of observing worm populations without mechanically manipulating or disturbing them as they continue to grow on the agar surface. Furthermore, with minor dimensional modifications to device architecture, we envision the use of this method in a wide variety of higher resolution biological imaging studies in *C. elegans*, including cell developmental and neuronal regeneration studies.

6.2 Techniques for manipulation of *Drosophila melanogaster*

6.2.1 Research need

The fruit fly, D. *melanogaster* (Figures 6.1 and 6.2), is one of the most well-studied model organisms and one of the first model organisms used for genetic studies [210]. Additionally, the *Drosophila melanogaster* larva is a widely used organism for modeling human biology and diseases at the behavioral, cellular and molecular level [211] [212] [213]. *Drosophila* larva is genetically tractable, has a translucent cuticle, a short life cycle and a simple neuroanatomy that is amenable to imaging [214] [215] [216] [217]. However, one of the biggest challenges associated with live imaging of *Drosophila* larvae is achieving an acceptable degree of immobilization. For high resolution imaging to observe cellular and sub-cellular events with high spatial and optical resolution, the larva body needs to be exceptionally stationary during immobilization. For time-lapse imaging of more long term events like the growth of new axons post injury requires an immobilization method that is very gentle on the animal's physiology [218]. Therefore, in order to image reliably cellular/sub cellular events over longer periods, an easy to use, reversible, low cost and chemical-free immobilization method is needed.

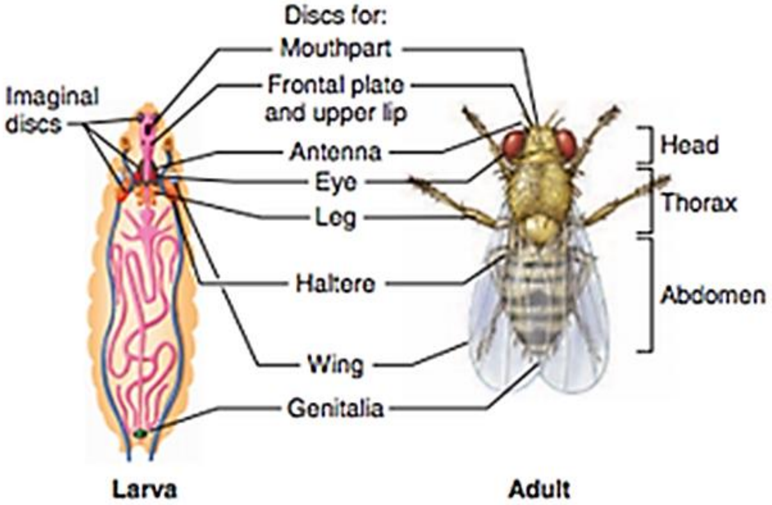

Figure 6.1: Anatomy of adult and larval *Drosophila melanogaster* [Figure and caption appears in [219]].

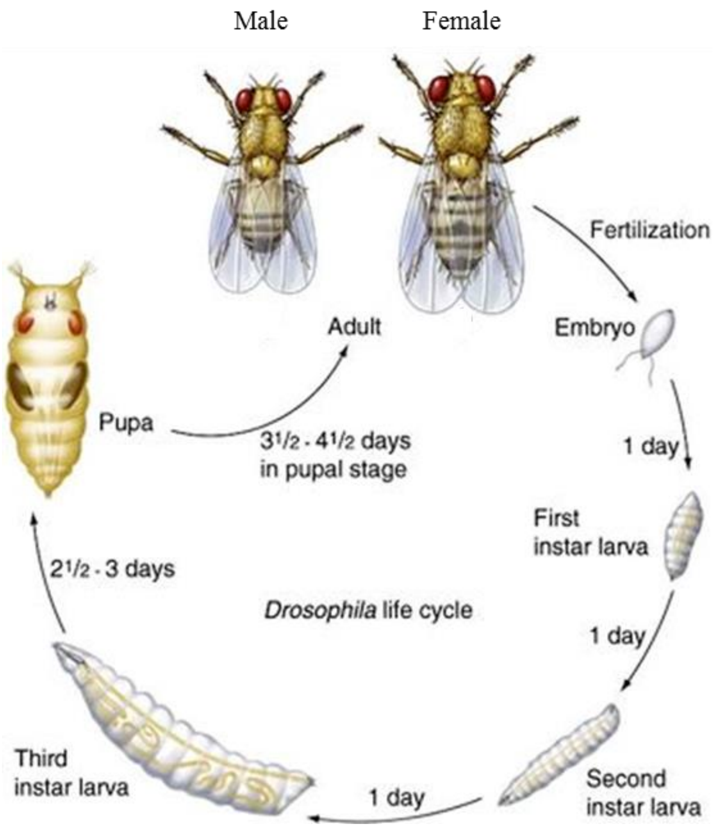

Figure 6.2: *Drosophila melanogaster* life cycle [Figure and caption appears in [220]].

6.2.1 Current practices

Current, conventional immobilization techniques include dissection [221] [222], the use of anesthetics [223] or glue and squeezing the larva body [224]. Dissection prevents imaging intact larvae while long term image acquisition is not possible. Glue is toxic, provides irreversible immobilization and is difficult to implement for very young animals. The use of anesthetics –such as isofluorane [225] [226] - has many advantages but they are known to affect the animal's neurophysiology and various biological processes. Additionally, imaging must be restricted to short intervals in order to allow recovery between doses [225] [226]. Besides affecting larval survival, conventional anesthetics also pose a threat to the user's safety. The most popular mechanical immobilization technique involves capturing the larva by flattening it between two microscope slides using light pressure. While this can be easily performed, the degree of control is poor and the immobilization is not adequate in order to allow stable high resolution imaging of cellular processes. Furthermore, the imaging duration is limited and larval recovery can be difficult if not impossible [227].

6.3 Techniques for manipulation of *C. elegans*

6.3.1 Research need

The nematode, *C. elegans* (Figures 6.3 and 6.4), is one of the most widely studied model organisms with several practical advantages like easy maintenance, short generation times and optical transparency well into adulthood [200] [228] with well established genetic manipulation techniques being applicable to them [229]. Biological studies of *C. elegans* often require that they remain immobile during observation, especially for experiments such as detailed structural analysis of anatomical features like the shape of the pharynx [230] or the structure of the muscles of the body [30], performing surgical ablation of tissues using laser pulses, [231] and acquiring time-series snapshots of neuronal responses to stimuli with fluorescent probes [232]. In addition, the ability to immobilize multiple worms at once is highly desirable as it would drastically decrease the amount of time needed to collect data from large worm populations. Furthermore, the immobilization method must be minimally toxic to worm physiology. With the advancement of microfluidics technology, several research groups have recently proposed microfluidic chip based systems for observing *C. elegans* populations. These systems are however expensive to fabricate with complicated designs that are difficult to implement, especially for low resolution imaging [233] [234] [235]. Moreover, there is no existing method that allows for the simultaneous imaging of worm populations without displacing them from their culture medium. Therefore, there is a need to develop a low cost, easy to implement tool that allows large worm populations to remain immobilized or at the very least, within the field of view of the imaging microscope for the duration of the observational procedure without being toxic to the worms while continuously maintaining them on an agarose culture medium.

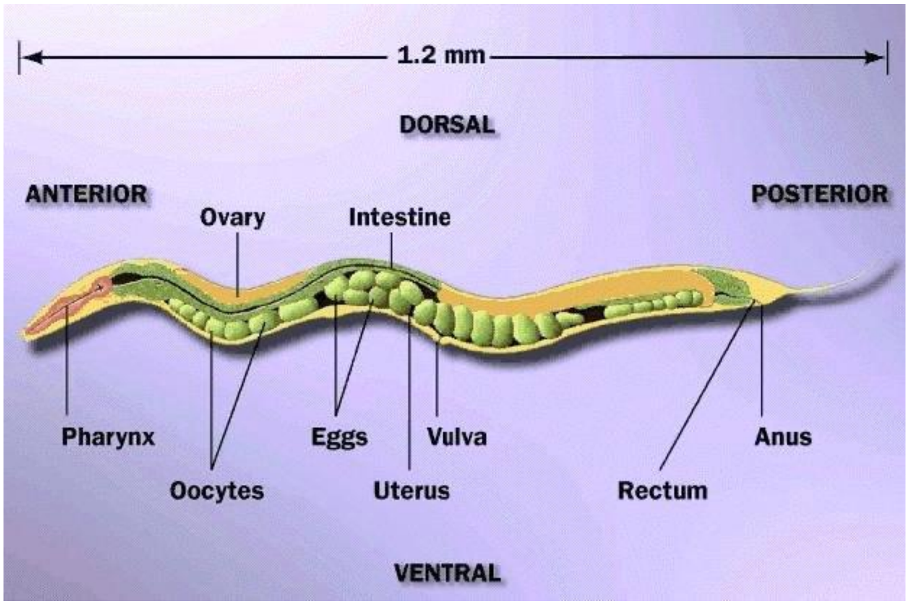

Figure 6.3: *C. elegans* hermaphrodite anatomy [Figure and caption appears in [236]].

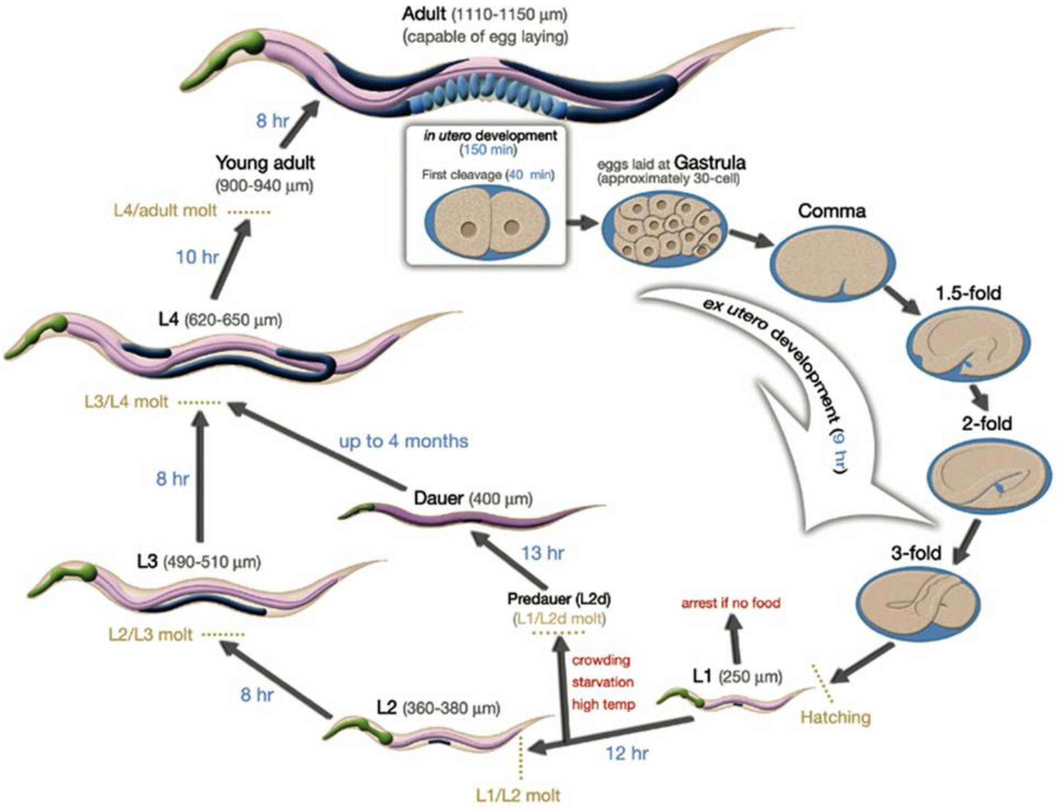

Figure 6.4: *C. elegans* life cycle where L stands for Larva [Figure and caption appears in [237]].

6.3.1 Current practices

Generally, *C. elegans* are immobilized in two ways: (i) The worms can be fixed to an agarose pad using a cyanoacrylate glue, [238] [239] or (ii) the worms maybe treated with chemical anesthetic drugs including metabolic inhibitors (like sodium azide) [240] [239] or cholinergic agonists (like levamisole) [241] [239].

Gluing a single worm takes several minutes which means that in order to examine a large number of worms, researchers must devote substantial time and effort to immobilize an entire population during an experiment thereby making this method highly inefficient. In addition, the glue adheres to the worm irreversibly. Apart from the fact that once an animal has been glued and that it cannot be released, the glue by itself is very likely to have a toxic effect on the organism. Treatment with anesthetic drugs is useful for paralyzing and thereby immobilizing very large worm populations at once. However, it unavoidably changes the internal biochemical state of the worm during the procedure thereby affecting experimental observations. On some occasions, individual worms have been immobilized with either their head or their tail being held by the researcher inside a micropipette using suction [242] [239]. Similar to the gluing method, a major limitation of this procedure is that it is possible to immobilize and image just one worm at a time making the process very tedious and impractical for population studies.

6.4 Thesis objectives

In order to conduct biological studies in small model organisms like *Drosophila melanogaster* and *C. elegans*, experimental methodologies need to be developed that would be simple to implement, not be skill intensive and allow precise manipulation of the animal and its micro-environment. This thesis aims at utilizing the potential of microfluidic and millifluidic technology as well as manufacturing processes like 3D printing for developing such methodologies for conducting neuroscience studies in *Drosophila melanogaster* and *C. elegans*. This thesis aims at achieving the following objectives:

1. To realize a microfluidic approach for immobilizing and performing high resolution imaging on *Drosophila melanogaster* larvae

Immobilization of the larvae is a critical step for high resolution neurobiological research studies that include laser ablation of neurons, imaging stimulus-evoked neuronal responses, analyzing anatomical features and imaging cellular development. However, the conventional immobilization techniques are labor and time intensive, low throughput, toxic and moreover, not amenable to automation. Here, we designed and fabricated a microfluidic platform for immobilizing and performing high resolution imaging on intact larvae across different age groups

(1st instar to late 3rd instar). The method is simple to implement, is not skill intensive, non-toxic, reversible, allows precise larval manipulation and is amenable to computer automation.

2. To fabricate an immobilization assay for *C. elegans* on an agarose plate.

We designed and fabricated a 3D printed milli-fluidic device for immobilizing worm populations as they are grown and maintained on an agarose surface. The method is appropriate for immobilizing worm populations for short periods of time (20-30 minutes), immobilizes worms of different age groups (L2's to adults), is easy to implement and allows worm recovery within a few minutes after immobilization. Moreover, the device architecture is compatible with low as well as high resolution optical microscopy.

6.4 Thesis organization

The work presented in Part B of this thesis is organized as follows :

Chapter 7 – Literature Review

This chapter reviews the recent developments in immobilization device technology for *Drosophila melanogaster* and *C. elegans* research studies.

Chapter 8 – Cold and Compressive Immobilization of Drosophila Larvae On-Chip for High Resolution Imaging Applications

In this chapter, we present a microfluidic approach for immobilizing the model organism, *Drosophila melanogaster* larva, on-chip for high resolution, live, imaging in whole animals. The chip creates a cold micro-environment around the larva while also utilizing a deformable PDMS membrane to mechanically restrict larval movement. After characterizing on chip temperature distribution and larval body movement, our results indicate that the method is appropriate for repetitive as well as reversible, short-term (several minutes) larval immobilization. The method offers the added advantage of using the same chip to accommodate and immobilize larvae across all developmental stages (1st instar to late 3rd instar). The process of loading larvae onto the chip is also quick and easy. Besides the demonstrated application of the chip in high resolution observation of sub cellular events such as mitochondrial trafficking in neurons, we envision the use of this method in a wide variety of biological imaging studies employing the *Drosophila* larval system, including cellular development and other studies.

Chapter 9 – The WormImm Plate: A 3D Printed Millifluidic Tool for CO2 Immobilization of C. elegans on Agar for Population Studies and Imaging Applications

In this chapter, we present a simple to use, practical, 3D printed milli-fluidic tool for immobilizing entire populations of the roundworm *C. elegans* as they are grown and maintained on an agar surface. A CO_2 environment is created on demand at the surface of the agar layer that causes a near immediate immobilizing effect on the worms. Our results indicate that the method is appropriate for short-term (20-30 minutes) immobilization which is sufficient for performing several experiments on entire worm populations like scoring lifespan assays and performing fluorescence imaging under a stereoscope. The method offers the additional advantage of observing worm populations without mechanically manipulating or disturbing them as they continue to grow on the agar surface. The device has a simple architecture that is compatible with both upright or inverted microscopes. Furthermore, with minor dimensional modifications to device architecture, we envision the use of this method in a wide variety of higher resolution biological imaging studies in *C. elegans*, including cellular developmental and neuronal regeneration studies.

Chapter 10 – Conclusions and Future Directions

This chapter summarizes the work presented in Part B of the thesis and discusses future directions for the biological micro-systems that have been developed.

CHAPTER 7

LITERATURE REVIEW

7.1 Introduction

As discussed in Chapter 5, small model organisms such as *Drosophila melanogaster* and *C. elegans* are used very commonly in biological studies as they provide unique opportunities for scientific discovery. Apart from the gold standard methods of using glue and/or chemical anesthesia, there have been significant breakthroughs in the development of technologies over the past few years to manipulate and image these organisms for a variety of experimental studies. Among these newer technologies, microfluidics based systems have been the most prominent. This chapter presents various microfluidics based methods that have been developed and used for immobilizing *Drosophila* larvae and *C. elegans* nematodes for imaging purposes.

7.2 Microfluidic technologies for micro-manipulating, imaging and phenotyping small model organisms

With the advancement of research in the biological sciences, soft materials, drug screening and lab on a chip assays, microfluidics has emerged as an attractive technology choice, especially for developing high throughput based systems [243] [244]. As it employs dimensions at the micron scale [245] [244], fluid flow is precisely controllable thereby allowing the application of accurate flow rates, concentration gradients and shear stresses to manipulate small model organisms in a regulated micro-environment. Additionally, manufacturing microfluidic devices involve the use of fabrication techniques that are very similar to those used in making MEMS devices with small features ranging between 1-100 µm. Generally, soft lithography replica molding of an optically transparent, soft, gas permeable, non-toxic and inert silicone based elastomer called PDMS is used to fabricate microfluidic devices. Moreover, the method is easy and quick to implement, relatively inexpensive and allows each chip to be used multiple times. In the past few years, three dimensional (3D) printing technology has also joined the effort of miniaturization with high resolution 3D printers capable of fabricating micrometer scale objects. Furthermore, the increase in material choice has led to an explosive growth in 3D printing technology for manufacturing microfluidic devices for biomedical/biological applications. These advantages make PDMS, soft lithography replica molding as well as 3D printing suitable for applications in biological experiments and microscopic imaging observations.

Given its status as a platform technology for biological studies, microfluidic devices have been used to handle and study cells as well as small model organisms. Specifically in the field of *Drosophila* larval research, microfluidic systems have been employed to perform embryo sorting [246] [247] [248], microinjection [248] [249] and arraying [250] [251] [248] among other experiments. Similarly, the field of *C. elegans* research has also been significantly impacted by microfluidic technology ([252]; [253]; [254]; [255]; [256]; [257]; [258]; [259]; [260]; [261]; [262]; [263]; [264]; [265]), as it not only allows controlled flows and targeted chemical stimuli delivery, but it also enables easy animal handling and manipulation. In general, microfluidics has helped transform *Drosophila* and *C. elegans* research from a laborious, time-consuming, low throughput process into an easier task, aided by the simple, precise and rapid on-chip animal handling, immobilization, and imaging capabilities that the technology offers. Additionally, the majority of microfluidics systems tend to avoid the use of glues and chemical anesthetics for studies that require worm immobilization which minimizes any potential negative impacts on animal physiology.

Most biological experiments require high resolution live imaging making the immobilization of the small model organism an important prerequisite. Any movement can lead to out of focus images that can render the observation useless. In general, the immobilization approaches that have been developed are either chemical or physical techniques. The first category includes methods that use chemical compounds such as metal ions or antibodies to achieve immobilization. Even though they provide good quality of immobilization, these techniques adversely affect animal physiology, even at very low concentrations [266]. The techniques in the second category cause immobilization by altering the viscosity of the medium or by using some means of capturing, holding and/or applying pressure on the animal. Even though negative effects on animal physiology is minimized, the quality of immobilization is usually inferior to a chemical method. The following sections describe and review in further detail, the microfluidic approaches that have been specifically developed and published in existing literature for immobilizing *Drosophila* larvae and *C. elegans* nematodes.

7.3 Immobilization approaches for *Drosophila melanogaster*

Several research groups have developed systems that either physically constrict/compress the larvae to restrict movement or use CO_2 to achieve immobilization. In the following paragraphs, the most notable device technologies will be briefly presented followed by a discussion of their advantages and disadvantages.

Mechanical micro-compression: Yan *et al.* (2014) [267] constructed a microfluidic device (Figure 7.1) to immobilize *Drosophila* larvae using a mechanical microcompressor. The microcompressor, made up of CNC machined brass, can be adjusted to precisely press down against a coverslip which bows and compresses against another coverslip with a larva mounted in between them. The mechanical pressure applied by the microcompressor flattens the larvae thereby immobilizing it. Additionally, the compression pressure visually enhances the appearance of sub-cellular structures and organelles while observing under a microscope. The device has microfabricated glass channels that allow on chip perfusion of fresh media or drugs to the animal during imaging (Figure 7.1(c)). The mechanical microcompressor was made out of CNC machined brass. Yan *et al.* [267] imaged E-cadherin dynamics in the eye imaginal disc in live third-instar larvae expressing an E-cadherin–GFP fusion using this immobilization approach coupled with a two-photon confocal microscope.

The device design is simple and compatible with either upright or inverted microscopes. It is possible to integrate the method with additional microfluidics modules which widens its range of applications in which high resolution bright field and/or fluorescence microscopy is required. However, despite these advantages, the method requires the use of complicated and expensive laser and CNC fabrication processes in addition to soft lithography replica molding. Additionally, given that the mechanical stress being applied on the animal is not well regulated while using this method, larval recovery post immobilization is poor. Since the animals do not survive after several hours, the application of this method in most time lapse imaging experiments is severely limited.

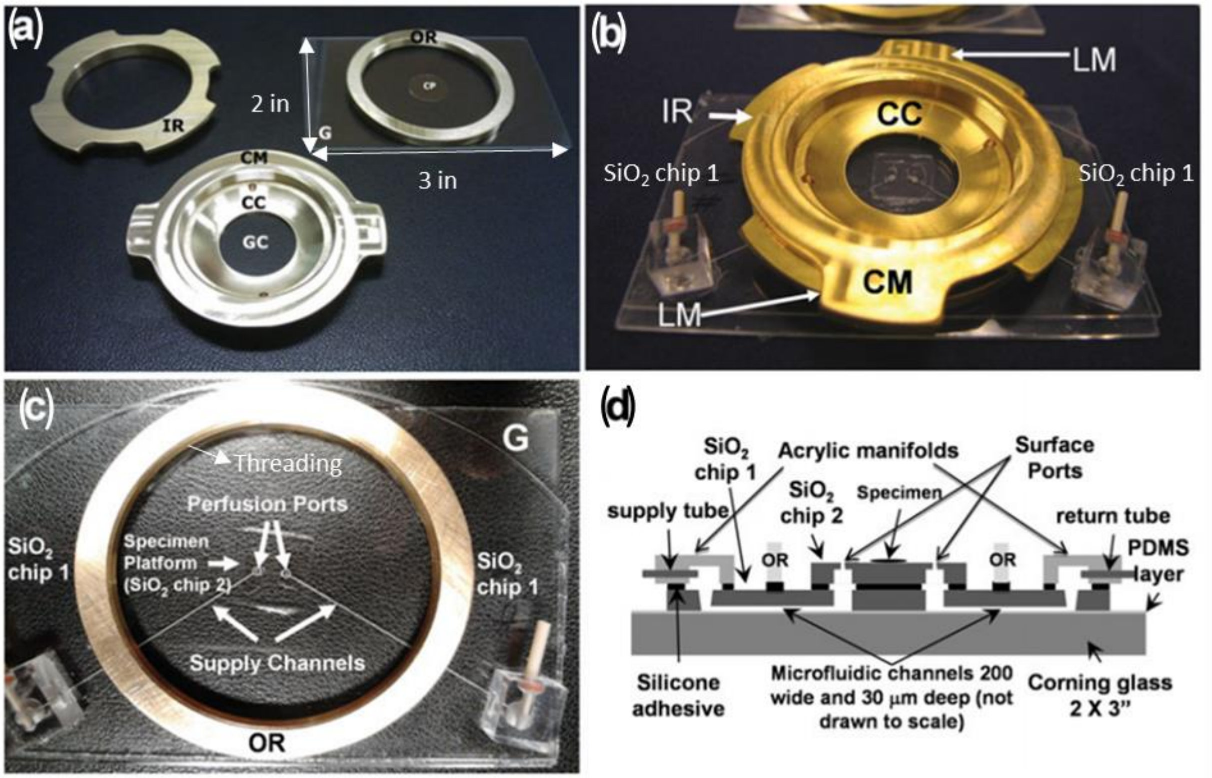

Figure 7.1: (a): The main components of the microcompressor consist of a commercially available glass slide (G), 4 precision machined brass pieces and a machined aluminum tool. The brass pieces consist of a threaded outer brass ring (OR) permanently attached to the glass plate, a threaded inner ring (IR) that is screwed into the OR and a brass coverslip mount (CM). The CM has a smooth outer face that slips into and engages the IR with two overhanging arms to form a locking mechanism (LM). The threaded inner face of the coverslip mount accepts the coverslip compressor (CC) and a machined step in the center of the mount creates a niche for a 25 mm commercially available glass coverslip (GC). The unique design of the coverslip mount bends the coverslip so that the very center of the coverslip will be the first section to touch a centered specimen on the 12 mm coverslip platform (CP). The platform can also be custom-designed for microfluidic control or for holding specimens in 3D volumes. (b): Depicts an assembled unit, incorporated with microfluidics, ready to be placed on a microscope stage. Samples are loaded on the glass specimen platform at the center of the unit, after which the coverslip mount is inserted into the threaded assembly. Vertical adjustment of the top coverslip is made by rotating the ring assembly, engaging the fine threads of the two rings. (c): The glass plate with outer ring from above incorporated with glass (SiO_2) microfluidics. SiO_2 chip 1 has two 200 mm wide and 30 mm deep channels machined into it that each run from an acrylic manifold on the bottom left and bottom right of the image. These manifolds both have connectors for tubing that would carry fluid via a pump. The channels connect to SiO_2 chip 2, which serves as the CP and has a 30 mm wide supply and return port for specimen perfusion. (d): Cross sectional schematic of the microfluidics. SiO_2 chip 1 is adhered to the glass base by plasma-bonding to a 25-mm-thick layer of polydimethylsiloxane. The acrylic manifold and SiO_2 chip 2 are adhered to SiO_2 chip 1 by a silicone adhesive. [Figures and captions appear in and are taken from **[267]**]

Mechanical clamping: Ghaemi *et al.* (2014) [227] developed two microfluidic devices (Figure 7.2) to immobilize 3rd in star larvae for performing live fluorescence functional imaging of the central nervous system in response to a controlled source of acoustic stimulation with neuronal responses peaking at 200 Hz.

The first device, referred to as the pneumatic chip, consists of an inlet port for larval loading, a channel for directing each larva to a tapered trap that mechanically immobilizes the animal during imaging and an outlet for larval ejection at the of experimentation. The chip therefore enables automated loading, immobilization, testing and unloading of the larvae. The immobilization trap consists of a narrowed channel, a primary gate, a secondary gate and a stopper. Once the larva is directed into the trap, the gates apply pressure on the body. The rest of the animal is encapsulated inside the narrow channel. The dimensions of the secondary gate allow just the nose of the immobilized larva to protrude through the gate which prevents it from escaping [227].

The second device, referred to as the FlexiChip, has a main channel that fits a 3rd instar larva and has a clasping clip mechanism that clamps the larval head. The clip opens when the PDMS is flexed and closes upon flexion reversal. There is a 100 μm diameter glass wire on top of the clip that creates an enclosed opening that prompts the larva to enter the channel while stabilizing the anchoring once the clip is closed. There are auxiliary channels for the possibility to introduce electrical/mechanical probes for body-wall stimulation during live-imaging. It must be noted that while being subjected to different sensory stimuli, the larva continues to breathe [227].

The pneumatic chip is a good choice for performing high throughput studies due to its automated loading and unloading feature. The FlexiChip, being more simple in its implementation, is better suited for smaller scale studies especially since the larvae maybe quickly loaded manually. Both chips have a simple principle of operation, use 3D printed molds that make their fabrication cheap and significantly reduce endogenous body movements to a large extent. However, small body movements are still present that do not allow higher resolution imaging of sub cellular structures. Additionally, the architecture of the devices is complicated and they are capable of accommodating only 3rd instar larvae making developmental studies impossible [227].

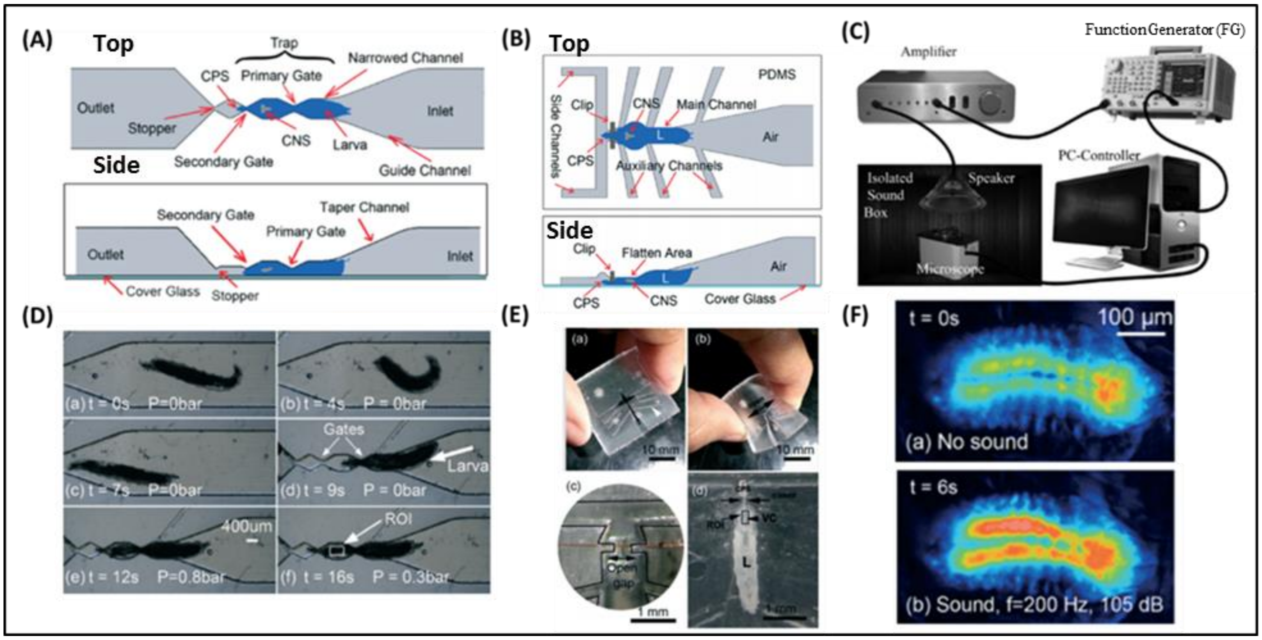

Figure 7.2: (A) Schematic design of the pneumatic chip– top view (top image) and side view (bottom image). The inlet channel is 25 mm in length, 3 mm in width and 2 mm in depth with an inlet port located at its end for loading animals. The outlet channel is 8 mm in length, 3 mm in width and 2 mm in depth for ejection of tested animals. (B) Schematic design of the FlexiChip – top view (top image) and side view (bottom image). (C) Schematic showing the experimental setup used to examine larval auditory response. An insulation box with sound damping foam is used to accommodate the microscope right beneath the speaker that is connected to a function generator (FG) through an amplifier for sound actuation. Both the microscope and the FG is connected to a PC for automated control of image acquisition and signal generation respectively. (D) Microscope images demonstrating the steps used to load individual larvae using the pneumatic chip (a–d). When loaded onto the chip, each larva swam freely into the trap, and (e–f) the larva was then pneumatically moved into the trap and immobilized. Time-lapsed fluorescence imaging was subsequently conducted on the Central Nervous System (CNS) located inside the Region of Interest (ROI). All the figures shown in (D) have a scale bar of 400 μm. (E) Images demonstrating the steps used to load individual larvae onto the FlexiChip. The FlexiChip (a) is squeezed and bent (b) so that the clip (c) opens up. Then, the larva is inserted into the gap that is created and the FlexiChip is then released and sealed by a coverslip (d). Time-lapsed fluorescence imaging was subsequently conducted on the CNS located inside the Region of Interest (ROI). (F) Snapshots of the fluorescence activities in the CNS of a larva (a) before and (b) during exposure to sound wave of duration 5 second with a frequency of 200 Hz and amplitude of 105 dB with the animal loaded onto the pneumatic chip. [Figures and captions appear in and are taken from **[227]**]

<u>Carbon dioxide immobilization with mechanical compression:</u> Ghannad-Rezaie *et al.* [1] developed two microfluidic chips (Figure 7.3): one for short-term imaging (up to 1 h) and the other for long-term imaging (up to 10 h) experiments using which they investigated short and long term cellular responses to neural injury.

Both devices are not permanently bonded to any substrate and are therefore reversibly attached to a glass coverslip. The first microfluidic device (Figure 7.3A) that maybe used for short term immobilization (termed the 'SI-chip' for *S*hort-term Immobilization over several minutes) contains a micro chamber that fits an early-stage 3rd instar larva. A microfluidic network surrounds the micro chamber and has a vacuum access port. Once connected to vacuum, the network creates a strong seal between PDMS, oil and the coverslip, thereby preventing the larva from escaping from the chip. The mechanical pressure applied through the PDMS/glass walls on the larval body, although mild, is sufficient to immobilize it. Additionally, the pressure brings internal body structures closer to the coverslip thereby allowing for easier high-resolution imaging. In order to remove the larva from the chip, the vacuum seal must be manually released. Given that the loading/unloading process is quick and simple without creating a permanent bond between glass and PDMS, the same chip can be used multiple times for additional experiments [1].

To increase the survival rate over more extended (>1 hour) periods of time compared to the SI chip, a second PDMS microfluidic device (Figure 7.3B) was developed (termed the LI-chip for Long-term Immobilization). With a double-layer architecture, a 'CO_2 micro-chamber' is incorporated above the immobilization micro-chamber containing the larva for delivering a mixture of CO_2/air that completely immobilizes the animal. The immobilization micro-chamber is dimensionally similar to the SI-chip and is separated from the CO_2 micro-chamber by a 10 µm thick PDMS membrane. CO_2 can diffuse through this gas permeable membrane into the immobilization micro-chamber. Furthermore, since CO_2 is supplied under moderate pressure (5 psi) to the LI-chip, the membrane separating the two micro-chambers deflects and collapses onto the larva body thereby applying a mechanical pressure on it. The LI-chip has food ports in the form of two microfluidic channels that are connected to the immobilization micro-chamber through which food maybe introduced to maintain the larva in between imaging sessions over several hours [1].

Although good immobilization results were obtained with the SI chip that mechanically compresses the larva against a coverslip while imaging with a very simple setup, only 3rd instar larvae were accommodated with poor long term survival. While younger larvae were poorly immobilized, older larvae did not fit inside the chip. The LI chip on the other hand was able to accommodate larvae of all ages due to the presence of the flexible membrane which is a significant advantage over the SI chip. However, CO_2 is known to negatively impact animal physiology over long exposures. While both devices significantly reduced movement compared to freely moving larvae, the level of immobilization was not satisfactory for imaging internal structures located deeper inside the larvae. Frequent, small body movements did not allow high spatial resolution imaging of subcellular structures (such as mitochondria at neuro-muscular junctions and axons) inside the larval body [1].

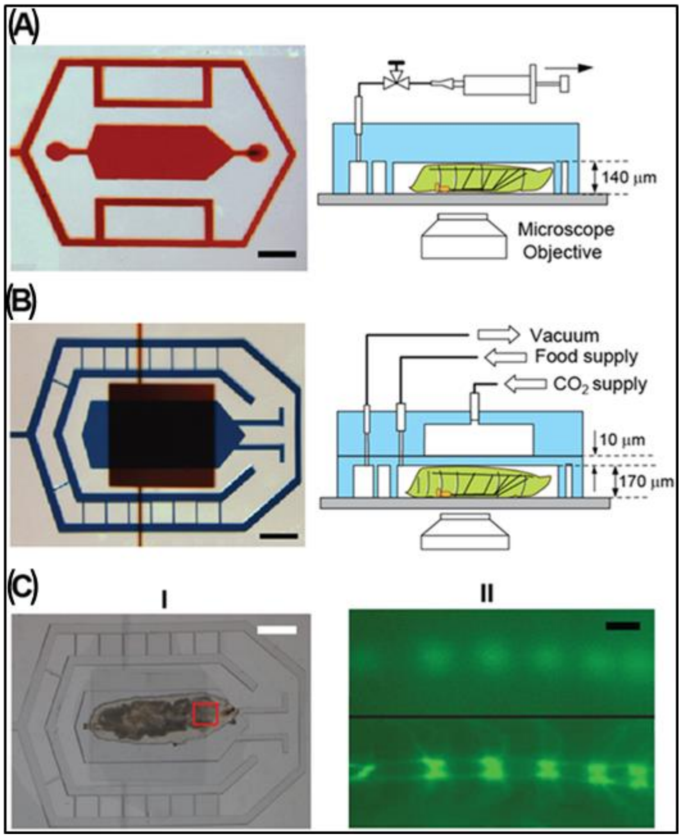

Figure 7.3: The Short-term Immobilization (SI) and Long-term Immobilization (LI) microfluidic chips for immobilizing *Drosophila* larva. (A) The SI-chip is a single-layer PDMS microfluidic device that utilizes a 140 µm thick immobilization microchamber to mechanically fix individual 3rd instar larve in the vertical direction. (Scale bar, 1 mm.) (B) the two-layer LI-chip. The first PDMS layer (labeled with blue color) has the larva immobilization microchamber (thickness 170 µm) and is connected to two microfluidic channels to supply food to the larva (typically delivered every 30 minutes). A second PDMS layer (labeled with red color) is vertically integrated on top of the first PDMS layer to deliver CO_2 through a 10 µm thick gas permeable, flexible PDMS membrane. In both the SI and LI chips, a microfluidic network surrounding the immobilization chamber is used to create a tight but reversible seal between the PDMS and the glass coverslip. (Scale bar, 1 mm.) (C) (I) Bright-field microscope image of a 3rd instar larva immobilized in the LI-chip. (Scale bar, 1 mm.) (II) Fluorescent images of the larval body (highlighted in the red square in C(I)) before (top image) and after (bottom image) immobilization. After application of CO_2 at 5 psi, the larva is immobilized and the GFP-labeled Ventral Nerve Cord (VNC) is brought into focus (bottom image). (Scale bar, 20 µm.) [Figures and captions appears in and are taken from **[1]**]

Fluid pressure immobilization: Mondal *et al.* [268] developed a two layer, membrane based microfluidic device to acquire imaging data at the millisecond time scale of GFP-tagged proteins on various cargoes at the sub cellular level. By immobilizing larvae expressing fluorescently labeled mitochondria, the researchers were able to monitor mitochondrial transport in live, unanesthetized animals.

To develop this method, they used a water column instead of gas to apply mechanical pressure on the larval body. Even though fabrication of the device involves two layers of polydimethylsiloxane (PDMS), it does not require sensitive alignment nor cleanroom facilities. The larvae are fed manually into the microfluidic chip without complex flow valves making this method very easy to implement. Due to the bilayer, membrane based architecture, the same device maybe used for accommodating all larval developmental stages. Additionally, the same device architecture was used to successfully immobilize *C. elegans* and observe vesicle transport in mechanoreceptor neurons (Figure 7.4). The operation of the device is shown schematically in Figure 7.4. However, the loading process is tedious and the larvae have to be squeezed against the microfluidic walls which can negatively impact their survival due to excessive mechanical stress.

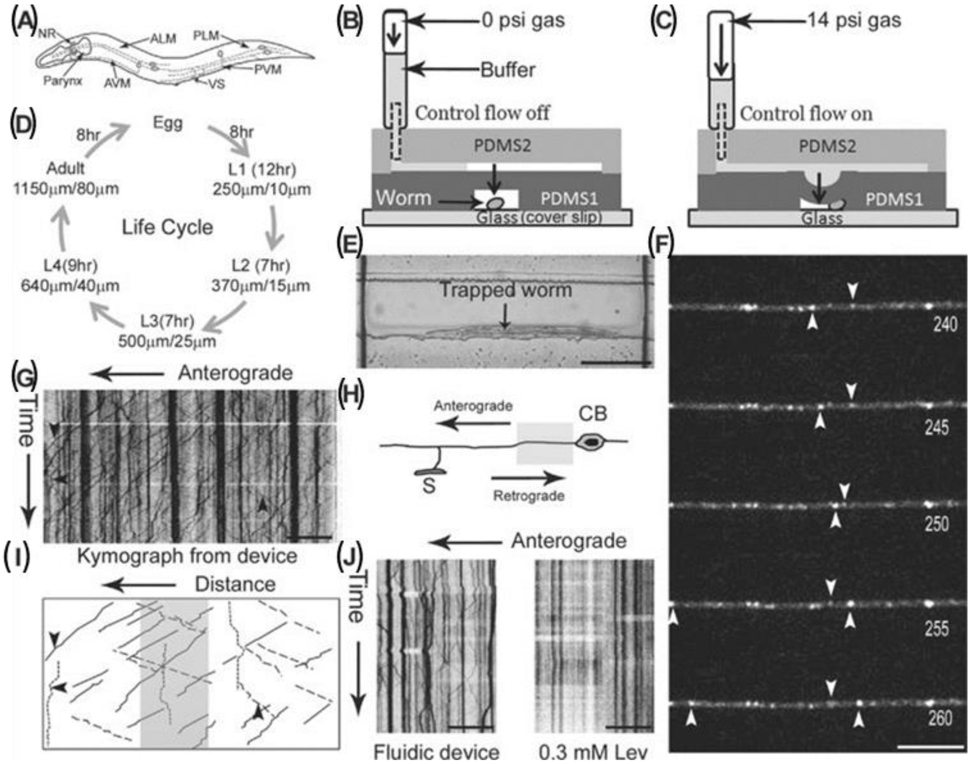

Figure 7.4: Imaging of GFP:RAB-3-marked vesicle transport in 1-day adult *C. elegans* mechanoreceptor neurons in a microfluidic device. (A) GFP::RAB-3 movement was imaged in the posterior lateral touch neuron (PLM) out of the six touch neurons [PLM, anterior lateral touch neuron (ALM), posterior ventral touch neuron (PVM), anterior ventral touch neuron (AVM)]. (B) and (C) Schematic of PDMS membrane device used for *C. elegans* immobilization. A deflected PDMS membrane using 14 psi nitrogen gas in the control channel in the PDMS 2 layer was used for immobilizing *C. elegans* present in the flow channel in the PDMS 1 layer. (D) Shows life cycle of *C. elegans* with the associated body length and body diameter in parenthesis. L stands for Larva. (E) Bright field image of a 1-day adult worm immobilized in a PDMS device. (F) Montage of five successive frames acquired at 5 fps with the frame numbers mentioned in each image. Anterograde (solid 'down' arrowhead) and retrograde (solid 'up' arrowhead) moving vesicles can be clearly seen in the neuronal process (cell body on the right side). (G) The image stacks (250 frames are shown) are analyzed using kymograph plugins of IMAGEJ to visualize particle displacement over time. (H) Schematic representation of a neuron with a 120 µm shaded region near the cell body with anterograde and retrograde movements indicated. I) Representative contours for anterograde (solid 'down' arrowhead), retrograde (solid 'up' arrowhead) and stationary (solid 'left' arrowhead) particle tracks are plotted. The shaded box shows the 20 µm window that is used to calculate vesicle flux. (J) Kymograph of an L1 worm imaged in a microfluidic device and anesthetized using 0.3 mM levamisole (lev), respectively. Scale bar is 200 µm(E),10µm (G and J) and 5 µm(F). [Figures and captions appear in and are taken from **[268]**]

7.3 Immobilization approaches for *C. elegans*

In recent years many techniques, almost exclusively microfluidics based, have been developed in order to obtain on-chip worm immobilization. The most notable ones use cooling [269], compression or restriction [270] [239], CO_2 [270] and gelation of the surrounding fluid [271] to immobilize the nematodes. In the following paragraphs, these techniques will be briefly presented followed by a discussion of their advantages and disadvantages [244].

Temperature induced on-chip immobilization: K. Chung *et al.* [269] developed a device (Figure 7.5) that created a cold micro environment (nematodes are cooled down to ~ 4 °C) to immobilize individual worms while providing automated manipulation and observation [244].

The device design comprises of a PDMS microfluidic chip with valves that are built-in in order to control the flow of nematodes that are suspended in solution. An algorithm performs high throughput image acquisition, analysis and worm sorting without any human intervention. Prior to reversible and short term cryo-immobilization, the worms are individually loaded into the chip by applying a constant pressure-driven flow. Once immobilized, a high resolution scan is obtained before phenotyping and sorting takes place. The images/videos that are acquired during the imaging session are then stored for further analysis. After imaging, the nematode is flushed out and a new animal is loaded on the chip [244].

Conventional soft lithography replica molding method is used for fabricating the microfluidic chip, which consists of two layers, one for regulating flow and the other for controlling temperature. The two layers are bonded together but separated by a 20 µm thick, flexible membrane. The device is bonded to a glass cover slip via oxygen plasma treatment. The worm loading process is automatically regulated by a built-in system which ensures that just a single worm is present inside the imaging chamber at a time. An automated positioning system places individual animals in the same location inside the chip with a high degree of precision. In order for immobilization to take place, the temperature around the animal needs to be controlled which is provided by a cooling system (Figure 7.6). The setup is fully compatible with any standard microscopy equipment and demonstrates high throughput and sorting efficiency. Since this method does not use any chemical anesthetic, any potential side effects of drugs use are eliminated. However, despite the many advantages presented by this method, its design is very complicated and requires a fairly elaborate setup consisting of cooling units, several control valves along with an air gas cylinder thereby making its implementation expensive and replication tedious [244].

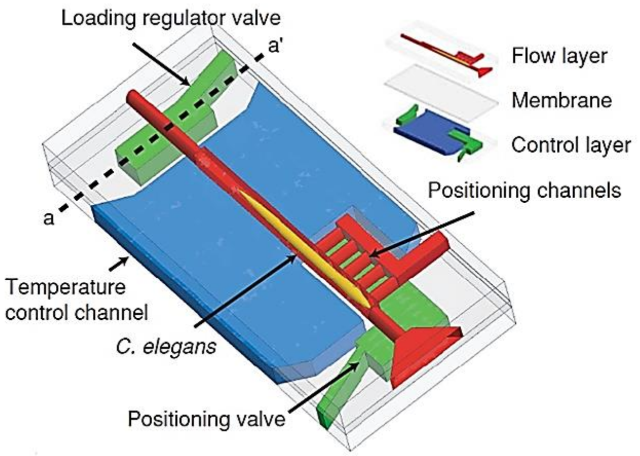

Figure 7.5: Schematic of the device showing 2 layer architecture and nematode placement. [Figure and caption appear in and are taken from **[269]**]

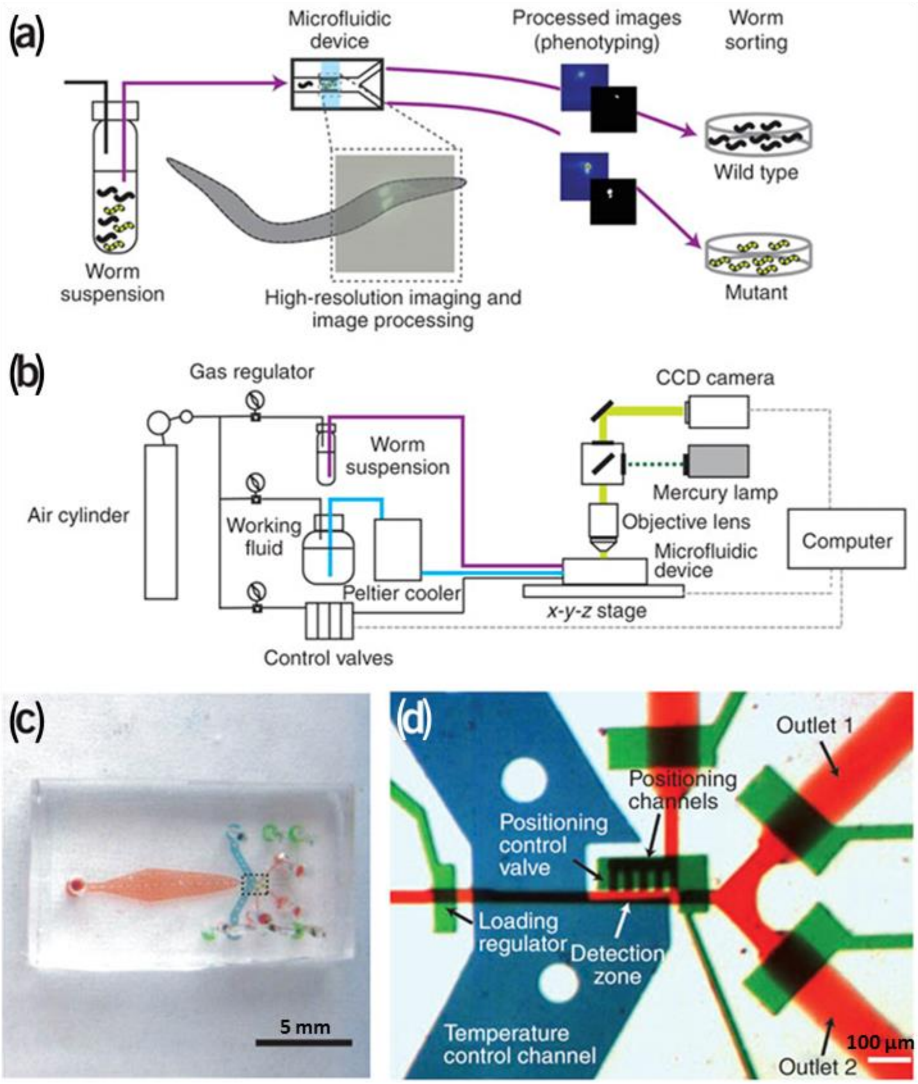

Figure 7.6: Schematics of the immobilization system and the microchip. (a) A mixed population of worms is injected into the device, worms are imaged, phenotyped and then sorted automatically. (b) System block diagram showing the on-chip and off-chip components and their connections. (c) Photograph of the microdevice. (d) Optical micrograph of the microchip's active region (boxed region in c). The channels were filled with dye to show specific features: blue - temperature control channel; green - valves; and red - sample-loading channel. (d). [Figures and captions appear in and are taken from **[269]**]

<u>Carbon dioxide immobilization:</u> The method developed by Chokshi *et al.* [270] for immobilizing *C. elegans* uses a microfluidic chip that creates a CO_2 micro environment around an individual nematode inside of an immobilization chamber. With the animal inside the chip, body movements are inhibited over extended periods of time (~ 2 hours). No lasting mechanical damage was observed with this method. Moreover, once CO_2 flow is cut off, the worms demonstrated quick recovery (within a few seconds) [244].

The device employs the popular two layer architecture (Figure 7.7) and has two modules. The behavior module, consisting of a saw shaped microchannel, revitalizes the animal after immobilization by mechanically stimulating it to move in a sinusoidal pattern. The immobilization module, consisting of two layers – an upper control layer and a lower flow layer separated by a flexible PDMS membrane, restricts movement during imaging once CO_2 is introduced into the control layer and diffused into the flow layer through the membrane. Additionally, worm loading is automated through a set of valves and control channels (Figure 7.7A) [244].

This technique can achieve long periods of immobilization making extended microscopic imaging possible. The lack of oxygen in the immobilization chamber due to CO_2 flow reduces photobleaching of fluorescent markers which further supports the applicability of this method for long-term fluorescence imaging experiments. Furthermore, due to the PDMS membrane, the chip can accommodate worms of different age groups - L4's to adults. However, even though this method effectively immobilizes worms for high magnification imaging without any supposed permanent damage, the physiological effects of CO_2 exposure on many cellular processes remain uncharacterized. Additionally, animals cannot be cultured and grown on-chip. *C. elegans* still need to be maintained on agarose plates external to the chip and must be serially loaded onto the device in order to perform imaging which subjects them to mechanical stresses. Furthermore, due to the device architecture, only one animal can be imaged at a time thereby not allowing the simultaneous observation of an entire nematode population [244].

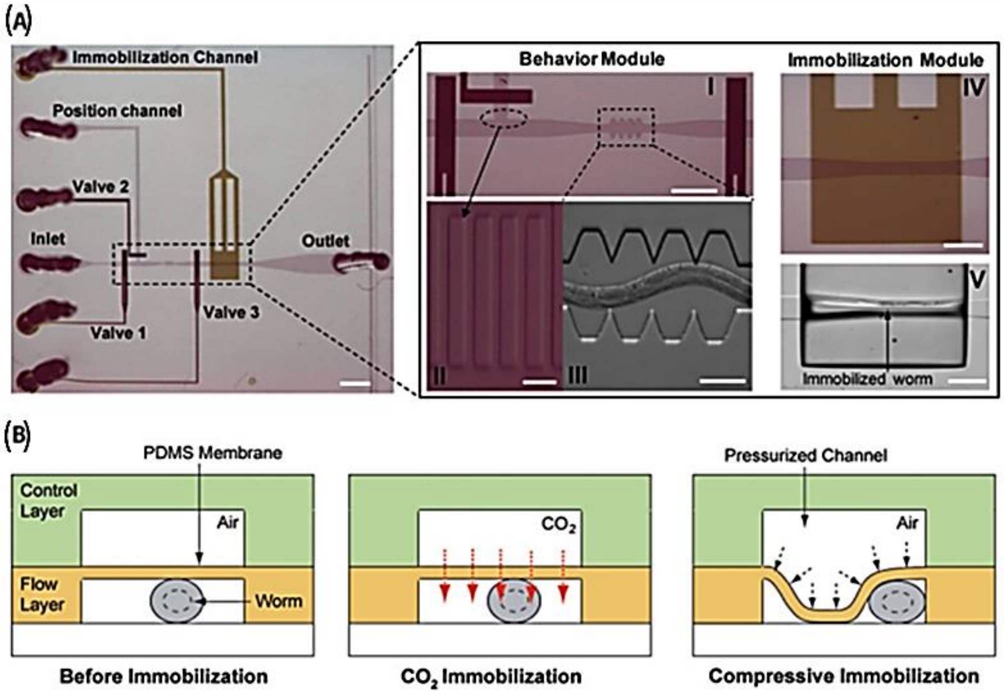

Figure 7.7: (A) The microfluidic device consists of the behavior (I, II and III) and immobilization modules (IV and V). The saw shape channel (III) is used to revitalize the worm post immobilization and to quantify on-chip the worm's locomotion pattern. PDMS pillars (II) do not allow the worm to enter the position channel. When high pressure (25 psi) is applied to the immobilization channel the worm is mechanically compressed on the microfluidic sidewalls (V). Scale bar, 1 mm (left picture). Scale bars are 300 mm, 500 mm, 10 mm, 100 mm, 300 mm for pictures I–IV respectively. (B) Immobilizing the worm by passing a CO_2 stream or by mechanically pressurizing the immobilization channel (control layer). [Figures and captions appear in and are taken from **[270]**]

Mechanical immobilization with microfluidic array of clamps for trapping: S. Elizabeth Hulme *et al.* [239] developed a microfluidic system that mechanically traps a large number of worms (>100) and enables biologists to observe entire worm populations simultaneously. Consisting of an array of wedge shaped channels (Figures 7.8 and 7.9) called clamps, each channel traps a single worm by physically restricting its movements [244].

The device architecture consists of a network of channels that feed into an array of clamps. The worms are driven into these clamps by a constant pressure flow. Once a worm is trapped, the fluidic resistance of the clamp channel is increased. Therefore, when another worm arrives at the junction of the same channel, it will not follow the same path as the previous worm which means that the device can load a given clamp with only one worm at a time. There is also no control over the orientation of the worm while it is loaded into a clamp. Upon completion of imaging, the flow is reversed to release them from the clamps which allows the same population to be viewed multiple times. Since they are mechanically immobilized, the normal physiological state of the worms is not affected. Additionally, since the clamps taper gradually, worms of different sizes maybe accommodated in the same clamp. Furthermore, this design feature can be used to analyze the size distribution in a population. It must be noted that the device design requires the application of constant pressure. If constant flow is applied instead, the resultant unbounded increase in pressure would cause permanent mechanical damage to the nematodes [244].

This technique therefore reversibly immobilizes a large population in a short period of time (~15 min) without using any chemical anesthetics making it a high throughput method. Moreover, its microfluidic platform makes the incorporation of further improvements/new features relatively easy. Finally, as an ordered array of immobilized worms is created, data acquisition maybe further automated with a motorized microscope system. However, despite these advantages, animals cannot be cultured and grown on-chip. *C. elegans* still need to be maintained on agarose plates external to the chip and must be loaded onto the device in order to perform imaging thereby subjecting the animals to multiple rounds of mechanical stress especially if time lapse imaging is performed [244].

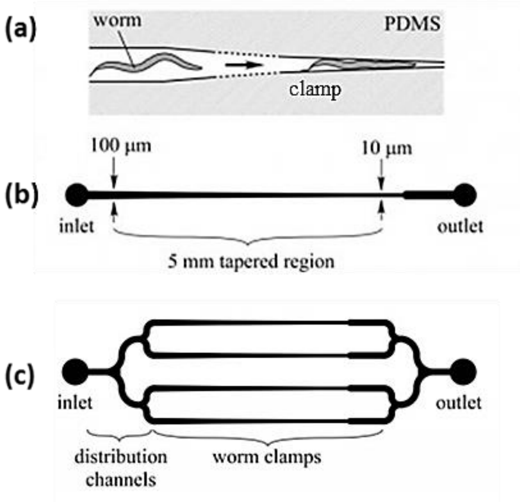

Figure 7.8: (a) Schematic illustration of the microfluidic worm clamp. The worm clamp consists of a tapered microfluidic channel in a slab of PDMS that is designed to physically restrain the motion of a worm. A pressure difference applied across the inlet and outlet drives the flow of liquid containing worms through the device. The resulting pressure-driven flow carries the worm into the wedge-shaped microchannel (the clamp) until the worm fits snugly within the channel. (b) Design of an individual worm clamp. (c) Design of an array of four worm clamps. The array is designed such that, on average, one worm is sorted into each clamp. [Figures and captions appear in and are taken from **[239]**]

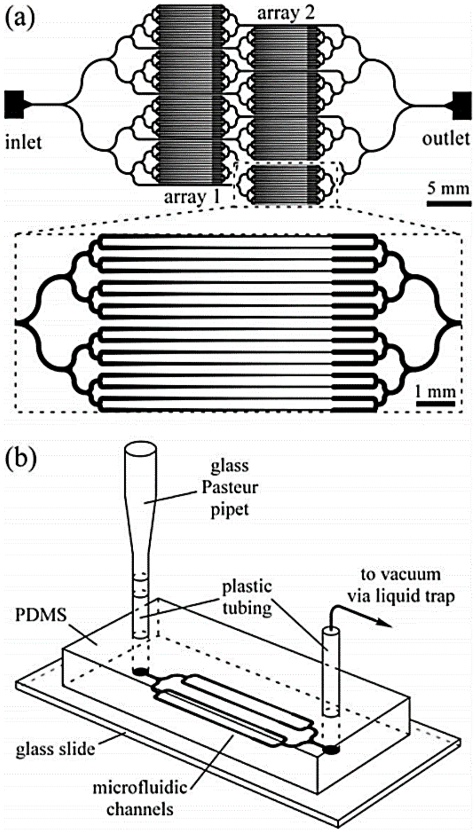

Figure 7.9: The worm clamp microfluidic device. (a) Design of an array of 128 worm clamps. The inset is a magnified view of the array showing 16 out of the 128 clamps. (b) The experimental set-up for the worm clamp device. Devices are made out of PDMS using soft lithography. An inlet reservoir is constructed by connecting a glass Pasteur pipette to the inlet of the device using a 2 cm long piece of polyethylene tubing. The inlet reservoir provides a loading point for introducing a fluid suspension of worms into the device. Connecting polyethylene tubing at the outlet of the device to a source of vacuum (295 kPa, or 20.94 atm, relative to the atmosphere) through a liquid trap (not shown) creates a pressure difference across the device, and produces the flow of worm containing liquid through the microfluidic device. [Figures and captions appear in and are taken from **[239]**]

Compressive immobilization: Chokshi *et al.* [270] developed a variation of the CO_2 method employing the same two layer PDMS chip structure. In this method, a high pressure (25 psi) air flow deflects the membrane which mechanically compresses the worm in order to immobilize it (Figure 7.7) [244].

In order to optimize the compression effect in order to minimize movement, the membrane was made more deformable compared to the membrane used in the CO_2 device. This was achieved by increased the PDMS to curing agent ratio while fabricating the membrane [244].

Chemical free immobilization, ease of manufacturing and implementation are the primary advantages of this method. Moreover, the same device can be used to immobilize animals of different ages. Additionally, worms maybe quickly and easily loaded serially thereby increasing throughput. However, a shortcoming of this method is the rather short (few minutes) immobilization time achievable compared to the other techniques. Additionally (and similar to the CO_2 method), animals cannot be cultured and grown on-chip. *C. elegans* still need to be maintained on agarose plates external to the chip and must be serially loaded onto the device in order to perform imaging. Furthermore, due to the device architecture, only one animal can be imaged at a time thereby not allowing the simultaneous observation of an entire population [244].

Chip-Gel Hybrid Immobilization: If worm morphology or phenotype needs to be investigated, then the methods that have been described until now would work very well. However, techniques like the cryo-immobilization method do not enable imaging of physiologically active processes as cooling down the animal would hinder these processes by significantly slowing them down. The compressive/mechanical methods, though usually effective and easy to implement, induce shifts in anatomical features which can disrupt imaging. Hang Lu *et al.* [271] tried to overcome these issues by developing a microfludic chip that houses a gel system to allow for long term high resolution imaging of biological processes at normal physiological conditions. Specifically, the device enables the growth, culture, immobilization and imaging of a nematode on the same chip as well as at the same time [244].

The worms are reversibly immobilized using Pluronic F127, a commercially available biocompatible polymer. The polymer undergoes a reversible thermally induced sol-gel transition when the temperature is shifted by ~2 ^{0}C. In its gel state, the viscosity increases and is high enough to prevent any nematode body movements [244].

The microfluidic device design incorporates the well known PDMS-based two layer chip (Figure 7.10), where the two layers are bonded together and separated by a thin PDMS membrane. One of the layers is for loading and controlling flow, whereas the other one is for delivering temperature control to the chip. A distinct advantage of this method is that worms maybe cultured on chip. Each chip consists of 8 culture chambers that provide nutrition as well as gas supply to the worm in each chamber. Given that these chambers keep animals separated, development of individual animals can be tracked easily through time. Flow inlets makeup the flow layer which is responsible for worm loading as well as supplying PF127. The pneumatic valves prevent the nematodes from escaping from the culture chambers. The temperature control layer triggers the transition of PF127 on the device by regulating flow of a heating fluid with a constant source temperature [244].

Given the principle of operation of this method, immobilization can take place anywhere in the chamber with no dependence on worm placement. Also, up to 8 worms maybe immobilized reversibly and for an undefined number of times for long durations without anything interfering with their biological functions. However, despite these significant improvements over other techniques, this method continues to have several disadvantages. Even though it claims to allow imaging multiple nematodes at once, only 8 animals maybe imaged at a time. If there is a need to increase throughput, enabling the device to accommodate more than 8 animals at a time will require significant modifications to design as well as increased fabrication effort, given the relatively complicated architecture. Additionally, the setup is also complicated as it employs several control valves as well as heating/cooling elements making the implementation of this method costly and its replication tedious. Furthermore, the fact that the polymer fluid needs to be flowed into and flushed out of the device chambers increases procedure time and reduces throughput [244].

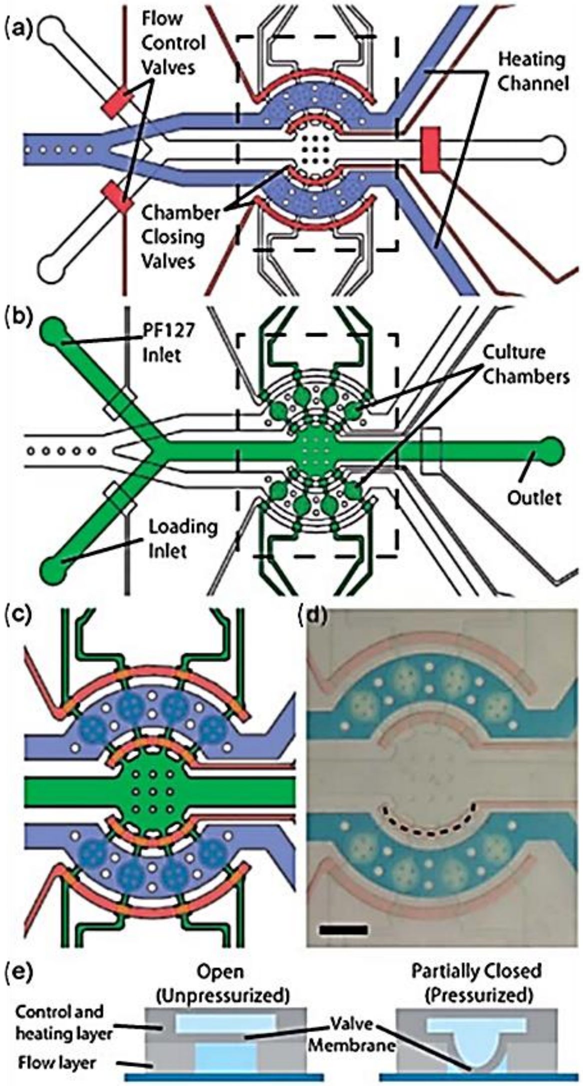

Figure 7.10: Two-layer microfluidic device used for chip-gel hybrid platform. The flow control and heating layer (a) contains pneumatic valves (shown in red) for flow control and trapping of worms inside chambers of the flow layer, as well as the channel used for flowing heating liquid (shown in blue). The flow layer (b) contains the loading inlet (for worms and bacterial solution) and an inlet for the PF127 solution, 8 culturing chambers for individual culture of worms, and a waste outlet. Design details of the chambers are depicted in (c); and a photograph of a dye-filled device is shown in (d); both correspond to the areas marked by dashed line rectangles in (a) and (b). The schematic in (e) represents the cross section of a partially closed valve, such as the one marked by a dashed line in (d). While unpressurized, the valve remains open. After pressurization, the valve membrane deflects into the flow layer, partially obstructing the channel. This prevents worms from escaping while allowing flow to continue. Scale bar represents 400 mm. [Figures and captions appear in and are taken from **[271]**]

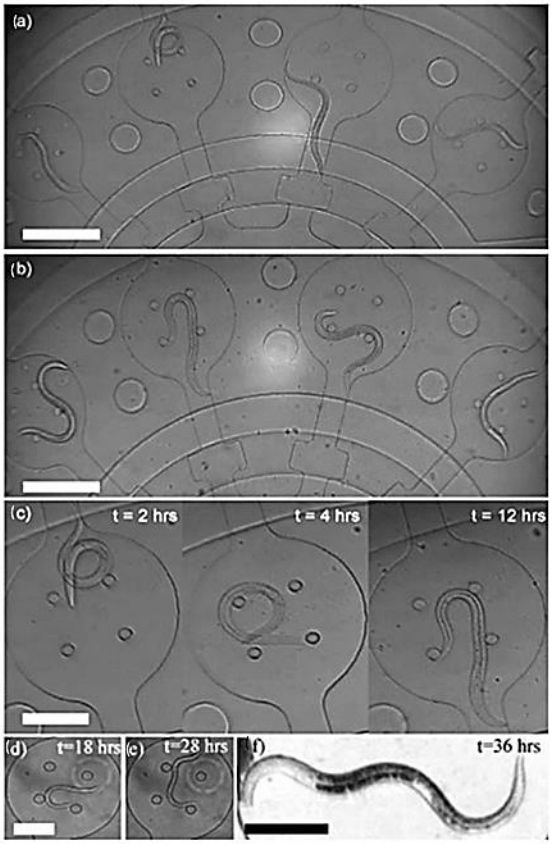

Figure 7.11: To culture worms long-term, they were loaded into the microfluidic device and trapped individually inside culture chambers (a), where they can remain for 12 hours (b). Worms are provided with bacterial food, allowing them to grow and develop normally (c). To demonstrate the ability of the device to culture worms long term, they were maintained from early L1 to L3 stage (d–f) where L stands for Larva. (d–e) show a worm during the L2 stage at 18 and 28 hours after hatching and loading; (f) shows an L3 worm at 36 hours past hatching. Scale bars represent 200 mm in (a–b) and 100 mm in (c–f). [Figures and captions appear in and are taken from **[271]**]

7.4 Conclusions

In this review chapter, the most notable methods - the majority of which happen to be microfluidics based systems - for immobilizing *Drosophila* larvae and *C. elegans* have been presented along with a discussion on each of their advantages and disadvantages. Conventional immobilization methods (glue or chemical anesthetics drugs) are time-consuming, labor intensive, and also potentially toxic in comparison to these alternative systems. With recent advancements in 3D printing, soft lithography replica molding has become significantly cheaper as the molds can now be 3D printed. However, there is no 3D printed device that maybe used as a standalone system to immobilize *Drosophila* larvae or *C. elegans*. The review also emphasizes the advantages of exploiting microfluidics, which is the primary technology that has been developed for immobilizing small model organisms.

This review chapter discusses the recent development of novel devices and systems have emerged for immobilizing *Drosophila* larvae. Many research groups have developed microfluidic devices that immobilize un-anesthetized larvae with the primary approach being the application of pressure to mechanically restrict movement. However, the majority of these device have complicated designs making their fabrication and implementation challenging. Additionally, either their architecture do not generally accommodate animals of all age groups or they have a tedious animal loading process. Moreover, while these methods significantly reduced movement compared to freely moving larvae, the level of immobilization is not satisfactory for imaging internal structures or structures that are only a few microns in size due to frequent, small body movements. Therefore, there exists a need for a method that is simple to use, easy to implement and allows for high spatial resolution imaging of subcellular structures located deeper inside the larval body.

For immobilizing *C. elegans,* all of the methods that have been reviewed provide good results by minimizing animal movement. However, the CO_2 method (Chokshi *et al.*, 2009 [270]) provides the best trade off in terms of being relatively easy to manufacture while providing superior quality of immobilization. The method demonstrates that CO_2 affects movement and minimizes it sufficiently in order to allow high resolution imaging of cellular and sub-cellular events . Furthermore, the fact that the method ensures quick recovery indicates that animal physiology is not permanently damaged. The chip has the popular two layer architecture that has a simple design and is easy to manufacture. Additionally, the same chip maybe used for both compressive (short term) as well as CO_2 (long term) immobilization, depending on the requirements of the biological study while being able to accommodate worms of all ages. However, the chip cannot be used to image more than a single worm at a time thereby making population studies impossible. Moreover, as the worm cannot be cultured on chip, animals need to be transferred back and forth from the culture plates to the chip thereby subjecting them to cycles of mechanical stress that might negatively affect their development. Therefore, there exists a gap for a method that takes advantages of the benefits of CO_2 induced immobilization to simultaneously image an entire population of worms without disturbing them from the culture medium. The method must also be easy to use and cheap to implement.

In conclusion, the mechanism of immobilization and fluidic device design that is selected would ultimately depend on the requirement of the specific end application. For instance, for imaging very small features, the method must provide absolute immobilization. If sorting post imaging is required, the device must be designed by taking flow control into consideration. Functional imaging of processes occurring in real time would require imaging under normal physiological conditions. Finally, all designs should ensure that the chosen immobilization scheme, whether it is temperature, CO_2 or mechanical pressure, does not significantly alter the biological features of interest/ process under study.

CHAPTER 8

ON CHIP CRYO-ANEASTHESIA OF *DROSOPHILA* LARVAE FOR HIGH RESOLUTION IMAGING APPLICATIONS

8.1 Introduction

Drosophila melanogaster is a widely used organism for modeling human biology and diseases at the behavioral, cellular and molecular level [272] [212] [273]. The larval stage has a translucent cuticle and a simple neuroanatomy that is amenable to imaging [274] [275] [276] [277]. However, one of the biggest challenges associated with live imaging of *Drosophila* larvae is achieving an acceptable degree of immobilization which is required for observing cellular and sub-cellular events with high spatial, optical resolution without affecting the animal's physiology.

Current immobilization techniques include dissection [278] [279], the use of anesthetics [280] [281] or glue, and squeezing the larva's body [282]. Methods such as dissection are lethal, which therefore prohibits long term imaging. Glue is toxic, provides irreversible immobilization and is difficult to implement for very young animals. The use of anesthetics –such as isofluorane [11] [12] or desflurance [281] - has many advantages, but they are known to affect the animal's neurophysiology and neural activity [283] [284] [268]. Additionally, imaging must be restricted to short intervals in order to allow recovery between doses [284] [283]. Conventional anesthetics pose a threat to the user's safety and being regulated chemicals, require installing several safety components. The most popular mechanical immobilization techniques involves capturing the larva by flattening it between two microscope slides using light pressure, by placing water in between a coverslip and glass slide to hold the larva with capillary pressure [282], or by taping the larva onto a coverslip [285]. While these methods can be easily implemented, the degree of control is not ideal and the immobilization is not necessarily adequate in order to allow stable high resolution imaging of sub-cellular processes in all regions of the larvae. Furthermore, the imaging duration is limited and larval recovery can be difficult, if not impossible, if too much pressure is inadvertently used to flatten the animals [227]. In order to image reliably cellular/sub cellular events while maintaining proper body orientation over longer periods, an easy to use, reversible, low cost and chemical-free immobilization method is needed.

With the recent development of micromachining and soft lithography fabrication techniques [286] [287], novel microfluidic devices and systems have emerged for manipulating small organisms. Many research groups have developed microfluidic devices that immobilize un-anesthetized larvae. The microfluidic device developed by Yan *et al.* [267] immobilizes 3rd instar larvae using a mechanical microcompressor. While proving to be a versatile platform, it requires the use of complicated and expensive laser and CNC fabrication processes in addition to PDMS soft lithography. Ghaemi *et al.* [227] constructed two pneumatically-driven microfluidic devices to immobilize and perform calcium imaging in 3rd instar larvae. Although the principle of operation is simple and standard soft lithography fabrication techniques were used, the architecture of the devices is complicated and capable of accommodating only 3rd instar larvae. Mondal *et al.* [268] developed a microfluidic device that can immobilize larvae at different developmental stages, but the loading process is tedious and the larva have to be squeezed against the microfluidic walls. Ghannad-Rezaie *et al.* [1] developed microfluidic devices for short term imaging. The device mechanically compresses the larva against a coverslip while imaging. Although good immobilization results were obtained without the use of a complicated setup, the chip could accommodate only 3rd instar larvae. Younger larvae were poorly immobilized whereas older larvae did not fit in the chip. While the device significantly reduced movement compared to freely moving larvae, the level of immobilization was not satisfactory for imaging internal structures. Frequent, small body movements did not allow high spatial resolution imaging of subcellular structures (such as neuro-muscular junctions and axons) inside the larval body.

In this work, we present a temperature based immobilization approach for high resolution imaging of sub-cellular structures and processes in *Drosophila* larvae. Specifically, we developed a microfluidic chip that creates a cold micro-environment around the larval body while effectively anesthetizing it. The microfluidic chip will henceforth be referred to as the cryo-larva chip. The experimental setup is made up of commercially available, off the shelf parts making its assembly and replication straight forward. While cryo-anesthesia has been previously implemented by Chung *et al.* [288] and Rhode *et al.* [289] to immobilize other model organisms such as C.*elegans*, a system dedicated towards performing low temperature immobilization of *Drosophila* larvae for high magnification imaging has not been demonstrated until now.

The cryo-larva chip [290] can be used to study a wide variety of biological processes, including the transport of organelles and proteins at the cellular/sub-cellular level as well as neuro-synaptic growth demonstrated here. Using the chip, we observed mitochondrial trafficking in neurons and the developmental growth of synapses at the neuromuscular junctions (NMJs). Nearly all studies of mitochondrial transport in neurons have previously been conducted in isolated cells in culture, while observation of the developmental growth of synapses is often inferred from cultured neurons “aged” over the course of a few days. Our technology therefore provides a powerful alternative for studying those events within intact animals .

Apart from its demonstrated use for neurobiological studies, the cryo-larva chip based immobilization method can help many other fields of *Drosophila* biology, since it should also allow for imaging over time of the salivary glands, fat bodies, body-wall muscles, and other commonly studied larval organs. Additionally, with the popularity of the use of genetically-encoded fluorescent reporters, live tissue is often required to utilize many newly developed fluorescent probes that provide a readout of real-time cellular physiology which is abolished with dissection and fixation. Some examples include autophagy reporters (mCherry-GFP fusions that measure pH in autophagosomes) [291] [292], intracellular pH indications (pHluorins) [293] [294], various calcium reporters (including GCaMPs and CaMPARI) [295] [296], and ATP biosensors (ATeam and Perceval) [297] [298]. Our chip will allow such reporters to be now used in intact animals, and changes in these physiological readouts can be tracked and compared within different genetic and environmental manipulations.

8.2 The Microfluidic chip and the cooling system

The Microfluidic Cryo-Larva Chip. The proposed immobilization method incorporates a PDMS/glass microfluidic chip with a two-layer architecture (Figure 8.1). The first layer (‘Layer 1’) contains a 5.0 mm long, 1.6 mm wide and 170 µm thick immobilization microchamber which accommodates the larva. The immobilization microchamber is surrounded by a network of microchannels that is held under vacuum applied through the vacuum port. The vacuum creates a reversible and strong seal between the PDMS, oil, and glass coverslip holding the larva in place after it is manually loaded onto the chip. After imaging is completed, the vacuum is released and the larva can be easily removed from the chip. The chip has also two ports (indicated as ‘food inlet’ and ‘food outlet’ in Figure 8.1(a)) for providing food to the larva if needed. The second layer (‘Layer 2’), contains a 5.5 mm long x 2.8 mm wide x 100 µm thick microchamber (the ‘cooling’ microchamber) and sits on top of the immobilization microchamber. The two microchambers are separated by a 10 µm thick PDMS membrane. Chilled coolant fluid is passed under moderate pressure (~ 3 psi) through Layer 2 via the coolant inlet/outlet ports. This creates a low temperature microenvironment (~5 ^{0}C), while at the same time the PDMS membrane deflects and compresses the larval body against the glass coveslip. Even though the membrane semi-restricts large body movements, cooling the larva down to ~5^{0}C is the dominant factor that anesthetizes the larva body. This dual approach cryo-anesthesia and mechanical compression results in effective immobilization allowing stable, long term, high resolution imaging.

The height and overall dimensions of the immobilization microchamber are large enough to accommodate larvae of different developmental stages (1st instar to late 3rd instar). In order to achieve membrane deflections large enough to mechanically restrict the larva, a 15:1 mixing ratio was used for fabricating the first PDMS layer. This reduces the elastic modulus by a factor of ~ 2 [299] when compared to the 10:1 mixing ratio used for the second PDMS layer.

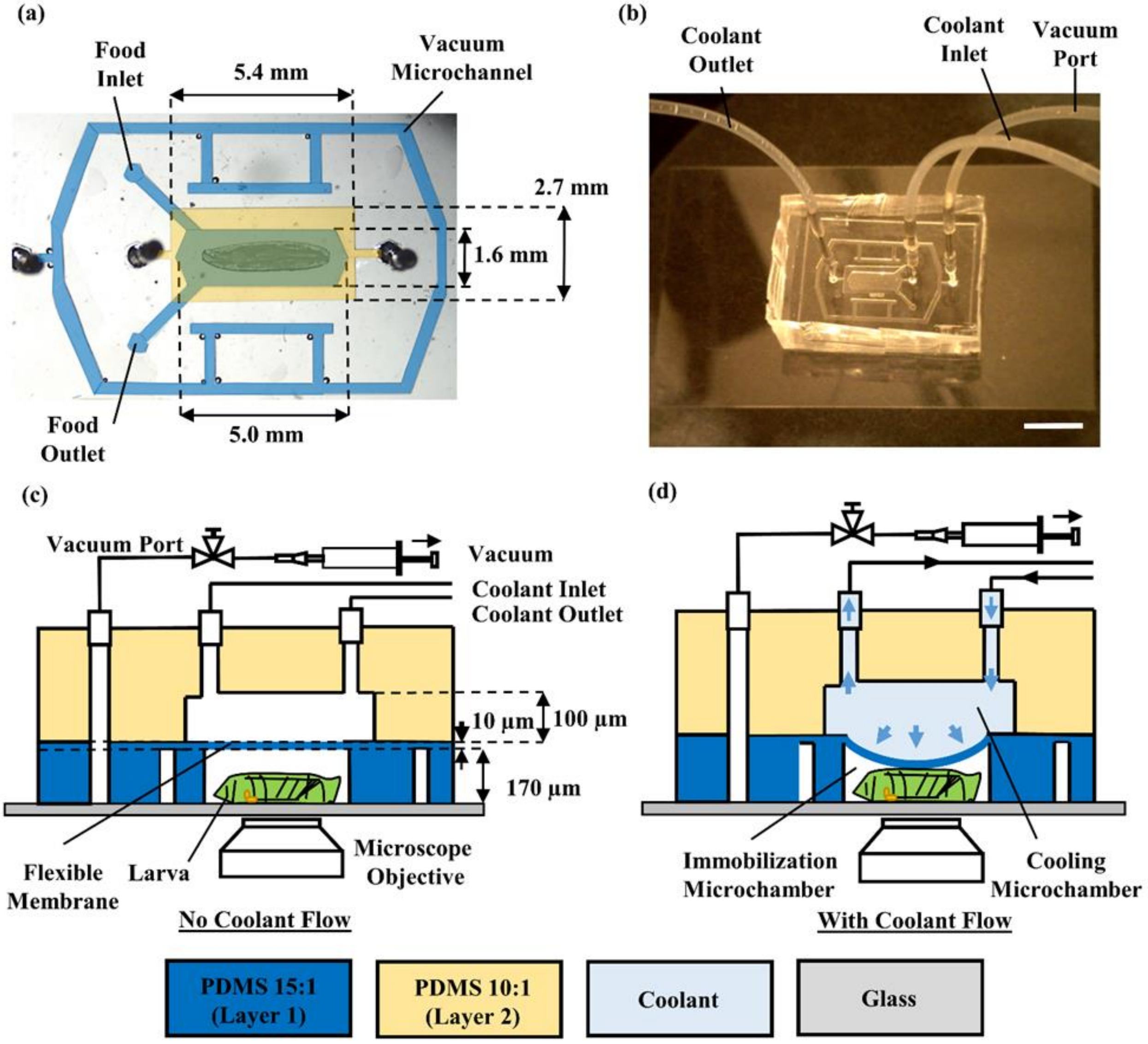

Figure 8.1: (a) Bright-field image of a 3rd instar larva immobilized in the microfluidic chip: The first and second PDMS layers are highlighted with blue color and yellow colors respectively. Passing the coolant fluid through the second layer decreases the temperature of the immobilization microchamber. (b) Stereoscopic image of the microfluidic chip (scale bar, 5 mm). (c) Cross sectional schematic of the chip that highlights its working principle. When there is no flow of the coolant fluid (left schematic), the larva freely moves in the immobilization microchamber (the PDMS membrane is not deflected). (d) When the coolant fluid is introduced, the larva is cryo-anesthetized and slightly compressed inside the immobilization microchamber.

The Cooling System**.** The microfluidic cryo-larva chip, that sits on the stage of an inverted microscope, is connected to a closed-loop, cooling system that consists of a peristaltic pump, a cooling module and a reservoir (Figure 8.2).

The peristaltic pump (GE P-1, GE Healthcare Life Sciences) circulates the coolant through the system.

The cooling module consists of two thermoelectric Peltier units (TEC1-12710, 50W), each mounted on an aluminum heatsink (41 mm x 41 mm x 13 mm), and a flow chamber that is sandwiched between the two Peltier units. A small fan is attached to each aluminum heatsink in order to remove the generated heat. The coolant leaves the flow chamber at a below-zero temperature and, after passing through the chip, returns to the closed reservoir

When immobilization is not required or the larva needs to be unloaded, the coolant is diverted away from the chip into the reservoir through a three port stopcock valve and bypass tube. Polyvinyl tubing is used for all fluidic connections. Silicone rubber tubing is used in the peristaltic pump. The length of tubing used is optimized to accommodate the cooling system around the inverted microscope while minimizing any parasitic heat gain (Appendix C, Figure C1).

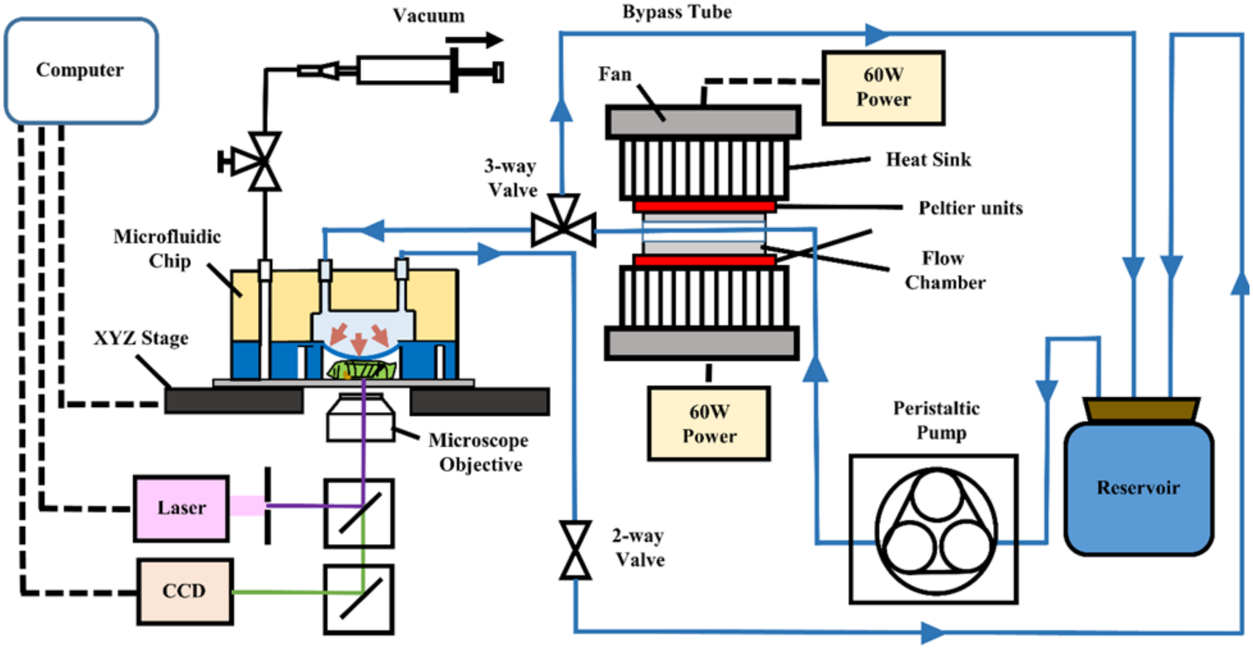

Figure 8.2: Schematic diagram of the experimental setup highlighting the components of the cooling system. The solid blue lines indicate coolant flow.

8.3 Results and discussion

8.3.1 Microfluidic chip and system characterization

We used an infrared camera (FLIR SC600) to obtain the temperature distribution within the chip. The average temperature of the immobilization microchamber was measured to be 5 ^{0}C ± 1°C at a coolant flow rate of 3.2 ml/min. (Figure 8.3), indicating a uniform temperature profile within the microchamber. Upon stabilization of the immobilization microchamber temperature to ~ 5^0C, the low-temperature environment was maintained over a period of several hours.

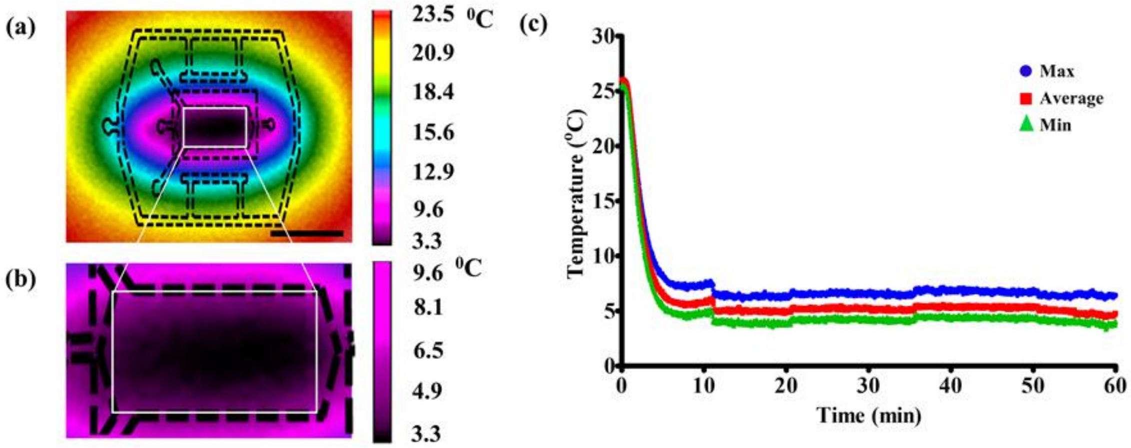

Figure 8.3: (a) Thermograph of the microfluidic chip at a coolant flow rate of 3.2 ml/min (viewed from the glass side). The dotted black lines indicate the outline of the chip (scale bar, 5 mm). The white rectangle represents the location of the immobilization microchamber. (b) Thermograph showing the temperature variation in the immobilization microchamber (~ 2.5 ^{0}C difference between the center and the sides). (c) Maximum, average and minimum temperature values obtained over the region bounded by the white rectangle shown in (a) versus time. The cooling modules are turned on and coolant flow (3.2 ml/min) through the chip starts at 0 sec with the average temperature stabilizing to ~5 ^{0}C in under 5 min.

A concentrated salt water solution (5M sodium chloride) was used as the coolant fluid. We used salt in order to eliminate freezing of the water (the coolant reaches below zero temperatures in the flow chamber). Additionally, it allows us to pre-cool the coolant before use (typically placed in a freezer at -10^0C for 1-2 hours). It was observed that the pre-cooling step reduced the response time needed for the temperature to stabilize by ~ 50%. (Appendix C, Figure C2). We define the response time of the system as the time needed for the temperature of the immobilization microchamber to reach 90% of its steady state temperature after the flow of the coolant has started. Increasing the flow rate of the coolant also reduces the response time (Figure 8.4) from ~ 2 minutes (at flow rate of 1.7 ml/min) to ~ 1 minute (at flow rate of 3.7 ml/min).

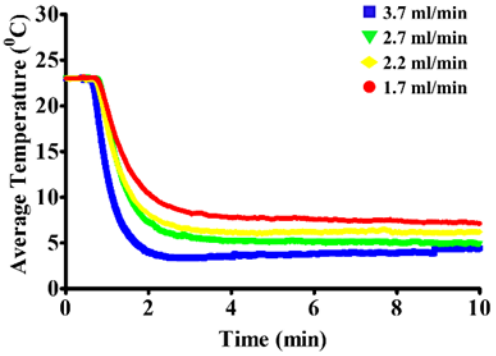

Figure 8.4: Average temperature of the immobilization microchamber versus time for different flow rates. Coolant flow through the chip started at 0 sec.

All experiments were conducted with the average ambient relative humidity maintained below 15% for optimal cooling. Higher humidity levels, especially above 50%, resulted in condensation on the tubing as well as on the cold surfaces of the Peltier modules that compromised the cooling performance of the system leading to reduced immobilization.

8.3.2 Time required for larval immobilization

An experiment was performed to quantify the dual effect of mechanical compression and cryo-anesthesia upon larval movement. Individual larvae were loaded into the chip and GFP-expressing neuronal cell bodies along the ventral nerve cord (VNC) were imaged (we used a confocal microscope at 250X magnification). A video where each frame is a single optical plane image (Section 8.4.4) was acquired for a total duration of 9 min (the flow of the coolant was turned on at 0.5 min and turned off at 5.5 min).

For each acquired frame, we selected the centroid of a cell body along the VNC that was visible in all frames in the video. The absolute distance moved by the centroid between consecutive frames was tracked over time using Metamorph software (Figure 8.5). Results show that with no coolant flow through the chip, the larvae were active and crawling in the immobilization microchamber. Once the coolant started flowing through the chip, rapid immobilization was observed with movement decreasing and stabilizing in under 3 minutes. As soon as flow was turned off, the larvae started to rapidly regain mobility inside the chip and recovered completely within 15 minutes after removal from the chip.

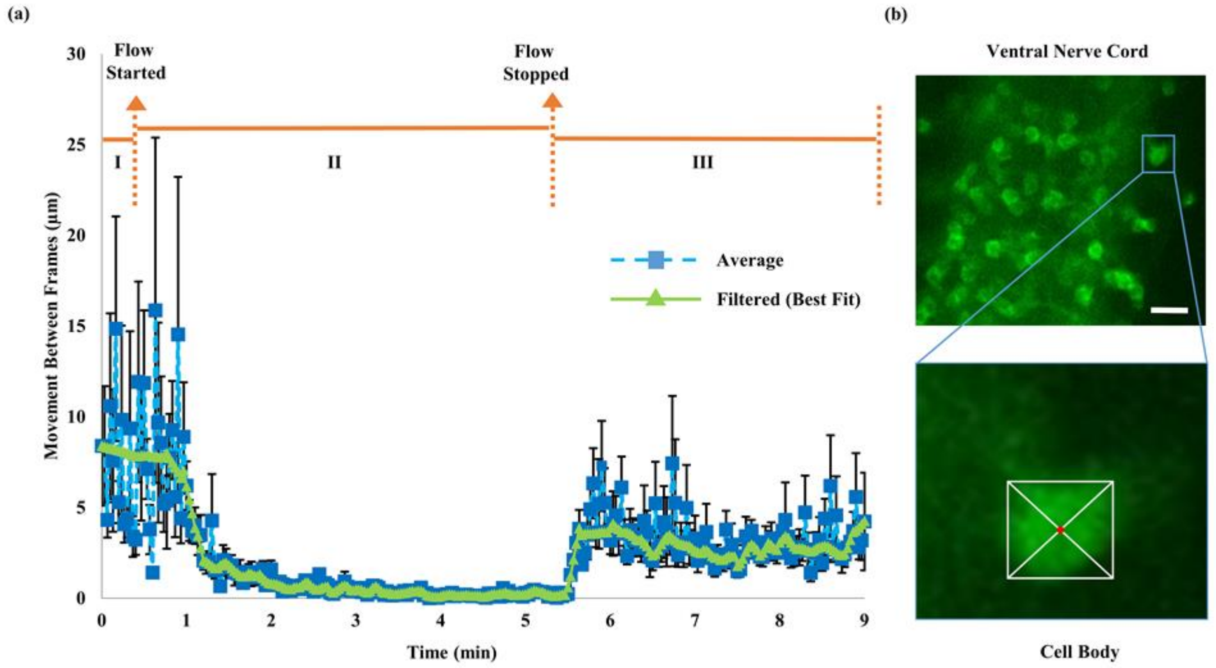

Figure 8.5: (a) Absolute distance moved by the centroid (point of intersection of the diagonals of the white box bordering the cell body and indicated as a red dot in (b)) of a cell body located at the VNC over time (acquired before (I), during (II) and after (III) immobilization). The dashed blue line represents average distance moved between frames for ten 3rd instar larvae. The solid green line represents best fit by non-parametric regression using locally weighted scatterplot smoothing. Error bars indicate standard error of mean of measurements taken from ten animals imaged on the same device. (b) A single frame showing the VNC and the centroid of a cell body (scale bar, 30 µm).

Furthermore, it takes ~ 1 min before any significant reduction in the body movement is observed. At that time point, the temperature has decreased to 10 ^{0}C (see Figure 8.4 for a flow rate of 3.2 ml/min) and the corresponding average body movement is ~ 5 µm (Figure 8.5). That result demonstrates that there is a correlation between the temperature of the immobilization microchamber and the magnitude of the body movement. We selected 5 ^{0}C as an optimum temperature at which body movements are negligible (< 0.5 µm) while chilling-induced injury is minimized.

8.3.3 Characterization of larval movement

To validate the proposed method we recorded the movement of various neuronal structures during immobilization under high magnification (400x).

Individual larvae were loaded onto the chip and pre-cooled coolant was placed into the reservoir. The flow rate was set to 3.2 ml/min and coolant flow through the chip was turned on.

After 4 minutes, a video where each frame is a collapsed z-stack of ~7 images of GFP-labelled neuronal structures of interest was collected over a 2 minute duration (Section 8.4.4) before diverting flow away from the chip using the bypass tube. Acquiring a collapsed z-stack of a focal volume within each larva instead of a single image of a focal plane allowed continuous observation of sufficient features of interest throughout the 2 minute period despite photobleaching effects and any potential movements along the z axis by the peristaltically deflecting membrane. To identify whether the low-temperature environment in the immobilization microchamber (4-6 ^{0}C) results in larval immobilization, a control experiment was performed with the coolant flowing through the chip without activating the Peltier units.

For every acquired frame, three features that were visible across all frames were selected; mitochondria within NMJ terminals, mitochondria within segmental nerve axons, and neuronal cell bodies within VNCs (Figure 8.6(a), (c)). The distance moved by the centroids of these features in between consecutive frames was estimated by tracking them over time and then averaged (Figure 8.6). Mitochondrial labeling was used for this analysis because the separated, distinguishable puncta (Figure 8.6) allowed for tracking of individual small features through time. Upon the initiation of coolant flow, we noticed that the pressure of unchilled coolant (still at room temperature) caused some reduction in larval movement. This is because the flexible membrane mechanically compresses the larva against the coverslip if there is coolant flowing through the chip, irrespective of coolant temperature. Additionally, mechanical compression aids optical access by bringing internal body structures close to the coverslip which are otherwise hard to observe. However, under the influence of purely mechanical compression, the larvae are not adequately immobilized to enable steady, high resolution imaging of sub-cellular structures necessary for performing neurobiological studies. The average movement of the neuronal structures was further minimized when chilled coolant was flowed through the chip (Figure(s) 8.6-8.8), thereby clearly indicating the immobilizing effect of cryo-anesthesia. This demonstrates that mechanical compression of the flexible membrane and the low-temperature environment act synergistically to promote larval immobilization. Imaging with the chilled coolant led to a significant improvement in imaging quality. Figure 8.7 shows the total trajectory of distances moved over a 2 minute duration, comparing chilled verses unchilled (at room temperature) coolant flow. The trajectories obtained with chilled coolant flowing through the chip are far more localized, further supporting the results shown in Figure 8.6. Histograms showing percentage of total number of movements occurring over a 2 minute duration (Figure 8.8) illustrate that immobilization of NMJs, VNCs and axons with the proposed method is predominantly due to the cryo-anesthetic effect of flowing chilled coolant through the chip. The probability density estimates fitted onto the histogram data (Figure 8.8) indicates that bigger movements (greater than one pixel) are much less likely to occur while imaging with chilled coolant use compared to with the control. Apart from having a larger spread of data points, the maximum distance moved was also larger while imaging all three neuronal structures for the control compared to with using chilled coolant as demonstrated by the box and whisker plots in Appendix C, Figure C3.

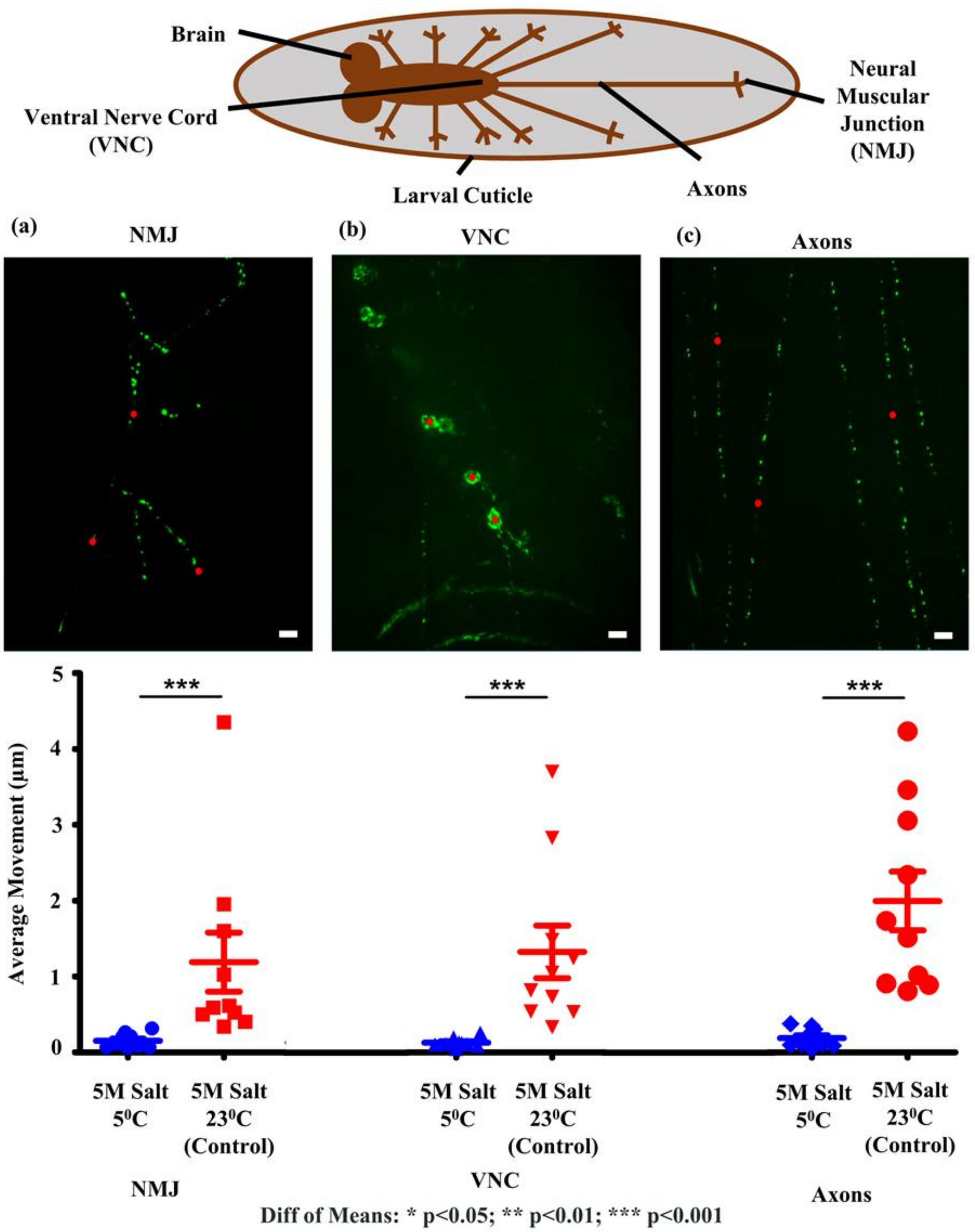

Figure 8.6: Schematic representation of larval neuronal structures of interest. Confocal micrographs showing fuorescently labeled: (a) Mitochondria at an NMJ with red dots representing centroids of individual mitochondria. (b) Cell bodies at the VNC with red dots representing centroids of individual cell bodies. (c) Mitochondria along axons with red dots representing centroids of individual mitochondria. Plots showing the average of distances moved by centroids of: (a) mitochondria at NMJs, (b) cell bodies along VNCs and (c) mitochondria along axons in between video frames collected over 2 minutes. The videos were collected with larvae loaded on the microfluidic chip with chilled as well as room temperature coolant (5M salt water) flowing (3.2 ml/min) through the chip respectively. Error bars indicate standard error of mean of measurements taken from ten larvae imaged on the same device. (scale bar, 11µm).

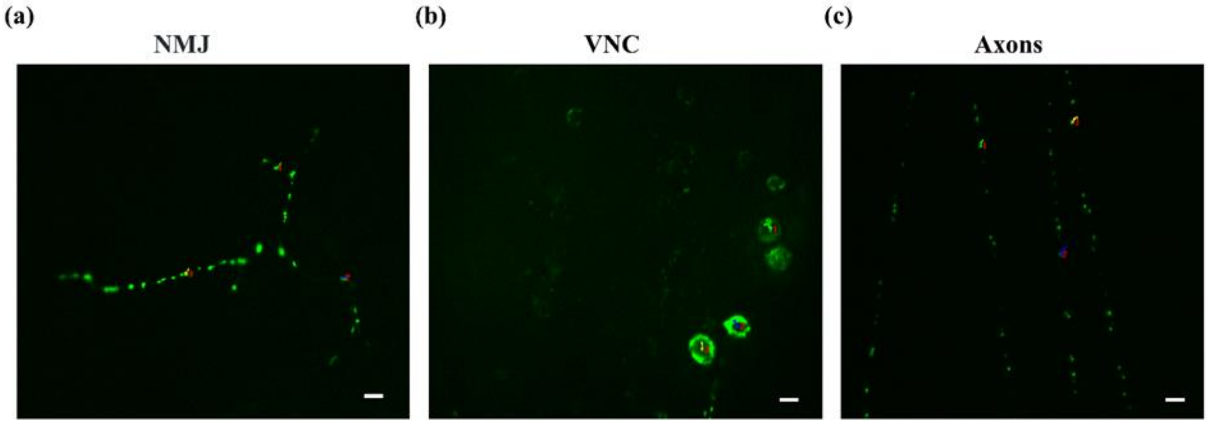

5M Salt at 5^{0}C **5M Salt at 5^{0}C** **5M Salt at 5^{0}C**

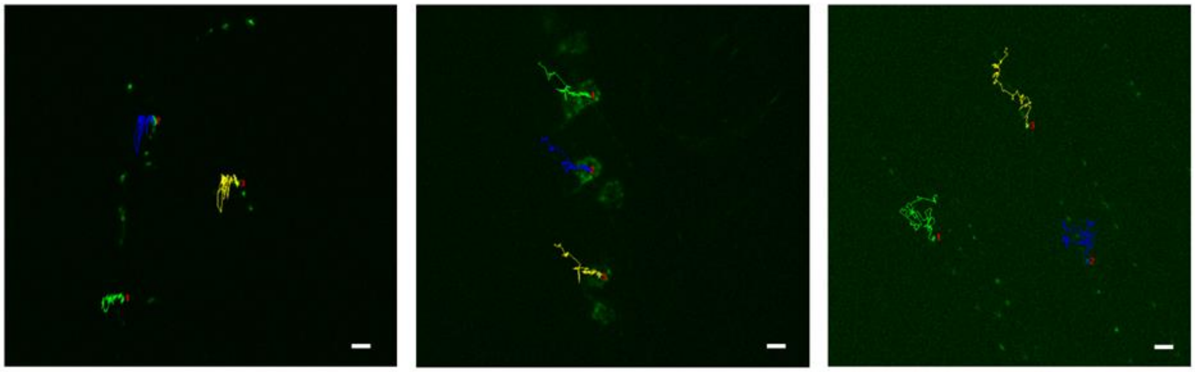

5M Salt at 23^{0}C (Control) **5M Salt at 23^{0}C (Control)** **5M Salt at 23^{0}C (Control)**

Figure 8.7: Confocal micrographs showing the trajectories (shown as green, blue and yellow paths and marked by red numbers) moved by three randomly selected centroids of (a) mitochondria at NMJs, (b) cell bodies along VNCs and (c) mitochondria along axons in between video frames collected over 2 minutes. The videos were collected with larvae loaded on the microfluidic chip with chilled as well as room temperature coolant (5M salt water solution) flowing (3.2 ml/min) through the chip respectively (scale bar, 11µm).

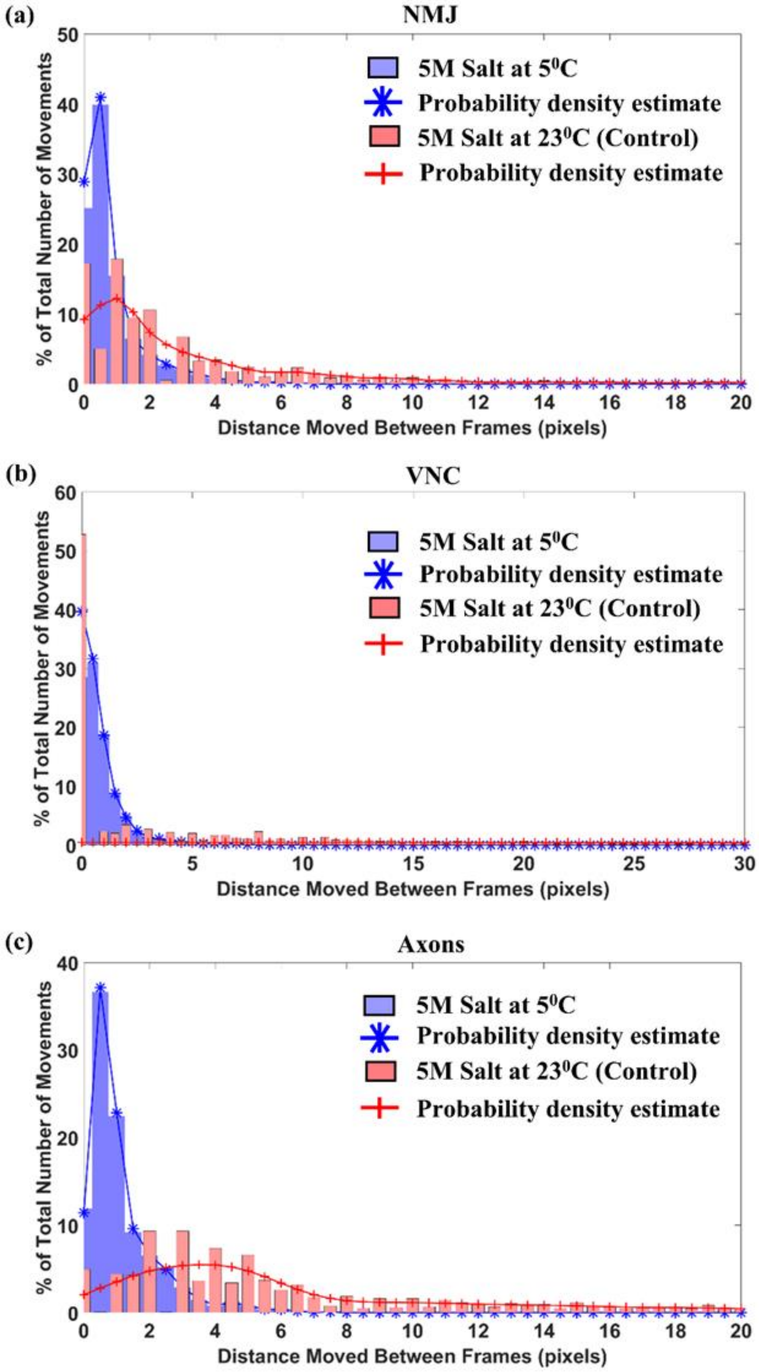

Figure 8.8: Histograms showing percentage of total number of movements in between frames of (a) mitochondria at NMJs, (b) cell bodies along VNCs and (c) mitochondria along axons in between video frames collected over 2 minutes. The solid lines (red and blue) represent probability density estimates fitted onto histogram data. The videos were collected with larvae loaded on the microfluidic chip with chilled (represented in blue) as well as room temperature (represented in red) coolant (5M salt water solution) flowing (3.2 mL/min) through the chip respectively. Pixel resolution is 0.18 µm.

8.3.4 Evaluating performance of alternative coolants

The main disadvantage of using 5M salt water solution as a coolant is that over time, salt precipitates out of the solution and can clog the coolant inlet/outlet ports if the device if not rinsed thoroughly after use. Furthermore, besides requiring a more rigorous cleaning/rinsing protocol, any accidental leakage of the coolant onto metallic microscope parts can lead to corrosion, which could cause significant and expensive long term damage. The metal flow chamber sandwiched in between the two Peltier modules can also get corroded over time, which can lead to release of debris that might enter the chip along with coolant flow and obstruct the fluidic channels. This may ultimately cause the membrane to burst under fluid pressure, which would cause permanent damage to the chip.

To overcome these disadvantages, we explored the use of two other commonly available, non-corrosive coolants with subzero freezing points: 40% ethanol and 50% glycerol solutions. Video frames of collapsed Z stacks (under 400x magnification) of mitochondria at NMJs, cell bodies in VNCs, and axonal mitochondria in segmental nerves were collected over 2 minute intervals and analyzed using the previously described experimental procedure (Section 8.4.4). 50% glycerol solution proved to be too viscous and affected peristaltic pump performance (flow rate was significantly reduced). Furthermore, as a result of its dense nature, movement artifacts were created along the z direction while imaging due to very large membrane deflections which in turn increased pressure on each larva leading to poor immobilization. 40% ethanol solution, being relatively less viscous, did not produce any significant reduction in flow rate (comparable to 3.2 ml/min with the flow rate potentiometer setting on the pump being constant) and did not produce any perceptible movement artifacts. Additionally, the immobilization microchamber stabilized to the same final steady state temperature of ~ 5^0C in ~ 1.8 minutes without requiring any precooling. This is comparable to the performance of pre-cooled 5M salt water solution maintained at -10 ^{0}C in the external coolant reservoir (Appendix C, Figure C4). Furthermore, the quality of immobilization within the VNCs and axons was comparable to the results obtained with 5M salt water solution. However, the structures at the NMJs were not as well immobilized by 40% ethanol solution (Figure 8.9). Given that PDMS is gas permeable and ethanol is highly volatile, it is likely that vapors of ethanol may reach the larva in the immobilization microchamber and affect the quality of immobilization. Ethanol is a well-known stimulant and has been proven to affect mobility in adult fruit flies [300] by inducing muscle contractions, but its effect on larvae are less well understood. To minimize any ethanol vapors from reaching the micro immobilization chamber, a 2 µm layer of parylene c was sandwiched in between two 10 µm PDMS layers creating a 22 µm thick PDMS-parylene c-PDMS membrane separating the immobilization microchamber from the cooling microchamber. Parylene c is sandwiched in between two thin PDMS layers instead of depositing it as a single layer on the bottom surface of the device in order to minimize any crack formation [301].

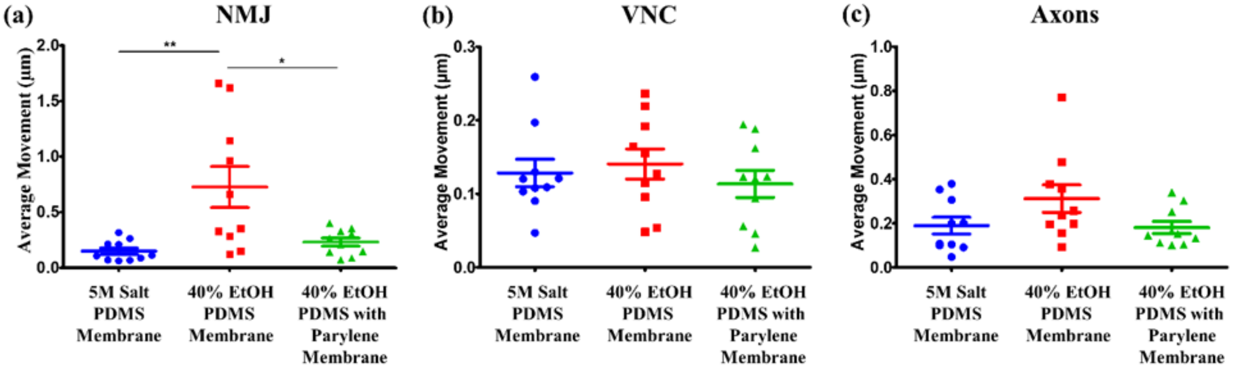

Diff of Means: $^*p<0.05$; $^{**}p<0.01$

Figure 8.9: Plots showing average of distances moved by (a) mitochondria at NMJs, (b) cell bodies along VNCs and (c) mitochondria along axons in between video frames collected over 2 minutes. The videos were acquired with larvae loaded on the microfluidic chip (without and with parylene c) with chilled coolant (5M salt water and 40% ethanol) flowing through the chip. Error bars indicate standard error of mean of measurements taken from ten animals imaged on the same device.

After the parylene c coating, the average movement of the neuronal structures at NMJs imaged with 40% ethanol coolant were significantly lower, and were comparable to results obtained using 5M salt water solution (Figure 8.9). Since the total membrane thickness is larger and parylene c is stiffer compared to PDMS (Young's modulus is three orders of magnitude higher), the resulting membrane deflection and therefore pressure being applied on the larvae is lower even though the final steady state temperature remains the same. Given that the quality of immobilization is similar despite membrane deflection being significantly lower in the parylene c coated chips, it may be concluded that the cooling effect is the dominant factor contributing towards causing immobilization compared to the effect of mechanical compression. In fact, making the membrane stiffer results in lower mechanical pressure being applied on each larva as it is being compressed against the coverslip implying the potential to have improved survival post immobilization. Therefore, apart from using 5M salt water solution, 40% ethanol solution can be used as an alternative coolant choice by using the modified chip post parylene c deposition.

It was seen that for the 5M salt solution, the flow rate increases with pump motor speed, which is adjusted with the flow rate potentiometer setting on the pump. However, for heavier more viscous fluids like 40% ethanol and 50% glycerol solutions, increasing load on the pump limits one's ability to control flow rate. Therefore, for these fluids, the steady state temperature and system response time will not reduce even if the flow rate potentiometer setting is increased beyond 4.

All the imaging experiments were performed at the same flow rate potentiometer setting for ease of comparison between different coolant performances. Additionally, higher flow rates would exert greater fluid pressure on the membrane causing it to deflect more and overcome the vacuum pressure generated by the syringe, leading to the chip detaching from the glass cover slip. Since it is possible for 5M salt water solution to reach lower temperatures with higher flow rates, in theory, it might be possible to achieve even better immobilization with increased pump motor speeds while using a stronger negative pressure source like a vacuum pump to maintain the chip on the coverslip. However, due to larger membrane deflection caused by higher flow rates, the fluid pressure acting on the membrane (Appendix C, Figure C5) would also lead to a larger mechanical compressive force on the larvae which could lead to reduced survival. A negative effect on the health of the larvae due to increased mechanical pressure could in turn potentially lead to a lower quality of immobilization. Therefore, the flow rate should be increased with caution, especially while using the cryo-larva chips without parylene c.

8.3.5 Larval survival

To determine the effect of cryo-anesthesia on larval survival, we subjected batches of 3rd instar larvae to repetitive fifteen minutes long cooling periods at 4 ^{0}C with a gap of 1 hour in between consecutive exposures. Even after six consecutive cycles, survival remained unaffected (Appendix C, Figure C6). A trial was considered a success if the larva was alive after being subjected to each cooling cycle.

While 3rd instar larvae showed good survival even after multiple imaging sessions, most of the 1st instar larvae did not survive long enough to develop into 2nd instars even after being subjected to single 10 minute imaging sessions on the microfluidic chip containing a PDMS membrane. However, survival of young animals was increased significantly when the parylene coating was used: 90% of the 1st instar larvae survived to develop into 2nd instars after being subjected to single 10 minute imaging sessions on the microfluidic chip containing a PDMS-parylene c-PDMS membrane. Being both thicker as well as stiffer, the mechanical compressive force applied by the PDMS- parylene c-PDMS membrane on the larvae is significantly lower compared to the pressure applied by just the PDMS membrane. This seems to confer significantly improved survival of the fragile 1st instar larvae.

8.3.6 Use of the cryo-larva chip to track mitochondria within neurons reveals stationary nature of synaptic mitochondria and heterogeneous mitochondrial turnover

As an application of the new immobilization method for imaging, we observed the trafficking of mitochondria from the cell bodies of larval motoneurons to their synaptic axon terminals through time. To track the trafficking of mitochondrial contents in neurons, we used the photo-convertible Dendra2 protein targeted to the mitochondrial matrix (mitoDendra2), which was expressed in a subset of motoneuron using Gal4/UAS system. Intact 3rd instar larvae were immobilized using the chip (without parylene c), and were subjected to focal application of UV light to irreversibly convert mitoDendra2 from green to red fluorescence specifically in the cell bodies in the VNC (section 8.4.4). With the immobility of the animal, the photo-conversion is specific to the VNC only, as no converted (red) mitoDendra2 can be observed at t=0h in distal regions like the axons and NMJ (Figure 8.10). The trafficking of red (photoconverted) mitochondria from cell bodies to axons and the axon terminals was then observed through time via successive imaging in the larval chip (Figure 8.10(a), (b)). Because of the non-invasive nature of the proposed method, the same neuronal structures within a single animal could be analyzed through time. Between imaging sessions the larvae were removed from the chip and allowed to crawl and feed unrestricted on grape-agar plates. Neither the photo conversion nor multiple imaging sessions in the microfluidic chip were toxic to the animals (Data not shown). Moreover, the degree of photo conversion (Appendix C, Figure C7) and the distribution of converted mitoDendra2 at different time points was reproducible from animal to animal (Figure 8.10).

The data suggest that mitochondrial contents distribute rapidly from cell bodies to axons where they merge with unconverted (green) mitochondria resident in axons, presumably via mitochondrial fusion (Figure 8.10(c)) [302]. Within 5 hours after photoconversion of the mitochondria in cells bodies, most of the mitochondria within axons contained both red and green mitoDendra2 protein, while only a few (green only, white arrows) remained devoid of converted mitoDendra2. This represents a population of axonal mitochondria that has not been subjected to fusion with cell-body derived mitochondria within this short time frame. Within 12 hours, the vast majority of the mitochondria in axons are both red and green, which suggests a continued mixing of mitochondrial contents throughout the axon with mitochondria derived from the cell body at the time of photoconversion (Figure 8.10(c)). Previously, mitochondrial fusion in axons was only assessed by observing individual events captured via time-lapse imaging [302], limiting the chance of observing a fusion event to only a few minutes at a time. With this new method, mitochondrial dynamics in axons can be assessed globally over the course of days, through time, and in the same animal.

At a further distance from the cell body, at the ends of the axon are the axon terminals at the NMJ synapse. We were able to observe the trafficking of cell-body derived mitochondria to the terminal through time by capturing the mixing of red mitochondria with the green/un-converted mitochondria that were resident in the NMJ (Figure 8.10(c)). Surprisingly, the time lapse imaging revealed that, in contrast to their high degree of motility in axons [303] for which we could not track the same mitochondria across individual time points (Figure 8.10(c)), mitochondria at NMJ synapses are stationary, maintaining the same relative position and shape between imaging sessions over time courses as long as 12 hrs. By observing the same pool of synaptic mitochondria over time, it can be inferred that the contents of the synaptic mitochondria are dynamic: the increase in red fluorescence, accompanied by a decrease in the green fluorescence (Figure 8.10(d)) suggests that the contents of synaptic mitochondria are slowly replaced over time with new material from the cell body. With this new method, we were able to quantitatively measure this delivery of cell-body derived mitochondria to the NMJ by plotting the frequency distributions of the average red to green fluorescent intensity ratio per mitochondria of individual mitochondria at the different time points (Figure 8.11(a)). On the population level, there is a clear progression of the increased delivery of cell body derived (red) mitochondria to the NMJ (higher red:green ratio) as time from conversion increases as shown by the distinct peaks in the distributions at 5 and 12h post conversion.

The immobility of individual mitochondria at the NMJ makes it straight-forward to recognize and quantify the changes that occur to individual mitochondria through time (Figure 8.11(b),(c)). As shown by the broad distributions in the 5 and 12h post conversion frequency distribution, incorporation of cell-body derived mitochondria is not homogenous to all NMJ mitochondria (Figure 8.11(a)), especially at the 5h time point. At 5h after photoconversion of cell body mitochondria, converted mitoDendra2 appears within some (Figure 8.11(b), pink arrowhead) but not all of the synaptic mitochondria (Figure 8.11(c), blue arrowhead), with some variation in intensity changes of green and red fluorescent intensities within individual mitochondria, even in the same position in the NMJ (Figure 8.11(b)). Within 12 hours, nearly all of the synaptic mitochondria contain photo-converted mitoDendra2 (Figure 8.10(d)), but with varying degrees of green and red intensities on the individual mitochondria level as shown by the red:green ratios of 19 individual mitochondria that were tracked across the 3 time points (Figure 8.11(c)). This time course implies that although on the global level, there is consistent delivery of mitochondria to the NMJ (Figure 8.11(a)), there seems to be non-uniform turnover of contents from individual mitochondria at the NMJ synapse that can be tracked with this method. We would ultimately be interested in understanding more about this heterogeneous turnover of mitochondria, and how it correlates with other subcellular events occurring in the NMJ synapse in the future.

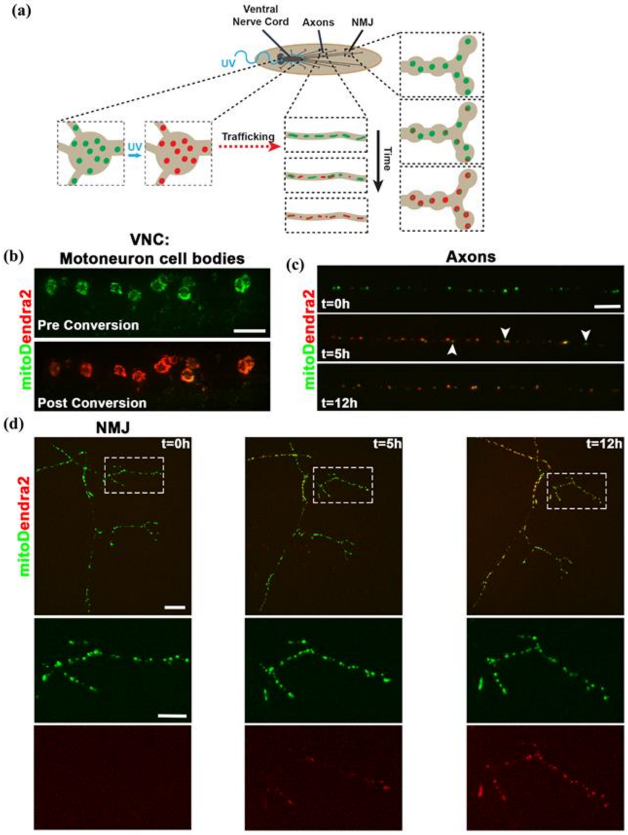

Figure 8.10: (a) Schematic representation of newly developed assay to measure mitochondrial trafficking from the cell-bodies of motor neurons in *Drosophila* larvae to axons and the NMJ synapse in intact larvae. While immobilized in the cryo-larva chip, whole larvae are subjected to focal application of UV light to their VNC to photo-convert labeled mitochondria (mitoDendra2). Converted cell-body derived mitochondria (red) can then be tracked as it is trafficked to distal neuronal processes. (b) Representative example of motor neuron cell-bodies on one side of the VNC expressing mitoDendra2 before (Pre-conversion) and immediately after (Post-conversion) photo-conversion. For all subsequent images in this figure: Green fluorescence is unconverted Dendra2, while red fluorescence is photo-converted Dendra2 protein (scale bar, 20 µm) (c) Representative example of the mitochondria in axons of motor neurons from the same animal through time following photo-conversion (0 hours (h) represents immediately following conversion). Notice at 5h post-conversion (middle), most resident axonal mitochondria have fused with cell-body derived mitochondria (green + red). Some axonal mitochondria have not fused with mitochondria trafficked from the cell body (green alone, arrowheads). By 12h, all axonal mitochondria contain content from trafficked cell-body derived mitochondria (green + red) (scale bar, 10 µm). (d) Representative example of an NMJ synapse from the same animal tracked through time for the delivery of cell-body derived mitochondria. Top panel shows whole synapse, while bottom panels represent a high magnification view a single branch of the NMJ (boxed region). Notice at 5h post conversion (middle panel), there is some trafficked mitochondrial material in the NMJ shown by the weak red-fluorescence in certain mitochondria (arrowheads). By 12h post-conversion, all mitochondria in the NMJ contain mitochondrial material that was present at the cell-body at the time of conversion (scale bars, 20µm and 10µm).

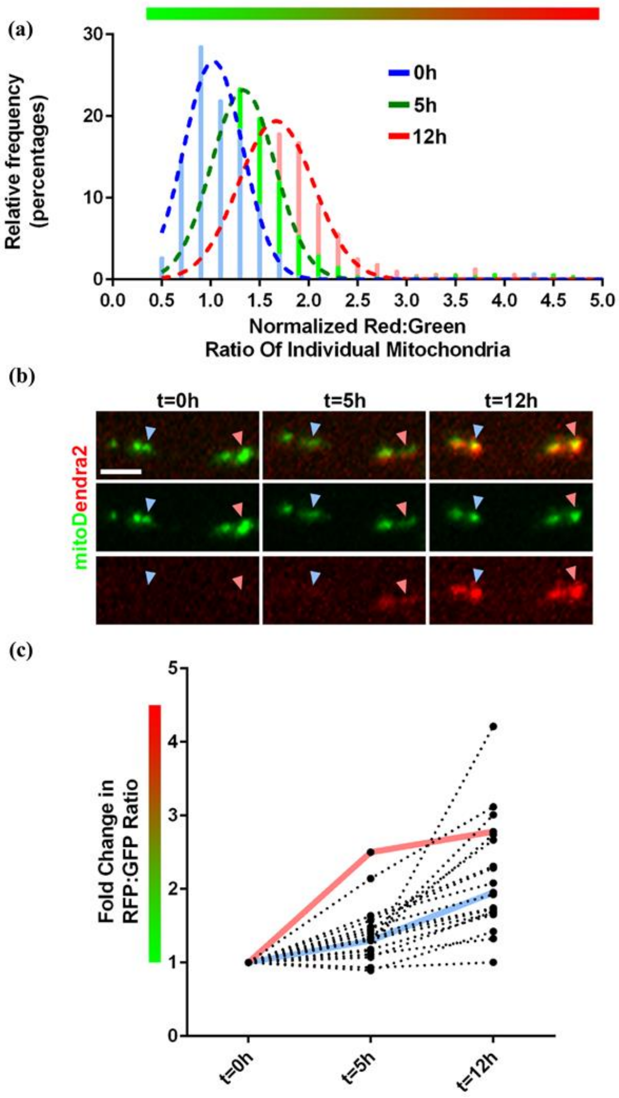

Figure 8.11: (a) Frequency distribution plot of the average red:green ratio of individual mitochondria at the NMJ from the three different time points observed in mitochondrial trafficking experiments (t=0h (blue), 5h (green) and 12h (red) post conversion). Each time point include >500 mitochondria from at least 6 NMJs originating from 3 different animals. Bars represent frequency histogram and dotted lines represent Gaussian fit curves for each individual time point. (b) Representative region of NMJ containing 4 recognizable stationary mitochondria across all time points (t=0h, 5h and 12h post conversion). Merged pictures are shown in top row, while middle row is un-converted (green) mitoDendra2 alone and bottom row shows cell-body dervived converted (red) mitoDendra2 alone. Colored arrowheads depict 2 different mitochondria with differing rates of incorporation of red material, and correspond to the colored lines in (c). (scale bar, 2.5µm) (c) Example plot of the individual red:green fluorescent intensity changes of 19 individual mitochondria across the three different time points shown in (b). Colored lines related to the corresponding colored arrowheads in (b). Note the differential changes in red:green ratios of neighboring mitochondria indicating a heterogeneous delivery and turnover of mitochondria in the NMJ.

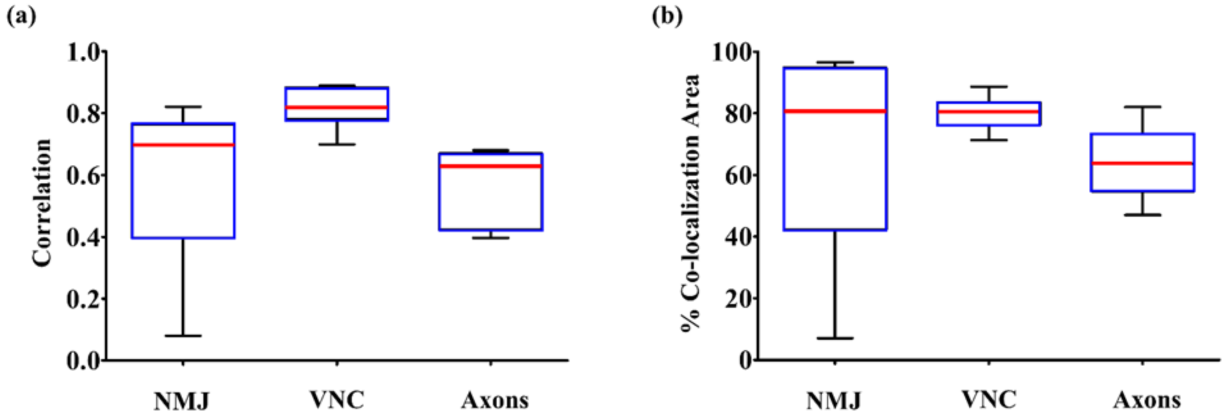

Figure 8.12: Box and whisker plots showing (a) correlation and (b) % co-localization area between red and green channels of mitochondria at NMJs, cell bodies along VNCs and mitochondria along axons. The image frames correspondonding to the red and green channels are 8 secs apart. The videos were collected with larvae loaded on the microfluidic chip with chilled coolant (5M salt water solution) flowing through the chip. Each box extends from the 25th to 75th percentiles, the line in the middle is plotted at the median and the whiskers span between the smallest and largest data values (measurements taken from ten animals imaged on the same device).

In trafficking experiments, co-localization of multiple fluorescent markers acquired sequentially (on the order of milliseconds of separation) is essential for proper interpretation of results. Therefore, mitochondrial identification and tracking is heavily dependent upon quality of immobilization, which directly influences how well the fluorescent features are spatially co-localized across image frames. To test how reliably our chip can immobilize larvae on short term time-scales that would be necessary for co-localization of dual fluorescent markers, we quantified the co-localization of fluorescent sub-cellular features in between image frames acquired 8 seconds apart (average time taken by image acquisition system to acquire image frames from both red and green channels). Co-localization has been evaluated both in terms of estimating correlation between (Section 8.4.7) the frames (Figure 8.12(a)) as well as quantifying percentage areal overlap of objects (Section 8.4.8) identified in and common to both frames (Figure 8.12(b)). The greater the value of correlation and percentage of areal overlap, the higher the degree of co-localization. Furthermore, it was observed that while co-localization of features at the NMJs was comparable to the results obtained from the chip developed by Ghannad-Rezaie *et al.* [1] (referred to as the mechanical chip) which mechanically immobilizes the larvae, the co-localization of features at the VNCs and axons is significantly improved with the proposed cryo-anesthetic method compared to the purely mechanical immobilization approach [18] by 30% and 50% respectively (Appendix C, Figures C8 and C9).

8.3.7 Use of the cryo-larva chip to observe neuro synaptic growth

Because of the powerful genetic tools available, the *Drosophila* larval NMJ has been a widely used model for studying and understanding the cellular machinery involved in synaptic growth. Various screens have been used to identify genetic mutations that result in the altered growth of the NMJ, typically assessed by observing the morphology of the NMJ at a later stage (ie, 3rd instar) [304]. This post-mortem analysis can be used to infer much information about synaptic growth, but few studies have been able to assess developmental growth, since this requires successively imaging the same larvae through multiple developmental stages [305] [306]. The method proposed in this paper can be used to observe the growth of synapses at the NMJs as the larvae grow dramatically in size, starting from the 1st instar and all the way up to the 3rd instar developmental stage. This is a significant improvement over the method previously developed by Ghannad-Rezaie *et al.* [1] in which the same device could not be used to image different larval sizes. Individual 1st instar larvae were immobilized and their NMJs imaged with the microfluidic chip containing a PDMS-parylene c-PDMS membrane. The same animals were then placed on the chip after they developed into 2nd and then 3rd instar larvae after 24 and 48 hours respectively and their NMJs were re-imaged. The growth of synapses at the NMJs, both in terms of size as as well as number of branches, can be easily observed across all larval developmental stages as seen in Figure 8.13. Although shown here is observing the developmental growth of a normal NMJ, with the wealth of genetic tools and mutations available from decades of research in the *Drosophila* NMJ field, the details of many of the synaptic growth defects can be looked at in a more in-depth manner using this method to track growth dynamics from 1st through 3rd instars larvae. Further, although we are observing the simple morphological growth in this particular example, with the abundance of endogenously tagged protein traps [307] and fluorescent reporters available in the *Drosophila* field, subcellular changes can be observed with this same method at different developmental stages of NMJ development.

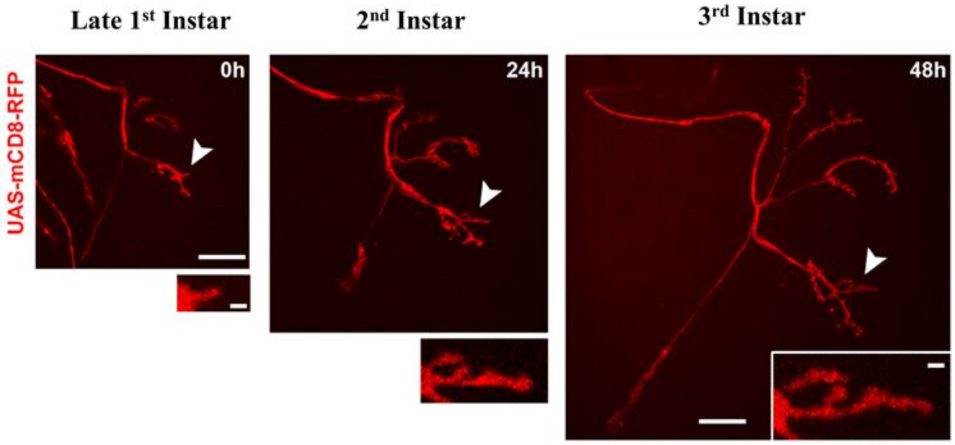

Figure 8.13: Representative images of growing NMJ terminals imaged successively during larval development in a single animal. To visualize the morphology of the NMJ synaptic terminal, a membrane tagged red fluorescent protein (UAS-mCD8-RFP) was driven in three motoneurons (onto muscles 26, 27, and 29) via the M12-Gal4 driver. Late 1st instar larvae were immobilized and imaged with the cooling chip on day 0 (left), and the same animal was imaged 24h (middle) and 48h (right) later. The different developmental stages of the animal are indicated on top. Arrowhead denotes the region of high magnification below and in inset, highlighting the growth and elaboration of one region of the NMJ. All pictures are at the same scale with scale bars of 20µm (whole NMJ pictures) and 2µm (high magnification images).

8.3.8 Comparison of cryo-larva chip to other approaches of immobilization

Even though low temperature larval immobilization has not been demonstrated for *Drosophila* before, cryo-anesthesia has previously been implemented to immobilize other model organisms such as C.*elegans*. Chung *et al.* [288] developed a fully automated microfluidic platform for performing high throughput microscopy and sorting of C.*elegans* with flow based pressure driven loading and robust temperature control on chip. While this platform has been very successfully implemented for worm populations studies, it would not be possible use a pressure driven flow based loading mechanism as the larvae cannot be maintained in a fluid suspension like C.*elegans*. Larvae would not be able to survive inside a fluid without having access to air while being manipulated by pressure driven flow inside tubing. Additionally, the *Drosophila* larval cuticle is tougher than the *C. elegans* cuticle, making them more susceptible to mechanical stresses during flow based manipulation. A flow based pressure driven loading approach cannot guarantee loading larvae with their ventral surface facing downwards which is the required orientation to perform most imaging applications. Furthermore, a significant change in device dimensions as well as architecture would be required to accommodate *Drosophila* larvae due to their significantly larger sizes. Rhode *et al.* [289] developed a high throughput technology for screening C.*elegans* inside multiwall plates by cryo-immobilizing and imaging worms using a custom made Peltier element array. While the method can be successfully used to perform imaging at the cellular level for C.*elegans*, *Drosophila* larvae being much larger and having a more turbid cuticle compared to C.*elegans* require slight mechanical compression for good optical accessibility, especially for imaging more internal structures and sub-cellular processes which is not possible with the platform developed by Rhode *et al.* [289].

Among the several approaches that have been developed for *Drosophila* larval immobilization, the method presented by Heemskerk *et al.* [281] enables imaging of larvae using desflurane with an immobilization chamber that is easy to implement. However, desflurane, a regulated chemical substance, requires additional safety components such as a gas collection assembly, transfer tubing, gas disposal assembly and gas disposal tubing making the use of desflurane more complicated. The device developed by Heemskerk *et al.* seems to be amenable for use with other gas anesthetic agents like CO_2, which is relatively easier to implement than desflurane. Given that the cryo-larva chip has a two layer architecture with a liquid impermeable, but gas permeable PDMS membrane separating the two layers, chilled coolant flow through the chip could be easily replaced with a gas anesthetic like CO_2. This feature makes the cryo-larva chip an “off the shelf” versatile alternative to previous devises used to immobilize larvae since it can utilize both liquid coolants, and potentially anesthetic gases (as previous shown by Ghannad-Rezaie *et al.* [1]).

Even though anesthetics like CO_2 are attractive choices for immobilization, chemical vapors have relatively more significant negative effects on larval physiology compared to chemical free cold immobilization. A study conducted by Badre *et al.* [308] concludes that apart from effects such as blocked synaptic transmission at the neuromuscular junction by decreased sensitivity to glutamate, an exposure to 100% CO_2 for 30 minutes will kill *Drosophila* larvae. On the other hand, a study conducted by Kostal *et al.* [309] concludes that viable larvae may be stored in quiescence at low temperatures (3-9^{0}C) for up to two months, with larval survival showing further improvement with a fluctuating thermal regime (stored at 5^{0}C for 20 hours followed by 4 hours at 11^{0}C for 60 days) indicating that exposure to warmer temperatures allows repair of potential chill injury. These results reflect positively on the utility of the cryo-larva chip that also subjects larvae to less than 10 minutes of cold temperatures (4-6^{0}C) followed by recovery over extended periods at room temperature. Even though the studies have been conducted over long durations under the fluctuating temperature regime, the results presented by Kostal *et al.* [309] provide evidence of larvae re-establishing ion balance, repair by heat shock protein assisted processing, replenishment of depleted ATP , management of oxidative damage and synthesis of cryo-protectants, all of which would be expected to take place using the cryo-larva chip. Additionally, the fact that ~ 80% of the larvae imaged with the cryo-larva chip subsequently pupariated (unpublished observation) demonstrates minimal long term physiological effects due to the cryo-immobilization method. Even though cooling the animal will effect biological processes on the order of tens of minutes, the intended use of the cryo-larva chip is to cool the animal for short periods of time (2-4 minutes) only to perform imaging, and then allow the animal to recover and develop back at normal temperature to provide a series of snapshots through time of long term processes like mitochondrial transport and synaptic growth that takes places over several hours if not days. It is not meant to perform shorter term (on the level of tens of minutes) time-lapse imaging of a physiological process taking place while the animal is being cooled inside the chip, for which the method developed by Heemskerk *et al.* [281] would be a better alternative.

The method developed by Heemskerk *et al.* [281] avoids mechanical compression to minimize tissue distortion which is very effective for applications where imaging of soft internal structures such as the wing disc is required. In applications in which the maintenance of the tissue architecture without distortion is absolutely necessary, the mechanical compression would be a downside, and the method utilized by Heemskerk *et al.* could be a better alternative. However, the mechanical pressure and subsequent tissue distortion would be generally consistent in different imaging sessions of the same animal, and therefore would be accounted for in comparisons through time. In our application, we notice no significant distortion of the structures we imaged (VNCs, axons, NMJs) in comparison to fixed larval tissue from dissected animals that are not compressed in any way. Further, *Drosophila* larvae have a turbid cuticle and slight mechanical compression is required for good optical accessibility, especially for higher resolution imaging of sub-cellular structures along the dorsal and ventral surfaces that are relatively much less distorted when squeezed compared to lateral organs like the wing disc. The PDMS membrane in the cryo-larva chip improves optical focus by pushing the larva against the glass coverslip. Additionally, since is it critical to have the animal lie straight with its ventral surface facing downwards on the coverslip to be able to locate anatomical landmarks while imaging, the mechanical compression applied by the membrane maintains proper body orientation and minimizes tissue distortion by preventing the larva from crawling around/coiling/twisting/flipping inside the chamber before the cooling effect immobilizes the animal. Furthermore, any potential effects of mechanical compression on cellular dynamics within the animal, can be minimized by making minor modifications to device dimensions such as making the membrane thicker and/or stiffer as already demonstrated by improved survival of 1st instars with the parylene membrane.

Simpler, physical constraint type techniques using capillary pressure developed by Nienhaus *et al.* [282] or using tape to mechanically immobilize larvae developed by Restrepo *et al.* [285] are convenient choices for imaging events at the tissue or cellular level. However, there are excessive small body movements that continue to take place while the animal is physically constrained with these mechanical approaches that will have a more substantial negative impact on higher resolution image quality while studying sub-cellular processes like mitochondrial transport. These movements also increase recording time as more image frames need to be acquired to correct for movement. Therefore, by supplementing the partial immobilizing effect provided by a mechanical constraint with cryo-anesthesia, the cryo-larva chip minimizes these small body movements, both in terms of magnitude and frequency. This greatly improves imaging quality and reduces the time to image sub-cellular structures/processes at high magnifications.

Additionally, the cryo-larva chip and associated cooling system is a universal approach as it maybe easily implemented with both inverted as well as upright transmission/reflection microscopes. Given that some high resolution imaging studies are performed on an inverted microscope in transmission mode, placing a peltier unit with heat dissipation modules directly on top of the animal or coverslip while imaging will require the construction of specialized mechanisms to prevent excess mechanical loading of the animal, as well as the microscope's piezo-stage while still allowing light to pass through. Implementing this approach will therefore significantly increase system complexity that would have to be specific to the user's microscope configuration. Therefore, even though biologists have been known to immobilize adult flies very easily by simply placing them directly on the surface of a Peltier element or ice in order to image on a microscope, implementing this approach would have to be able to be accommodated by the microscope configuration and not be universally usable like the cryo-larva chip set up.

8.4 Experimental methods

8.4.1 Device fabrication

Soft lithography was used to fabricate the microfluidic device. Master molds for Layer 1 and Layer 2 were micro fabricated on two different silicon wafers. A 170 µm mold was created for Layer 1 by spinning and patterning SU-8-2100 photoresist on a silicon wafer (Appendix C, Section C1). Similarly, a 100 µm mold was created for Layer 2 by spinning and patterning SU-8-2050 photoresist on another silicon wafer (Appendix C, Section C1). To fabricate Layer 1, a 15:1 PDMS mixture ratio was spun cast at 400 rpm for 50 secs over the 170 µm mold and cured at 65 ^{0}C for 5 hours. To fabricate Layer 2, a 10:1 PDMS elastomer to curing agent mixture was poured over the 100 µm mold and allowed to cure for 5 hours at 65 ^{0}C. Layer 2 (~ 3.5 mm thick) was peeled off from the 100 µm SU-8 master mold and the coolant inlet/outlet ports were punched using a sharpened, 19-gauge needle (0.031 inch I.D., O.D: 0.042 inch O.D.; Kathetics). Layer 2 was then aligned and air plasma bonded (50 W, 250 mTorr, 60 s) to Layer 1. The two layer PDMS structure was then peeled off from the 170 µm SU-8 master mold followed by the creation of vacuum and food ports using the sharpened, 19-gauge needle that was previously used to create fluidic ports in Layer 2. Leak proof access to Layers 1 and 2 was provided using polyvinyl tubing (0.023 inch I.D., 0.038 inch O.D.; BD Intramedic) connected via a steel pin (0.016 inch I.D., 0.025 inch O.D.) to the coolant inlet/outlet and vacuum ports on the device.

For fabricating devices with PDMS-parylene c-PDMS membranes, the same master molds for Layers 1 and 2 were used. Layer 1 was fabricated by spinning 15:1 PDMS elastomer to curing agent mixture at 400 rpm for 50 secs and curing it at 65 ^{0}C for 5 hours. A 2 µm parylene-c polymer using the physical vapor deposition (PVD) process [310] was deposited in a conformal manner onto the surface of PDMS on Layer 1. A 15:1 PDMS elastomer to curing agent mixture was spun cast at 400 rpm for 50 secs over the parylene c layer and cured at 65 ^{0}C for 5 hours to create a 22 µm thick PDMS-parylene c-PDMS membrane. Layer 2 was fabricated with coolant inlet/outlet ports punched into it and plasma bonded to Layer 1, ports for vacuum and food were punched and fluidic access was provided as previously described.

8.4.2 Animal preparation

For experiments tracking immobilization upon the onset of coolant flow (Figure 8.5), membrane targeted GFP was expressed in all motoneurons using the Gal4/UAS system (OK6-Gal4; UAS-mCD8GFP). For experiments measuring immobility at specific neuronal structures

(VNC, Axons, or NMJ) (Figures 8.6, 8.7, 8.8, 8.9 and 8.10), mitochondria were labeled by driving expression of the fluorescent protein Dendra2 fused to the mitochondrial targeting sequence from cytochrome C oxidase subunit VIII under the control of a UAS promoter (UAS-mitroDendra2) [311]. Expression of UAS-mitoDendra2 [311] was driven using the m12-Gal4 driver line [1] [312] [313] which expresses in 2 motoneurons per hemi-segment allowing for the visualization of individual mitochondria through time. For photo-conversion experiments (Figure 8.10) UV light was applied using epi-fluorescence (UV dichroic, 405nm) which was focused onto the VNC using the microscope's condenser at full power for 8 seconds. The approximate region converted was ~25µm circular region over individual pairs of motoneurons in the VNC, performed multiple times to convert all visible motoneurons in the lateral VNC expressing mitoDendra2. Images of the VNC were taken before and after conversion, and initial t=0h images of the axons and NMJ were taken after photo-conversion. In between imaging sessions (at 5h and 12h), animals were removed from the chip and placed on grape-agar plates to freely crawl around and feed. All animals were 3rd instar larvae and were cultured and reared using standard *Drosophila* protocols.

For tracking synaptic growth (Figure 8.13), adult crosses were set 3 days prior to collection of late 1st instar/early 2nd instar animals. Larvae chosen for study varied slightly in size from 1-2mm in overall length, no animals >2mm were chosen for initial imaging on day 0. On day 0, collected larvae (genotype:M12-Gal4, UAS-mCD8RFP/+) were washed in water and placed on the chip containing a PDMS-parylene c-PDMS membrane. After imaging, animals were removed from the chip and placed individually on grape-agar dishes supplemented with yeast paste (dry baker's yeast mixed with water) in a 25°C incubator to freely crawl and forage for 24 hours before the next imaging session (the same procedure was followed in subsequent imaging sessions).

8.4.3 Larval loading and manipulation

Individual larvae were placed in halocarbon oil 700 (cat. # H8898 Sigma Aldrich Inc.), put on a glass coverslip (#12-544E, Fisherbrand), and then covered by placing the transparent chip on top using manual alignment under a stereo dissection microscope. A tight seal between the PDMS chip, oil and coverslip was created by applying vacuum pressure (600 mTorr) using a 20 cc syringe to the vacuum port of the microfluidic network in 'Layer 1' [314].

8.4.4 Fluorescence imaging

All imaging acquisitions were conducted using a spinning disk confocal system (Perkin Elmer), consisting of a Yokagawa Nipkow CSU10 scanner, and a Hamamatsu C9100-50 EMCCD camera, mounted on a Zeiss Axio Observer with an oil objective. Volocity software (Perkin Elmer) was used for image acquisition.

For experiments tracking immobilization upon the onset of coolant flow to determine the time required to immobilize the larvae (Figure 8.5), a single optical plane was captured with a 25x (0.8 NA) oil objective lens every 2 seconds for 9 minutes in total. In each typical imaging session, animals were kept in the chip for approximately 9 minutes.

For experiments measuring immobility at specific neuronal structures (VNC, Axons or NMJ) (Figure(s) 8.6, 8.7, 8.8, 8.9), a collapsed z-stack of the whole structure was acquired every 1 second over 2 minutes with a 40x (1.3 NA) oil objective lens. Each collapsed z stack, containing 6-7 z planes with step size 0.5-1.5 µm and exposure time of 100-115 milli-seconds, took ~1 second to acquire. In each typical imaging session, animals were kept in the chip for approximately 10 minutes.

For photo-conversion experiments (Figure(s) 8.10, 8.11), each image was captured with a 40x (1.3 NA) oil objective lens. All images were confocal collapsed z-stacks taken of sequential red and green channels of neuronal structures at all time points. If slight movements occurred during the z-stack and red/green channels were slightly mis-aligned, another z-stack was acquired until no movement was observed during the z-stack. Each collapsed z stack, containing 6-7 z planes with step size 0.5-1.5 µm and exposure time of 100-115 milli-seconds, took ~1 second to acquire. In each typical imaging session, animals were kept in the chip for approximately 5 minutes.

For tracking synaptic growth (Figure 8.13), imaging of NMJs was initiated two minutes after onset of flow of coolant. Typically, 3 NMJs per animal were imaged with a confocal z-stack using a 40x (1.3 NA) oil objective lens and single channel acquisition. Each z-stack containing 6-7 z-planes, spaced 0.5µm apart, was acquired with an exposure time of 100-115 milliseconds and took ~ 1 second to acquire. In each typical imaging session, animals were kept in the chip for approximately 5 minutes.

8.4.5 Quantification of on-chip larval movement

In order to quantify on chip larval movement and comment on the quality of immobilization, for every video acquired with the animal immobilized, three random features were selected after ensuring that they are visible across all collapsed z stack frames in the video (Figure(s) 8.6-8.9). For videos that were acquired of the larval VNCs, these features corresponded to fluorescently labeled neuronal cell bodies located at the VNC. Whereas for videos that were acquired of the larval NMJs and axons, the features corresponded to fluorescently labeled mitochondria. For a given video, the three chosen features were tracked across every frame and the absolute distance moved by their centroids in between consecutive frames was estimated using Metamorph 7.7.0.0 Imaging software. The video was accessed by the software in the form of 8-bit grayscale multi-tiff image frames. The features to be tracked were manually selected on the first frame by drawing a box around their periphery which formed their template images. The centroid of each box was defined as the corresponding feature centroid. After defining the template images, the search regions (the area in which the software should search for the feature to have moved to) around the features were also defined. The template matching algorithm [315] was then employed by the software to track the location of the features within the search regions in every frame. While running the template matching algorithm, the correlation coefficient threshold was set to 0.5. If the software failed to locate a feature in any given frame, tracking was stopped and the correct location of the feature was manually redefined by visual inspection before proceeding with automated tracking. The average distance moved in between frames was then calculated for every feature centroid followed by the estimation of the average distance moved across all frames for all three feature centroids. The optical resolution of the microscope setup that was used for distance estimation with 400x magnification is 0.18 µm (1 image pixel corresponds to 0.18 µm) respectively.

In order to quantify the larval response time to immobilizing effects, for every video acquired before, during and after immobilization, a point (centroid of a cell body along the VNC) was selected that was visible across all frames (Figure 8.5). The point was then manually tracked across every frame and the distance moved in between consecutive frames was estimated using Metamorph 7.7.0.0 Imaging software. The optical resolution of the microscope setup that was used for distance estimation with 250x magnification is 0.29 µm (1 image pixel corresponds to 0.29 µm). Automated tracking with template matching was not possible as there was a lot of movement before and after immobilization.

8.4.6 Quantification of mitochondria fluorescent changes

Individual mitochondria were extracted from merged Z-stacks of confocal images of the NMJ using the Volocity software (Perkin Elmer), with an algorithm that selected individual puncta via a determined fluorescent threshold above background. From each mitochondria, an average fluorescent intensity of the whole mitochondria in the red and green channel were used to determine the red:green ratio. For population changes (Figure 8.11(a)), the average red:green ratio of pooled mitochondria at t=0h (where there is no red fluorescence) was used to normalize all data. For measuring changes in individual mitochondria (Figure 8.11(c)), mitochondrial ratios at time points after t=0h were compared to their original red:green ratio at t=0h to determine a fold change. Only mitochondria that we were certain to be present and accounted for (based on visual landmarks) all time points were used for this analysis.

For measuring the conversion efficiency (Figure C7), all converted cell bodies from a merged Z-stack image pre conversion and post conversation were compared in their overall average red:green fluorescent intensity ratios (similar to what is shown in Figure 8.10(b)). The ratios were compared to themselves to determine the fold change in the ratio displayed in the graph.

8.4.7 Quantification of correlation coefficient as a measure of co-localization

Image frames that are temporally 8 seconds apart at the start of each 2 minute video were chosen to be the green and red channels. Pearson's correlation coefficient [315] was calculated between these two frames (Figure 8.12(a)) using the CellProfiler software [316].

8.4.8 Quantification of % co-localization area

Image frames that are temporally 8 seconds apart (determined to be the average time to complete 2 color sequential z stack in our experiments) at the start of each 2 minute video were chosen to be the green and red channels. Objects (mitochondria and cell bodies) were identified in these two frames using the CellProfiler software. The objects were identified using the three-class Otsu thresholding method [317]. The % area of pixels that spatially overlapped between the two segmented images was then calculated and defined as % co-localization area (Figure 8.12(b)).

8.4.9 On chip temperature measurement

We estimated the temperature distribution created by the chilled coolant flowing through the microfluidic device as well as the temperature in the micro-immobilization chamber using non-invasive infrared thermal imaging [318]. Given the dimensions of the microfluidic device, the region of interest is too small to enable accurate contact measurement based conventional thermometer systems. A FLIR SC600 (measurement range: -20^{0}C – 150°C, accuracy: ± 2°C or 2%), 7.5 – 13 µm pre-calibrated long-range infrared thermal camera fitted with a FLIR T198059 close up lens (spatial resolution: ±50 µm) was used to measure the temperature of the immobilization microchamber in the chip. The chip was connected to the cooling setup and mounted upside down with the coverslip facing the camera mounted on top. The coverslip was placed at the focal distance of the infrared lens with its plane lying perpendicular to the vertical axis of the camera. As it is difficult to measure the temperature of transparent surfaces, a piece of thin (100 µm) black tape with known surface emissivity (0.95) was cut to ~ 5.5 mm x 2.8 mm (size of the immobilization microchamber) and pasted on the coverslip over the immobilization microchamber. Images of the chip were then collected at 1 frame per second after starting coolant flow through the chip. Data acquisition and post processing of the infrared images was handled by the FLIR ExaminIR software. The software was also used to specify emissivity (0.95), ambient temperature (23^0C) and ambient humidity corrections (15%).During data acquisition and/or during post processing, the minimum, maximum and average temperatures over the region of interest (region covered by the black tape) was estimated and plotted over time. Given that the coverslip (~ 150 µm) and the tape (~ 100 µm) are extremely thin, the time taken by these surfaces to equilibrate to the steady state temperature of the immobilization microchamber inside the chip maybe considered to be negligible.

8.4.10 On chip fluid pressure measurement

In order to estimate the pressure exerted by the PDMS membrane on the larva, the deflection of the membrane was first calibrated with the application of known static air pressure. The cooling microchamber was pressurized with air at known pressure using an air flow regulator (Elveflow microfluidic AF1 pressure pump) while plugging off the cooling microchamber outlet thereby causing the PDMS membrane to deflect. Membrane deflection was measured by optically focusing on the center of the membrane before and during pressurization using an upright microscope (Olympus BX-51), 10x objective lens (MPLFLN10x, Olympus) and bright field illumination mode. Food color was added to PDMS during the fabrication of Layer 1 to enhance optical contrast and improve membrane deflection measurement accuracy. The calibration data was curve fitted using a 3rd order polynomial function (Figure C5). After calibration was completed, the chip was connected to the cooling setup without adding the coverslip and coolant (5M salt water solution) was pumped through the cooling microchamber in the chip. The resulting membrane deflection under pressurized coolant flow was optically estimated and measurements were obtained at different flow rates of the coolant. The higher the flow rate, the greater the membrane deflection. Using the calibration curve and measured membrane deflection for a given flow rate, the fluid pressure being applied on the membrane was estimated.

8.4.11 Coolant preparation

5M salt water solution was prepared by mixing 73.05 g of sodium chloride (cat. # S9888 Sigma Aldrich Inc.) with 200 ml of ddH_2O while stirring. Additional ddH_2O was added until the final volume was 250 ml. 250 ml of 40% (v/v) ethanol solution was prepared by mixing 100 ml of 100% ethanol (cat. # 2701 Decon Laboratories Inc.) with 150 ml of ddH_2O by stirring. 250 ml of 50% (v/v) glycerol solution was prepared by mixing 125 ml of 100% glycerol (cat. # 536407 Sigma Aldrich Inc.) with 125 ml of ddH_2O by stirring.

8.4.12 Statistical significance test

The two tailed unpaired non parametric Man-Whitney test was performed to test the significance of the difference in mean of average movement measurements (Figure 8.6) from features at NMJs, VNC and axons between using the proposed method with chilled coolant flow and coolant flow at room temperature (control).

A one way ANOVA test followed by Tukey's multiple comparison test was performed to test the significance of the difference in mean of average movement measurements (Figure 7.9) from features at NMJs, VNC and axons between using the proposed method with chilled 5M salt water solution flow, chilled 40% ethanol solution flow above the PDMS membrane and chilled 40% ethanol solution flow above the PDMS-parylene c-PDMS membrane.

8.5 Conclusion

We developed and characterized a microfluidic method for immobilizing *Drosophila melanogaster* larvae which enables imaging in intact animals. The method uses a microfluidic cryo-larva chip to create a low-temperature micro-environment to deliver a combination of mechanical compression and cryo-anesthesia to immobilize individual larvae. A deformable membrane is used to mechanically compress each larva while simultaneously flowing chilled coolant over the PDMS/PDMS-parylene c-PDMS membrane and subjecting the larva to cold temperatures. The method is easy to implement, allows complete larval recovery and can be used to immobilize larvae of different developmental stages. Additionally, since the device is not permanently bonded to the glass coverslip, it can be subjected to multiple uses while making the larval loading process extremely quick and easy. Our results indicate that the proposed method is appropriate for repeated short-term (less than 10 minutes) immobilization sessions, with immobilization sufficient to perform high resolution imaging of sub-cellular structures.

Besides demonstrating high resolution imaging of larval NMJs, VNCs and axons, the proposed immobilization approach can have an impact on a variety of other imaging applications in *Drosophila* neuroscience, including neuronal laser microsurgery for studying axon regeneration, neuronal circuits and time lapse imaging for studying synapse development. Furthermore, technical challenges (mainly survival) have limited the successive imaging of the same *Drosophila* larvae across developmental stages without the use of anesthetics [305] [306]. The combined pressure/cooling immobilization of young larvae presented here allowed for an acceptable level of survival of imaging young larvae across their developmental ages. This alone will make this technique of high value for developmental biologists. Although the focus of this particular data was on the mitochondrial trafficking in neurons, the technique of local photo-conversion and trafficking that we were able to perform using this chip can be utilized for a variety of different long-term time lapse applications. These include imaging of subcellular trafficking, tracking of long range cell migration, and imaging proliferation dynamics. Having such a powerful tracking ability within an intact animal over multiple imaging sessions can be a great resource to many biological fields.

CHAPTER 9

THE WORMIMM PLATE: A 3D PRINTED MILLIFLUIDIC TOOL FOR CO_2 IMMOBILIZATION OF *C. ELEGANS* ON AGAR FOR POPULATION STUDIES AND IMAGING APPLICATIONS

9.1 Introduction

C. elegans is a popular model organism for studying various biological processes including cell apoptosis, ageing and neural plasticity among several others due to its completely sequenced genome [319] [320] [321] [322], easy maintenance, fast generation times and optical transparency. At the heart of these biological studies lies the necessity to immobilize them sufficiently in order to produce high quality live videos and/or images thereby allowing biologists to analyze anatomical features [323], observe biological processes like axonal regeneration [324] [325] [217], cellular development/gene expression [326], monitor neuronal response with various stimuli [232] or for even scoring lifespan assays [327]. The immobilization method should therefore minimize any movement of the organisms that would otherwise cause them to crawl out of the recorded field of view as well as minimize any motion artifacts such as loss of focus.

Conventional techniques for worm immobilization incorporate the use of glue [238] [328] or anesthetic compounds [329] [241] to minimize body movement but even though these methods are and have been very popular, they have certain limitations. If glue is used, only a single animal can be immobilized at a time thereby making the process very labor-intensive and low-throughput. Therefore, the 'glue' technique makes the immobilization of a large population of worms for simultaneously study impractical. Furthermore, it is a permanent method as the worms may not be released alive after they are glued. Chemical anesthetic compounds can be used to immobilize large worm populations but their effect on nematode physiology and overall toxicity is unknown [330]. Additionally, transferring the animals from their agar culture media to a coverslip or chip to either glue or anesthetize them can induce mechanical stress on them, thereby negatively impacting the biological process under observation with the study of aging being especially relevant here. Therefore, novel techniques that enable reversible immobilization, are minimally toxic and are easy to implement while eliminating any mechanical stress associated with plate transfers would be a great tool for performing studies that require simultaneous imaging of large worm populations.

Motivated by the unique ability of microfluidics to handle small-size biological objects, scientists have designed a variety of microfluidic devices for the precise manipulation of *C. elegans*. Chronis *et al.* [256] have developed microtraps that maybe used to immobilize worms before correlating their neuronal activity to their locomotion patterns while Chalasani *et al.* [254] used the same microtraps to image worm olfactory response. For immobilizing large worm populations simultaneously, Hulme *et al.* [239] developed an array of fixed size clamps that mechanically restrict movement. Rohde *et al.* [289] developed a two step approach using suction posts that maybe used to immobilize a single animal at a time. Zeng *et al.* [331] in turn further improved Rhode *et al.*'s device by integrating a deformable membrane for more stable immobilization. In these studies, immobilization was for a short time period (seconds) and in an environment different from the agarose medium on which they are normally cultured. To achieve prolonged immobilization, Chokshi *et al.* [270] developed a microfluidic approach for immobilizing *C. elegans* on-chip by creating a CO_2 micro-environment around the worm. Apart from allowing stable, long term immobilization (1-2 hours), the CO_2 method offers the additional advantage of minimizing photobleaching should fluorescent imaging be required during immobilization. However, the worms need to be serially loaded since it is possible to only image one animal at a time. Additionally, the worms need to be transferred from their agar culture plate and placed onto the chip before imaging can take place thereby applying some mechanical stress on the animal. Therefore, there is no existing method that allows for the simultaneous observation of entire worm populations that require extended periods of immobilization (tens of minutes) without displacing them from their culture medium.

Moreover, the different techniques available for the large scale fabrication of microfluidics devices such as micro-machining, soft lithography, embossing, in situ construction injection molding and laser ablation [332] require expensive equipment facilities, are labor intensive involving multiple step processes to make the final product and incorporating any design changes is time consuming. For small scale production of microfluidic devices for analysis in a laboratory environment, soft lithography, an expensive and multiple step process is the current gold standard. A quick and easy fabrication method for fluidic devices is highly preferred [333] as biologists may not necessarily have the time to learn the fabrication process and employing a process engineer is expensive [334]. Recent advancements in 3D printing in terms of resolution and speed have simplified the fabrication process for micro and millifluidics devices into a single step. 3D printing can now create intricate and minute layered structures that offer great topography flexibility that allows high precision construction of multi-layered channel networks in the range of 100- 300 μm with an accuracy of tens of microns [335] [336] [337].

Taking advantage of the advances made in 3D printing technology as well as the benefits of CO_2 immobilization as outlined by Chokshi *et al.* [270], we developed a 3D printed millifluidic device, the WormImm Plate, for immobilizing worm populations as they are grown and maintained on an agar surface. The device creates a high concentration CO_2 environment on the surface of the agar layer which ceases worm body movement and has been demonstrated to be appropriate for immobilizing worm populations for short periods of time (20-30 minutes). The method maybe used to immobilize worms of all ages from larvae to adults, is very easy to implement and allows quick post immobilization recovery within a few minutes. Moreover, the device architecture allows optical access to the immobilized worms through a transparent glass plate below the agar layer making the method compatible with low as well as high resolution optical microscopy techniques employing a transmitted light source.

9.2. Device design

The device has a modular design and incorporates 3D printed, annular, lower and upper chambers, a lid, a microporous PolyEthylene (PE) membrane gas diffuser, a Teflon light diffuser, a PolyMethylMethAcrylate (PMMA) window, Light Emitting Diode (LED) housing cap and an electronics control unit (Figure 9.1) .The lower chamber consists of a series of interconnected, milli-fluidic channels connected to a main gas (CO_2) inlet through a Luer connector interface. The micro-porous PE membrane gas diffuser which is also annular in shape is incorporated into the lower chamber and above the milli-fluidic channels. The upper chamber consists of an enclosed, continuous milli-fluidic channel, the walls of which have multiple (eight), equally spaced openings/windows that act as CO_2 outlets. The upper chamber is placed onto the lower chamber with the PE membrane in between separating the two chambers. A circular, optically transparent, 2 mm thick PMMA disk is inserted into the annular region in the center and rests on the lower chamber along its edges. A circular lid that houses four white LEDs with a notch at the side for allowing wiring from the LEDs to pass through is fitted onto the bottom of the lower chamber. A circular, 0.5 mm thick translucent Teflon optical diffuser disk is inserted over the PMMA disk. The LEDs are connected through wires to a 3D printed, electronics control box that consists of a micro USB rechargeable battery, a charging circuit board and a push button switch.

The gap between the top surface of the Teflon disk and the bottom of the CO_2 outlet windows creates a region that can accommodate a circular disk (diameter 37 mm, thickness 2 mm) of agar to be placed/molded into the region at the center of the device.

9.3 Principle of Operation

CO_2 (99.9% bone dry) enters the device through the main gas inlet from a gas cylinder with a regulated outflow pressure of 1.5 psi, flows through the milli-fludic channels in the lower chamber, is slowed down by and passes through the PE micro-porous membrane gas diffuser. After passing though the membrane, the gas enters the upper chamber and then exits through the outlet windows thereby creating a high gas concentration above the agar layer containing the worm population on its surface. This high concentration CO_2 environment that is created by the membrane diffuser induces an almost immediate immobilization effect on the entire worm population. The Teflon sheet diffuses white light from the LEDs at the bottom which enables viewing the worms with dark field illumination under a stereoscope/ camera microscope. The LEDs are powered by a micro USB rechargeable battery that can be manually turned on and off using a toggle switch in the electronics control unit (Figure 9.1). Given the modular architecture, the LEDs at the bottom maybe easily removed and the device can also be used with a microscope with external illumination.

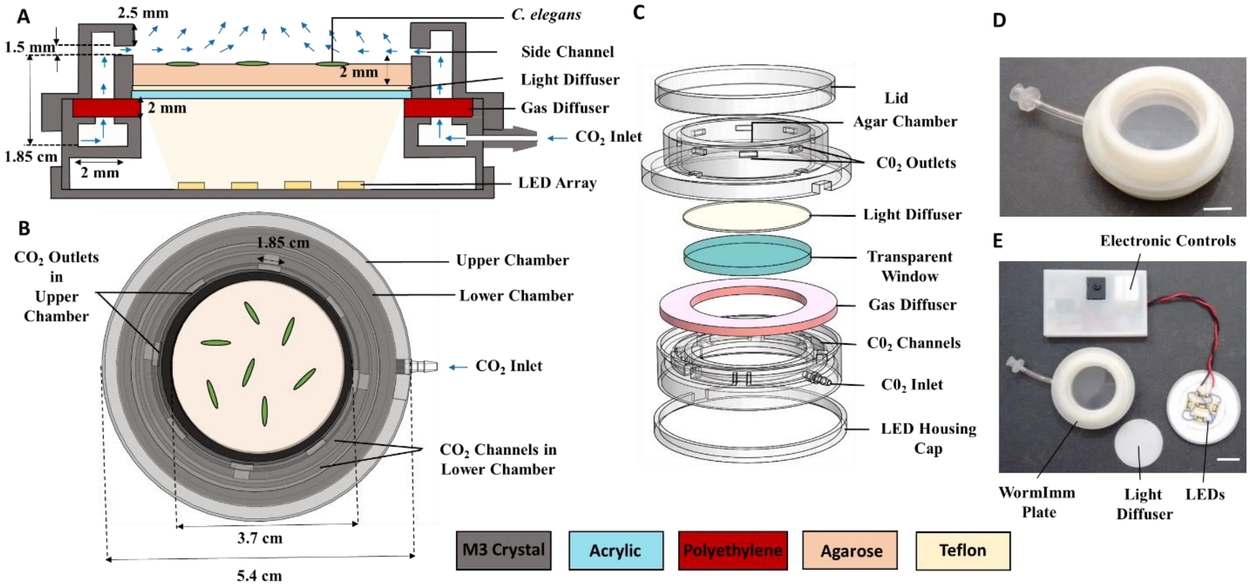

Figure 9.1: (A) Cross sectional schematic of the device assembly, components of the electronics control unit with device dimensions and CO$_2$ flow (blue arrows). (B) Top view of the device showing CO$_2$ flow (blue arrows). (C) Exploded view of the device components. The gas diffuser, light diffuser and transparent window are not 3D printed. (D) Photograph of the WormImm plate showing upper and lower chambers, main CO$_2$ inlet, transparent PMMA base and CO$_2$ outlet windows (scale bar, 1 cm). (E) Photograph of the device with electronics control unit showing LEDs placed on the housing cap (scale bar, 1.5 cm).

When the CO$_2$ supply is turned off, the worms recover within several minutes and continue to grow on the agar surface.

9.4 Fabrication

The upper and lower chambers were 3D printed using the Fused Deposition Modeling (FDM) [180] method on the ProJet 3500 HD Max printer. During the printing process, polymer materials are heated and ejected from the nozzles of the inkjet printer onto an aluminum build plate. The print was performed vertically upwards with a layer resolution of 16 µm in the axial direction and 32 µm in the lateral resolution. Building (VisiJet EX 200, 3D Systems Inc., Rock Hill, SC, USA) [181] and sacrificial materials (VisiJet S100, 3D Systems Inc., Rock Hill, SC, USA) [182] were deposited alternatively from the dual nozzles to form the printed parts, in which the building material defines the solid structures in the device, while the sacrificial material occupies the hollow channels/cavities. Upon completion of the printing process, the 3D structure and the aluminum plate were placed in a refrigerator at 4 °C for 20 minutes to easily remove the structure from the plate. The structure was then subjected to a post-printing procedure to remove the sacrificial material. First, the entire 3D-printed sample was immersed in a mineral oil (Bayes® high performance food-grade mineral oil) bath at 60 °C while sonicating at ~ 45 kHz for 2 hours to dissolve the sacrificial material. Second, the residual mineral oil was removed by thoroughly washing the parts in detergent soap and water (both at 60 ^{0}C, sonicated at ~45 kHz) baths in sequence. The structures were then air dried for 24 hours to remove any water remaining inside the milli-fluidic channels/cavities.

A commercially available micro-porous PE sheet (1/8in. UHMW porous polyethelene, Genesee Scientific) was machined with a Computer Numeric Controlled (CNC) mill to create the annular membrane gas diffuser. The membrane gas diffuser was incorporated on top of the milli-fluidic channels in the lower chamber by securing its sides to the walls at the periphery of the lower chamber with Loctite super glue, an adhesive which creates a permanent bond between plastics. After air drying for 24 hours which is the time required by the adhesive to attain maximum bond strength, the bottom of the upper chamber was then glued to the lower chamber and the membrane towards the periphery using the same adhesive. A commercially available transparent PMMA sheet and translucent Teflon sheet were CNC machined to create the circular optical base and light diffuser respectively.

9.5 Results and discussion

To visualize the immobilizing effect of the proposed method on worm populations, we obtained video recordings of the movement of individual worms on the device. As part of the experimental procedure, worms were loaded onto the agar surface of the device and were immobilized using CO_2 supplied to the main inlet from a compressed gas cylinder with a pressure of 1.5 psi. We tracked over time, the absolute distance moved by the tip of the head of each worm in between the video frames (Figure 9.2B) before, during and after immobilization. The worms were initially active before immobilization and became immobile in the presence of CO_2 (immobilization periods up to 20 minutes were performed) flowing through the device. Once CO_2 flow was turned off, the worms recovered back to their initial level of activity pre immobilization as shown in Figure 9.2A. As part of the control experiment, we also recorded on-device, the movement of individual worms with air supplied to the main inlet with a pressure of 1.5 psi. From Figure 9.2B, it maybe observed that the worms continued to crawl around even with air flowing through the device and it can therefore be concluded that the presence of CO_2 is the dominant factor that causes immobilization. As the flow rate of any gas (air and CO_2) is substantially reduced by the PE membrane diffuser, it is unlikely to significantly affect worm locomotion. Furthermore, the membrane diffuser creates a high concentration of CO_2 on the surface of the agar thereby anesthetizing the worms. Given that the bacterial lawn was located at the center of the agar layer, worm movement was mostly clustered around this food source prior to immobilization. If the bacterial lawn were to be spread uniformly, we anticipate that the size of the region accommodating the agar layer (circular region of diameter 3.7 cm as shown in Figure 9.1B) is small enough for CO_2 to be distributed equally over the agar layer and not cause any significant differences in the quality of immobilization in worms located towards the periphery and at the center. However, if the size of the device is substantially increased, movement seen in worms that are distributed across the agar layer must be characterized to determine differences in quality of immobilization, if any.

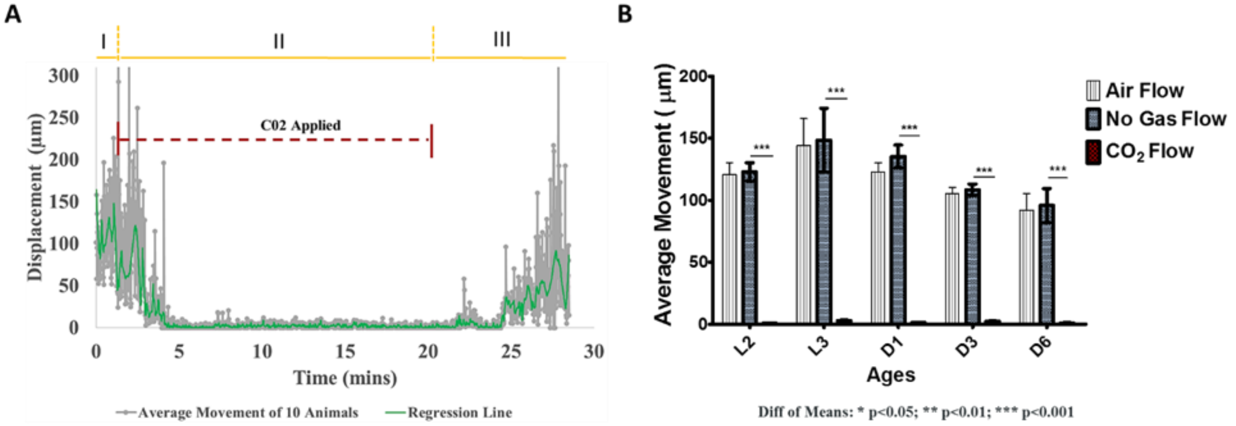

Figure 9.2: Effect of on-device exposure to CO_2 on worm movement. (A) Absolute distance moved by the tip of the head in age L2 over time (acquired before (I), during (II) and after (III) CO_2 immobilization). The grey line represents average distance moved between frames for ten L2 larvae. The solid green line represents best fit by non-parametric regression using locally weighted scatterplot smoothing. (B) Bar graphs showing the average of distances moved by the tip of the head in ages L2, L3, D1, D3 and D6 in between video frames (1.3 frames per second**)** collected over 15 minutes. The videos were collected with worms loaded on the 3D printed device with air flowing through the chip (at 1.5 psi gas pressure), with CO_2 flowing through the chip (at 1.5 psi gas pressure) as well as with neither air nor CO_2 flowing through the device respectively. Error bars indicate standard error of mean of measurements taken from ten worms imaged on the same device.

To evaluate the effectiveness of the proposed method to immobilize worm populations belonging to different developmental stages, we acquired videos of worm populations loaded onto the agar surface in the device before, during and after the application of CO_2 flow (Section

9.6.2).The absolute distance moved in between the video frames by the tip of the head, tail and the center of each worm body (Figure 8.3A) before, during and after immobilization was then tracked over time using a video processing software (Section 9.6.2). The experiment was performed for synchronized populations of worms belonging to L2, L3, D1, D3 and D6 developmental stages. For every developmental stage, worms were active before immobilization and freely crawling all over the agar surface. However, when CO_2 flow was introduced through the device, worm locomotion was drastically reduced in under 0.5 minutes. Even though the worms were not able to crawl over the agar surface and became fixed in position with respect to each other, some movement was still observed, especially at the head region (Figure 9.3A). With CO_2 flow through the device maintained for 20 minutes, the movement of the worms dropped off sharply and then settled to lie within a variation of 10% in under 2.5 minutes for all developmental stages. Upon removing the flow of CO_2, the worms seem to fully recover to their initial activity level within 10 minutes for all developmental stages. This is further supported by the fact that there is no statistically significant difference between the average movement speed (Section 9.6.3) computed 10 minutes before and 10 minutes after CO_2 flow is turned off post the 20 minute immobilization period, as shown in Figure 9.4.

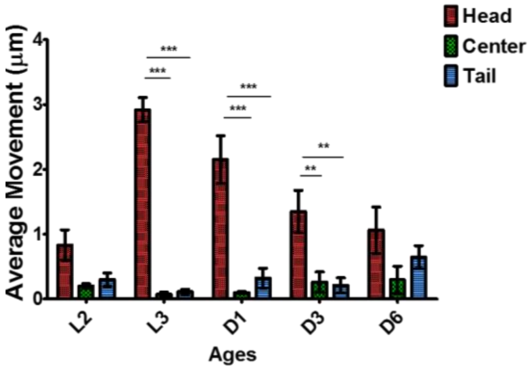

Diff of Means: *p<0.05; **p<0.01; ***p<0.001

Figure 9.3: Effect of on-device exposure to CO_2 on worm head, tail and mid-body movement. Bar graphs showing the average of distances moved by the tip of the head, center of the body and tail in ages L2, L3, D1, D3 and D6 in between video frames collected over 15 minutes. The videos were collected with worms loaded on the 3D printed device with CO_2 flowing through the chip (at 1.5 psi gas pressure). Error bars indicate standard error of mean of measurements taken from ten worms imaged on the same device.

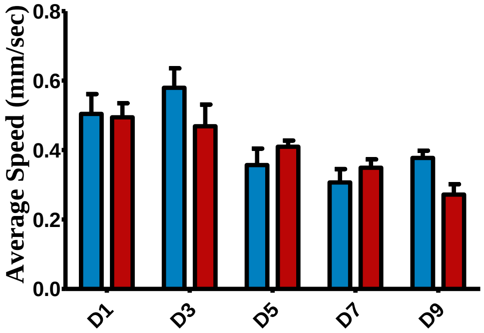

Figure 9.4: Effect of on-device exposure to CO_2 on worm speed. Bar graphs showing the average speed of the tip of the head in ages D1, D3, D5, D7 and D9 in between video frames collected over 10 minutes before and after CO_2 flow through the device is turned on (1 pixel corresponds to 10 mm). D stands for Day. Error bars indicate standard error of mean of measurements taken from ten worms imaged on the same device. All p values are greater than 0.5.

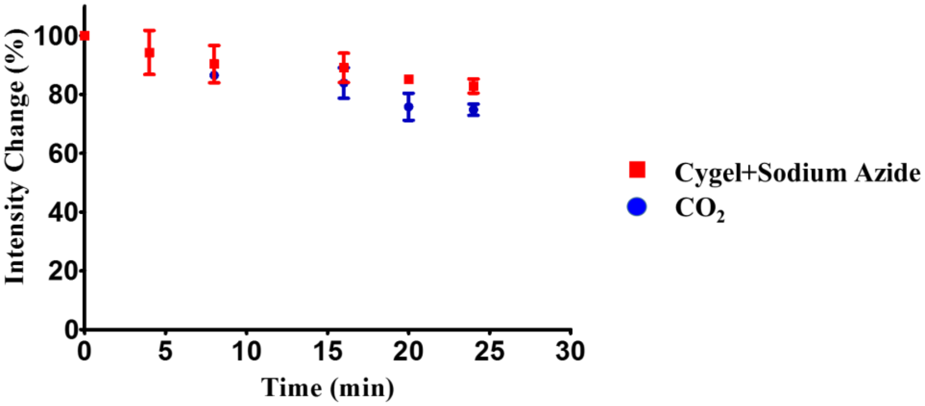

Figure 9.5: Photobleaching following on-device exposure to CO_2. Line plots showing photobleaching of GFP-expressing neurons during CO_2 immobilization and immobilization with Cygel and sodium azide respectively. Line plots shows percentage change in fluorescence intensity over time with respect to the intensity measured at start of imaging. Error bars represent standard error of mean from ten worms imaged on the same device.

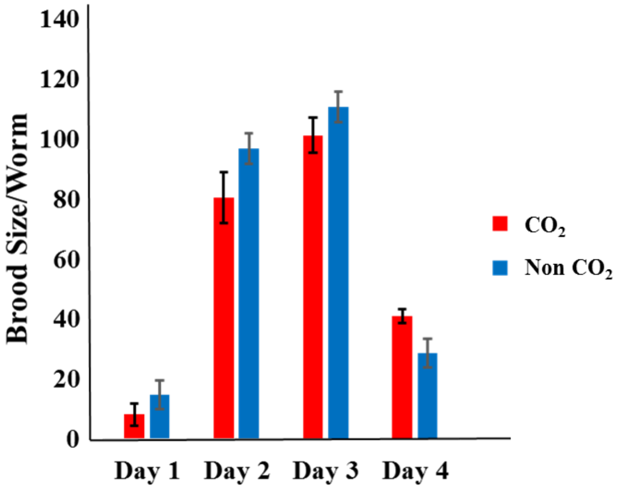

Figure 9.6: Brood size following on-device exposure to CO$_2$ during development**.** Total brood size was determined from 21 worms exposed for 20min in CO$_2$ every 18-20 hrs during their passage from L1 to L4 larval stage. Values represent the mean for each condition. Error bars indicate standard error of mean of measurements taken from 17 naïve worms imaged on the same device. All p values are greater than 0.5.

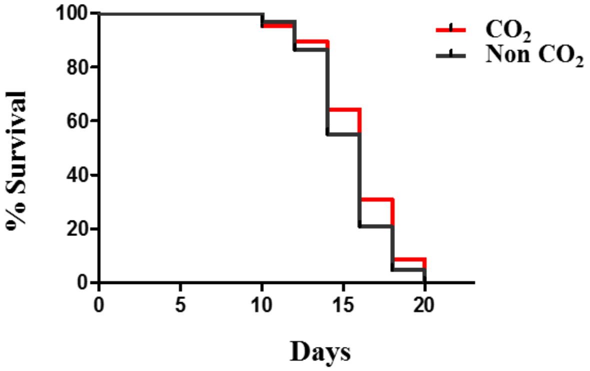

Figure 9.7: Lifespan following on-device exposure to CO$_2$ during development. Worms were exposed for 20 min to CO2 every 18-20 hrs during their passage from L1 to L4 larval stage. Median survival: non CO$_2$ = 16, (n=127); CO$_2$ = 16, (n=125).

To test to what extent the CO$_2$ application affects *C. elegans* physiology, we tested the fecundity and lifespan of worms by exposing them to CO$_2$ during their developmental stages. Given that larval developmental stages are more sensitive to any changes in their environment, stages L1 through L4 were exposed to CO$_2$. We did not observed any statistically significant differences (all p values are greater than 0.5) on the brood size of worms during their reproductive period (Day1 to Day 4 of adulthood) (Figure 9.6).

It has been shown that exposure of worms in the early developmental stages to elevated concentrations of CO_2 (19%) over hours at a time extends lifespan [338]. However, for the same CO_2 exposure protocol that was used for studying the effect of the WormImm Plate on progeny which was limited to just 20 minutes, we did not see any effect of $C0_2$ on the mean lifespan of worm populations (Figure 9.7) (all p values are greater than 0.5).

Furthermore, we studied the effect of the CO_2 environment on photobleaching of fluorescent markers to test the applicability of CO_2 immobilization for long term observation of worms on agar media. Photobleaching was quantified by imaging fluorescent YPF-expressing motor neurons (Figure 9.5). Upon immobilization, the fluorescent intensity of the neuronal cell body was recorded over 20 minutes. As part of the control, the same experiment was repeated by attaching the worms to a glass cover slip using a combination of Cygel and an anesthetic (10mM of sodium azide) which is the more conventional, non-microfluidic approach that is known to be popularly employed [339]. A ~25% reduction in the fluorescent intensity was observed in a CO_2 environment at the end of the 20 minute period. This is comparable to the ~20% reduction observed with the non-microfluidic cygel-sodium azide based immobilization approach.

9.6 Experimental methods

9.6.1 *C. elegans* maintenance, lifespan assay and fecundity.

Standard procedures were followed for *C. elegans* strain maintenance [229]. Nematode Growth Medium (NGM) agar was aseptically poured into the 3D printed device on top of the Teflon disk to a maximum thickness of 2 mm just below the level of the CO_2 outlet windows. Lifespan studies were performed at 20 ^{0}C in the presence of FuDR [340] that made the worms sterile. Worms were exposed for 20 min to CO_2 every 18-20 hrs during their passage from L1 to L4 larval stage. Survival was scored every 2 days, and worms were censored if they crawled off the plate, hatched inside, or lost vulva integrity during reproduction. Survival plots were generated using GraphPad Prism. The log-rank (Mantel-Cox) test was performed to determine statistical significance.

For the same CO_2 exposure protocol, the brood size was measured by individually placing worms in plates at 20 ^{0}C at the L4 stage and then moving them to new plates every 18-20 hours until Day 4 of adulthood. Live offspring were counted at each time point after adults were removed to new plates. A one-way ANOVA and t-test pairwise analysis was performed to determine statistical significance.

9.6.2 Quantification of worm locomotion pattern

The experiments to characterize worm movement (Figures 9.2 and 9.3) were performed using a camera microscope (200X 0.3MP 8-LED Zoom USB Digital Microscope) at 135x magnification. A grayscale real-time video stream of worm movement was obtained (1.3 frames/sec) and analyzed in the image processing software Metamorph. Worm body movement was tracked by the software that extracted the coordinates of points chosen at the tip of the head, tail as well as on the mid-section of each individual worm's body (optical pixel resolution of microscope: 2.35 µm).

A one way ANOVA test followed by Tukey's multiple comparison test was performed to test the significance of the difference in mean of average movement measurements (Figure 9.2B) from the head between using the WormImm Plate with CO_2 flow, no CO_2 flow and air flow through the device.

A one way ANOVA test followed by Tukey's multiple comparison test was performed to test the significance of the difference in mean of average movement measurements (Figure 9.3) from the head, body and tail while using the WormImm Plate with CO_2 flow through the device.

9.6.3 Speed measurement

Worms were placed on the device and CO_2 was applied for 20 minutes. The movement of individual worms were recorded (1.3 frames per second, optical pixel resolution of microscope: 10 mm) using a camera microscope (200X 0.3MP 8-LED Zoom USB Digital Microscope) for 10 minutes prior to and 10 minutes after the CO_2 application period. Worm body movement was tracked in Metamorph that extracted the coordinates of points manually chosen at the tip of the head. Speed was estimating by dividing the distance moved by the tip of the head in between consecutive frames with the time to acquire an image frame.

The two tailed unpaired non parametric Man-Whitney test was performed to test the significance of the difference in mean of average movement measurements (Figure 9.4) from the head before and after CO_2 immobilization.

9.6.4 Fluorescence imaging

The fluorescence imaging experiments were performed using an epifluorescent stereoscope (8X-50X Track Stand Stereo Zoom Parfocal Trinocular Microscope) at 25x magnification. An image processing software (Metamorph) was used to calculate the average fluorescence intensity relative to the average intensity recorded at time t=0 from the real-time video stream captured with an exposure time of 60 ms for each frame. A back-illuminated camera (QUANTEM:512SC, Photometrics) was used to acquire the video stream.

9.7 Conclusions

We developed a simple to use, practical, hybrid 3D printed milli-fluidic tool for immobilizing entire populations of the roundworm *C. elegans* as they are grown and maintained on an agar surface. A CO_2 environment is created on demand at the surface of the agar layer that causes a near immediate immobilizing effect on the worms. Our results indicate that the method is appropriate for short-term (20-30 minutes) immobilization which is sufficient for performing several experiments on entire worm populations like scoring lifespan assays, counting and observing ageing while performing fluorescence imaging under a stereoscope. The method offers the additional advantage of observing worm populations without mechanically manipulating or disturbing them as they continue to grow on the agar surface. Furthermore, with minor dimensional modifications to device architecture, we envision the use of this method in a wide variety of higher resolution biological imaging studies in *C. elegans*, including cellular developmental and neuronal regeneration studies. Moreover, the device architecture allows optical access to the immobilized worms through a transparent glass plate below the agar layer making the method compatible with low as well as high resolution optical microscopy techniques employing a transmitted light source.

CHAPTER 10

CONCLUSIONS AND FUTURE DIRECTIONS

10.1 Conclusions

The important contributions of Part B in this thesis include:

10.1.1 Cry-larva chip

The thesis presents the development and characterization of a microfluidic method for immobilizing *Drosophila melanogaster* larvae and the results indicate that it is appropriate for repeated short-term (less than 10 minutes) immobilization sessions, with immobilization sufficient to perform high resolution imaging of sub-cellular structures. A microfluidic cryo-larva chip is used to create a low-temperature micro-environment to deliver a combination of mechanical compression and cryo-anesthesia to immobilize individual larvae. The method is easy to implement, allows complete larval recovery and can be used to immobilize larvae of different developmental stages.

Besides demonstrating high resolution imaging of larval neuronal structures, the proposed immobilization approach may be used on a variety of other imaging applications including neuronal laser microsurgery for studying axon regeneration, neuronal circuits and time lapse imaging for studying synapse development. Poor survival has limited the successive imaging of the same *Drosophila* larvae across developmental stages without the use of anesthetics [305] [306]. However, as already discussed in Chapter 8, the combined pressure/cooling immobilization of young larvae with the cryo-larva chip allowed for an acceptable level of survival while imaging young larvae across their developmental ages. This alone makes this technique of high value for developmental biologists. Although the focus of the results presented in the thesis was on the mitochondrial trafficking in neurons, the technique of local photo-conversion and trafficking that we were able to perform using this chip can be utilized for a variety of different long-term time lapse applications including imaging of subcellular trafficking, tracking of long range cell migration, and imaging proliferation dynamics.

10.1.2 The WormImm plate

The WormImm Plate is a simple to use, practical, 3D printed milli-fluidic tool for immobilizing entire populations of the roundworm *C. elegans* as they are grown and maintained on an agar surface by creating a CO_2 environment. As discussed in Chapter 9, the results indicate that the method is appropriate for short-term (20-30 minutes) immobilization which is sufficient for performing several experiments like scoring lifespan assays and performing fluorescence imaging under a stereoscope. With this method, worm populations can be observed without mechanically manipulating or disturbing them. The device architecture allows optical access to the immobilized worms through a transparent glass plate below the agar layer making the method compatible with low resolution optical microscopy techniques employing a transmitted light source. Finally, with minor dimensional modifications to device architecture, we envision the use of this method for higher resolution biological imaging studies in *C. elegans* as well.

10.2 Future directions

We envision that the work presented in Part B of this thesis chapter can be extended in the following research directions:

10.2.1 Cryo-larva chip

In all the time lapse imaging experiments that are presented in this chapter, the larvae were removed from the chip in between successive imaging sessions and maintained externally on a grape plate. However, the inclusion of food ports as part of device architecture provides the possibility to maintain animals on chip and in between imaging sessions, similar to Ghannad-Rezae *et al.*'s [1] studies, in which food is delivered every 30 minutes to keep larvae alive on chip for 10 hours. Apart from incorporating the ability to accommodate multiple larvae on the chip and computer enabled flow and Peltier control, employing the food ports will facilitate any attempt at transitioning to a more automated version of the system in the future to increase throughput.

Besides immobilizing *Drosophila* larvae, the cryo-larva chip has the potential to be used to study cellular biological events across developmental stages in other model organisms like *C. elegans*. Immobilization of *Drosophila* larvae is more difficult than that of *C. elegans* as they are much larger in size and therefore exert stronger body forces. Additionally, even if the outer larval body is completely immobilized by physical encapsulation, imaging internal organs of interest such as the CNS (Central Nervous System) capsule is extremely challenging as they can freely move inside the hemolymph-filled body cavity. Given that the proposed method successfully immobilizes *Drosophila* larvae for high resolution imaging, it is extremely likely that with minor modifications to the device architecture, the method will prove to effectively immobilize *C. elegans* as well, thereby expanding its potential applications.

10.2.2 The WormImm plate

It was observed that the worms were significantly immobilized within 1–2 minutes upon CO_2 flow being turned on through the device. This delay might be the time that CO_2 requires to diffuse into the chamber and displace the air content from above the agar layer. However, this hypothesis needs to be validated by measuring the exact concentration of CO_2 on top of the agar layer that the animals are being exposed to by using a pH sensitive dye such as thymol blue.

Even though it was observed that air flowing into the device with a pressure of 1.5 psi caused no appreciable change in worm movement, increasing the flow rate by increasing gas pressure (5 psi) did produce some noticable slowing of body movement. This could be due to the mechanical pressure exerted by the air flowing against the worm’s body which is a hypothesis that needs to be validated in future experiments. To our knowledge there has not been a systematic investigation of how the rate of change of air flow influences movement response in *C. elegans* and must be further characterized. If at higher flow rates, the quality of immobilization is acceptable, the response and recovery times are fast and if there is no significant impact on progeny and lifespan, then CO_2 could potentially be replaced by air thereby eliminating any physiological effects of CO_2 while further simplifying the implementation of the WormImm Plate.

Even though there was no visible effect on progeny and lifespan with the worms exposed to CO_2 during their early developmental stages, tests on adult *C. elegans* are needed to conclusively investigate CO_2 exposure effects on egg laying and lifespan. It also needs to be determined if *E. coli*, the food source of *C. elegans*, get affected by CO_2 or not.

Furthermore, instead of using commercially available PE, the gas diffuser maybe 3D printed with a porous material such as PORO-LAY LAY-FOMM in which case the entire device will be 3D printed.

Last but not the least, alternate applications of the WormImm plate could be explored. For instance, the device could be used as a behavioral assay by incorporating the ability to locally vary the temperature across the plate to study thermostaxis [341] followed by the quantification of fluorescence at the population level post CO_2 immobilization. Similarly, by incorporating different wavelength LEDs [342], the response of a population to light maybe determined. Finally, the device maybe easily modified to create gas concentration gradients by administering multiple gases at the same time or administer volatile compounds mixed with air followed by the observation of the worm decision making process in response to these altered environmental stimuli [343].

APPENDICES

APPENDIX A: OPTO-MECHANICAL PRESSURE MICROSENSORS FOR MONITORING INTRAOCUALR PRESSURE

Section A1: Procedure for preparing QD-PMMA mixture

1. The master solution is prepared by manually stirring 10 g of Poly (Methyl Methacrylate) (PMMA) with 50 mL of Methyl Methacrylate (MMA).
2. 5 mL of the master solution is mixed with 5 g of MMA by manually stirring.
3. 225mg of ground Benzoyl Peroxide (BP) is added to the solution created in step 2 and stirred until BP gets dissolved (Warm to 40^0C if necessary to aid dissolution and then bring back to room temperature).
4. Add dropwise 1.5 mL of QD in organic solvent (toluene) to 1.5 mL of the solution from step 3 with constant manual stirring.
5. Place the mixture created in step 4 in a water bath at 90^0C, for 5 min then transfer the mixture to 60^0C bath for 20 minutes. Evaporation of organic solvent is minimized by capping the mixture.

Section A2: Procedure for patterning the QD micropillars

1. Spread PMMA (950 A2) at 500 rpm for 5 seconds followed by spinning at 3000 rpm for 30 seconds to obtain a layer that is approximately 100 nm thick.
2. Bake on a hot plate at 150^0C for 10 minutes.
3. Spread the QD (840 nm)-PMMA mixture (prepared in section A1) at 500 rpm for 5 seconds followed by spinning at 3000 rpm for 30 seconds to obtain a layer that is approximately 100 nm thick.
4. Bake on a hot plate at 110^0C for 10 minutes.
5. Spread SU-8 2010 at 500 rpm for 5 seconds followed by spinning at 3000 rpm for 30 seconds to obtain a layer that is 8 µm thick.
6. Bake on a hot plate at 95^0C for 2.5 minutes.
7. Expose to UV light via the appropriate mask using the ‘soft contact’ mode for approximately 10 seconds.

8. Perform post exposure bake on a hot plate at 95^0C for 3.5 minutes.

9. Spread PMMA (950 A2) at 500 rpm for 5 seconds followed by spinning at 3000 rpm for 30 seconds to obtain a layer that is approximately 100 nm thick.

10. Bake on a hot plate at 110^0C for 10 minutes.

11. Spread the QD (940 nm) -PMMA mixture (prepared in section A1) at 500 rpm for 5 seconds followed by spinning at 3000 rpm for 30 seconds to obtain a layer that is approximately 100 nm thick.

12. Bake on a hot plate at 110^0C for 10 minutes.

13. Spread SU-8 2002 at 500 rpm for 5 seconds followed by spinning at 4000 rpm for 30 seconds to obtain a layer that is approximately 1.5 µm thick.

14. Bake on a hot plate at 95^0C for 1 minutes.

15. Expose to UV light via the appropriate mask using the ‘soft contact’ mode for approximately 4 seconds.

16. Perform post exposure bake on a hot plate at 95^0C for 2 minutes.

17. Develop with SU-8 developer for approximately 15 seconds.

18. Perform RIE (1-2 minutes) to remove PMMA deposited around the QD micropillars.

APPENDIX B: A 3D PRINTED TOUCH-ACTIVATED SANITIZER DISPENSING SYSTEM FOR IMPROVING HAND HYGIENE

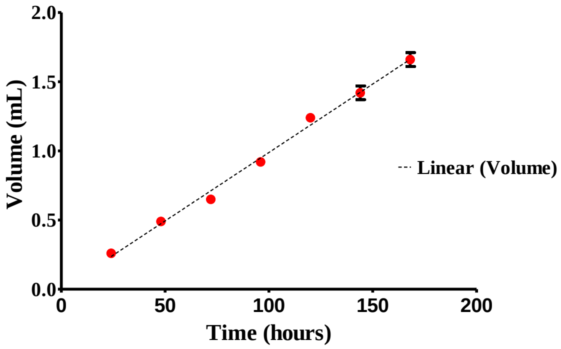

Figure B1: Plot showing volume of liquid disinfectant lost due to evaporation from the 3D printed device over time. The dashed line represents best fit by linear regression and the square of the correlation coefficient R demonstrates a good linear relationship between liquid volume and time. Error bars indicate standard error of mean (SEM) of three measurements performed on the same device.

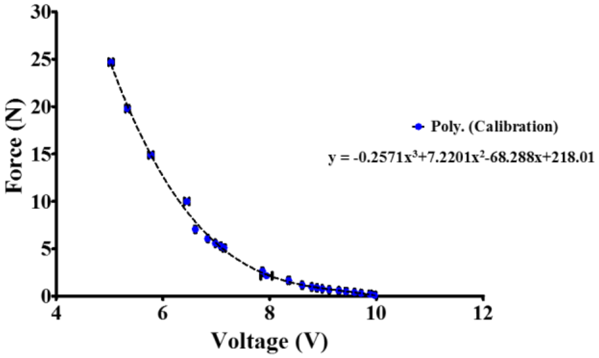

Figure B2: Calibration plot showing applied force versus measured voltage. The solid line represents best fit by a third-order polynomial. Error bars indicate standard error of mean (SEM) of three measurements performed on the same device and is represented by the data points.

Table B1: Material properties of M3 Crystal

Material Properties	**Value**
Elastic Modulus	1463 MPa
Poisson's Ratio	0.35
Mass Density	1020 kg/m^3
Yield Strength	42.4 MPa

Section B1: Formulae for coil compression spring fatigue analysis

Table B2: List of parameters for evaluating fatigue performance

Symbol	**Definition**	**Value**
F_{max}	Maximum cyclic force	1.269 N
F_{min}	Minimum cyclic force (preload)	0.729 N
D	Spring mean diameter	0.05 in
d	Wire diameter	0.007 in
S_{ut}	Ultimate tensile strength of material	2840 MPa

Force Amplitude F_a:

$$F_a = \frac{F_{max} - F_{min}}{2} \quad \text{---------- (1)}$$

Midrange force F_m:

$$F_m = \frac{F_{max} + F_{min}}{2} \quad \text{---------- (2)}$$

Spring outer diameter OD:

$$OD = D + d \quad \text{---------- (3)}$$

Spring inner diameter ID:

$$ID = D - d \quad \text{---------- (4)}$$

Spring index C:

$$C = \frac{D}{d} \quad \text{---------- (5)}$$

Whal factor K_w:

$$K_w = \frac{4C-1}{4C-4} + \frac{0.615}{C} \quad \text{---------- (6)}$$

Shear stress amplitude τ_a:

$\tau_a = K_w \frac{8F_a D}{\pi d^3}$ ---------- (7)

Midrange shear stress τ_m:

$\tau_m = K_w \frac{8F_m D}{\pi d^3}$ ---------- (8)

Torsional rupture strength S_{su}:

$S_{su} = 0.67S_{ut}$ ---------- (9)

Slope line r:

$r = \frac{\tau_a}{\tau_m}$ ---------- (10)

Amplitude strength component for infinite life (Shot peened)-(Zimmerli Data) S_{sa_zim}: 398 MPa (57.5 kpsi)

Midrange strength component for infinite life (Shot peened)-(Zimmerli Data) S_{sm_zim}: 534 MPa (77.5 kpsi)

Shear endurance limit according to Gerber (with Zimmerli Data) S_{se}:

$S_{se} = \frac{S_{sa\_zim}}{1-\left(\frac{S_{sm\_zim}}{S_{su}}\right)^2}$ ---------- (11)

Shear stress amplitude limit (According to Gerber failure criteria) S_{sa}:

$S_{sa\_lim} = \frac{r^2 S_{su}^2}{2S_{se}}\left[-1 + \sqrt{1 + \left(\frac{2S_{se}}{rS_{su}}\right)^2}\right]$ ---------- (12)

Shear endurance limit according to Goodman (with Zimmerli Data) S_{se}:

$S_{se} = \frac{S_{sa\_zim}}{1-\left(\frac{S_{sm\_zim}}{S_{su}}\right)}$ ---------- (13)

Shear stress amplitude limit (According to Goodman failure criteria) S_{sa}:

$S_{sa\_lim} = \frac{rS_{se}S_{su}}{rS_{su}+S_{se}}$ ---------- (14)

Shear stress amplitude limit (According to Sines failure criteria) S_{sa}:

$S_{sa\_lim} = S_{sa\_zim}$ ---------- (15)

Factor of safety against fatigue fos_f:

$fos_f = \frac{S_{sa\_lim}}{\tau_a}$ ---------- (16)

Section B2: Formulae for estimating critical frequency of coil springs

Table B3: List of parameters for evaluating critical frequency

Symbol	**Definition**	**Value**
D	Spring mean diameter	0.05 in
d	Wire diameter	0.007 in
ρ	Spring material density	0.284 lb./in^3
k	Spring rate	3.1 lbf./in
Na	Number of coils	11

Spring index C:

$$C = \frac{D}{d} \qquad \text{----------} (1)$$

Spring outer diameter OD:

$$OD = D + d \qquad \text{----------} (2)$$

Spring inner diameter ID:

$$ID = D - d \qquad \text{----------} (3)$$

Mass of the active coils m:

$$m = \frac{\pi^2 d^2 D N_a \rho}{4} \qquad \text{----------} (4)$$

Natural frequency of the spring f:

$$f = \frac{1}{2}\sqrt{\frac{k}{m}} \qquad \text{----------} (5)$$

Section B3: Formulae for estimating buckling of coil springs

Table B4: List of parameters for evaluating buckling performance

Symbol	**Definition**	**Value**
D	Spring mean diameter	0.05 in
α	End condition constant	0.5
E	Elastic modulus	203.4 GPa
G	Modulus of rigidity	82.7 GPa
L_f	Free Length	0.25 in

Spring stability condition:

$$L_f < \frac{\pi D}{\alpha}\left[\frac{2(E-G)}{2G+E}\right]^{\frac{1}{2}} \quad \text{----------} (1)$$

Factor of safety against buckling fos$_b$:

$$fos_b = \frac{\frac{\pi D}{\alpha}\left[\frac{2(E-G)}{2G+E}\right]^{\frac{1}{2}}}{L_f} \text{ ---------- } (2)$$

APPENDIX C: ON CHIP CRYO-ANEASTHESIA OF *DROSOPHILA* LARVAE FOR HIGH RESOLUTION IMAGING APPLICATIONS

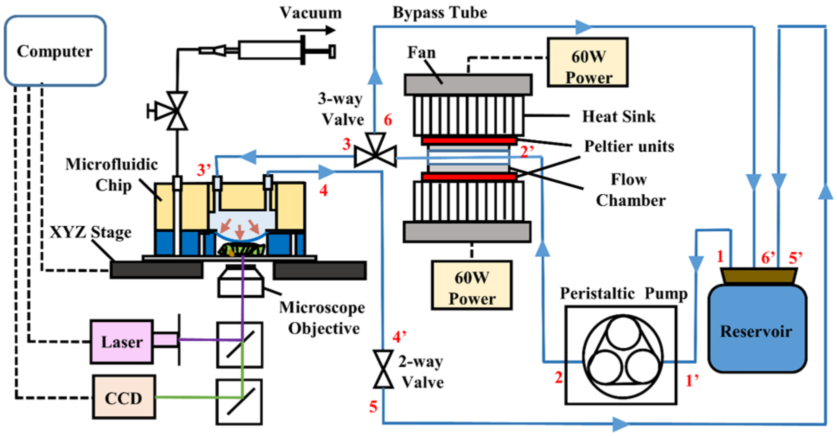

Tubing	Length	Material	Diameter
1-1'	57.4 cm	Polyvinyl	1.60 mm I.D. 3.18 mm O.D.
2-2'	73.9 cm	Polyvinyl	1.60 mm I.D. 3.18 mm O.D.
3-3'	14.0 cm	Polyvinyl	0.58 mm I.D. 0.97 mm O.D.
4-4'	14.0 cm	Polyvinyl	0.58 mm I.D. 0.97 mm O.D.
5-5'	105.2 cm	Polyvinyl	1.60 mm I.D. 3.18 mm O.D.
6-6'	81.0 cm	Polyvinyl	1.60 mm I.D. 3.18 mm O.D.
Pump Tubing	14.0 cm	Silicone rubber	2.03 mm I.D. 3.56 mm O.D.

Figure C1: Schematic diagram of the experimental setup highlighting the components of the cooling system. The table shows lengths, diameters and material for all tubing used to make fluidic connections.

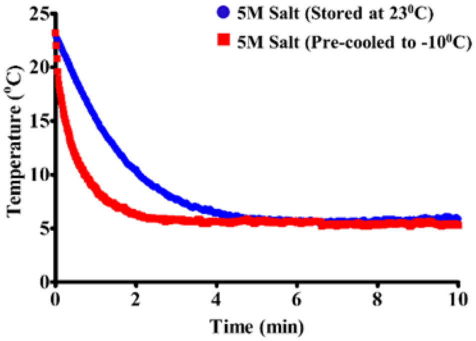

Figure C2: Average temperature of the immobilization microchamber in the chip versus time. After turning on the Peltier units, chilled coolant flow (3.2 ml/min) through the chip is started at 0 seconds with temperature of the coolant in the external reservoir being at 23 ^{0}C (room temperature) and -10 ^{0}C respectively (pre-cooled).

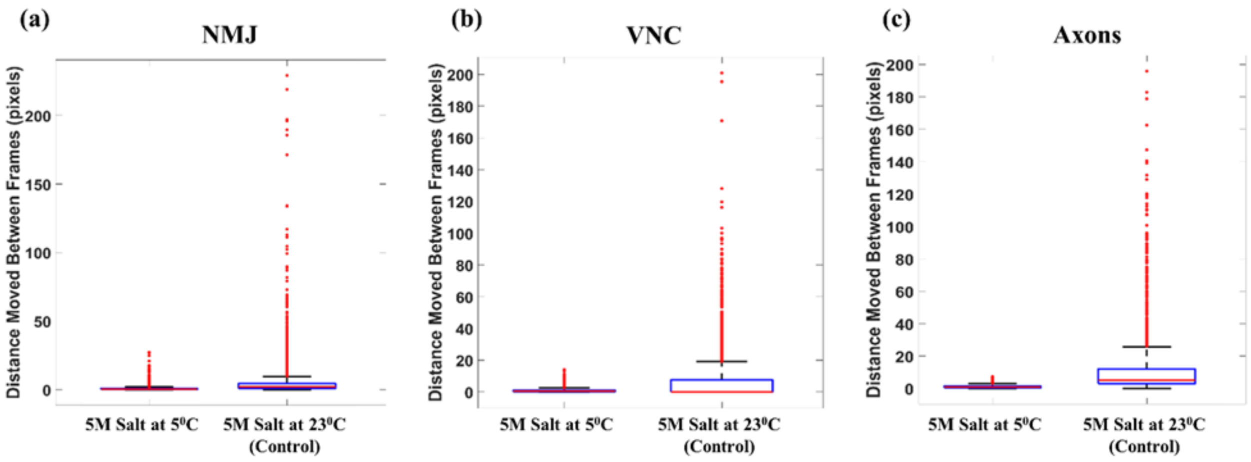

Figure C3: Box plots showing all distances moved in between frames by (a) mitochondria at NMJs, (b) cell bodies along VNCs and (c) mitochondria along axons in between video frames collected over 2 minutes for ten animals loaded onto the same chip. The videos were collected with larvae loaded on the microfluidic chip with chilled coolant (5M salt water solution) as well as with coolant at room temperature flowing (3.2 ml/min) through the chip respectively. Each box extends from the 25th to 75th percentiles, the line in the middle is plotted at the median and the whiskers span between the ends of the interquartile ranges to the furthest observations within the whisker length (1.5 times the interquartile range). Observations lying beyond the whiskers are displayed with a red + sign. Pixel resolution is 0.18 µm.

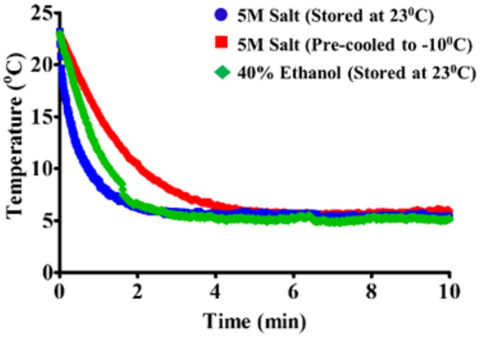

Figure C4: Average temperature of the immobilization microchamber in the chip versus time. After turning on the Peltier units, chilled coolant flow (at 3.2 ml/min) through the chip is started at 0 seconds with: (a) Temperature of 5M salt water solution in the external coolant reservoir being at 23 ^{0}C (room temperature), temperature of 5M salt water solution in the external coolant reservoir being at -10 ^{0}C (pre-cooled) and temperature of 40% ethanol solution in the external coolant reservoir being at 23 ^{0}C (room temperature) respectively.

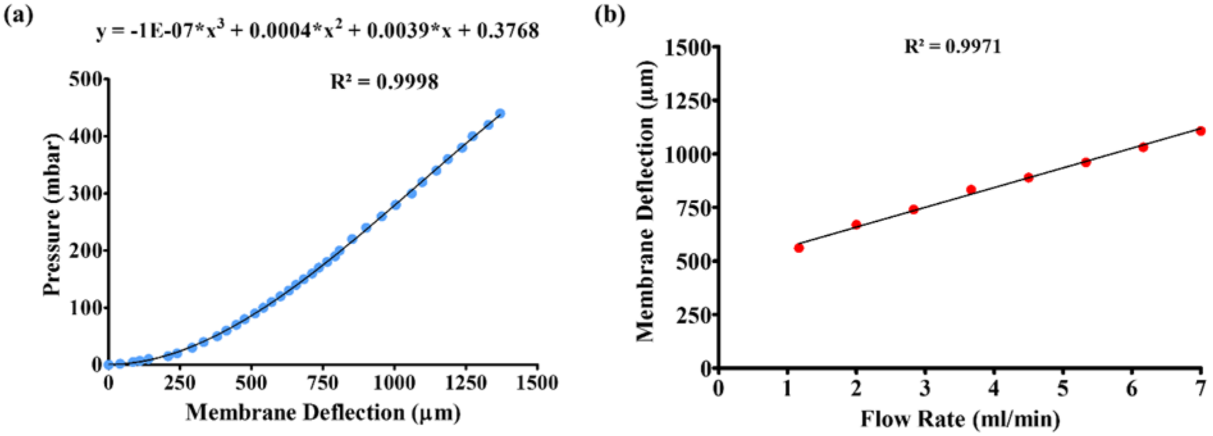

Figure C5: (a) Known (accurately controlled) applied static air pressure versus experimentally measured deflection of flexible PDMS membrane. The solid line represents a fit by a third-order polynomial. (b) Fluid (5M salt water solution) pressure exerted on the PDMS membrane versus known (accurately-controlled) fluid flow rate. The solid line represents best fit by linear regression. Error bars indicate standard deviation of three measurements performed on the same device and is given by the data point.

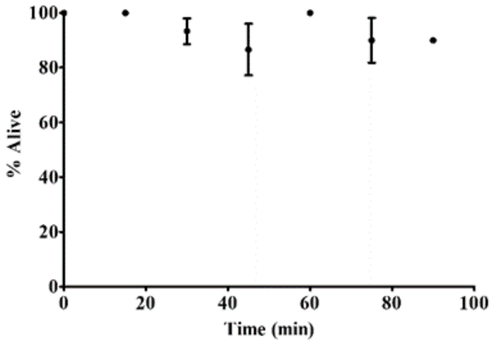

Figure C6: Survival rate versus time after six consecutive cycles. Error bars indicate standard deviation of ten animals.

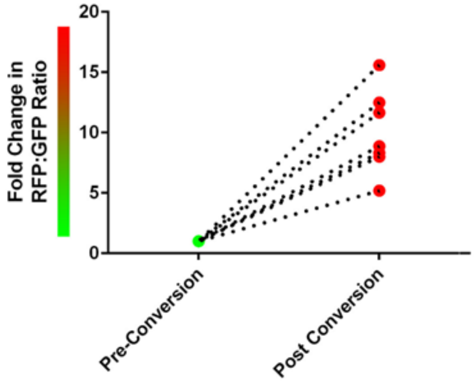

Figure C7: Conversion efficiency of seven individual VNCs as measured pre and post conversion in their red:green ratio of the average fluorescent intensities at the cell bodies. Fold change was compared to pre-conversion ratio.

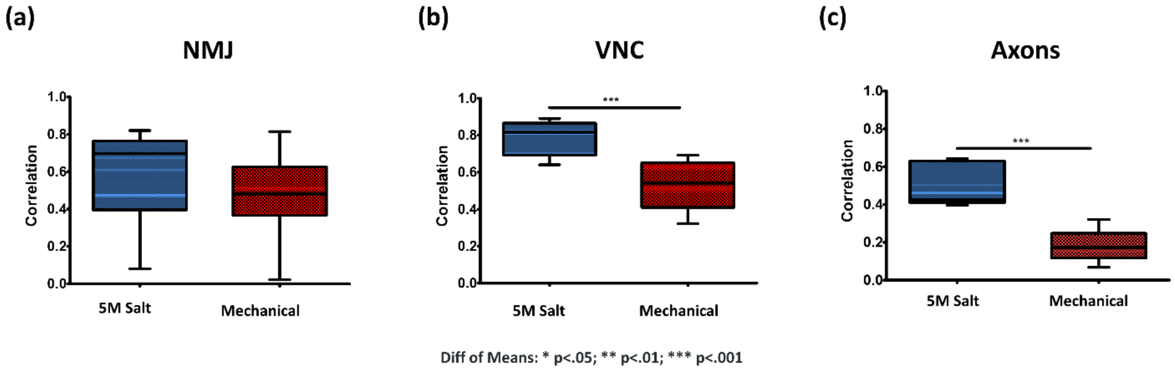

Figure C8: Box and whisker plots showing correlation of red and green channels of: (a) mitochondria at NMJs, (b) cell bodies along VNCs and (c) mitochondria along axons. The image frames corresponding to the red and green channels are 8 secs apart. The videos were collected with larvae loaded on the chip developed by Ghannad-Rezaie *et al.* [266] (mechanical) that performs mechanical immobilization and on the microfluidic chip with chilled coolant (5M salt water solution) flowing through the device. Each box extends from the 25th to 75th percentiles, the line in the middle plotted at the median and the whiskers span between the smallest and largest data values (ten measurements performed on the same device).

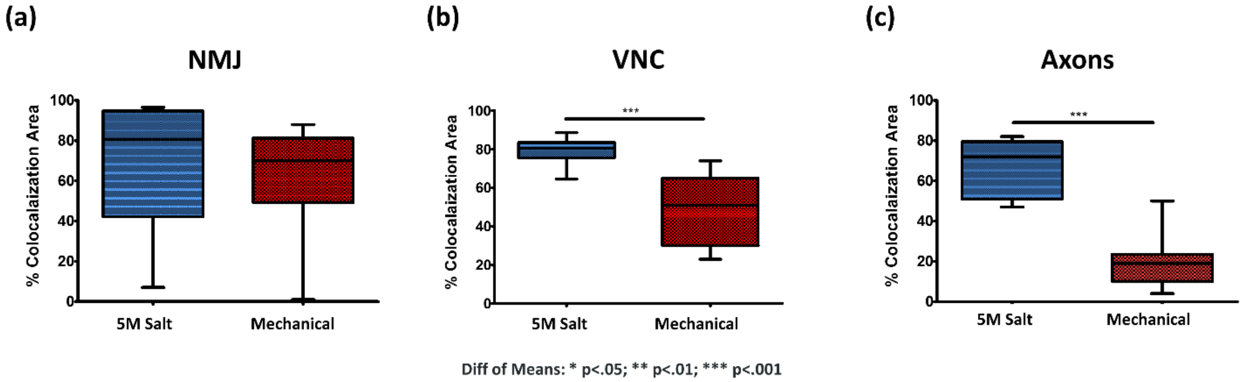

Figure C9: Box and whisker plots showing % area co-localized between red and green channels of: (a) mitochondria at NMJs, (b) cell bodies along VNCs and (c) mitochondria along axons. The image frames corresponding to the red and green channels are 8 secs apart. The videos were collected with larvae loaded on the chip developed by Ghannad-Rezaie *et al.* [266] (mechanical) that performs mechanical immobilization and on the microfluidic chip with chilled coolant (5M salt water solution) flowing through the device. Each box extends from the 25th to 75th percentiles, the line in the middle plotted at the median and the whiskers span between the smallest and largest data values (ten measurements performed on the same device).

Section C1: Procedure for microfabricating SU-8 molds

Layer 1:

1. Rinse the wafer with acetone, isopropyl alcohol and DI water. Dehydrate the wafer on a hot plate at 160 ^{0}C for 20 minutes.

2. Spread 3 mL of SU-8-2100 at 500 rpm for 30 seconds followed by spinning at 1350 rpm for 50 seconds.

3. Perform soft baking in the following sequence: 1) At room temperature for 4 hours. 2) Place wafer on a hot plate and ramp temperature from 20 ^{0}C to 65 ^{0}C with ramp rate of 10 ^{0}C/hours. Leave wafer at 65 ^{0}C for 5 hours. 3) Ramp temperature from 65 ^{0}C to 70 ^{0}C with ramp rate of 5 ^{0}C/hours. Leave wafer at 70 ^{0}C for 1 hour. 4) Ramp temperature from 70 ^{0}C to 75 ^{0}C with ramp rate of 5 ^{0}C/hours. Leave wafer at 75 ^{0}C for 1 hour. 5) Ramp temperature from 75 ^{0}C to 80 ^{0}C with ramp rate of 5 ^{0}C/hours. Leave wafer at 80 ^{0}C for 1 hour.

4. Expose to UV light via the appropriate mask (Figure C10) using the ‘soft contact’ mode for approximately 36 seconds.

8. Perform post exposure bake on a hot plate at 65 ^{0}C for 10 minutes and at 95 ^{0}C for 20 minutes.

9. Develop with SU-8 developer for approximately 10 minutes.

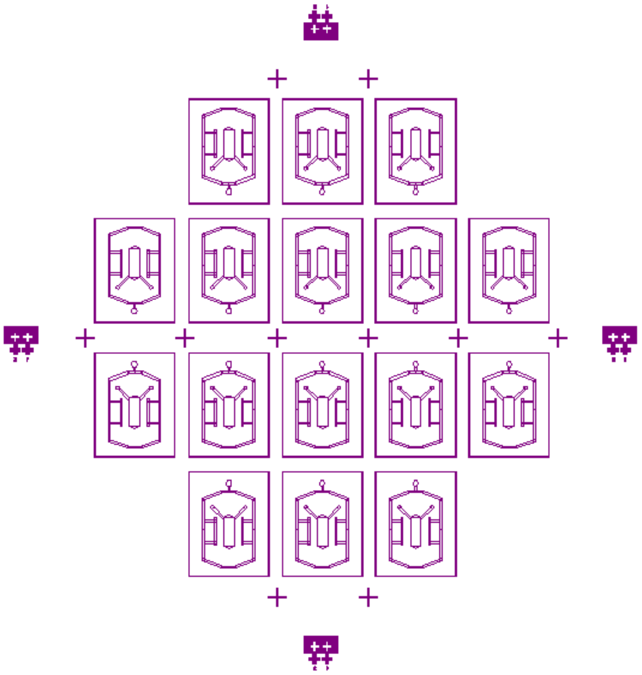

Figure C10: Mask layout for Layer 1 of the cryo-larva chip.

Layer 2:

1. Rinse the wafer with acetone, isopropyl alcohol and DI water. Dehydrate the wafer at 160 ^{0}C for 20 minutes.

2. Spread 3 mL of SU-8-2050 at 500 rpm for 30 seconds followed by spinning at 1300 rpm for 50 seconds.

3. Perform soft baking in the following sequence: 1) At room temperature for 4 hours. 2) Place wafer on a hot plate and ramp temperature from 20 ^{0}C to 65 ^{0}C with ramp rate of 10 ^{0}C/hours. Leave wafer at 65 ^{0}C for 5 hours. 3) Ramp temperature from 65 ^{0}C to 70 ^{0}C with ramp rate of 5 ^{0}C/hours. Leave wafer at 70 ^{0}C for 1 hour. 4) Ramp temperature from 70 ^{0}C to 75 ^{0}C with ramp rate of 5 ^{0}C/hours. Leave wafer at 75 ^{0}C for 1 hour. 5) Ramp temperature from 75 ^{0}C to 80 ^{0}C with ramp rate of 5 ^{0}C/hours. Leave wafer at 80 ^{0}C for 1 hour.

4. Expose to UV light via the appropriate mask using the 'soft contact' mode for approximately 30 seconds.

8. Perform post exposure bake on a hot plate at 65 ^{0}C for 10 minutes and at 95 ^{0}C for 20 minutes.

9. Develop with SU-8 developer for approximately 7 minutes.

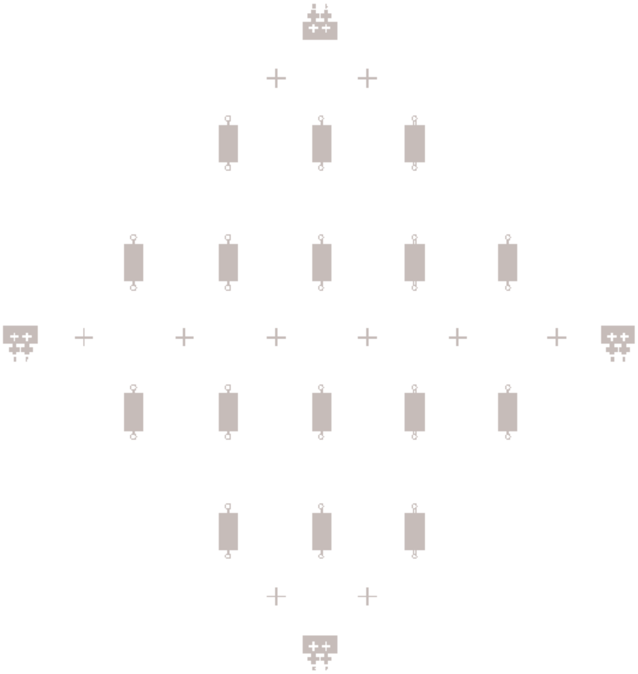

Figure C11: Mask layout for Layer 2 of the cryo-larva chip.

BIBLIOGRAPHY

[1] M. Ghannad-Rezaie, X. Wang, B. Mishra, C. Collins and N. Chronis, "Microfluidic Chips for In Vivo Imaging of Cellular Responses to Neural Injury in Drosophila Larvae," *PLOS One,* vol. 7, no. 1, 2012.

[2] K. Bazaka and M. V. Jacob, "Implantable Devices: Issues and Challenges," *Electronics,* vol. 2, no. 1, pp. 1-34, 2013.

[3] S. Majerus, S. Garverick, M. Suster, P. Fletter and M. Damaser, "Wireless, ultra-low-power implantable sensor for chronic bladder pressure monitoring.," *J. Emerg. Technol. Comput. Syst.,* vol. 8, p. 1–13, 2012.

[4] A. Cheng and L. Tereshchenko, "Evolutionary innovations in cardiac pacing.," *J. Electrocardiol.,* vol. 44, p. 611–615, 2011.

[5] Bolz, Kramme, R. Hoffmann and K. Eds., Cardiac Pacemaker Systems, Heidelberg, Germany: Springer, 2012, p. 767–783.

[6] S. Boveda, S. Garrigue, P. Ritter, Picichè and M. Ed, Dawn and Evolution of Cardiac Procedures, Milan, Italy: Springer, 2013.

[7] D. Halperin, T. Kohno, T. Heydt-Benjamin, K. Fu and W. Maisel, "Security and privacy for implantable medical devices.," *IEEE Pervasive Comput.,* vol. 7, p. 30–39, 2008.

[8] C. Stellbrink and H. Trappe, "The follow-up of cardiac devices: What to expect for the future?," *Eur. Heart J. Suppl.,* vol. 9, p. I113–I115, 2007.

[9] E. Pararas, D. Borkholder and J. Borenstein, "Microsystems technologies for drug delivery to the inner ear.," *Adv. Drug Deliv. Rev.,* vol. 64, p. 1650–1660, 2012.

[10] S. Lee, M. Park, C. Park, J. Lee, M. Prausnitz and Y. Choy, "Microchip for sustained drug delivery by diffusion through microchannels.," *AAPS PharmSciTech,* vol. 13, p. 211–217, 2012.

[11] C. Lowrie, M. Desmulliez, L. Hoff, O. Elle and E. Fosse, "Fabrication of a MEMS accelerometer to detect heart bypass surgery complications.," *Sens. Rev.,* vol. 29, p. 319–325, 2009.

[12] C. Stevenson, J. Jr Santini and R. Langer, "Reservoir-based drug delivery systems utilizing microtechnology.," *Adv. Drug Deliv. Rev.,* vol. 64, p. 1590–1602, 2012.

[13] H. Chirra and T. Desai, "Emerging microtechnologies for the development of oral drug delivery devices.," *Adv. Drug Deliv. Rev.,* vol. 64, p. 1569–1578, 2012.

[14] "Drugs.com," [Online]. Available: https://www.drugs.com/health-guide/implantable-cardioverter-defibrillator-icd.html.

[15] "Todays Medical Developments," [Online]. Available: http://www.todaysmedicaldevelopments.com/article/measuring-pulmonary-artery-pressures-cardiomems-6214/.

[16] "Med Gadget," [Online]. Available: https://www.medgadget.com/2006/05/the_northstar_s.html.

[17] "Wikipedia," [Online]. Available: https://en.wikipedia.org/wiki/Cochlear_implant.

[18] C. Dagdeviren, Y. Su, P. Joe, R. Yona, Y. Liu, Y.-S. Kim, Y. Huang, A. R. Damadoran, J. Xia, L. W. Martin, Y. Huang and J. A. Rogers, "Conformable amplified lead zirconate titanate sensors with enhanced piezoelectric response for cutaneous pressure monitoring.," *Nature Communications,* vol. 5, no. 4496, 2014.

[19] M. S. Mannoor, H. Tao, J. D. Clayton, A. Sengupta, D. L. Kaplan, R. R. Naik, N. Verma, F. G. Omenetto and M. C. McAlpine, "Graphene-based wireless bacteria detection on tooth enamel.," *Nature Communications* , vol. 3, no. 763, 2012.

[20] Y. S. Rim, S.-H. Bae, H. Chen, J. L. Yang, J. Kim, A. M. Andrews, P. S. Weiss, Y. Yang and H.-R. Tseng, "Printable Ultrathin Metal Oxide Semiconductor-Based Conformal Biosensors.," *ACS Nano* , vol. 9, no. 12, pp. 12174-12181, 2015.

[21] W. Gao, S. Emaminejad, H. Y. Y. Nyein, S. Challa, K. Chen, A. Peck, H. M. Fahad, H. Ota, H. Shiraki, D. Kiriya, D.-H. Lien, G. A. Brooks and R. W., "Fully integrated wearable sensor arrays for multiplexed in situ perspiration analysis.," *Nature,* vol. 529, p. 509–514 , 2016.

[22] W. Ko, "Early history and challenges of implantable electronics.," *J. Emerg. Technol. Comput. Syst.,* vol. 8, p. 1–9, 2012.

[23] C. Kennergren, "Reliability of cardiac implantable electronic device leads.," *Europace,* 2012.

[24] T. V. Lueder and H. Krum, "Current modalities for invasive and non-invasive monitoring of volume status in heart failure.," *Heart,* vol. 98, p. 967–973, 2012.

[25] M. Nkosi, F. Mekuria and S. Gejibo, "Challenges in Mobile Bio-Sensor Based mHealth Development.," *In Proceedings of the 13th IEEE International Conference on e-Health Networking Applications and Services, ColumbiaMO, USA, June,* pp. 21-27, 2011.

[26] F. Mancini, K. Mughal, S. Gejibo and J. Klungsoyr, "Adding Security to Mobile Data Collection.," *In Proceedings of the 13th IEEE International Conference on e-Health Networking Applications and Services, Columbia, Mo, USA, June,* p. 86–89, 2011.

[27] B. Thylefors and A. Négrel, "The global impact of glaucoma.," *Bull. World Health Organ.,* vol. 72, pp. 323-326, 1994.

[28] L. Bell, Enercon Technologies, 16 12 2016. [Online]. Available: https://www.mdtmag.com/article/2013/12/managing-electronic-component-obsolescence-medical-devices.

[29] S. Bhunia and D. Young, "Introduction to special issue on implantable electronics.," *J. Emerg. Technol. Comput. Syst.,* vol. 8, pp. 1-2, 2012.

[30] N. Opie, A. Burkitt, H. Meffin and D. Grayden, "Heating of the eye by a retinal prosthesis: modeling, cadaver and in vivo study.," *Biomed. Eng., IEEE Trans.,* vol. 59, p. 339–345, 2012.

[31] B. Rapoport, L. Turicchia, W. Wattanapanitch, T. Davidson and R. Sarpeshkar, "Efficient universal computing architectures for decoding neural activity.," *PLoS One,* vol. 7, p. e42492, 2012.

[32] M. Haghi, K. Thurow and S. R. , "Wearable Devices in Medical Internet of Things: Scientific Research and Commercially Available Devices.," *Healthcare Informatics Research,* vol. 23, no. 1, pp. 4-15, 2017.

[33] D. Hemapriya, P. Viswanath, V. M. Mithra, S. Nagalakshmi and G. Umarani, "Wearable medical devices — Design challenges and issues.," in *Innovations in Green Energy and Healthcare Technologies (IGEHT), 2017 International Conference on*, Coimbatore, India, 2017.

[34] L. Yu, B. J. Kim and E. Meng, "Chronically Implanted Pressure Sensors: Challenges and State of the Field," *Sensors,* vol. 14, pp. 20620-20644, 2014.

[35] M. Lashutka, A. Chandra, H. Murray, G. Phillips and B. Hiestand, "The relationship of intraocular pressure to intracranial pressure.," *Ann Emerg Med,* vol. 43, no. 5, pp. 585-591, 2004.

[36] H. Quigley and A. Broman, "The number of people with glaucoma worldwide in 2010 and 2020.," *Br. J. Ophthalmol.,* vol. 90, pp. 262-267, 2006.

[37] T. E. D. P. R. Group, "Prevalence of Open-Angle Glaucoma Among Adults in the United States.," *Archives of Ophthalmology,* vol. 122, no. 4, p. 532–538, 2004.

[38] B. Thylefors and A. Négrel, "The global impact of glaucoma.," *Bull. World Health Organ.,* vol. 72, pp. 323-326, 1994.

[39] D. Pascolini and S. Mariotti, "Global estimates of visual impairment: 2010.," *Br. J.Ophthalmol.,* vol. 96, pp. 614-618, 2012.

[40] B. Klein, R. Klein and K. Linton, "Intraocular pressure in an American community. The Beaver Dam Eye Study.," *Invest. Ophthalmol. Vis. Sci.,* vol. 33, p. 2224–2228, 1992.

[41] A. Coleman, "Advances in glaucoma treatment and management: surgery.," *Invest. Ophthalmol. Vis. Sci.,* vol. 53, p. 2491–2494, 2012.

[42] E. Hughes, P. Spry and J. Diamond, "24-hour monitoring of intraocular pressure inglaucoma management: a retrospective review.," *J. Glaucoma,* vol. 12, p. 232–236, 2003.

[43] R. P. Wisse, N. Peeters, S. M. Imhof and A. v. d. Lelij, "Comparison of Diaton transpalpebral tonometer with applanation tonometry in keratoconus," *Int J Ophthalmol.,* vol. 9, no. 3, p. 395–398, 2016.

[44] Q. K. Farhood, "Comparative evaluation of intraocular pressure with an air-puff tonometer versus a Goldmann applanation tonometer," *Clin Ophthalmol.,* vol. 7, p. 23–27, 2013.

[45] A. Cervino, "Rebound tonometry: new opportunities and limitations of non-invasive determination of intraocular pressure.," *The British Journal of Ophthalmology,* vol. 90, no. 12, pp. 1444-1446, 2006.

[46] [Online]. Available: http://medinstrum.com/applanation-tonometer/.

[47] M. Leonardi, P. Leuenberger, D. Bertrand, A. Bertsch and P. Renaud, "First steps toward noninvasive intraocular pressure monitoring with a sensing contact lens," *Invest Ophthalmol Vis Sci.,* vol. 45, p. 3113–3117, 2004.

[48] K. Stangel, S. Kolnsberg, Hammerschmidt, H. K. Trieu and W. Mokwa, "A programmable Intraocular CMOS pressure sensor system Implant," *IEEE J. Solid State,* vol. 36, no. 7, p. 1094–1100, 2001.

[49] K. C. Katuri, S. Asrani and M. K. Ramasubramanian, "Intraocular Pressure Monitoring Sensors," *IEEE Sensors,* vol. 8, pp. 12-19, 2008.

[50] D. Cusano, Health 2.0 Fall Conference 2013, 31 July 2013. [Online]. Available: http://telecareaware.com/2013/07/.

[51] Implandata Ophthalmic Products GmbH, [Online]. Available: http://implandata.com/en/was-wir-machen/eyemate/.

[52] WHO , [Online]. Available: http://www.who.int/gpsc/country_work/gpsc_ccisc_fact_sheet_en.pdf.

[53] T. Horan, R. Gaynes, W. Martone, W. Jarvis and T. Emori, "CDC definitions of nosocomial surgical site infections, 1992: a modification of CDC definitions of surgical wound infections.," *Infection Control.,* vol. 13, p. 606–608, 1992.

[54] W. H. Statistics, 2011.

[55] D. Weber, W. Rutala, M. Miller, K. Huslage and E. Sickbert-Bennett, "Role of hospital surfaces in the transmission of emerging health care-associated pathogens: norovirus, Clostridium difficile, and Acinetobacter species.," *Am J Infect Control.,* vol. 5, no. 1, pp. S25-S33, 2010.

[56] C. Buck, A. Llopis, E. Najera and M. Terris, "The challenge of epidemiology—issues and selected readings.," *Washington: PAHO Scientific Publication,* pp. 46-59, 1988.

[57] D. Pittet, "Improving Adherence to Hand Hygiene Practice: A Multidisciplinary Approach," *4th Decennial International Conference on Nosocomial and Healthcare-Associated Infections,* vol. 7, no. 2, 2001.

[58] C. Boschi-Pinto, L. Velebit and K. Shibuya, "Estimating child mortality due to diarrhoea in developing countries.," *Bull World Health Organ,* vol. 86, p. 710–717, 2008.

[59] J. Al-Tawfiq, M. Abed, N. Al-Yami and R. Birrer, "Promoting and sustaining a hospital-wide, multifaceted hand hygiene program resulted in significant reduction in health care-associated infections.," *American Journal of Infection Control,* vol. 41, no. 6, p. 482–486, 2013.

[60] M. Rotter, Hospital epidemiology and infection control, Baltimore: Williams& Wilkins, 1996.

[61] S. Selwyn and H. Ellis, "Skin bacteria and skin disinfection reconsidered.," *Br Med J.,* vol. 1, no. 5793, pp. 136-140, 1972.

[62] E. J. L. Lowbury, H. A. Lilly and J. P. Bull, "Disinfection of Hands: Removal of Transient Organisms," *Br Med J.,* vol. 2, no. 5403, pp. 230-233, 1964.

[63] M. Rotter and W. Koller, "European test for the evaluation of theefficacy of procedures for the antiseptic handwash.," *Hygiene and Medicine,* vol. 16, pp. 4-12, 1991.

[64] E. Larson, "APIC Guidelines Committee: APIC guideline for handwashing and hand antisepsis in healthcare settings.," *Am J Infect Control,* vol. 23, pp. 251-269, 1995.

[65] N. Ehrenkranz, "Bland soap handwash or hand antisepsis? The pressing need for clarity.," *Infect Control Hosp Epidemiol.,* vol. 13, no. 5, pp. 299-301, 1992.

[66] A. Aiello, R. Coulborn, V. Perez and E. Larson, "Effect ofhand hygiene on infectious disease risk in the community setting:a meta-analysis.," *Am J Public Health*, vol. 98, p. 1372–1381, 2008.

[67] D. Gould and N. Drey, "Types of interventions used to improve hand hygiene compliance and prevent healthcare associated infection.," *Journal of Infection Prevention*, vol. 14, no. 3, p. 88–93, 2013.

[68] L. Conway, L. Riley, L. Saiman, B. Cohen, P. Alper and L. Larson, "Implementation and impact of an automated group monitoring and feedback system to promote hand hygiene among health care personnel.," *Joint Commission Journal on Quality and Patient Safety / Joint Commission Resources.,* vol. 40, no. 9, p. 408–417, 2014.

[69] C. Carboneau, E. Benge, M. Jaco and M. Robinson, "A lean Six Sigma team increases hand hygiene compliance and reduces hospital-acquired MRSA infections by 51%.," *Journal for Healthcare Quality,* vol. 32, no. 4, p. 61–70, 2010.

[70] A. Chagpar, C. Banez, R. Lopez and J. Cafazzo, "Challenges of hand hygiene in healthcare: The development of a tool kit to create supportive processes and environments.," *Healthcare Quarterly,* vol. 13, no. Sp, p. 59–66, 2010.

[71] A. Hendrich, M. Chow, B. Skierczynski and Z. Lu, "A 36-hospital time and motion study: How do medical-surgical nurses spend their time?," *The Permanente Journal,* vol. 12, no. 3, p. 25–34, 2008.

[72] M. McGuckin, R. Waterman and J. Govednik, "Hand hygiene compliance rates in theUnited Statesda one-year multicenter collaboration using product/volume usage measurement and feedback.," *Am J Med Qual,* vol. 24, pp. 205-213, 2009.

[73] G. Lebovic, N. Siddiqui and M. Muller, "Predictors of hand hygiene compliance in theera of alcohol-based hand rinse.," *J Hosp Infect,* vol. 83, pp. 276-283, 2013.

[74] M. Ghannad-Rezaie, L. Yang, H. Garton and N. Chronis, "A Near Infrared Opto-Mechanical Intracranial Pressure Microsensor," *(JMEMS) IEEE/ASME Journal of Microelectromechanical Systems,* vol. 21, no. 1, pp. 23-33, 2012.

[75] M. Ghannad-rezaie, M. Gulari, R. d. M. Franco, S. Mian and N. Chronis, "A powerless optical microsensor for monitoring intraocular pressure with keratoprostheses," *Transducers & Eurosensors XXVII: The 17th International Conference on Solid-State Sensors, Actuators and Microsystems, 16-20 June, Barcelona, Spain,* vol. 16, no. 20, pp. 2708-2711, 2013.

[76] M. E. Greene and B. G. Gilman, "Intraocular pressure measurement with instrumented contact lens," *Invest Ophthalmol,* p. 299–302, 1974.

[77] J. G. E. Waters and R. L. Thommen, "Intraocular pressure sensor". United States of America Patent 4922913.

[78] M. Leonardi, P. Leuenberger, D. Bertrand, A. Bertsch and P. Renaud, "First steps toward noninvasive intraocular pressure monitoring with a sensing contact lens," *Investigative Ophthalmol. Vis. Sci,* vol. 45, no. 9, 2004.

[79] M. Leonardi, P. Leuenberger, D. Batrand, A. Bertsch and P. Renaud, "A soft contact lens with a mems strain gage embedded for intraocular pressure monitoring," *Proc. 12th Int. Conf. Solid State Sensors, Actuators, Microsyst., ,Boston, MA, Jun.8–12,* vol. 2, p. 1043–1046, 2003.

[80] J. Hjortdal and P. K. Jensen, "In vitro measurement of corneal strain, thickness, and curvature using digital image processing," *Acta Ophthalmol. Scand.,* vol. 73, p. 5–11, 1995.

[81] A. K. C. Lam and W. A. Douthwaite, "The effect of an artificially elevated intraocular pressure on the central corneal curvature," *Ophthalmic Physiol. Opt,* vol. 17, pp. 18-24, 1997.

[82] C. Collins, "Miniature passive pressure transensor for implanting in eye," *IEEE Trans.Bio-Med.Eng,* vol. 14, no. 2, pp. 74-83, 1967.

[83] Y. Backlund, L. Rosengren, B. Hok and B. Svedbergh, "Passive silicon transensor intended for biomedical remote pressure monitoring," *Sens. Actuators,* Vols. A21-A23, pp. 58-61, 1990.

[84] K. V. Schuylenbergh and R. Pures, "Passive telemetry by harmonics detection," *Proc. 18th Annu. Int. Conf. IEEE Eng. Med. Biol. Soc.,* vol. 1, pp. 299-300, 1996.

[85] R. Puers, G. Vandevoorde and D. D. Bruyker, "Electrodeposited copper inductors for intraocular pressure telemetry," *J. Micromech. Microeng,* vol. 10, pp. 124-129, 2000.

[86] P.-J. Chen, D. C. Rodger, S. Saati, M. S. Humayun and Y.-C. Tai, "Microfabricated Implantable Parylene-Based Wireless Passive Intraocular Pressure Sensors," *Journal of Microelectromechanical Systems,* vol. 17, no. 6, pp. 1342-1351, 2008.

[87] O. Akar, T. Akin and K. Najafi, "A wireless batch sealed absolute capacitive pressure sensor," *Sens. Actuator A,* vol. 95, p. 29–38, 2001.

[88] S. Lizón-Martínez, R. Giannetti, J. L. Rodríguez-Marrero and B. Tellini, "Design of a system for continuous intraocular pressure monitoring," *IEEE Trans. Instrument. Measure,* vol. 54, no. 4, p. 1534–1540, 2005.

[89] A. Baldi, W. Choi and B. Ziaie, "A self-resonant frequency modulated micromachined passive pressure transensor," *IEEE Sensors,* vol. 3, no. 6, p. 728–733, 2003.

[90] K. Scluylenbergh, E. Peeters, B. Puers, W. Sansen and A. Neetens, "An implantable telemetric tonometer for direct intraocuar pressure measurements," *Abstr. 1st Eur. Cod. Biomed. Eng, Nice, France,* p. 194–195, 1991.

[91] R. Puers, "Linking sensors with telemetry: Impact on system design," *Proc. 8th Int. Conf. Solid-State Sens. Actuators, Eurosens. IX, Stockholm, Sweden, Jun. 25–29,* p. 169–174, 1995.

[92] J. McLaren, R. Brubaker and J. F. Simon, "Continuous measurement of intraocular pressure in rabbits by telemetry," *Invest. Ophthalmol. Visual Sci,* vol. 37, no. 6, p. 966–975, 1996.

[93] U. Schnakenberg, P. Walter, G. V. Bögel, C. Krüger, H. C. LüdtkeHandjery, H. A. Richter, W. Specht, P. Ruokonen and W. Mokwa, "Initial investigations on systems for measuring intraocular pressure," *Sens. Actuators,* vol. 85, p. 287–291, 2000.

[94] S. Ullerich, W. Mokwa, G. v. Bogel and U. Schnakenberg, "Micro coils for an advanced system for measuring intraocular pressure," *Proc. 1st Annu. Int. IEEE-EMBS Special Topic Conf. Microtechnol. Med. Biol., Lyon, France, Oct. 12–14,* p. 470–474, 2000.

[95] W. Mokwa and U. Schnakenberg, "Micro-transponder systems for medical applications," *IEEE Trans. Instrument. Measure,* vol. 50, no. 6, p. 1551–1555, 2001.

[96] W. Mokwa, "Opthalmic implants," *Proc. IEEE Sensors,* vol. 2, p. 980–986, 2003.

[97] W. Fink, E.-H. Yang, Y. Hishinuma, C. Lee, T. George, Y.-C. Tai, E. Meng and M. Humayun, "Optically Powered and Optically Data Transmitting Wireless Intraocular Pressure Sensor Device". United States of America Patent 20040116794, 2004.

[98] B. Bae, K. Park and M. A. Shannon, "Low pressure treatment control of glaucoma using an electromagnetic valve actuator with a piezoresistive pressure senso," *Proc. 3rd Annu. Int. IEEE EMBS Special Topic Conf. Microtechnolog. Med. Biol., Oahu, HI, May 12–15,* p. 126–129, 2005.

[99] B. Bae, B. R. Flachsbart, K. Park and M. A. Shannon, "Design optimization of a piezoresistive pressure sensor considering the output signal-to-noise ratio," *J. Micromech. Microeng,* vol. 14, p. 1597–1607, 2004.

[100] P.-J. Chen, D. C. Rodger, E. Meng, M. S. Humayun and Y.-C. Tai, "In vivo characterization of implantable unpowered parylene MEMS intraocular pressure sensors," p. 834–836, 2006.

[101] P.-J.Chen, D. C.Rodger, M. S.Humayun and Y.-C. Tai, "Unpowered spiral-tube parylene pressure sensor for intraocular pressure sensing," *Sens. Actuators A,* vol. 127, p. 276–282, 2006.

[102] E. Meng, P.-J. Chen, D. Rodger, Y.-C. Tai and M. Humayun, "Implantable parylene MEMS for glaucoma therapy," *Proc. 3rd Annu. Int. IEEE EMBS Special Topic Conf. Microtechnol. Med. Biol., Oahu, HI, May 12–15,* p. 116–119, 2005.

[103] H. Humphreys, "Self-disinfecting and microbiocide-impregnated surfaces and fabrics: what potential in interrupting the spread of healthcare-associated infection?," *Clin Infect Dis.,* vol. 58, no. 6, pp. 848-53, 2014.

[104] C. Chang, F. O. John, S. Lobe, D. David, M. M. Dumais, Q. Constance, D. Robert and J. Johnson, "UV Inactivation of Pathogenic and Indicator Microorganisms," *Applied and environmental microbiology,* vol. 48, pp. 699-701, 1984.

[105] B. Andersen, H. Bånrud, E. Bøe, O. Bjordal and F. Drangsholt, "Comparison of UV C light and chemicals for disinfection of surfaces in hospital isolation units," *Infect Control Hosp Epidemiol.,* vol. 27, no. 7, pp. 729-734, 2006.

[106] H. Foster, I. Ditta, S. Varghese and A. Steele, "Photocatalytic disinfection using titanium dioxide: spectrum and mechanism of antimicrobial activity," *Appl Microbiol Biotechnol.,* vol. 3, p. 1847–1868, 2011.

[107] L. Dubay, "BioOptics World," 9 7 2014. [Online]. Available: http://www.bioopticsworld.com/articles/2014/07/uv-disinfection-robot-tru-d-slays-hospital-superbugs.html.

[108] M. Schmidt, H. Attaway and P. Sharpe, "Sustained reduction of microbial burden on common hospital surfaces through introduction of copper," *J Clin Microbiol,* vol. 50, pp. 2217-2223, 2012.

[109] A. H. Tamimi, S. Carlino and C. P. Gerba, "Long-term efficacy of a self-disinfecting coating in an intensive," *American Journal of Infection Control,* vol. 42, pp. 1178-1181, 2014.

[110] E. E. Mann, D. Manna, M. R. Mettetal, R. M. May, E. M. Dannemiller, K. K. Chung, A. B. Brennan and S. T. Reddy, "Surface micropattern limits bacterial contamination," *Antimicrobial Resistance & Infection Control,* vol. 3, no. 28, pp. 1-8, 2014.

[111] J. Ferenc, "Health Facilities Management," 18 12 2014. [Online]. Available: https://www.hfmmagazine.com/articles/1444-new-door-handle-with-sanitizer-aims-to-make-hand-hygiene-easy.

[112] G. Schwartz and H. Quigley, "Adherence and persistence with glaucoma therapy.," *Surv Ophthalmol.,* vol. 53, no. 6, pp. S57-S68, 2008.

[113] M. Doughty and M. Zaman, "Human corneal thickness and its impact on intraocular pressure measures: a review and meta-analysis approach.," *Surv Ophthalmol.,* vol. 44, no. 5, pp. 367-408, 2000.

[114] M. Whitacre and R. Stein, "Sources of error with use of Goldmann-type tonometers.," *Surv Ophthalmol,* vol. 38, pp. 1-30, 1993.

[115] S. Pandav, A. Sharma, A. Gupta, S. Sharma, A. Gupta and B. Patnaik, "Reliability of ProTon and Goldmann applanation tonometers in normal and postkeratoplasty eyes.," *Ophthalmology.,* vol. 109, p. 979–984, 2002.

[116] S. Vincent, R. Vincent, D. Shields and G. Lee, "Comparison of intraocular pressure measurement between rebound, non-contact and Goldmann applanation tonometry in treated glaucoma patients.," *Clinical & experimental ophthalmology.,* vol. 40, p. e163–170, 2012.

[117] N. S. Ting, J. F. L. Yim and J. Y. Ng, "Different strategies and cost-effectiveness in the treatment of primary open angle glaucoma," *Clinicoecon Outcomes Res.* , vol. 6, p. 523–530, 2014.

[118] M. Ghannad-Rezaie, M. Gulari, R. d. M. Franco, S. Mian and N. Chronis, "A powerless optical microsensor for monitoring intraocular pressure with keratoprostheses," in *Solid-State Sensors, Actuators and Microsystems (TRANSDUCERS & EUROSENSORS XXVII), 2013 Transducers & Eurosensors XXVII: The 17th International Conference on*, 2013.

[119] R. Hardman, "A Toxicologic Review of Quantum Dots: Toxicity Depends on Physicochemical and Environmental Factors," *Environ Health Perspect.* , vol. 114, no. 2, p. 165–172, 2006.

[120] L. Shi, L. A. Sordillo, A. Rodríguez-Contreras and R. Alfano, "Transmission in Near-Infrared Optical Windows for Deep Brain Imaging," *J Biophotonics.,* vol. 9, no. 1-2, p. 38–43, 2016.

[121] H. Quigley, E. Addicks and W. Green, "Optic nerve damage in human glaucoma. III.Quantitative correlation of nerve fiber loss and visual field defect in glaucoma, ischemic neuropathy.," *Archives of ophthalmology,* vol. 100, no. 1, pp. 135-146, 1982.

[122] J. Li, M. Greiner, J. Brandt, M. Lim and M. Mannis, "Long-term Complications Associated with Glaucoma Drainage Devices and Boston Keratoprosthesis.," *Am J Ophthalmol.,* vol. 152, pp. 209-218, 2011.

[123] P. Netland, H. Teruda and C. Dohlman, "Glaucoma Associated with Keratoprosthesis.," *Ophthalmology,* vol. 105, pp. 751-757, 1998.

[124] M. Klufas, N. Yannuzzi, D. D'Amico and S. Kiss, "Vitreoretinal aspects of permanent keratoprosthesis.," *Surv Ophthalmol.,* vol. 60, no. 3, pp. 216-228, 2015.

[125] R. Lee, Z. Khoueir, E. Tsikata, JamesChodosh, C. H. Dohlman and T. C.Chen, "Long-term Visual Outcomes and Complications of Boston Keratoprosthesis Type II Implantation," *Ophthalmology,* vol. 124, no. 1, pp. 27-35, 2017.

[126] A. Roszkowska and L. Torrisi, "Intraocular lens employed for cataract surgery," in *Journal of Physics: Conference Series,* 2015.

[127] Glaucoma Research Foundation, [Online]. Available: https://www.glaucoma.org/treatment/cataracts-and-glaucoma.php.

[128] B. Svedbergh, Y. Bäcklund, B. Hök and L. Rosengren, "The IOP-IOL. A probe into the eye.," *Acta Ophthalmol ,* vol. 70, no. 2, pp. 266-274, 1992.

[129] I. E. Araci, B. Su, S. R. Quake and Y. Mandel, "An implantable microfluidic device for self-monitoring of intraocular pressure.," *Nature Medicine,* vol. 20, p. 1074–1078, 2014.

[130] A. Bozkurt and B. Onaral, "Safety assessment of near infrared light emitting diodes for diffuse optical measurements.," *Biomed Eng Online.,* pp. 3-9, 2004.

[131] S. Laura, P. Yang, P. Sebastião, B. Yury and A. Robert, "Deep optical imaging of tissue using the second and third near-infrared spectral windows.," *Journal of biomedical optics.,* vol. 19, no. 5, pp. 1-6, 2014.

[132] E. Zrenner, K. Kohler, H. Haemmerle, W. Nisch and M. Stelzle, "Biocompatibility and long term stability of silicon photodiode arrays implanted in the subretinal space.," *Soc Neurosci Abstr,* vol. 25, no. 219, pp. 1-2, 1999.

[133] G. Kotzara, M. Freas, P. Abel, A. Fleischman, S. Roy, C. Zorman, J. M. Moran and J. Melzak, "Evaluation of MEMS materials of construction for implantable medical devices," *Biomaterials,* vol. 23, p. 2737–2750, 2002.

[134] P. Aspenberg, A. Anttila, Y. Konttinen, R. Lappalainen, S. Goodman, L. Nordsletten and S. Santavirta, "Benign response to particles of diamond and SiC: bone chamber studies of new joint replacement coating materials in rabbits.," *Biomaterials.,* vol. 17, no. 8, pp. 807-819, 1996.

[135] [Online]. Available: https://en.wikipedia.org/wiki/Poly(methyl_methacrylate).

[136] O. Findl, Intraocular Lens Materials and Design.

[137] F. Mauron, "Improvements in Glass Encapsulation Technology Offer Significant Advantages for Implantable Medical Devices," Valtronic.

[138] A. M. Derfus, W. C. Chan and S. N. Bhatia, "Probing the Cytotoxicity of Semiconductor Quantum Dots," *Nano Letters,* vol. 4, no. 1, pp. 11-18, 2004.

[139] C. Kirchner, T. Liedl, S. Kudera, T. Pellegrino, A. Muñoz Javier, H. Gaub, S. Stölzle, N. Fertig and W. Parak, "Cytotoxicity of colloidal CdSe and CdSe/ZnS nanoparticles.," *Nano Letters,* vol. 5, no. 2, pp. 331-339, 2005.

[140] N. Lewinski, V. Colvin and R. Drezek, "Cytotoxicity of nanoparticles.," *Small.,* vol. 4, pp. 26-49, 2008.

[141] M. Park, A. Neigh, J. Vermeulen, L. de la Fonteyne, H. Verharen, J. Briedé, H. van Loveren and W. de Jong, "The effect of particle size on the cytotoxicity, inflammation, developmental toxicity and genotoxicity of silver nanoparticles.," *Biomaterials,* vol. 32, no. 36, pp. 9810-9817, 2011.

[142] A. Derfus, W. Chan and S. Bhatia, "Probing the cytotoxicity of semiconductor quantum dots.," *Nano Letters,* vol. 8, pp. 4-11, 2004.

[143] N. Chen, Y. He, Y. Su, X. Li, Q. Huang, H. Wang, X. Zhang, R. Tai and C. Fan, "The cytotoxicity of cadmium-based quantum dots," *Biomaterials,* vol. 33, pp. 1238-1244, 2012.

[144] G. Fragiacomo, K. Reck, L. Lorenzen and E. V. Thomsen, "Novel Designs for Application Specific MEMS Pressure Sensors.," *Sensors,* vol. 10, pp. 9541-9563, 2010.

[145] W. Schomburg, Membranes, Verlag Berlin Heidelberg: Springer, 2011.

[146] J. Vlassak and W. Nix, "A new bulge test technique for the determination of Young's modulus and Poisson's ratio of thin films.," *J Mater Res,* vol. 7, no. 12, p. 3242–3249, 1992.

[147] L. Jacak, "Semiconductor quantum dots - towards a new generation of semiconductor devices.," *European Journal of Physics,* vol. 21, no. 6, pp. 487-497, 2000.

[148] S. Liu, W. Liu, W. Ji, J. Yu, W. Zhang, L. Zhang and W. Xie, "Top-emitting quantum dots light-emitting devices employing microcontact printing with electricfield-independent emission.," *Scientific Reports,* vol. 6, pp. 1-9, 2016.

[149] S. J. Rosenthal, J. C. Chang, O. Kovtun, J. R. McBride and I. D. Tomlinson, "Biocompatible Quantum Dots for Biological Applications," *Chemistry & Biology,* vol. 18, no. 1, pp. 10-24, 2011.

[150] M. Z. Hu and T. Zhu, "Semiconductor Nanocrystal Quantum Dot Synthesis Approaches Towards Large-Scale Industrial Production for Energy Applications," *Nanoscale Res Lett.* , vol. 10, no. 469, pp. 1-15, 2015.

[151] S. C. Farmer and T. E. Patten, "Photoluminescent Polymer/Quantum Dot Composite Nanoparticles," *Chemistry of Materials,* vol. 13, no. 11, p. 3920–3926, 2001.

[152] V. Colvin, M. Schlamp and A. Alivisatos, "Light-emitting-diodes made from cadmium selenide nanocrystals and a semiconducting polymer.," *Nature,* vol. 370, no. 354, 1994.

[153] J. Drbohlavova, V. Adam, R. Kizek and J. Hubalek, "Quantum Dots — Characterization, Preparation and Usage in Biological Systems," *Int J Mol Sci.,* vol. 10, no. 2, p. 656–673, 2009.

[154] L. Pang, Y. Shen, K. Tetz and Y. Fainman, "PMMA quantum dots composites fabricated via use of pre-polymerization.," *Opt Express.,* vol. 13, no. 1, pp. 44-53, 2005.

[155] H. Lorenz, M. Despont, N. Fahrni, N. LaBianca and P. Renaud, "SU-8: a low-cost negative resist for MEMS," *J. Micromech. Microeng.,* vol. 7, pp. 121-124, 1997.

[156] Y. K. Pang, J. C. W. Lee, H. F. Lee, W. Y. Tam, C. Chan and P. Sheng, "Chiral microstructures (spirals) fabrication by holographic lithography," *Optics Express,* vol. 13, no. 19, pp. 7615-7620, 2005.

[157] J. C. Lötters, J. C. Lotters, W. Olthuis, P. H. Veltink and P. Bergveld, "The mechanical properties of the rubber elastic polymer polydimethylsiloxane for sensor applications," *Journal of micromechanics and microengineering,* vol. 7, no. 3, pp. 145-147, 1997.

[158] A. Karczemska and A. Sokolowska, "Materials for DNA Sequencing Chip," *Journal of Wide Bandgap Materials,* vol. 9, pp. 243-259, 2002.

[159] R. Lovchik, H. Wolf and E. Delamarche, "High-grade optical polydimethylsiloxane for microfluidic applications.," *Biomed Microdevices.,* vol. 13, no. 6, pp. 1027-1032, 2011.

[160] A. Grosse, M. Grewe and H. Fouckhardt, "Deep wet etching of fused silica glass for hollow capillary optical leaky waveguides in microfluidic devices.," *Journal of Micromechanics and Microengineering.,* vol. 11, no. 3, pp. 257-262, 2001.

[161] I. Ciprian, "Wet etching of glass for MEMS applications.," *Romanian Journal of Information Science and Technology.,* vol. 9, pp. 285-310, 2006.

[162] S. Inoué, Video microscopy: the fundamentals, Springer, 1997.

[163] A. Chaudhury, A. Pantazis and N. Chronis, "An image contrast-based pressure sensor.," *Sensors and Actuators A: Physical,* vol. 245, pp. 63-67, 2016.

[164] M. A. Eddings, M. A. Johnson and B. K. Gale, "Determining the optimal PDMS-PDMS bonding technique for microfluidic devices.," *J. Micromech. Microeng.,* vol. 18, no. 6, p. 067001, 2008.

[165] R. C. Gonzales, Digital Image Processing, New Jersey: Prentice-Hall, 2006.

[166] E. Lowbury, H. Lilly and J. Bull, "Disinfection of hands: removal oftransient organisms.," *BMJ,* vol. 2, pp. 230-233, 1964.

[167] G. Ayliffe, J. Babb and A. Quoraishi, "A test for hygienic hand disinfection.," *J Clin Pathol,* vol. 31, pp. 923-931, 1978.

[168] C. Buck, A. Llopis, E. Najera and M. Terris, The challenge of epidemiology—issues and selected readings., Washington: PAHO Scientific Publication, 1988.

[169] M. Rotter, "150 years of hand disinfection—Semmelweis' heritage.," *Hyg Med,* vol. 22, pp. 332-341, 1997.

[170] "Word Health Organization," 2009. [Online]. Available: https://www.ncbi.nlm.nih.gov/books/NBK144042/.

[171] H. Morton, "The relationship of concentration and germicidal efficiency of ethyl alcohol.," *Ann N.Y. Acad. Sci.,* vol. 53, pp. 191-196, 1950.

[172] Y. Ali, M. Dolan, E. Fendler and E. Larson, Disinfection, sterilization, and preservation., Philadelphia: Lippincott: Williams & Wilkins, 2001.

[173] Center for Disease Control and Prevention, [Online]. Available: https://www.cdc.gov/handhygiene/campaign/promotional.html .

[174] E. Cloutman-Green, O. Kalaycioglu, H. Wojani, J. Hartley, S. Guillas, D. Malone and N. Klein, "The important role of sink location in handwashing compliance and microbial sink contamination.," *American Journal of Infection Control,* vol. 42, no. 5, pp. 554-555, 2014.

[175] W. Bischoff, T. Reynolds and C. Sessler, "Handwashing compliance by health care workers: the impact of introducing an accessible, alcohol-basedhand antiseptic.," *Arch Intern Med,* vol. 160, pp. 1017-1031, 2000.

[176] S. Dancer, "How do we assess hospital cleaning? A proposal for microbiological standards for surface hygiene in hospitals.," *J Hosp Infect.*, vol. 56, no. 1, 2004.

[177] A. Kramer, I. Schwebke and G. Kampf, "How long do nosocomial pathogens persist on inanimate surfaces? A systematic review.," *BMC Infect Dis.*, vol. 6, 2006.

[178] M. Schmidt, C. Stewart, M. Bailey, A. Nieszkowska, J. Kelly and L. Murphy, "Mechanical ventilation management during extracorporeal membrane oxygenation for acute respiratory distress syndrome: a retrospective international multicenter study.," *Crit Care Med.*, vol. 43, no. 3, p. 654–664, 2015.

[179] R. May, C. Magin and E. Mann, "An engineered micropattern to reduce bacterial colonization, platelet adhesion and fibrin sheath formation for improved biocompatibility of central venous catheters.," *Clinical and Translational Medicine.*, pp. 4-9, 2015.

[180] 3D Systems, [Online]. Available: http://www.3dcreationlab.co.uk/pdfs/projet-hd-3000.pdf.

[181] 3D Systems, [Online]. Available: http://www.3dsystems.com/products/datafiles/visijet/msds/visijet-crystal/24184-S02-00-B-MSDS-US-English-EX-200-Crystal.pdf.

[182] 3D Systems, [Online]. Available: http://www.3dsystems.com/products/datafiles/visijet/msds/s100-s300/23126-S02-02-B-MSDS-US-VisiJet-S100-S300.pdf.

[183] S. Lampman, in *Characterization and Failure Analysis of Plastics*, ASM International, 2003.

[184] W. Gerrard, "Friction and other measurements of the skin surface.," *Bioengineering and the Skin.* , vol. 3, pp. 123-139, 1987.

[185] F. P. Zimmerli, "Human Failures in Spring Applications," in *The Mainspring, no. 17, Associated Spring Corporation* , Bristol, Conn., August–September 1957, 1957.

[186] J. Shigley and C. Mischke, Standard Handbook of Machine Design, 2nd edition, 1996.

[187] Budynas.R and Nisbett.K., Shigley's Mechanical Engineering Design . 8th edition., McGraw-Hill, 2008.

[188] B. 1. Part1, *Guide For the Design of Helical Compression Springs*, 1987.

[189] G. Kampf, S. Ruselack, S. Eggerstedt, N. Nowak and M. Bashir, "Less and less–influence of volume on hand coverage and bactericidal efficacy in hand disinfection.," *BMC Infectious Diseases.*, vol. 13, 2013.

[190] J. Lee, J. Choi and H. Kim, "Determination of body surface area and formulas to estimate body surface area using the alginate method.," *J Physiol Anthropol,* vol. 27, no. 2, p. 71–82, 2008.

[191] J. Flammer, S. Orgül, V. Costa, N. Orzalesi, G. Krieglstein, L. Serra, J. Renard and E. Stefánsson, "The impact of ocular blood flow in glaucoma.," *Prog Retin Eye Res.,* vol. 21, no. 4, pp. 359-393, 2002.

[192] F. Galassi, B. Giambene, A. Corvi and G. Falaschi, "Evaluation of ocular surface temperature and retrobulbar haemodynamics by infrared thermography and colour Doppler imaging in patients with glaucoma," *Br J Ophthalmol.,* vol. 91, no. 7, pp. 878-881, 2007.

[193] S. Li, K. Zhang, J.-M. Yang, L. Lin and H. Yang, "Single Quantum Dots as Local Temperature Markers.," *Nano Letters,* vol. 7, no. 10, pp. 3102-3105, 2007.

[194] O. Ley and T. Kim, "Calculation of arterial wall temperature in atherosclerotic arteries: effect of pulsatile flow, arterial geometry, and plaque structure.," *Biomed Eng Online.* , vol. 6, no. 8, pp. 1-18, 2007.

[195] E. Schena, D. Tosi, P. Saccomandi, E. Lewis and T. Kim, "Fiber Optic Sensors for Temperature Monitoring during Thermal Treatments: An Overview.," *Sensors (Basel).*, vol. 16, no. 7, pp. 1-20, 2016.

[196] A. Fonseca, M. Allen, M. J. G Allen, K. Jason and W. Jason, "Flexible wireless passive pressure sensors for biomedical applications.," *Tech. Dig. Solid State Sensor, Actuator, and Microsystems Workshop.,* 2005.

[197] R. Haque and K. Wise, "A 3D implantable microsystem for intraocular pressure monitoring using a glass-in-silicon reflow process.," in *Micro Electro Mechanical Systems (MEMS), 2011 IEEE 24th International Conference on*, Cancun, Mexico, 2011.

[198] C. D. Marco, S. M. Eaton, R. Suriano, S. Turri, M. Levi, R. Ramponi, G. Cerullo and R. Osellame, "Surface Properties of Femtosecond Laser Ablated PMMA.," *ACS Appl. Mater. Interfaces.,* vol. 2, no. 8, p. 2377–2384, 2010.

[199] J. Sulston and H. Horvitz, "Post-embryonic cell lineages of the nematode, Caenorhabditis elegans.," *Developmental Biology.,* vol. 56, no. 1, pp. 110-156, 1977.

[200] H. Hwang and H. Lu, "Microfluidic tools for developmental studies of small model organisms—nematodes, fruit flies, and zebrafish.," *Biotechnol J,* vol. 8, p. 192–205, 2013.

[201] V. Lam, T. Tokusumi, D. Cerabona and R. Schulz, "Specific cell ablation in Drosophila using the toxic viral protein M2(H37A).," *Fly,* vol. 4, no. 4, p. 338–343, 2010.

[202] L. Berkowitz, A. Knight, G. Caldwell and K. Caldwell, "Generation of Stable Transgenic C. elegans Using Microinjection.," *Journal of Visualized Experiments: JoVE,* vol. 18, no. 833, 2008.

[203] L. Wong and P. Schedl, "Dissection of Drosophila Ovaries.," *Journal of Visualized Experiments : JoVE,* vol. 1, no. 52, 2006.

[204] G. Whitesides, "The origins and the future of microfluidics.," *Nature,* vol. 442, p. 368–373, 2006.

[205] E. Sackmann, A. Fulton and D. Beebe, "The present and future role of microfluidics in biomedical research.," *Nature,* vol. 507, p. 181–189, 2014.

[206] G. Salieb-Beugelaar, G. Simone, A. Arora, A. Philippi and A. Manz, "Latest developments in microfluidic cell biology and analysis systems.," *Anal Chem,* vol. 82, p. 4848–4864, 2010.

[207] S. Sia and G. Whitesides, "Microfluidic devices fabricated in poly(dimethylsiloxane) for biological studies.," *Electrophoresis,* vol. 24, p. 3563–3576, 2003.

[208] M. Yanik, C. Rohde and C. Pardo-Martin, "Technologies for micromanipulating, imaging, and phenotyping small invertebrates and vertebrates.," *Annu Rev Biomed Eng.,* vol. 13, p. 185–217, 2011.

[209] K. Chung, Y. Kim, J. Kanodia, E. Gong, S. Shvartsman and H. Lu, "A microfluidic array for large-scale ordering and orientation of embryos.," *Nat Methods,* vol. 8, p. 171–176, 2011.

[210] I. Conlon and M. Raff, "Size control in animal development.," *Cell,* vol. 96, p. 235–244, 1999.

[211] S. Russell and S. Tickoo, "Drosophila melanogaster as a model system for drug discovery and pathway screening.," *Current Opinion in Pharmacology,* vol. 2, no. 5, pp. 555-560, 2002.

[212] S. Lenz, P. Karsten, J. B. Schulz and A. Voigt, "Drosophila as a screening tool to study human neurodegenerative diseases," *Journal of Neurochemistry,* vol. 127, no. 4, p. 453–460, 2013.

[213] E. Bier, "Drosophila, the golden bug, emerges as a tool for human genetics," *Nature Reviews Genetics* , vol. 6, no. 1, pp. 9-23, 2005.

[214] N. Ziv and M. Spira, "Localized and transient elevations of intracellular Ca2+ induce the dedifferentiation of axonal segments into growth cones," *Journal of Neuroscience,* vol. 17, no. 10, pp. 3568-3579, 1997.

[215] Z. Wu, A. Ghosh-Roy, M. Yanik, J. Zhang and Y. Jin, "Caenorhabditiselegans neuronal regeneration is influenced by life stage, ephrin signaling, and synaptic branching," *Proceedings of the National Academy of Sciences,* vol. 104, no. 38, p. 15132–15137, 2007.

[216] B. Neumann, K. Nguyen, D. Hall, A. Ben-Yakar and M. Hilliard, "Axonal regeneration proceeds through specific axonal fusion in transected C. elegans neurons," *Developmental Dynamics,* vol. 240, no. 6, p. 1365–1372, 2011.

[217] S. Chung, D. Clark, C. Gabel, E. Mazur and A. Samuel, "The role of the AFD neuron in C. elegansthermotaxis analyzed using femtosecond laser ablation," *BMC Neuroscience,* vol. 7, no. 30, pp. 1-11, 2006.

[218] M. Ghannad-Rezaie, X. Wang, B. Mishra, C. Collins and N. Chronis, "A MICROFLUIDIC CHIP FOR IMMOBILIZING AND IN VIVO IMAGING," in *15th International Conference on Miniaturized Systems for Chemistry and Life Sciences,* Seattle, Washington, 2011.

[219] V. Nguyen. [Online]. Available: https://morphologicallydisturbed.weebly.com/the-biology.html.

[220] C. C. Diagnostics. [Online]. Available: http://www.creative-diagnostics.com/Drosophila.htm.htm.

[221] A. D. Pilling, D. Horiuchi, C. M. Lively and W. M. Saxton, "Kinesin-1 and Dynein Are the Primary Motors for Fast Transport of Mitochondria in Drosophila Motor Axons," *Molecuar Biology of the Cell,* vol. 17, no. 4, pp. 2057-2068, 2006.

[222] S. Gunawardena, L.-S. Her, R. G. Brusch, R. A. Laymon, I. R. Niesman, B. Gordesky-Gold, L. Sintasath, N. M. Bonini and L. S. Goldstein, "Disruption of Axonal Transport by Loss of Huntingtin or Expression of Pathogenic PolyQ Proteins in Drosophila," *Neuron,* vol. 40, no. 1, p. 25–40, 2003.

[223] K. E. Miller, J. DeProto, N. Kaufmann, B. N. Patel, A. Duckworth and D. V. Vactor, "Direct Observation Demonstrates that Liprin-α Is Required for Trafficking of Synaptic Vesicles," *Current Biology,* vol. 15, no. 7, p. 684–689, 2005.

[224] G. M. Whitesides, E. Ostuni, S. Takayama, X. Jiang and D. E. Ingber, "Soft Lithography in Biology and Biochemistry," *Annual Review of Biomedical Engineering,* vol. 3, pp. 335-373, 2001.

[225] D. J. Sandstrom, "Isoflurane depresses glutamate release by reducing neuronal excitability at the Drosophila neuromuscular junction," *The Journal of Physiology,* vol. 558, no. 2, p. 489–502, 2004.

[226] D. J. Sandstrom, "Isoflurane Reduces Excitability of Drosophila Larval Motoneurons by Activating a Hyperpolarizing Leak Conductance," *Anesthesiology,* vol. 108, no. 3, pp. 434-446, 2008.

[227] R. Ghaemi, a. P. Rezai, B. G. Iyengara and P. R. Selvaganapathy, "Microfluidic devices for imaging neurological response of Drosophila melanogaster larva to auditory stimulus," *Lab on a Chip,* vol. 15, pp. 1116-1122, 2015.

[228] M. Crane, K. Chung, J. Stirman and H. Lu, "Microfluidics-enabled phenotyping, imaging, and screening of multicellular organisms.," *Lab Chip,* vol. 10, p. 1509–1517, 2010.

[229] S. Brenner, "The genetics of Caenorhabditis elegans.," *Genetics,* vol. 77, p. 71–94, 1974.

[230] L. Avery and B. Shtonda, "Food transport in the C. elegans pharynx.," *J. Exp. Biol.,* vol. 206, no. 14, p. 2441–2457, 2003.

[231] S. Chung, D. Clark, C. Gabel, E. Mazur and A. Samuel, "The role of the AFD neuron in C. elegans thermotaxis analyzed using femtosecond laser ablation.," *BMC Neurosci.,* vol. 7, no. 30, 2006.

[232] M. Hilliard, A. Apicella, R. Kerr, H. Suzuki, P. Bazzicalupo and W. Schafer, "In vivo imaging of C. elegans ASH neurons: cellular response and adaptation to chemical repellents.," *EMBO J.,* vol. 24, no. 1, pp. 63-72, 2004.

[233] N. Kim, C. M. Dempsey, J. V. Zoval, J.-Y. Sze and M. J. Madou, "Automated microfluidic compact disc (CD) cultivation system of Caenorhabditis elegans," *Sens. Actuators, B,* vol. 122, no. 2, pp. 511-518, 2007.

[234] D. Lange, C. W. Storment, C. A. Conley and G. T. A. Kovacs, "A microfluidic shadow imaging system for the study of the nematode Caenorhabditis elegans in space," *Sens. Actuators, B,* vol. 107, pp. 904-914, 2005.

[235] X. Heng, E. Hsiao, D. Psaltis and C. Yang, "An optical tweezer actuated, nanoaperture-grid based Optofluidic Microscope implementation method," *Optics Express,* vol. 15, no. 25, pp. 16367-16375, 2007.

[236] "A Review of the Universe - Structures, Evolutions, Observations, and Theories," [Online]. Available: http://universe-review.ca/R10-33-anatomy04.htm.

[237] "www.wormatlas.org," [Online].

[238] R. Kerr, V. Lev-Ram, G. Baird, P. Vincent, R. Tsien and W. Schafer, "Optical imaging of calcium transients in neurons and pharyngeal muscle of C. elegans.," *Neuron.,* vol. 26, no. 3, pp. 583-594, 2000.

[239] S. Hulme, S. Shevkoplyas, J. Apfeld, W. Fontana and G. Whitesides, "A microfabricated array of clamps for immobilizing and imaging C. elegans.," *Lab Chip,* vol. 7, pp. 1515-1523, 2007.

[240] J. Sulston and J. Hodgkin, *The Nematode Caenorhabditis elegans, ed. Community of C. elegans Researchers,* vol. 17, 1988.

[241] J. A. Lewis, C. Wu, H. Berg and J. H. Levine, "The Genetics of Levamisole Resistance in the Nematode CAENORHABDITIS ELEGANS," *Genetics.,* vol. 95, no. 4, p. 905–928, 1980.

[242] D. Raizen and L. Avery, "Electrical activity and behavior in the pharynx of Caenorhabditis elegans.," *Neuron,* vol. 12, p. 483–495, 1994.

[243] G. M. Whitesides, "The origins and the future of microfluidics," *Nature,* vol. 442, no. 7101, pp. 368-373, 2006.

[244] A. San-Miguel and H. Lu., "Microfluidics as a tool for C. elegans research," WormBook: The Online Review of C. elegans Biology, [Online]. Available: https://www.ncbi.nlm.nih.gov/books/NBK174829/.

[245] A. Bretscher, K. Busch and M. d. Bono, "A carbon dioxide avoidance behavior is integrated with responses to ambient oxygen and food in Caenorhabditis elegans.," *Proc. Natl. Acad. Sci. U. S. A.,* vol. 105, pp. 8044-8049, 2008.

[246] E. Furlong, D. Profitt and M. Scott, "Automated sorting of live transgenic embryos.," *Nat. Biotechnol.,* vol. 19, p. 153–156, 2001.

[247] C. Chen, S. Zappe, O. Sahin, X. Zhang and M. Fish, "Design and operation of a microfluidic sorter for Drosophila embryos.," *Sens. Actuators B,* vol. 102, p. 59–66, 2004.

[248] T. J. Levario, B. Lim, S. Y. Shvartsman and H. Lu, "Microfluidics for High-Throughput Quantitative Studies of Early Development," *Annual Review of Biomedical Engineering,* vol. 18, pp. 285-309, 2016.

[249] D. Delubac, C. Highley, M. Witzberger-Krajcovic, J. Ayoob and E. Furbee, "Microfluidic system with integrated microinjector for automated Drosophila embryo injection.," *Lab Chip,* vol. 12, p. 4911–4919, 2012.

[250] K. Chung, Y. Kim, J. Kanodia, E. Gong, S. Shvartsman and H. Lu, "A microfluidic array for large-scale ordering and orientation of embryos.," *Nat. Methods,* vol. 8, p. 171–176, 2011.

[251] T. Levario, M. Zhan, B. Lim, S. Shvartsman and H. Lu, "Microfluidic trap array for massively parallel imaging of Drosophila embryos.," *Nat. Protoc.,* vol. 8, p. 721–736, 2013.

[252] D. Albrecht and C. Bargmann, "High-content behavioral analysis of Caenorhabditis elegans in precise spatiotemporal chemical environments.," *Nat. Methods,* vol. 8, pp. 599-605, 2011.

[253] A. Ben-Yakar, N. Chronis and H. Lu, "Microfluidics for the analysis of behavior, nerve regeneration, and neural cell biology in C. elegans.," *Curr. Opin. in Neurobiol.,* vol. 19, pp. 561-567, 2009.

[254] S. Chalasani, N. Chronis, M. Tsunozaki, J. Gray, D. Ramot, M. Goodman and C. Bargmann, "Dissecting a circuit for olfactory behaviour in Caenorhabditis elegans.," *Nature,* vol. 450, pp. 63-70, 2007.

[255] N. Chronis, "Worm chips : Microtools for C . elegans biology.," *Lab Chip,* vol. 10, pp. 432-437, 2010.

[256] N. Chronis, M. Zimmer and C. Bargmann, "Microfluidics for in vivo imaging of neuronal and behavioral activity in Caenorhabditis elegans.," *Nat. Methods,* vol. 4, pp. 727-731, 2007.

[257] M. Crane, K. Chung, J. Stirman and H. Lu, "Microfluidics-enabled phenotyping, imaging, and screening of multicellular organisms.," *Lab Chip,* vol. 10, pp. 1509-1517, 2010.

[258] J. Gray, D. Karow, H. Lu, A. Chang, J. Chang, R. Ellis, M. Marletta and C. Bargmann, "Oxygen sensation and social feeding mediated by a C. elegans guanylate cyclase homologue.," *Nature,* vol. 430, pp. 317-322, 2004.

[259] S. Hulme, S. Shevkoplyas and A. Samuel, "Microfluidics: streamlining discovery in worm biology.," *Nat. Methods,* vol. 5, pp. 589-590, 2008.

[260] S. Lockery, "Channeling the worm: microfluidic devices for nematode neurobiology.," *Nat. Methods,* vol. 4, pp. 691-692, 2007.

[261] S. Lockery, K. Lawton, J. Doll, S. Faumont, S. Coulthard, T. Thiele, N. Chronis, K. McCormick, M. Goodman and B. Pruitt, "Artificial dirt: microfluidic substrates for nematode neurobiology and behavior.," *J. Neurophysiol.,* vol. 99, pp. 3136-3143, 2008.

[262] K. McCormick, B. Gaertner, M. Sottile, P. Phillips and S. Lockery, "Microfluidic devices for analysis of spatial orientation behaviors in semi-restrained Caenorhabditis elegans.," *PLoS One,* vol. 6, p. e25710, 2011.

[263] M. Yanik, C. Rohde and C. Pardo-Martin, "Technologies for micromanipulating, imaging, and phenotyping small invertebrates and vertebrates.," *Annu. Rev. of Biomed. Eng.,* vol. 13, pp. 185-217, 2011.

[264] Y. Zhang, H. Lu and C. Bargmann, "Pathogenic bacteria induce aversive olfactory learning in Caenorhabditis elegans.," *Nature,* vol. 438, pp. 179-184, 2005.

[265] M. Zimmer, J. Gray, N. Pokala, A. Chang, D. Karow, M. Marletta, M. Hudson, D. Morton, N. Chronis and C. Bargmann, "Neurons detect increases and decreases in oxygen levels using distinct guanylate cyclases.," *Neuron,* vol. 61, pp. 865-879, 2009.

[266] Elveflow, [Online]. Available: https://www.elveflow.com/microfluidic-tutorials/cell-biology-imaging-reviews-and-tutorials/microfluidic-for-cell-biology/c-elegans-immobilization-via-microfluidics-a-short-review/.

[267] Y. Yan, L. Jiang, K. Aufderheide, G. Wright, A. Terekhov, L. Costa, K. Qin, W. McCleery, J. Fellenstein, A. Ustione, J. Robertson, C. Johnson, D. Piston, M. Hutson, J. Wikswo, W. Hofmeister and C. Janetopoulos, "A microfluidic-enabled mechanical microcompressor for the immobilization of live single- and multi-

cellular specimens," *Microscopy and Microanalysis,* vol. 20, no. 1, pp. 141-151, 2014.

[268] S. Mondal, S. Ahlawat, K. Rau, V. Venkataraman and S. Koushika, "Imaging in vivo Neuronal Transport in Genetic Model Organisms Using Microfluidic Devices," *Traffic,* vol. 12, no. 4, p. 372–385, 2011.

[269] K. Chung, M. Crane and H. Lu, "Automated on-chip rapid microscopy, phenotyping and sorting of C. elegans.," *Nat. Methods,* vol. 5, pp. 637-643, 2008.

[270] T. Chokshi, A. Ben-Yakar and N. Chronis, "CO2 and compressive immobilization of C. elegans on-chip.," *Lab Chip,* vol. 9, pp. 151-157, 2009.

[271] J. Krajniak and H. Lu, "Long-term high-resolution imaging and culture of C. elegans in chip-gel hybrid microfluidic device for developmental studies.," *Lab Chip,* vol. 10, pp. 1862-1868, 2010.

[272] S. Russell and S. Tickoo, "Drosophila melanogaster as a model system for drug discovery and pathway screening.," *Current Opinion in Pharmacology,* vol. 2, no. 5, pp. 555-560, 2002.

[273] E. Bier, "Drosophila, the golden bug, emerges as a tool for human genetics," *Nature Reviews Genetics* , vol. 6, no. 1, pp. 9-23, 2005.

[274] N. Ziv and M. Spira, "Localized and transient elevations of intracellular Ca2+ induce the dedifferentiation of axonal segments into growth cones," *Journal of Neuroscience,* vol. 17, no. 10, pp. 3568-3579, 1997.

[275] Z. Wu, A. Ghosh-Roy, M. Yanik, J. Zhang and Y. Jin, "Caenorhabditiselegans neuronal regeneration is influenced by life stage, ephrin signaling, and synaptic branching," *Proceedings of the National Academy of Sciences,* vol. 104, no. 38, p. 15132–15137, 2007.

[276] B. Neumann, K. Nguyen, D. Hall, A. Ben-Yakar and M. Hilliard, "Axonal regeneration proceeds through specific axonal fusion in transected C. elegans neurons," *Developmental Dynamics,* vol. 240, no. 6, p. 1365–1372, 2011.

[277] S. H. Chung, D. A. Clark, C. V. Gabel, E. Mazur and A. D. Samuel, "The role of the AFD neuron in C. elegans thermotaxis analyzed using femtosecond laser ablation," *BMC Neuroscience,* vol. 7, 2006.

[278] A. D. Pilling, D. Horiuchi, C. M. Lively and W. M. Saxton, "Kinesin-1 and Dynein Are the Primary Motors for Fast Transport of Mitochondria in Drosophila Motor Axons," *Molecuar Biology of the Cell,* vol. 17, no. 4, pp. 2057-2068, 2006.

[279] S. Gunawardena, L.-S. Her, R. G. Brusch, R. A. Laymon, I. R. Niesman, B. Gordesky-Gold, L. Sintasath, N. M. Bonini and L. S. Goldstein, "Disruption of Axonal Transport by Loss of Huntingtin or Expression of Pathogenic PolyQ Proteins in Drosophila," *Neuron,* vol. 40, no. 1, p. 25–40, 2003.

[280] K. E. Miller, J. DeProto, N. Kaufmann, B. N. Patel, A. Duckworth and D. V. Vactor, "Direct Observation Demonstrates that Liprin-α Is Required for Trafficking of Synaptic Vesicles," *Current Biology,* vol. 15, no. 7, p. 684–689, 2005.

[281] H. Idse, L. Thomas and L. Loïc, "Dynamic clonal analysis based on chronic in vivo imaging allows multiscale quantification of growth in the Drosophila wing disc," *Development,* vol. 141, pp. 2339-2348, 2014.

[282] N. Ulrike, A.-W. Tinri and M. A. Christof, "In-Vivo Imaging of the Drosophila Wing Imaginal Disc over Time: Novel Insights on Growth and Boundary Formation," *PLOS ONE,* vol. 7, no. 10, 2012.

[283] D. J. Sandstrom, "Isoflurane Reduces Excitability of Drosophila Larval Motoneurons by Activating a Hyperpolarizing Leak Conductance," *Anesthesiology,* vol. 108, no. 3, pp. 434-446, 2008.

[284] D. J. Sandstrom, "Isoflurane depresses glutamate release by reducing neuronal excitability at the Drosophila neuromuscular junction," *The Journal of Physiology,* vol. 558, no. 2, p. 489–502, 2004.

[285] R. Simon and B. Konrad, "Drosophila wing imaginal discs respond to mechanical injury via slow InsP3R-mediated intercellular calcium waves," *Nature Communications,* 2015.

[286] M. Unger, H. Chou, T. Thorsen, A. Scherer and S. Quake, "Monolithic microfabricated valves and pumps by multilayer soft lithography," *Science,* vol. 288, no. 5463, pp. 113-116, 2000.

[287] G. M. Whitesides, E. Ostuni, S. Takayama, X. Jiang and D. E. Ingber, "Soft Lithography in Biology and Biochemistry," *Annual Review of Biomedical Engineering,* vol. 3, pp. 335-373, 2001.

[288] C. Kwanghun, M. Crane Matthew and L. Hang, "Automated on-chip rapid microscopy, phenotyping and sorting of C. elegans," *Nature Methods,* vol. 5, pp. 637 - 643, 2008.

[289] B. R. Christopher and F. Y. Mehmet, "Subcellular in vivo time-lapse imaging and optical manipulation of Caenorhabditis elegans in standard multiwell plates," *Nature Communications,* 2011.

[290] A. R. Chaudhury, R. Insolera, R. D. Hwang, Y. W. Fridell, C. Collins and N. Chronis, "On chip cryo-anesthesia of Drosophila larvae for high resolution in vivo imaging applications.," *Lab on a Chip,* vol. 17, no. 13, pp. 2303-2322, 2017.

[291] S. Pankiv, T. Clausen, T. Lamark, A. Brech, J. Bruun, H. Outzen, A. Øvervatn, G. Bjørkøy and T. Johansen, "p62/SQSTM1 binds directly to Atg8/LC3 to facilitate degradation of ubiquitinated protein aggregates by autophagy.," *The Journal of Biological Chemistry,* vol. 282, no. 33, pp. 24131-24145, 2007.

[292] I. Nezis, B. Shravage, A. Sagona, T. Lamark, G. Bjørkøy, T. Johansen, T. Rusten, A. Brech, E. Baehrecke and H. Stenmark, "Autophagic degradation of dBruce controls DNA fragmentation in nurse cells during late Drosophila melanogaster oogenesis," *The Journal of Cell Biology,* vol. 190, no. 4, pp. 523-531, 2010.

[293] S. Sankaranarayanan, D. De Angelis, J. Rothman and T. Ryan, "The use of pHluorins for optical measurements of presynaptic activity," *Biophysical Journal,* vol. 79, no. 4, pp. 2199-2208., 2000.

[294] K. Poskanzer, K. Marek, S. Sweeney and G. Davis, "Synaptotagmin I is necessary for compensatory synaptic vesicle endocytosis in vivo," *Nature,* vol. 426, no. 6966, pp. 559-563, 2003.

[295] D. Reiff, A. Ihring, G. Guerrero, E. Isacoff, M. Joesch, J. Nakai and A. Borst, "In vivo performance of genetically encoded indicators of neural activity in flies," *The Journal of Neuroscience,* vol. 25, no. 19, pp. 4766-4778, 2005.

[296] B. Fosque, Y. Sun, H. Dana, C. Yang, T. Ohyama, M. Tadross, R. Patel, M. Zlatic, D. Kim, M. Ahrens, V. Jayaraman, L. Looger and E. Schreiter, "Neural circuits. Labeling of active neural circuits in vivo with designed calcium integrators," *Science,* vol. 347, no. 6223, pp. 755-760, 2015.

[297] M. Tantama, J. Martínez-François, R. Mongeon and G. Yellen, "Imaging energy status in live cells with a fluorescent biosensor of the intracellular ATP-to-ADP ratio," *Nature Communications,* vol. 4, no. 2550, 2013.

[298] T. Tsuyama, J. Kishikawa, Y. Han, Y. Harada, A. Tsubouchi, H. Noji, A. Kakizuka, K. Yokoyama, T. Uemura and H. Imamura, "In vivo fluorescent adenosine 5'-triphosphate (ATP) imaging of Drosophila melanogaster and Caenorhabditis elegans by using a genetically encoded fluorescent ATP biosensor optimized for low temperatures," *Analytical Chemistry,* vol. 85, no. 16, pp. 7889-7896, 2013.

[299] Z. Wang, A. A. Volinsky and N. D. Gallant, "Crosslinking Effect on Polydimethylsiloxane Elastic Modulus Measured by Custom-Built Compression Instrument.," *Journal of Applied Polymer Science,* vol. 131, no. 22, pp. 41050-41053, 2014.

[300] D. Guarnieri and U. Heberlein, "Drosophila melanogaster, a genetic model system for alcohol research," *International Review of Neurobiology,* vol. 54, pp. 199-228, 2003.

[301] Y. Heo, L. Cabrera, J. Song, N. Futai, Y. Tung, G. Smith and S. Takayama, "Characterization and resolution of evaporation-mediated osmolality shifts that constrain microfluidic cell culture in poly(dimethylsiloxane) devices," *Analytical Chemistry,* vol. 79, no. 3, p. 1126–1134, 2007.

[302] Y. Yu, H. Lee, K. Chen, J. Suhan, M. Qiu, Q. Ba and G. Yang, "Inner membrane fusion mediates spatial distribution of axonal mitochondria.," *Scientific Reports,* vol. 6, no. 18981, pp. 1-14, 2016.

[303] S. Devireddy, H. Sung, P. Liao, E. Garland-Kuntz and P. Hollenbeck, "Analysis of mitochondrial traffic in Drosophila.," *Methods in Enzymology,* vol. 547, p. 131–150, 2014.

[304] K. Harris and J. Littleton, "Transmission, Development, and Plasticity of Synapses.," *Genetics,* vol. 201, no. 2, pp. 345-375, 2015.

[305] K. Zito, D. Parnas, R. Fetter, E. Isacoff and C. Goodman, "Watching a synapse grow: noninvasive confocal imaging of synaptic growth in Drosophila.," *Neuron,* vol. 22, no. 4, pp. 719-729, 1999.

[306] T. Rasse, W. Fouquet, A. Schmid, R. Kittel, S. Mertel, C. Sigrist, M. Schmidt, A. Guzman, C. Merino, G. Qin, C. Quentin, F. Madeo, M. Heckmann and S. Sigrist, "Glutamate receptor dynamics organizing synapse formation in vivo.," *Nature Neuroscience,* vol. 8, no. 7, pp. 898-905, 2005.

[307] K. Venken, K. Schulze, N. Haelterman, H. Pan, Y. He, M. Evans-Holm, J. Carlson, R. Levis, A. Spradling, R. Hoskins and H. Bellen, "MiMIC: a highly versatile transposon insertion resource for engineering Drosophila melanogaster genes.," *Nature Methods,* vol. 8, no. 9, pp. 737-743, 2011.

[308] H. B. Nicholas, M. M. Elisabeth and C. Robin L., "The physiological and behavioral effects of carbon dioxide on Drosophila melanogaster larvae," *Comparitive Biochemistry and Physiology, Part A,* vol. 140, pp. 363-376, 2005.

[309] K. Vladimír, K. Jaroslava, Š. Tomáš, P. Rodolphe, C. Hervé, Z. Helena, O. Iva, M. Martin and Š. Petr, "Physiological basis for low-temperature survival and storage of quiescent larvae of the fruit fly Drosophila melanogaster," *Scientific Reports,* vol. 6, no. 32346, 2016.

[310] N. Selvakumar and H. C. Barshilia, "Review of physical vapor deposited (PVD) spectrally selective coatings for mid- and high-temperature solar thermal applications.," *Solar Energy Materials and Solar Cells,* vol. 98, pp. 1-23, 2012.

[311] R. Hwang, L. Wiemerslage, C. LaBreck, M. Khan, K. Kannan, X. Wang, X. Zhu, D. Lee and Y. Fridell, "The neuroprotective effect of human uncoupling protein 2 (hUCP2) requires cAMP-dependent protein kinase in a toxin model of Parkinson's disease.," *Neurobiology of disease,* vol. 69, pp. 180-191, 2014.

[312] E. Brace, W. Chunlai, V. Vera and D. Aaron, "SkpA Restrains Synaptic Terminal Growth during Development and Promotes Axonal Degeneration following Injury," *Journal of Neuroscience,* vol. 34, no. 25, pp. 8398-8410, 2014.

[313] X. Xiong, X. Wang, R. Ewanek, P. Bhat, A. Diantonio and C. Collins, "Protein turnover of the Wallenda/DLK kinase regulates a retrograde response to axonal injury," *The Journal of Cell Biology,* vol. 191, no. 1, pp. 211-223, 2010.

[314] B. Mishra, M. Ghannad-Rezaie, J. Li, X. Wang, Y. Hao, B. Ye, N. Chronis and C. Collins, "Using Microfluidics Chips for Live Imaging and Study of Injury Responses in Drosophila Larvae.," *Journal of Visualized Experiments,* vol. 84, 2014.

[315] R. C. Gonzales, Digital Image Processing, New Jersey: Prentice-Hall, 2006.

[316] K. Dunn, M. Kamocka and J. McDonald, "A practical guide to evaluating colocalization in biological microscopy," *American Journal of Physiology - Cell Physiology,* vol. 300, no. 4, pp. C723-C742, 2011.

[317] C. Hongmin, Y. Zhong, C. Xinhua, X. Weiming and X. Xiaoyin, "A New Iterative Triclass Thresholding Technique," *IEEE Transactions on Image Processing,* vol. 23, no. 3, pp. 1038-1047, 2014.

[318] X. Maldague, T. Jones, H. Kaplan, S. Marinetti and M. Prystay, Nondestructive Handbook, Infrared and Thermal Testing, Volume 3, Columbus: ASNT Press, 2001.

[319] G. Lettre and M. O. Hengartner, "Developmental apoptosis in C. elegans: a complex CEDnario.," *Nature Reviews Molecular Cell Biology,* vol. 7, no. 2, pp. 97-108, 2006.

[320] L. Herndon, P. Schmeissner, J. Dudaronek, P. Brown, K. Listner, Y. Sakano, M. Paupard, D. Hall and M. Driscoll, "Stochastic and genetic factors influence tissue-specific decline in ageing C. elegans.," *Nature,* vol. 419, no. 6909, pp. 808-814, 2002.

[321] O. Hobert, "Behavioral plasticity in C. elegans: paradigms, circuits, genes.," *J Neurobiol.,* vol. 54, no. 1, pp. 203-223, 2003.

[322] S. Emmons and J. Lipton, "Genetic basis of male sexual behavior.," *J Neurobiol.,* vol. 54, no. 1, pp. 93-110, 2003.

[323] L. Avery and B. Shtonda, "Food transport in the C. elegans pharynx.," *J Exp Biol.,* vol. 206, no. Pt 14, pp. 2441-257, 2003.

[324] I. Mori and Y. Ohshima, "Neural regulation of thermotaxis in Caenorhabditis elegans.," *Nature,* vol. 376, no. 6538, pp. 344-352, 1995.

[325] M. Yanik, H. Cinar, H. Cinar, A. Chisholm, Y. Jin and A. Ben-Yakar, "Neurosurgery: functional regeneration after laser axotomy.," *Nature*, vol. 432, no. 7019, p. 822, 2004.

[326] A. Nagy, N. Perrimon, S. Sandmeyer and R. Plasterk, "Tailoring the genome: the power of genetic approaches.," *Nat. Genet.*, vol. 33(Suppl.), p. 276–284, 2003.

[327] N. Stroustrup, B. E. Ulmschneider, Z. M. Nash, I. F. López-Moyado, J. Apfeld and W. Fontana, "The Caenorhabditis elegans Lifespan Machine.," *Nature Methods* , vol. 10, p. 665–670, 2013.

[328] M. Goodman, D. Hall, L. Avery and S. Lockery, "Active currents regulate sensitivity and dynamic range in C. elegans neurons.," *Neuron.*, vol. 20, no. 4, pp. 763-772, 1998.

[329] J. Hodgkin, R. Plasterk and R. Waterston, "The nematode Caenorhabditis elegans and its genome.," *Science.*, vol. 270, no. 5235, pp. 410-414, 1995.

[330] S. X. Guo, F. Bourgeois, T. Chokshi, N. J. Durr, M. A. Hilliard, N. Chronis and A. Ben-Yakar, "Femtosecond laser nanoaxotomy lab-on-a-chip for in vivo nerve regeneration studies," *Nature Methods*, vol. 5, no. 6, pp. 531-533, 2008.

[331] F. Zeng, C. B. Rohde and M. F. Yanik, "Sub-cellular precision on-chip small-animal immobilization, multi-photon," *Lab on Chip*, vol. 8, p. 653–656, 2008.

[332] D. Beebe, G. Mensing and G. Walker, "Physics and applications of microfluidics in biology.," *Annu Rev Biomed Eng.*, vol. 4, pp. 261-286, 2002.

[333] A. Waldbaur, H. Rapp, K. Längea and B. E. Rapp, "Let there be chip—towards rapid prototyping of microfluidic devices: one-step manufacturing processes," *Analytical Methods*, vol. 12, pp. 2681-2716 , 2011.

[334] G. M. Whitesides, "Cool, or simple and cheap? Why not both?," *Lab on Chip*, vol. 13, pp. 11-13, 2013.

[335] T. Horn and O. Harrysson, "Overview of current additive manufacturing technologies and selected applications.," *Sci Prog.*, vol. 95, no. Pt 3, pp. 255-282, 2012.

[336] B. Gross, J. Erkal, S. Lockwood, C. Chen and D. Spence, "Evaluation of 3D printing and its potential impact on biotechnology and the chemical sciences.," *Anal Chem.,* vol. 86, no. 7, pp. 3240-3253, 2014.

[337] A. Bertsch and P. Renaud, Microstereolithography, Boston, MA: Springer, 2011.

[338] K. Sharabia, A. Hurwitza, A. J. Simonb, G. J. Beitelc, R. I. Morimotoc, G. Rechavib, J. I. Sznajderd and Y. Gruenbauma, "Elevated CO2 levels affect development, motility, and fertility and extend life span in Caenorhabditis elegans.," *Proceedings of the National Academy of Sciences,* vol. 106, no. 10, p. 4024–4029, 2008.

[339] C. J. Luke, J. Z. Niehaus, L. P. O'Reilly and S. C. Watkinsb, "Non-microfluidic methods for imaging live C. elegans.," *Methods.* , vol. 68, no. 3, p. 542–547, 2014.

[340] D. Mitchell, J. Stiles, J. Santelli and D. Sanadi, "Synchronous growth and aging of Caenorhabditis elegans in the presence of fluorodeoxyuridine.," *J Gerontol.,* vol. 34, no. 1, pp. 28-36, 1979.

[341] T. Kimata, H. Sasakura, N. Ohnishi, N. Nishio and I. Mori, "Thermotaxis of C. elegans as a model for temperature perception, neural information processing and neural plasticity.," *Worm.,* vol. 1, no. 1, p. 31–41, 2012.

[342] A. Ward, J. Liu, Z. Feng and X. Z. S. Xu, "Light-sensitive neurons and channels mediate phototaxis in C. elegans.," *Nat Neurosci.* , vol. 11, no. 8, p. 916–922, 2008.

[343] E. Troemel, "Chemosensory signaling in C. elegans.," *Bioessays.,* vol. 21, no. 12, pp. 1011-1020, 1999.

[344] L. Theogarajan, "Strategies for restoring vision to the blind: Current and emerging technologies.," *Neurosci. Lett.,* vol. 519, p. 129–133, 2012.

[345] [Online]. Available: http://www.laser-eye-surgery-review.com/.

[346] "U.S. National Library of Medicine," NIH, [Online]. Available: https://ghr.nlm.nih.gov/condition/early-onset-glaucoma.

[347] C. Jin-Chern, H. Yu-Chieh and Y. Guan-Ting, "A capacitor-based sensor and a contact lens sensing system for intraocular pressure monitoring," *Journal of Micromechanics and Microengineering,* vol. 26, no. 1, 2016.

[348] S. Á. F. Lopes, "Social representations of community-acquired infection by primary care professionals.," *Acta paul. enferm.,* vol. 28, no. 5, pp. 454-459, 2015.

[349] [Online]. Available: https://en.wikipedia.org/wiki/Hospital-acquired_infection.

[350] H. A. Lilly and E. J. Lowbury, "Transient skin flora: their removal by cleansing or disinfection in relation to their mode of deposition.," *J Clin Pathol.,* vol. 31, no. 10, pp. 919-922, 1978.

[351] D. Pittet, "Improving adherence to hand hygiene practice: a multidisciplinary approach.," *Emerg Infect Dis.,* vol. 7, no. 2, p. 234–240, 2001.

[352] G. Bergmann, F. Graichen, J. Dymke, A. Rohlmann, G. Duda and P. Damm, "High-tech hip implant for wireless temperature measurements in vivo.," *PLoS One,* vol. 7, 2012.

[353] S. Kelly, D. Shire, C. Jinghua, P. Doyle, M. Gingerich, S. Cogan, W. Drohan, S. Behan, L. Theogarajan and J. Wyatt, "A hermetic wireless subretinal neurostimulator for vision prostheses.," *IEEE Trans. Biomed. Eng.,* vol. 58, pp. 3197-3205, 2011.

[354] J. Koo, J. Seo and T. Lee, "Nanomaterials on flexible substrates to explore innovative functions: From energy harvesting to bio-integrated electronics.," *Thin Solid Films,* vol. 524, p. 1–19, 2012.

[355] R. Farra, N. Sheppard, L. McCabe, R. Neer, J. Anderson, J. Santini, M. Cima and R. Langer, "First-in-human testing of a wirelessly controlled drug delivery microchip.," *Sci. Transl. Med.,* vol. 4, p. 122–122ra21, 2012.

[356] J. Garner and M. Favero, "CDC Guideline for Handwashing and Hospital Environmental Control, 1985.," *Infect Control.,* vol. 7, no. 4, pp. 231-243, 1986.

[357] A. Pickering, A. Boehm, M. Mwanjali and J. Davis, "Efficacy of Waterless Hand Hygiene Compared with Handwashing with Soap: A Field Study in Dar es Salaam, Tanzania.," *The American Journal of Tropical Medicine and Hygiene.,* vol. 82, no. 2, pp. 270-278, 2010.

[358] D. Maki and J. Hecht, "Antiseptic containing hand-washing agents reduce nosocomial infections: a prospective study," *22nd Program and abstracts of the Interscience Conference of Antimicrobial Agents and Chemotherapy, Miami, Oct 4-6, Washington,* 1982.